



3 1293 00892 9667

This is to certify that the
thesis entitled
**USE OF CONCURRENT TASKS
FOR EFFECTIVE STRUCTURAL CONTROL MODELING**

presented by
MARK WOLSCHON

has been accepted towards fulfillment
of the requirements for
M.S. degree in MECH ENG

C. V. Gandhi
Major professor

Date 7/16/93



PLACE IN RETURN BOX to remove this checkout from your record.
TO AVOID FINES return on or before date due.

DATE DUE	DATE DUE	DATE DUE
081		

**USE OF CONCURRENT TASKS
FOR EFFECTIVE STRUCTURAL CONTROL MODELING**

By

Mark Edward Wolschon

A THESIS

**Submitted to
Michigan State University
in partial fulfillment of the requirements
for the degree of**

MASTER OF SCIENCE

Department of Mechanical Engineering

1993

ABSTRACT

USE OF CONCURRENT TASKS FOR EFFECTIVE STRUCTURAL CONTROL MODELING

By

Mark Edward Wolschon

Concurrent engineering is the simultaneous acquisition, dissemination, and application of multi-disciplinary information during product design. Over the past decade it has been applied successfully to almost every aspect of the product life cycle. However, its use in analysis, testing, and mathematical modeling has been limited. In this study, a procedure based on concurrent engineering principles is presented for developing and evaluating mathematical models for actively controlled structures. One advantage of this procedure is that it exploits uncertain linear systems analysis and the methods of robust control design. Specifically, it assumes and treats the model not as a single, precise entity but rather as a set of models, inside of which the actual system lies. As an example we apply the procedure to a cantilever beam with a concentrated tip mass. Subsequently, the procedure is applied to a distributed-parameter plate structure that incorporates a distributed-parameter actuator.

**To my parents,
for all their inspiration and support,**

ACKNOWLEDGEMENTS

The author wishes to express his thanks Dr. Mukesh V. Gandhi, Dr. Philip M. FitzSimons, and Dr. Brian Feeny for serving as his thesis committee and for their helpful considerations and recommendations. Special thanks is extended to Dr. FitzSimons, whose countless hours of consultation and information have proved invaluable for this and other projects. His help, guidance, and inspiration has provided an environment where professional, as well as, academic skills could be developed.

In addition, the author would like to thank the faculty and students in the Intelligent Materials and Structures Laboratory at Michigan State University for providing the ideas and resources necessary to complete portions of this thesis.

Finally, the finished version of this thesis would not have been possible without the help and encouragement of Kelly S. Ulrich. Her patience, proof-reading and corrections, and undivided moral support are gratefully and greatly appreciated.

TABLE OF CONTENTS

List of Tables	<u>Page</u> viii
List of Figures	ix
 <u>Chapter 1</u> - INTRODUCTION	
1.0 Motivation Behind Work	1
1.1 Thesis-Related Background Topics	6
1.1.1 Concurrent engineering	6
1.1.2 Structural control	8
1.1.3 Spatially-distributed actuators	14
1.2 Some Issues in Practical Structural Control Design	17
1.2.1 Obtaining reduced-order models	18
1.2.2 Actuator modeling and dynamics	21
1.3 Thesis Organization	23
 <u>Chapter 2</u> - A METHOD FOR CONCURRENT STRUCTURAL CONTROL MODELING	
2.0 Introduction	25
2.1 Large-Scale System Modeling	26
2.1.1 Modeling uncertainty in systems	29
2.1.2 Modeling the system in the presence of uncertainty	31

2.2 A Concurrent Modeling Method for Large-Scale Systems	40
2.2.1 The analysis problem	41
2.2.2 The synthesis problem	43
2.3 A Numerical Example	48
2.3.1 Analytical analysis formulation	48
2.3.2 Experimental analysis formulation	57
2.3.3 Synthesis problem formulation	65
2.4 Chapter Summary	80
 <u>Chapter 3</u> - EXPERIMENTAL ANALYSIS FORMULATION FOR A DISTRIBUTED-PARAMETER STRUCTURE	
3.0 Introduction	80
3.1 Electrorheological Fluids	82
3.1.1 Rheology of suspensions	82
3.1.2 The electrical behavior of ER fluids	84
3.1.3 The rheological behavior of ER fluids	89
3.2 Constitutive Model for the Actuator	93
3.2.1 Preliminary considerations	93
3.2.2 Identification of an electrorheological fluid	95
3.2.3 A model for the actuator	102
3.2.4 Numerical comparisons	105
3.3 Electrorheological Plate Identification	113
3.3.1 Experimental apparatus	115
3.3.2 Plate modal analysis	116
3.3.3 Input verification	122
3.3.4 Electrical and rheological dynamic coupling	134

3.4 Chapter Summary	137
<u>Chapter 4</u> - ANALYTICAL AND NUMERICAL ANALYSIS FORMULATIONS FOR A DISTRIBUTED-PARAMETER STRUCTURE	
4.0 Introduction	139
4.1 Structural Kinematics	141
4.2 Constitutive Equations	149
4.3 Governing Equations	156
4.4 Comparative Results	165
4.4.1 Static results	165
4.4.2 Dynamic results	168
4.5 Chapter Summary	175
<u>Chapter 5</u> - CONCLUDING REMARKS AND RECOMMENDATIONS FOR FUTURE WORK	177
BIBLIOGRAPHY	180

LIST OF TABLES

	<u>Page</u>
Table 2.1 Material and geometric properties for the flexible beam configuration.	54
Table 2.2 Measured cantilevered beam natural frequencies.	59
Table 2.3 A comparison between measured and calculated cantilever beam natural frequencies.	60
Table 2.4 Measured cantilever beam damping ratios.	60
Table 2.5 Physical bounds on model parameters.	63
Table 3.1 Dimensions for the two actuator models.	108
Table 3.2 Experimentally determined damping ratios at $V = 0$ kV.	121
Table 3.3 Experimentally determined plate natural frequencies.	123
Table 4.1 Material and geometric properties for the plate configuration.	167
Table 4.2 Nondimensionalized deflections for two three-layer sandwich plates.	168
Table 4.3 Comparison of the measured and computed natural frequencies for the square plate.	172
Table 4.4 Comparison of the measured and computed natural frequencies for the rectangular plate.	172
Table 4.5 Material Properties for the composite structural layers.	173

LIST OF FIGURES

	<u>Page</u>
Figure 1.1 The electrorheological effect.	16
Figure 1.2 Principles of practical low-order control design.	19
Figure 2.1 A standard large-scale system modeling procedure.	27
Figure 2.2 Generalized uncertainty problem where the actual dynamic system $M^* \in Z$.	29
Figure 2.3 Common perturbation structures for representing uncertainty.	33
Figure 2.4 A general block-diagonal bounded perturbation diagram.	35
Figure 2.5 An example of a plant with weighted multiplicative input and output uncertainty.	39
Figure 2.6 A hierarchical structure for constructing and completing the <i>analysis problem</i> for large-scale systems.	42
Figure 2.7 A concurrent scheme for evaluating dynamical system models and uncertainty.	44
Figure 2.8 A generalized nominal and uncertainty model optimization procedure.	46
Figure 2.9 An example of uncertainty regions for a family Γ graphically shown in the Nyquist plane.	47
Figure 2.10 The configuration for the cantilever beam example.	48
Figure 2.11 The variation of λ_k with concentrated tip mass ratio.	50
Figure 2.12 First four normal mode shapes for various concentrated tip mass ratios.	51
Figure 2.13 Step input response for various concentrated tip mass ratios.	55
Figure 2.14 Step input response for various beam bending stiffness.	55

Figure 2.15	Step input response for various values of β with α constant.	56
Figure 2.16	Step input response for various values of α with β constant.	56
Figure 2.17	Receptance response for various mass ratios.	58
Figure 2.18	Transient impulse response of the beam tip for two mass ratios.	61
Figure 2.19	Transient step response of the beam tip for two mass ratios.	62
Figure 2.20	Fuzzy Nyquist diagram associated with plant set.	66
Figure 2.21	Local fuzzy Nyquist diagram showing parametric uncertainty.	67
Figure 2.22	A pole-zero map outlining global uncertainty regions included in the plant set.	68
Figure 2.23	Pole map showing averaged poles and their associated uncertainty regions.	68
Figure 2.24	Bode plots for the three 4-mode nominal models.	69
Figure 2.25	Step response of the lower and upper parametric uncertainty bounds.	71
Figure 2.26	Multiplicative uncertainty for both lower and upper perturbations on A.	71
Figure 2.27	A comparison of the SV and SSV representations for M.	73
Figure 2.28	SSV stability evaluation for the parametric uncertainty model.	74
Figure 2.29	SSV stability evaluation for the nonparametric uncertainty models.	76
Figure 2.30	Variation of additive nonparametric uncertainty and frequency bound.	78
Figure 3.1	A strain rate versus viscosity curve for a typical suspension.	83
Figure 3.2	Representative colloidal interaction potential over particle surface separation.	86
Figure 3.3	Double-electric layer theory for ER fluids.	87
Figure 3.4	Changes in the structure as a result of dielectric polarization of the suspension.	88
Figure 3.5	A schematic of observed shear stress/strain behavior of an ER fluid.	90
Figure 3.6	A figurative description of the shear stress versus shear-rate Bingham model fit.	91

Figure 3.7	Isothermal shear modulus for the insulate material.	95
Figure 3.8	Shear modulus curve fit for the insulate material data at 25 °C.	96
Figure 3.9	Experimentally determined non-Newtonian viscosity for a hydrous ER fluid.	97
Figure 3.10	Experimentally determined shear stress for a hydrous ER fluid.	97
Figure 3.11	Curve fit comparison for the non-Newtonian viscosity of the ER fluid.	98
Figure 3.12	Curve fit comparison for the shear stress of the ER fluid.	99
Figure 3.13	Equivalent transient electrical behavior for an ER fluid.	100
Figure 3.14	Actual voltage of the ER fluid medium for an applied electric field of 2 kV.	100
Figure 3.15	A comparison between experimental and simulated voltages for the ER fluid medium.	102
Figure 3.16	Geometric configuration of the actuator and its unit cell.	104
Figure 3.17	Geometric configuration and loading of the actuator models.	106
Figure 3.18	Discretized geometry for the two models.	107
Figure 3.19	Time response of the ER fluid model under periodic excitation.	109
Figure 3.20	Power spectral density of the ER fluid model for various constant voltage inputs.	111
Figure 3.21	Steady-state comparison between models 1 and 2 for zero voltage input.	112
Figure 3.22	Deformed configurations for: (a) model 1, and (b) model 2 for zero voltage input.	112
Figure 3.23	Time response of the actuator model under periodic excitation.	114
Figure 3.24	Power spectral density of the actuator model for various constant voltage inputs.	114
Figure 3.25	Schematic of the two plate specimens.	115
Figure 3.26	Experimental arrangement and instrumentation.	117
Figure 3.27	Experimental plate discretization.	117

Figure 3.28	Receptance for: (a)square plate, and (b) rectangular plate at $V = 0$ kV.	119
Figure 3.29	Mobility frequency response for the square plate at $V = 0$ kV.	119
Figure 3.30	Mobility frequency response for the rectangular plate at $V = 0$ kV.	120
Figure 3.31	Mobility responses for: the (a) square, and (b) rectangular plates at $V = 0$ kV.	120
Figure 3.32	Mode shape identification results for each plate at $V = 0$ kV.	121
Figure 3.33	Transient response of the rectangular plate for $V = 2$ kV and $\Omega = 0.5$ Hz.	124
Figure 3.34	Transient response of the rectangular plate for $V = 2$ kV and $\Omega = 0.5$ Hz.	125
Figure 3.35	Transient response of the rectangular plate for $V = 2$ kV and $\Omega = 0.5$ Hz.	125
Figure 3.36	Transient response of the square plate for $V = 2$ kV and $\Omega = 0.5$ Hz.	125
Figure 3.37	Frequency response of the rectangular plate for a sinusoidal input of $V = 2$ kV.	127
Figure 3.38	Frequency response of the rectangular plate for a sinusoidal input of $V = 2$ kV.	127
Figure 3.39	Frequency response of the recangular plate for a square input of $V = 2$ kV.	128
Figure 3.40	Frequency response of the square plate for a square input of $V = 2$ kV.	128
Figure 3.41	Frequency response of the recangular plate for a pulse input of $V = 2$ kV.	129
Figure 3.42	Frequency response of the square plate for a pulse input of $V = 2$ kV.	129
Figure 3.43	Frequency response of the recangular plate for different voltage inputs at $\Omega = 1$ Hz.	130
Figure 3.44	Frequency response of the square plate for different voltage inputs at $\Omega = 1$ Hz.	131

Figure 3.45	Mode shape identification for the square plate activated with a square pulse voltage input at various frequency.	133
Figure 3.46	Mode shape identification for the rectangular plate activated with a square pulse voltage input at various frequency.	134
Figure 3.47	Reduction of the ER effect with time for a pulse length of 10 msec.	135
Figure 3.48	Reduction of the ER effect with time for a pulse length of 500 msec.	135
Figure 3.49	Reduction of the ER effect with time for a pulse length of 1 second.	136
Figure 3.50	Reduction of the ER effect with time for a pulse length of 5 seconds.	136
Figure 4.1	Cross-section in the x-z plane of a distributed-parameter composite structure.	141
Figure 4.2	Cross-section in the x-z plane of the displacement pattern for the structure.	143
Figure 4.3	A single structural layer fabricated as a composite laminate.	149
Figure 4.4	Configuration of the distributed-parameter plate.	157
Figure 4.5	Discretized geometry for a quarter of the distributed-parameter rectangular plate.	169
Figure 4.6	Mode shape results for both plates at $V = 0$ kV.	170
Figure 4.7	Mode shapes for the clamped-edge square plate.	173
Figure 4.8	Natural frequencies for a multi-layered square clamped-edge (a) aluminum plate, and (b) composite plate for $V = 0$ kV.	174
Figure 4.9	Natural frequencies for a three-layer square clamped-edge aluminum plate with varying actuator thickness and $V = 0, 1$ and 2 kV.	174

Chapter 1

INTRODUCTION

1.0 Motivation Behind Work

Competition on a global scale has driven every sector of American industry to search for greater efficiency and productivity in the product life cycle. Striving to improve a product while maintaining high quality, minimal cost, and shorter concept-to-market life is a challenging task. Since performance is dependent on myriad conditions that enter all phases of product life, the challenge to produce successful products can be met only with careful planning and systematic execution. With an organized plan, a particular idea or concept can be designed so that major tasks, operations, and requirements are considered in the initial stages of development. Subsequent execution of the development plan must then include an ability to address problems that occur during development in a quick and truly logical and rational manner. Systematic execution possesses this capability and can produce solutions to these problems very quickly. Clearly, product development strategies that are based on an organized and systematic plan and that do not impose any restrictions on creativity and innovation are very useful to the design engineer.^{27, 33} The ability to strive to improve and to guarantee the success of the product will be directly related to these amenable characteristics of the product life cycle, and their use will definitely determine future global leaders in industry.

Strategies that have such salient features are known throughout the industrial community as *concurrent engineering*, *simultaneous engineering*, or *design-for-manufacture and assembly*. These development strategies are not new, but are very different from conventional industrial practices. Success stories have been mainly esoteric in knowledge. Unfortunately, a majority of industries have relegated these methods to a level of thinking believed to be too difficult to employ in existing technology. This expectation may be attributed to the large investments of time and money deemed necessary to replace traditional product lines with concurrent ones.²⁷ We find that significant product development changes in conventional practices have been very slow. Therefore, in order to capitalize on the advantages that these methods may have, it is essential to break traditional barriers and introduce new, innovative concepts, and products using a concurrent approach.

Innovative design concepts and ideas that have potential commercial marketability must be synthesized in a manner that guarantees their success. We find that many of the potential problems associated with traditional product development are a direct result of an unsystematic, inefficient allocation of resources, and an inappropriate processing of information, experience, and knowledge. For these reasons, conventional techniques needlessly make efficient and effective product development an insurmountable challenge.

In this thesis the preliminary stages of a particular concept that involves structural control is investigated in an attempt to provide computer-based tools necessary for concurrent engineering tasks. These preliminary stages will include research, theoretical studies, testing, experimental development, and analysis, not necessarily in any specific order. The problems associated with the preliminary stages of structural control design are problems that arise because of the multidisciplinary nature of the field. Structural control involves a large number of engineering disciplines, in particular, analytical dynamics, structural dynamics and testing analysis, materials science, and control system theory. In the sense of concurrent engineering, the various

disciplinary functions might be planned for optimal execution in a parallel fashion. Such functions will include obtaining a mathematical model of the structure and of all its components, reducing the order of the model for practical considerations, verifying the reduced-order dynamic model for acceptable accuracy, and optimizing and implementing a control strategy that accommodates the reduced-order dynamic model and that meets stability constraint and all required levels of performance. It is possible to execute several of these functions concurrently and with significant improvement in design quality and accuracy through the use of computer-based tools. Therefore, we see that through extensive preliminary planning, concurrent functions can be linked to tasks that allow the design engineer to address specific problems.

Problems arising in these stages of structural control modeling are attributable to the fact that they are essentially distributed-parameter systems represented by partial differential equations. Hence their parameters vary explicitly with position. Models for distributed-parameter systems have an infinite number of degrees-of-freedom and are characterized by nonrational frequency transfer functions and infinite-order state space matrices. This characteristic causes problems in structural control because much of control theory has been developed for lumped or discrete-parameter systems, or systems of finite-order. These systems are typically represented by linear ordinary differential equations. One finds that a practical control system for distributed-parameter systems requires linear reduced-order models that are robust with respect to system parameter changes and disturbances. Thus, the common practice in distributed-parameter control is to obtain a full order model, either analytically or through identification, and to then synthesize the controller using a reduced or finite-order model that captures the salient features of the system dynamics. When this approach is used, it is necessary to discern resonant frequencies to within 5 percent accuracy, and mode shapes to within 20 percent accuracy, as required to enhance stability and performance.¹⁸ It is very important that the design engineer extract reduced-order models that retain critical modes, yet account for neglected ones.

Other issues that are important to the design engineer in the modeling stage are the dynamics and positions of the actuators and sensors. Such details are discussed very infrequently in the technical literature, although their characteristics can have a significant effect on the dynamics of the structure. This lack of discussion may be attributable to the various types of sensors and actuators used and their particular application. Different results are observed for collocated systems and for noncollocated systems. In the collocated system, the actuators and sensors are coincidentally located on the structure, which is beneficial for reducing instability. In the latter system, especially for a reduced-order model, instability and performance degradation are possible unless precautions are taken before hand. In addition, certain actuators must be accommodated for in the initial design of the structure, whereas other may be included later as a possible add-on device. Hence, if the dynamics and location of the sensor and actuator have a large impact on the structure's dynamics, it becomes quite time consuming to develop general governing equations for each different design generated.

The trend in structural control design has been the development of high fidelity reduced-order models of the dynamics to improve design, analysis, and to aid in understanding system behavior. With the increasing use of computer-based tools aimed at improving controlled structural stability and performance through optimization, it is plausible to conclude that accurate dynamic models are quite complex. Model uncertainty reduces our ability to make precise and significant statements concerning the dynamics of the system. The closer we examine the physical behavior of the structure's dynamics, the more apparent is the need to represent and investigate the effects of this uncertainty. Since uncertainty is apparent in all phases of the preliminary stages of the structural control design, it is unavoidable and must be dealt with in a rational and systematic manner. Consequently, the design engineer must have tools that are compatible with physically meaningful descriptions of uncertainty, and that can be mathematically modeled to an accurate level for improved structural control design.

The problems discussed previously are investigated here for structures that incorporate embedded electrorheological (ER) fluid actuators. These structures are represented by a specific class of distributed-parameter systems, one that involves a spatially distributed actuator. Since these structures or actuators are nonconventional, they enjoy several advantages over conventional actuators. For example, they provide a uniformly distributed control input, all changes are completely reversible and response times quick. They are fully contained within the structure and are not exposed to the environment, they contain no moving parts, and their dynamic response can be readily controlled using electric signals. These advantages make the ER fluid structure a practical candidate for active structural control. Thus, when integrated with modern sensors and control technologies, ER fluid structures can be essential components in a large, flexible systems and industrial applications.

However, the dearth of adequate ER fluids and a lack of satisfactory understanding of their behavior have been the primary barriers in the establishment of commercial applications.¹³⁹ Accurate mathematical ER fluid models are very complex and difficult to develop, and current models are usually limited to special cases. Much of this is due to the complex behavior of the fluid, the significant effects of various parameters on the macroscopic properties of the fluid, the reproducible manufacture of the fluid, and the dynamic interaction of the fluid and device boundary. Clearly, these deficiencies preclude an effective commercial design of ER fluid devices and control systems.

It is the primary objective of this thesis to develop a framework for manipulating, interpreting, and parallel processing analytical, numerical, and experimental data for ER fluid structures in a logical and systematic manner. More specifically, this framework will be established using concurrent engineering to formulate certain tasks, some of which will include computer-aided engineering. These tasks will then be used to obtain good experimental and theoretical correlations for full-order mathematical models of ER fluid structures, such as plates

and beams. These structures serve as useful examples for active control methods because of their ability to be readily included as components of larger systems. Moreover, the application of computer-aided engineering tools to structure development should prove that their role in design is critical to the evolution of this diverse technology.

1.1 Thesis-Related Background Topics

Structural control is a subject that has been attracting more attention over the past few decades. Much of the interest in this subject stems from the idea that the stability and performance of certain structures can be improved by somehow enhancing the characteristic behavior of the structure, either through the use of materials, devices, or control systems. Good performance of the controlled structure demands a good interaction and understanding of all the disciplines and areas involved. Certainly, trade-offs are necessary due to the innate conflicts that develop between the different disciplines. Moreover, we see in structural control that there is a definite boundary between what must be integrated within the design process and what must be added to the structure after its completion. Accordingly, it may be reasoned that a concurrent engineering approach towards structural control would be applicable and useful.

1.1.1 Concurrent engineering

The continuous execution of all different phases during the product life cycle is commonly referred to as product development, and the full process from conception-to-completion is properly denoted the product cycle life. In conventional practices, product development is subdivided into three major phases: conception, design, and production or manufacturing.¹⁰⁹

Typically, these three tasks are treated as discrete and separate entities whereby each is executed in a sequential manner, and where all changes are performed in an iterative manner. In any

given phase, an engineer will be concerned mainly with a particular design or operation only within his/her own discipline, so that discussion between engineers of different disciplines and in different phases is quite limited. As a consequence, the likelihood of not meeting specified requirements would lead to increased production cycle time due to the repetitive cycling of design changes and modifications.

Clearly, product development involves a broad spectrum of engineering disciplines that can influence and overlap each other to a considerable extent. Problems initiated during conception are likely to be exacerbated in the design phase. For instance, constraints that must be met by the electrical component group may conflict with a completed prototype fabricated by the mechanical design group because of a severe lack of multidisciplinary integration. Likewise, parts that were optimally designed for easy assembly, for some reason, require a force fit in the factory due to conflicting objectives stated in the design and manufacturing phases. In these hypothetical cases, prospective solutions, which may have been overlooked in the initial phases of design, need to be explored and executed. Obviously, conventional methods hinder further advancement and show that, given the vast requirements imposed during development, serial-based processes do not allow the design to stay abreast with emerging technology and knowledge. Hence, we see that satisfying design objectives and stringent requirements from every aspect of engineering, at every phase, is a major concern that cannot be efficiently resolved in traditional product design methodologies.

Concurrent engineering permits all practical knowledge from the relevant multidisciplinary fields to be combined and processed in a parallel manner. In such a large program, this is accomplished through exceptional communication and collaboration, computer-aided engineering tools, and databases. Thus, a designer must establish close links with other personnel so that a good flow of information and experience are equally shared.⁶³ The traditional "top-down," or serial-based, approach to product design and development eventually could have organizational

repercussions that render inefficient activity. Therefore, close collaboration between different engineers of different disciplines is necessary for a successful concurrently engineered product. With the successful implementation of concurrent engineering, it follows that the difficulties prevalent in current industrial practice are usually overcome when as much information as possible is integrated and interpreted throughout the development process.

1.1.2 Structural control

Structural control can be subdivided into two specific categories: passive and active control. Passive control is used to improve the performance of the structure by enhancing its stiffness and damping properties with the use of materials or devices. Passive structural control methods share many similarities, the most common being their versatility. Not only can they be used in many different applications, but these methods also have the capability of being implemented during any phase of development. Required design modifications can be verified and made using experimental or analytical optimization techniques, so that the structure's response may be tailored for specific frequency ranges, inputs, deflections, etc., without large delays in production.¹⁰² In contrast, active structural control requires more intensive planning in the initial design stages because a closed-loop feedback system is used to control the structure. This closed-loop feedback system incorporates actuators to provide the necessary forces to the structure, as described by the sensors, which measure that response. The many advantages that active control has over passive control are basically attributed to the design of the structure and the controller. Active control permits a structure to be designed lighter than those without or with passive control.⁹⁵ However, active control also dictates early consideration of the controller design during the initial stages of the structural design.³⁰ Once the structure is completed, a control system may not be viable and/or may be too costly to implement. One advantage of an early consideration of the control system in the active control design is its permission of the use of a

variety of controller design and optimization techniques to stabilize the structure and achieve required levels of performance. These advantages have caused a great increase in interest in active structural control and its use in so many diverse applications.

A cursory review of the literature concludes that much of the motivation behind the work in active structural control has evolved from the development of large, flexible structures intended for space. Much of this directly relates to the Galileo spacecraft and the construction of the U.S. Space Station scheduled to be launched in the near future.^{33, 80} Clearly, a structure intended for space must be fabricated from materials with high stiffness- and strength-to-weight ratios. These ratios must be large due to structural integrity and weight constraints, and also because of the reliability and accurate positioning requirements for the structural appendages. Extra weight will cause the rigid body dynamics to tightly couple with the flexible body motions.³³ Evidence has shown that structures with these characteristics also tend to possess a low amount of damping. As a result, they may sustain long lasting vibrations during maneuvers or due to disturbances that can significantly degrade performance. For various other structures that depend on precise tracking or positioning, i.e., robots, long boom antennas, telescopes, and solar arrays, this problem is very important and critical to ensure an operation's success.

Early work in structural control used models that were reduced to limit the full-order model to include only its first few system modes. This is called Modal Control modeling.^{42, 83, 128} Modal control was developed in these studies based on the assumption that the structure's response is dominated by its first few modes and that its residual modes can be neglected because they are not directly affected by closing the loop. The modal control method has worked well when applied to discrete-parameter structural systems, which amount to controlling the lumped structure by controlling a finite number of modes.⁹⁵ As one of the original strategies for finite-dimensional control, modal control has since been proven both theoretically and experimentally inadequate for infinite-dimensional or distributed-parameter systems. The main difficulty is that the reduced-

order model necessary for modal control is developed with only a finite number of modes, so control over truncated modes is non-existent. Consequently, this implies that the control gains must be of infinite-dimension to attain sufficient control using the modal control method. This is truly impractical.

Other control theories that have been established for distributed-parameter systems have been developed for both time and frequency domain analysis. Each control theory has its own advantages, to be discussed here, however, all suffer a similar disadvantage manifest by the infinite-dimensionality of the structure. This disadvantage is one that requires the finite-dimensional controller to satisfy certain criteria for realization and existence. Specifically, these theories are based on modal approximations that must satisfy necessary and sufficient conditional criteria for the selection of an appropriate number of critical modes and dynamic boundary conditions. This criteria must be satisfied to have a stable control design.⁶⁴

In a paper by Vidyasagar,¹³⁷ necessary and sufficient conditions were defined for a large class of distributed-parameter transfer functions in the frequency domain under the assumption that the dynamic models for these systems were known precisely. Lions⁴⁵ developed a general mathematical theory for the control of distributed-parameter systems that recognizes and details three important steps in solving the optimal control problem. Convergence and stability criteria for the modal control laws were considered by Gibson.⁵⁷ This study focussed attention on certain essential criteria and on its direct correspondence with increasing system dimensionality. Lin⁸⁴ surveyed the possible application of output feedback control using modal decoupling, pole assignment, sub-optimal control, and optimal control to make some detailed conclusions about assumptions and techniques associated with the theory of distributed-parameter control. Sakawa¹¹⁵ presented good results for the coupled bending and torsional vibration control of a cantilevered beam using a hybrid feedback control scheme. Bruch³⁰ introduced an approach for orthotropic plates with rotatory shear that minimizes two performance indices subject to the amount of

feedback force that can be spent in the control process. Numerical examples of this open-closed loop theory are given, however, with no discussion on how it is realistically feasible. Additional control theories that have been developed in the manner described above include optimal control,⁷⁴ adaptive control,^{13, 106, 116} pole allocation,^{29, 41} and direct velocity feedback control methods.⁷⁰

The idea of introducing invariant natural modal coordinates to obtain a reduced-order model for feedback control was introduced by Creedon,⁴⁰ Takahashi,¹²⁸ and was further developed by Meirovitch.^{91, 95} Although natural coordinates vary slightly from the general modal coordinate descriptions aforementioned, they can be used to obtain a global and unique optimal closed-form solution to the linear control problem for distributed-parameter systems in the time domain. This theory has been termed the independent modal-space control theory⁹⁵ (IMSC), or natural control theory,¹²⁸ which is based on the notion that the stability of a linear system is determined purely by the system eigenvalues and that no control effort can be unnecessarily used. In particular, IMSC makes use of a distributed control force to control the system's eigenvalues, thus leaving the system's eigenfunctions unaltered. Both theories have been used in numerous applications with adequate results. However, one specific problem involves finding a suitable control theory to complement IMSC in order to determine the appropriate control gains for the system, since a distributed actuator is necessary to provide the control force.

More recently, distributed-parameter optimal control theories have been modified for combined controller and structure design. These modifications are made to include many objectives that employ various constraints on the structure and controller's performance. For example, such objectives and/or constraints imposed on the determination of feedback gains, sensor and actuator locations, structural natural frequencies and damping ratios, and structure dimensions have been used in the optimization procedure. Typically, these objectives are

optimized for specific control/structure cost functions, such as weight, power consumption, and/or vibrational response.

An integrating strategy for both structure and control system optimization was developed by Khot, *et al.*,⁷¹ who obtained a finite-element model of the structure and optimized the closed-loop system for minimal weight. The constraint used to modify the structure was based on the amount of internal damping, with a linear regulator used for the controller. Onoda¹⁰⁵ combined direct feedback and linear quadratic optimal control laws with a disturbance structural model to establish total cost. The approach taken in this paper is similar to the large spectrum of literature available on this subject, mainly considering a span of various costs posed in a single control/structure objective function. Milman, *et al.*,⁹⁹ employs a different method, one that consists of a multi-objective approach for combined structure and control design, and uses a family of weighted structural and control cost functions. The optimization problem here is posed such that the combined approach is a natural extension of most well-established current optimization strategies currently being used. Although the combined control and structure optimization philosophy is sensible, its problems are very similar to most problems encountered in optimization routines. Solutions are computationally demanding and require iterative minimization algorithms which suffer from many difficulties, such as the choice of the starting guesses, convergence, and multiple local minima.

The theories above present many fundamental mathematical principles for distributed-parameter structures and their control designs in both the time and frequency domains. Many of these theories are based on reduced-order modal coordinate characterizations and approximation methods in optimal and feedback control. However, very few of these methods can be classified as robust since they are dependent on the assumption that the dynamic models are precisely known, i.e. have no uncertainty. Control designs that account for uncertainty in the dynamic system model are defined as robust control theories. Several specific theories central

to robust control include loop transfer recovery (LTR) techniques, linear quadratic gaussian (LQG) methods, and H_2 and H_∞ optimal control. For distributed-parameter systems, robust control has been employed by many investigators over the past two decades.^{10, 48, 82} These methodologies suggest a controller design based on a nominal model with uncertainty described by some perturbation from this model. After a model has been selected, robust control theory guarantees the controller to perform satisfactorily under all possible deviations from the nominal model as long as certain stability and performance criteria are satisfied.⁴⁸ Hence, the modeling of uncertainty is very crucial to how the final controller design rejects disturbances and follows tracking inputs.

Most of these methods are linear time-invariant (LTI) frequency domain methods that require very high bandwidth controllers. The need for high bandwidth controllers is manifest by the large gain-phase margins necessary to make the structure robust to specified uncertainties. However, with robust LTI systems, some inevitable trade-offs exist in the design process for which accommodation must be made. Trade-offs such as unstable poles, nonminimum phase zeros, and time-delays impose fundamental constraints on achievable performance, and imply restrictions on the closed loop bandwidth of the system.⁹⁶ Generally, nonminimum phase zeros place an upper bound on the system bandwidth. Since it is well known that distributed-parameter transfer functions can have nonminimum phase zeros,^{31, 101, 141} arbitrary truncation of the model order may not include these zeros and give a false sense of full-order system stability. The implications of this trade-off on robust control has been discussed by O'Young and Francis.¹⁰⁷ Unstable poles impose a severe constraint on the system and can be clearly seen to worsen structural control performance. Hence, it is very important that robust stability bounds are satisfied. A model with a time-delay is actually a finite dimensional system of very high order, so approximations are usually necessary. The use of a Padé approximation introduces modeling

error, which consequently limits achievable bandwidth, yet, the loss of performance is insignificant compared to the robustness properties placed on stability and performance.¹⁰¹

1.1.3 Spatially-distributed actuators

Essentially, actuators provide the motion, mobility, and changes that govern the response of a controlled structure. Most conventional actuators accomplish this by using discretely located forces or motion. A severe problem can occur when these discrete devices are placed at modal nodes or lines. To observe and control the full continuum, the use of spatially-distributed actuators is highly desirable.⁹⁴ Certain materials can be used for these actuation purposes to control damping, stiffness, and mass properties of or within the structure. Some of the more common distributed-parameter actuator materials are shape-memory alloys, piezoelectric materials, magnetostrictive materials, magnetorheological fluids and electrorheological fluids. These materials all have unique innate characteristics that allow them to either change shape, stiffness, position, energy dissipation, natural frequency, friction, and fluid flow rate in response to changes in temperature, magnetic field, or electric field. Characteristics, applications, and the history of these actuators are detailed by Gandhi and Thompson.⁵⁵

The concept of using a distributed-parameter actuator for control is not new. Applications using distributed-parameter actuators date back to the 1950's, where Olson¹⁰⁴ first used a distributed-parameter actuator for electronic noise control. However, it was not until the 1970's that they were applied to mechanical structures.⁹⁹ Presently, the amount of research dedicated to active structural control has dictated intensive interest in the use of distributed-parameter actuators. Much of the work has been focussed on the application and control of structures using piezoelectric and shape-memory materials.⁵⁵ Piezoelectric materials exert mechanical forces in response to an applied voltage. These materials change shape when their electric dipoles spontaneously align in the electric field, causing deformation within the material. Work in active

control using piezoelectric actuators has demonstrated their range of feasibility and applicability. Examples are numerous, ranging from optical tracking devices to ink-jet printers, and in recent years, acoustic attenuation, and active structural damping control.¹² Shape-memory materials also change shape. However, rather than having their dipolar properties change, they undergo a solid-to-solid phase transformation in response to temperature changes. Under heating and cooling, this phase transformation allows them to exhibit large, recoverable strains of up to eight percent.¹¹⁴ Applications for shape-memory materials include engine mounts, suspension systems, and robotic actuators, which mimic the smooth motions of human muscles.⁵⁵

A rather detailed study of piezoelectric actuators applied to a one-dimensional beam analysis is given by Crawley and de Luis.³⁹ They analyzed stresses, strains, and loads for a cantilever beam with piezoelectric ceramic surface treatment. Bailey and Hubbard,⁷ developed three different control algorithms for cantilever beam configurations to control transient vibration. These algorithms were implemented in an experimental analysis to verify theoretical equations of motion and predicted response. Others contributing to this area have demonstrated the potential of distributed-parameter actuators by simultaneously controlling a number of modes with reduced spillover.^{19, 49, 66} Active vibration control of plates using piezoelectric ceramics was conducted by Dimitriadis, *et al.*⁴⁵ Conclusions drawn from this investigation include the ability to excite the plate using distributed actuators, the observation that the input frequency of the excitation markedly affects the modal response, and the location of the actuator strongly influences excitation as well as spillover. Tzou^{134, 135} introduced a theory for distributed actuators that was discretized for isoparametric piezoelectric finite-element formulations. A distributed modal analysis was examined and several case studies using Lyapunov control and constant gain proportional feedback control were implemented.

The type of actuator used in this investigation is an electrorheological (ER) fluid. An ER fluid is composed of fine conductive particles suspended in insulatory fluid. When an electrical

potential is applied to the ER fluid the conductive particles become polarized and structure themselves to drastically alter the fluid's stiffness and energy dissipation properties. Hence, the ER fluid can be activated simply by placing it between electrodes of opposing polarity. However, the magnitude and duration of the electrical potential determines the intensity and rate of these changes. Thus, the capability of controlling the fluid is manifest by the electro-coagulation of the particle. This phenomena is defined in the literature as the electrorheological effect (ERE).²⁴

⁴³ It is the very nature of the ERE that permits it to be used as a spatially-distributed actuator in a structural domain.

Throughout the past two decades, the focus on ER fluid technology and research has become quite intensive.^{24, 43, 120, 124, 136} ER activity and the ERE has merited extraordinary interest due to the number of practical actuator applications. Detailed investigations have focussed on the deformation, motion, and the rheological and electrical properties of ER fluids. Much of this attention has been motivated by observed changes in the fluid's appearance and constitutive

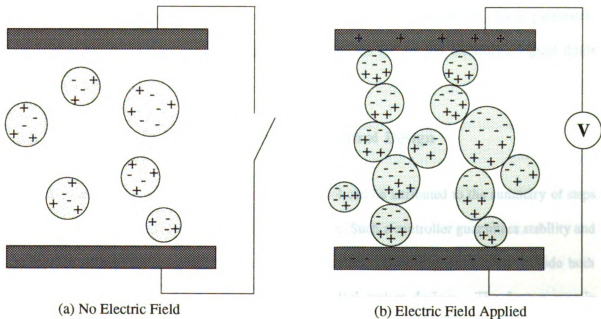


Figure 1.1 - The electrorheological effect.

behavior. At zero electrical potential, the random dispersion of particles (see Fig. 1.1 (a)) in the fluid medium has minimal influence on its rheological properties. In fact, its behavior can be easily identified with that of typical Newtonian fluids. Although when it is subjected to an electrical field, a detailed and unique formation of the particles (see Fig. 1.1 (b)) causes an instantaneous transition in the fluid's properties. These constitutive changes are comparable to that of non-Newtonian fluid behavior. A marked distinction of this transition is the fluid's ability to support an increasing shear stress with increasing field intensity and without flow.²⁶ Clearly, without doubt, this characteristic of a yield stress is one possessed only by non-Newtonian fluids.¹²⁵

Nonetheless, as the overall behavior and capability of controlling an ER fluid has been established, the actual controllability of the fluid depends on many inter-dependent parameters that can have profound effects on the amount of ER activity. For example, the uniformity of electrical field used, the rate of deformation of the disperse particles, the various additives and the overall composition of the fluid,¹³² the surrounding temperature,³⁷ the dielectric characteristics of the dispersion,¹³⁶ and particle concentration all need to be considered. Such parametric interaction has made constructing constitutive descriptions for general electrorheological fluids a very complex task.

1.2 Some Issues in Practical Structural Control Design

A substantial number of problems in structural control can be attributed to the summary of steps used in arriving at a practical reduced-order controller. Such a controller guarantees stability and is capable of meeting acceptable performance constraints. Generally, constraints include both frequency and time domain statements in these control system designs. The former usually represents explicit performance criteria, while the latter reflects physical bounds such as actuator limits, parameter ranges, rise time, overshoot, or sensor limits. Much of the difficulty with

ensuring that these constraints are not violated has to do with the representation of the modeled structure. When the reduced-order model is linear, the problem is especially cumbersome, due to the numerous assumptions and approximations that must be made about the actual plant. Conventional modeling and controller design techniques frequently use the assumption that exact knowledge of the system's dynamics can be obtained. However, mathematical models and control designs based on this assumption can be too restrictive and fail in reality. Conventional control design leads to controllers that are too tight and may become unstable during operation.¹⁰¹ Moreover, in a real system, the internal and external disturbances that act on the uncertain system cannot be excluded due to the complex interaction between the system and its environment. Thus, all possible perturbations within the plant model must be bounded to guarantee stability and requirements on performance in the face of uncertainty.

1.2.1 Obtaining reduced-order models

For practical distributed-parameter structural control design, simple linear controllers are preferred over complex linear controllers for linear time-invariant plants. There are many reasons for this, yet most result from the reduced amount of time and computational effort needed to understand and operate them. Methods used to design low-order controllers for high-order plants can be divided into two broad categories: (i) the *direct* method, where parameters defining a low-order controller are computed by some optimization routine, and, (ii) the *indirect* method, where a high-order controller or low-order plant model are first found, and a specific procedure is used for further reduction.⁴ These two approaches are shown graphically in Fig. 1.2 along with a short listing of the different procedures used for system reduction. The fundamental difference between model and controller reduction is that model reduction is based on open-loop considerations. Controller reduction techniques must be based on mathematical existence arguments that should, after all, preserve the closed-loop system stability and performance

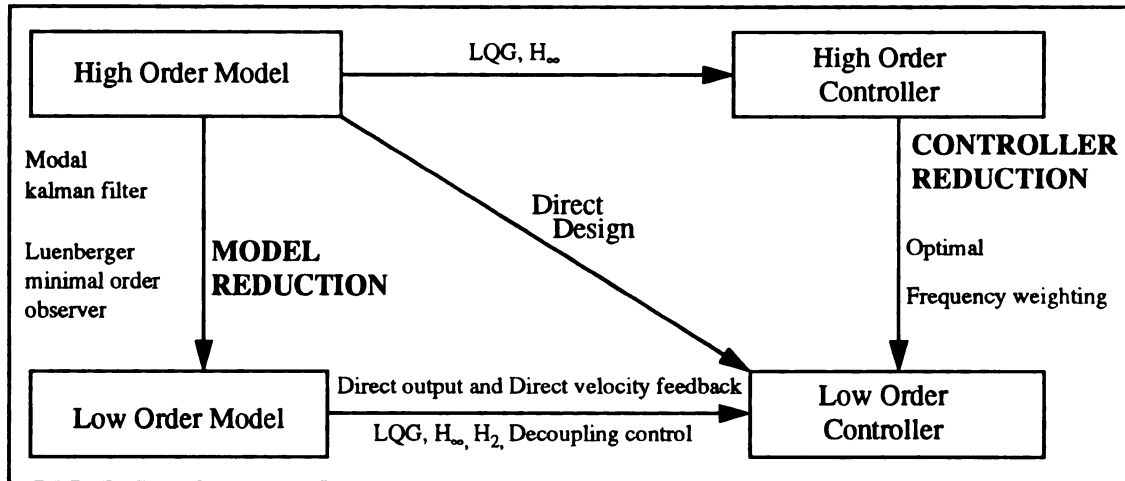


Figure 1.2 - Principles of practical low-order control design.

The key objective in the direct method is to minimize a quadratic performance index subject to the constraint that the controller be fixed degree, stabilizing, and linear time-invariant.^{61, 65} Direct methods have much promise and have been a research topic of interest in recent years due to the ease of their implementation in control design packages. Nevertheless, a disadvantage with the direct method is that it is unclear as to what mathematical basis is applicable for a large variety of systems. For this reason, the remainder of this thesis will focus on indirect methods of model reduction.

As for indirect methods, there are many different approaches, ranging from the very crude modal approximations to the very sophisticated H_{∞} methods. There are at least two specific methods for designing high-order controllers, and both are highly capable of using the large amount of existing qualitative and conceptual knowledge that pertain to algorithms and applications.⁴ However, the procedures necessary for reducing high-order controllers to low-order controllers are less developed. These procedures require precise, rational arguments in order to retain the critical aspects of the system's closed-loop dynamics. On the contrary, a very

crude approximation technique that can be performed to approximate the plant model in the time domain is called modal reduction.⁴² This approach is quite similar to modal control, and when used for distributed-parameter systems has similar drawbacks in the resulting low-order controller design. A more sophisticated frequency domain model reduction method is the projection-and-assembly method presented by Lee.³⁰ In this method, modes that contribute significantly to the control input and output are selected at the system level, and are then projected in a mathematical sense onto the components of the system. The resulting reduced-order mathematical model of the components are then assembled to yield a rather accurate model of the system dynamics for only the selected modes. Reddy,¹¹¹ proposed a method for minimizing the integral of the square of the error between corresponding real and imaginary parts of original and assumed transfer functions to evaluate coefficients of the approximate model. An advantage of his approach is that it is computationally simple. Nonetheless, a few disadvantages are entailed by these frequency domain methods, as with other time domain reduced-order methods, which have to do with accuracy and mismatched transfer function zeros due to truncated or undesired modes.

In particular, the primary issue with the former indirect model reduction methods is the inability to account for realistic actuators and sensors within the low-order control scheme. In reality, actuators and sensors will not necessarily operate in a select frequency range, hence, residual modes may become excited by the actuators and/or measured by the sensors. This results in what is known as control and observation spillover, and both have been attributed to instabilities and degradation of system performance.^{8, 14, 40} Over the past few decades, various techniques have been established for minimizing the effects of spillover in discrete-parameter systems. Curtain⁴¹ developed estimates on spillover effects for all modes using a pole placement method. Orthogonal and modal filters have also been used to better accommodate spillover by several authors.^{93, 122} Filters were used to approximate and extract convergence properties from distributed measurements over given time intervals rather than estimate the modal response of the

structure. Yang¹⁴² eliminated instability by introducing a specific time delay in the control system for certain mechanical structures. These techniques were initially developed for collocated and noncollocated actuators and sensors. Only in the recent decade have they been applied to distributed-parameter actuators and sensors. Balas⁹ used modal equations to obtain output feedback control over a finite number of modes for a distributed-parameter elastic system, specifically treating the problem of control spillover into the uncontrolled modes by instituting spillover bounds. To alleviate spillover, Meirovitch and Baruh⁹² proposed a technique that is compatible with a limited amount of inherent damping to eliminate observation spillover instability.

1.2.2 Actuator modeling and dynamics

In the former discussions, consideration of the issues pertaining to the physical effects that actuators have on the mathematical model of a distributed-parameter system has been mentioned briefly. Essentially, the type, location, and dynamics of the actuators are very critical when implementing successful operations because most conventional actuators are discrete actuators. They are discrete in the sense that they can only be located in select, finite regions of the full structural system. Spatially distributed actuators will also suffer many of the same dilemmas, because it would be impossible to actuate every member within a structure due to weight constraints. Therefore, the consideration of the actuators must be sufficiently detailed to describe their behavior on the system.

Actuators used in distributed-parameter systems not only require a detailed analysis of their functions, but also detailed analysis for their dynamics and positioning. Spatially distributed actuators have certain slight advantages here but are also inflicted with the same problem that exists with all actuators, this being that they possess mass and inertia. In most cases, their mass may be considered to be negligible if the structure is very large and heavy. However, for

vibration suppression of thin, lightweight structures, the distribution of the actuators will certainly alter the modal response of the system significantly. Non-negligible actuator mass in structural control design has been addressed only by a limited number of authors. Zimmerman¹⁴⁴ focused on required actuator masses for discrete actuators using optimal design techniques to minimize control and position error subject to total mass and frequency constraints. This paper provides an important inner-loop for the design of controlled structures with discrete actuators that recognizes their critical duty for successful structural control. Such techniques have yet to be applied to distributed-parameter actuators because of the myriad procedures for applying them to the structure. However, this inevitable problem may lead to greater instability in the controlled structure than what was initially encountered. Therefore, all actuated structures must be designed to be sufficiently robust in order to account for variations in their inertial and dynamic properties.

In structural control design, the dynamics of the actuators must be taken into consideration early in the simulation work, because their presence will have significant effects on the structure's performance.¹⁴⁴ In a paper by Maghama and Joshi,⁹⁸ the effect that actuator dynamics have on their optimal actuator and sensor placement scheme vastly reduced controllability of their system. Reduction became more pronounced as actuator bandwidth decreased or when it was near the operational closed-loop bandwidth of the control system. The problem with these actuators is that their bandwidth is finite, while that of structural system is infinite. Hence, extreme care must be exercised so that control spillover of the low-frequency modes does not destabilize the intermediate or higher frequency modes, and that critical modes of operation in the actuator are never attained.⁹⁸

Other minor issues such as reliability, functionability, and possible malfunction are very important in the selection of actuators and control system design. Three possible motivations usually exist for using active structural control: (i) to stabilize the structure at all time, thus, the actuators are constantly in operation, (ii) to stabilize the structure over limited motion, thus, the

actuators must be dependable, especially during continuous on-off cycles, and (iii) to stabilize the structure only during critical motion, hence, the actuators must be reliable when they have been inactive for long durations. As illustrated, these motivations impose important design requirements in the reliability and functionality of the actuators. However, a review of the literature reveals minimal information on these important topics.

1.3 Organization of the Thesis

The organization of this thesis is based on the ideas introduced in Chapter 2. In Chapter 2, a rather novel technique is presented for large-scale systems modeling. Specifically, this technique addresses actively controlled large-scale structure modeling with controllers designed using robust control theory. The framework of robust control theory is useful because it is very compatible with concurrent engineering principles. In the past, concurrent engineering has been applied to many aspects of the product life cycle, but its use in the preliminary or initial stages of the design process has been limited. Naturally, this is because system modeling is unique to the problem at hand and no cookbook formula could exist that would be useful for the myriad problems encountered. Therefore, these principles are used to develop a technique that deviates from conventional structural control modeling procedures by taking into consideration uncertain linear systems analysis. Take note that this modeling strategy is more of an outline that can be applied to modeling than a strict standardized procedure.

The modeling procedure described above is applied to a simple example in the final section of Chapter 2. For illustrative purposes, the example is a simple cantilevered beam. In this example, analytical and experimental techniques are used to obtain an efficient linearized model and an associated uncertainty model. It will be shown that modeling uncertainty is a necessity in any system because of its innate presence and its effect on the results of the mathematical model. However, the goal here is not to model uncertainty where is mathematically convenient,

but where it actually occurs. Unfortunately, this objective is the most arduous task in the modeling procedure, yet, as shown in this simple example, it yields the most benefits.

The final chapters specifically focus on the development of a linearized mathematical model for distributed-parameter plates containing ER fluid actuators. Chapter 3 begins by giving a detailed review of the current knowledge of ER fluids and the ER fluid effect. Both the rheological and electrical aspects of the ER fluids physical properties are considered. Subsequently, models for the viscosity, shear stress, and electrical behavior are developed for a specific ER fluid. These models are based on experimental identification techniques, as well as, numerical and empirical methods.

Chapter 3 concludes with an experimental identification of ER fluid plates. Experimentally determined information is obtained for two ER fluid plate configurations in an effort to characterize their dynamics. This process is conducted using the structure's frequency response to set and identify bounds for constant and dynamic inputs. Unfortunately, this information is presented in graphical form only due to the limitations of the data acquisition system. Finally, the experimental results are compared to results generated from commercial finite element analysis software. A unique characteristic of this software is that the nonlinear ER fluid model can be incorporated via a subroutine written in Fortran.

In Chapter 4, an analytical model is developed for the ER fluid plate using assumptions based on sandwich theory^{89, 90, 140} and constrained layer theory.¹⁶ The governing equations of motion and their associated boundary conditions are obtained using Hamilton's principle. Subsequently, comparative results are generated for the static response of the plate using the Naiver approach.¹⁴⁰ These results show good agreement with a previously obtained three-dimensional elasticity solution,¹⁰⁸ for the case of a simply supported three-layer sandwich plate. Finally, conclusions are drawn from the above work and recommendations for future work are discussed in Chapter 5.

Chapter 2

A METHOD FOR CONCURRENT STRUCTURAL CONTROL MODELING

2.0 Introduction

Modeling is the basis for many types of system analysis and design. Mathematical models should be expressive, easy to understand, should map all properties of interest, and should allow analysis and decision-making concerning the real system.²¹ In the case of large-scale dynamical systems, however, there is a fundamental problem. These models sometimes tend to fail to describe the behavior of the whole model appropriately because they are usually constructed by combining various models of the system's parts. During structural control modeling, this occurs as a result of several important issues. Such issues pertain to uncertainty in all the approximations, ill-posed component models, and/or inefficiently linked system component models. Generally, the combined effects of all three issues that lead to deleterious effects on the dynamic mathematical description of the system.

Models of large, controlled, structural systems can be either stochastic or deterministic. They may also reflect the system's behavior, the desired qualities of that system, or the exogenous input conditions that may act on the system. There is a multitude of ways to represent large-scale systems; however, there are three views of a system that need to be captured in the model:²²

Structural viewpoint: accurately represents the structure of the system, its components, and interactions between these components.

Functional viewpoint: reflects the ability of the modeled system to satisfy required needs of the true system and to function as a whole unit.

Behavioral viewpoint: represents all the various states that the system goes through, and the flow of processes.

A good modeling scheme is one that captures all three viewpoints of the system and translates them to an appropriate working mathematical model. We find that there is no simple method for doing this, because the components of most systems in practice are constantly active, thus, every input change causes a state change in the system. Most structural control problems definitely fit this category. For convenience it is useful to approximate the system by characterizing it as a black box, in which every input is transformed into an output.²¹ Nevertheless, a complete modeling procedure must include not only what we know about the system, but also what we do not know about the system. Only then can we capture the three viewpoints of the approximate model and make significant statements about its dynamics.

It is the goal of this chapter to develop and outline a modeling method for representing large scale systems. This representation will be based on a hierarchical procedure that integrates the crucial aspects of communication among the system components. Structural control systems are active systems that must operate in a concurrent nature, hence the models used in design of these systems must also reflect this concurrent methodology.

2.1 Large-Scale System Modeling

Modeling of systems can be carried out in many ways: by theoretical methods, by experiment, and by any variety of combined theoretical and experimental techniques. In the case of large-

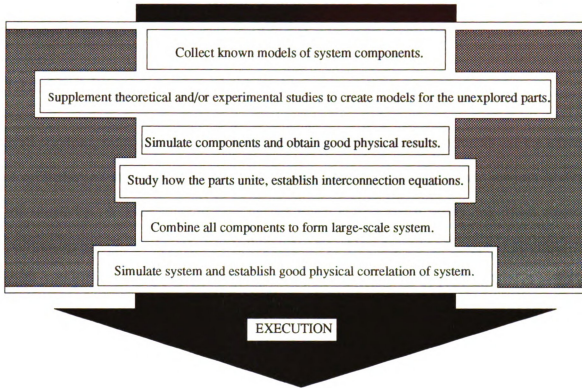


Figure 2.1 - A standard large-scale system modeling procedure.

scale dynamic systems there is a standard modeling procedure that makes use of the results from previous research in order to complete the analysis within a reasonable time period.¹²⁹ This procedure, graphically outlined in Fig. 2.1, is indicative of typical serial-based, top-down approaches because it is highly dependent on good representations of the system's components **and their interactions. Hence, the steps in this procedure must be repeated until good correlation of experimental and analytical results are obtained for the system's components.** Of course, it would be natural to expect this standard methodology to yield accurate results for the system as long as accurate results were obtained for its components. However, this expectation is sometimes unfounded even after many iterations. This is because mathematical models are only approximations of the true physical process. When these models are combined model uncertainty due to neglected, truncated, or approximated dynamics can cause substantial problems in system

behavior. Therefore, to make certain statements about a system and its components, it is necessary to use precise, well-defined models that account for uncertainty.

2.1.1 Modeling uncertainty in systems

In all problems, small or large, linear or nonlinear, one has to evaluate uncertainty and the effects of uncertainty on the dynamic model. An inherent trade-off in modeling occurs between fidelity and simplicity. It is desirable to have models which closely match reality, yet which remain easily analyzed. Obviously, solutions to this trade-off problem depend on the type of assumptions made during the modeling process. Whether the model was arrived at by physical laws or perhaps by measured data, these assumptions need to be evaluated and analyzed, as uncertainty is innate to any modeling procedure.

This suggests a methodology which assumes and treats the system and its components not as precise, single models, but rather as a set of models, inside of which the actual physical system will lie. Hence, the dynamic system model can be viewed as a "fuzzy" description of the actual process. This approach, referred to as set membership or unknown-but-bounded uncertainty,⁹⁷ ¹¹⁸ has been described as a realistic technique for characterizing uncertainty. It has several advantages, for example, it is less demanding than associated statistical descriptions because it shows that the unknown process behavior cannot be modeled, and it is easier to use with nonlinear systems and/or convert to a linear representation.⁹⁷ Thus, if we know that our nominal model is closed and bounded by the set, then significant statements regarding stability and performance can be made about that set. The mathematical framework for these two problem will be discussed below.

The unknown-but-bounded uncertainty method adopted here falls into the deterministic category,³⁴ where uncertainty may be nonlinear (in terms of its influence on the system), and time-varying (possibly fast), but its statistical information is never assumed.¹¹⁸ In turn, all that

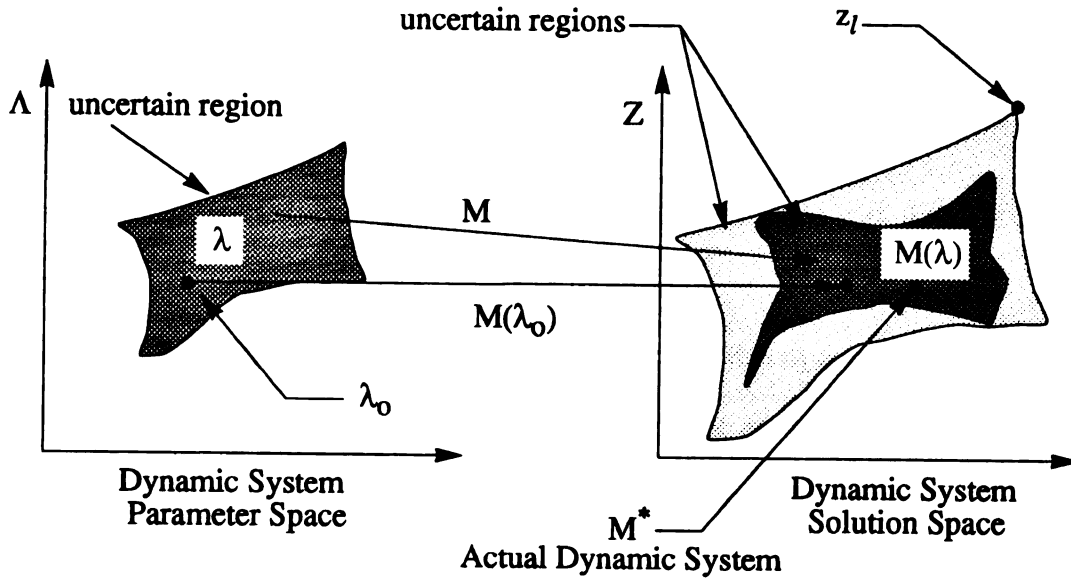


Figure 2.2 - Generalized uncertainty problem where the actual dynamic system $M^* \in Z$.

is required is the knowledge of the set in which the uncertainty values lie, which is characterized via certain deterministic properties such as compactness (closed and bounded). A graphical interpretation of this framework is given in Fig. 2.2. Here we have all the dynamical system parameters represented by λ and the known or nominal parameters represented by λ_0 . We suppose to know λ not exactly, but have some information on it since it can be bounded and nominal values can be identified. We are then interested in evaluating some model function $M(\lambda)$ of this system to obtain an approximate solution to the dynamical system. If we let Λ represent a normed n -dimensional space and Z be a normed l -dimensional space, then given the operator M , Λ is mapped into Z as follows:

$$M: \Lambda \rightarrow Z. \quad (2.1)$$

We also have in this mapped region $M(\lambda) = z \in Z$, and outside this region $z \in Z$. Hence, our objective is to approximate an element $M(\lambda)$ of the space Z , knowing approximate information about the elements λ , or approximate information about an element z referenced from $M(\lambda)$.

Unless otherwise specified, these objectives are met by assuming that Λ and Z are equipped with L_2 norms, and two infinity norms, L_∞ and L_∞^w , where the latter can be written as

$$\|\lambda\|_\infty^w = \max_i w_i |\lambda_i|, \quad w_i > 0. \quad (2.2)$$

Note that if an L_∞^w is used, component-wise bounds can be weighted with different values on every element.

Figure 2.2 illustrates two particular types of uncertainty descriptions that can be classified under the unknown-but-bounded formulation. These two type are known as: (i) parametric or structured uncertainty, and (ii) nonparametric or unstructured uncertainty. To establish conditions for these models, let us consider the sets of the following form to describe some perturbation from the nominal or known model:

i) *A finite perturbation set:*

$$Z^N = \{z_1, z_2, z_3, \dots, z_l\} \in Z \quad (2.3)$$

ii) *A parameterized perturbation set:*

$$Z^P = \{M(\lambda) \mid \{\lambda_1, \lambda_2, \lambda_3, \dots, \lambda_n\} \in \Lambda\} \in Z \quad (2.4)$$

iii) *A mixed perturbation set:*

$$Z^{N \cup P} = Z^N \cup Z^P \in Z \quad (2.5)$$

Eq. (2.3) is a nonparametric uncertainty description which is expressed in terms of specific single perturbations. Nonparametric uncertainty descriptions are generally conservative, however, they are useful for modeling small or large perturbations, unmodelled parasitic or neglected dynamics, and system failure modes. In contrast, Eq. (2.4) represents the parametric uncertainty description. This description corresponds to specified bounded uncertainty in the model parameters, uncertainty with respect to the inputs, actuators, sensors, or outputs which are

represented directly and not lumped together as in Eq. (2.3). By assuming normed bounds on this uncertainty description, it is possible to derive necessary and sufficient conditions, and very non-conservative representations. Eq. (2.5) provides a characterization of uncertainty similar to that graphically shown in Fig. 2.2. This representation is very powerful because it gives a realistic portrayal of uncertainty by combining the advantages of the parametric and non-parametric descriptions. In each of the perturbation sets listed above, a useful and meaningful description will depend on its accuracy. By using the mechanistic arguments posed in this mathematical formulation, we can norm-bound each perturbation to get "tight" uncertainty descriptions for the dynamic model.

2.1.2 Modeling the system in the presence of uncertainty

The importance of accurate uncertainty descriptions has been stressed in regard to uncertainty model conservatism. We want our uncertainty descriptions to be as "tight" and as realistic as possible, otherwise, mathematically-derived bounds may possibly give an invalid representation of the real system.¹⁰¹ For this reason, necessary and sufficient conditions on robustness of the uncertainty descriptions will be introduced here for a particular family of systems. These conditions must be established to determine how uncertainty restricts the dynamic system model. The term "robustness" is used in a context so to explicitly state that our uncertainty description must be well-posed and maintain the true degree of system stability. Robustness conditions require that even with the worst perturbed model substituted into the nominal model, the true stability of the system will hold.

To begin let us consider the nonlinear, finite dimensional system

$$\begin{aligned}\dot{\underline{x}}(t) &= f(\underline{x}, u; t) \\ y(t) &= g(\underline{x}, u; t)\end{aligned}\tag{2.6}$$

where $\mathbf{x}(t)$ is an n -dimensional state vector, $\mathbf{u}(t)$ is an r -dimensional input vector, and $\mathbf{y}(t)$ is an m -dimensional output vector. The functions f and g are assumed to satisfy conditions for the existence, uniqueness, and continuity of the solution of Eq. (2.6). The employment of a first-order Taylor series expansion about an equilibrium point or a known solution of Eq. (2.6) yields the following

$$\begin{aligned}\dot{\mathbf{x}}(t) &= \mathbf{A}\mathbf{x}(t) + \mathbf{B}\mathbf{u}(t) \\ \mathbf{y}(t) &= \mathbf{C}\mathbf{x}(t) + \mathbf{D}\mathbf{u}(t)\end{aligned}\tag{2.7}$$

where \mathbf{A} , \mathbf{B} , \mathbf{C} and \mathbf{D} are matrices of appropriate dimension. Eq. (2.7) is a linear time-invariant, finite-dimensional system which can be represented by a rational transfer function matrix

$$\begin{aligned}\mathbf{y}(s) &= \mathbf{P}(s)\mathbf{u}(s) \\ \mathbf{P}(s) &= \mathbf{C}(s\mathbf{I} - \mathbf{A})^{-1}\mathbf{B} + \mathbf{D} \in \Pi\end{aligned}\tag{2.8}$$

where $\mathbf{P}(s) \in \mathbb{C}^{m \times r}$ and a member of the set Π and \mathbf{I} denotes the identity matrix.

Now, assuming that Eq. (2.7) represents an uncertain linear system such that in state-space form, we have

$$\begin{aligned}\mathbf{A} &= \mathbf{A}_o + \Delta\mathbf{A} \in \Omega_A, & |[\Delta\mathbf{A}]_y| &\leq \delta a_y \\ \mathbf{B} &= \mathbf{B}_o + \Delta\mathbf{B} \in \Omega_B, & |[\Delta\mathbf{B}]_y| &\leq \delta b_y \\ \mathbf{C} &= \mathbf{C}_o + \Delta\mathbf{C} \in \Omega_C, & |[\Delta\mathbf{C}]_y| &\leq \delta c_y \\ \mathbf{D} &= \mathbf{D}_o + \Delta\mathbf{D} \in \Omega_D, & |[\Delta\mathbf{D}]_y| &\leq \delta d_y\end{aligned}\tag{2.9}$$

where all quantities with $(\bullet)_o$ refer to the nominal system model, Ω_A , Ω_B , Ω_C and Ω_D denote compact, bounded spaces, and δa_y , δb_y , δc_y and δd_y restrict the additive uncertain perturbations $\Delta\mathbf{A}$, $\Delta\mathbf{B}$, $\Delta\mathbf{C}$ and $\Delta\mathbf{D}$ to parallelepipeds within their appropriate spaces. We see that Eq. (2.9) represents a generalized form for determining parametric uncertainty descriptions. By substituting Eq. (2.9) into Eq. (2.8), we can postulate uncertainty descriptions for this system in terms of a specific structure or as a relative uncertainty written as a rational Laplace transfer matrix. To accomplish this, let us assume that each element p_y in \mathbf{P} is confined to a disk with

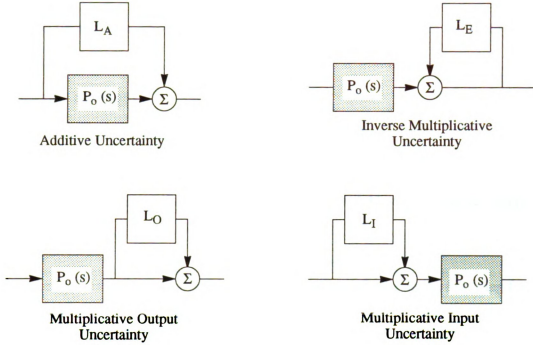


Figure 2.3 - Common perturbation structures for representing uncertainty.

radius $a_y(\omega)$ centered at the nominal $[p_o]_y$ in the Nyquist plane

$$|p_y - (p_o)_y| \leq a_y \quad (2.10)$$

or equivalently we can write

$$|p_y - (p_o)_y| \leq r_y |(p_o)_y| \quad (2.11)$$

where $a_y(\omega)$ and $r_y(\omega)$ are the additive and multiplicative (relative) uncertainty respectively. In these two forms we are able to directly see how uncertainty affects the nominal model. Then with this information we can select an appropriate uncertainty description.

If we wish to consider a structure for either a parametric and/or nonparametric uncertainty description the following four perturbation structures are commonly used: additive (L_A), multiplicative output (L_O), multiplicative input (L_I), and inverse multiplicative output (L_E). These four descriptions, which involve a perturbation L , are shown in Fig. 2.3. Initially, without

establishing the details between parametric and nonparametric let us consider L to be an actual lumped perturbation. Now the magnitude of this perturbation may be measured in terms of a bound on the maximum singular value of L , which is needed later to obtain the necessary robustness conditions

$$\bar{\sigma}(L) \leq l(\omega) = \max_{P \in \Pi} \bar{\sigma}(L), \quad \forall \omega \quad (2.12)$$

where the bound $l(\omega)$ can also be interpreted as a scalar weight on a normalized perturbation $\Delta(s)$

$$L(s) = l(s) \Delta(s), \quad \bar{\sigma}(\Delta(i\omega)) \leq 1 \quad \forall s = i\omega. \quad (2.13)$$

The four perturbation structures that correspond to Fig. 2.3 take on the following form

$$\begin{aligned} P &= P_o + L_A \\ P &= (I + L_o) P_o \\ P &= P_o (I + L_I) \\ P &= (I - L_E)^{-1} P_o \end{aligned} \quad (2.14)$$

where the subscript $(\cdot)_o$ refers to the nominal plant model.

In particular, input and output uncertainty descriptions are useful for representing actuator or sensor errors, neglected high frequency dynamics, or changing numbers of right half plane zeros. The additive uncertainty description is applicable to plant errors, and the inverse output uncertainty description is useful for representing low frequency errors and a changing number of right half plane poles.⁴⁸ Generally, the nonparametric uncertainty description $l(s)$ will not constitute a very tight description of the "real" uncertainty, since it reflects the relative uncertainty r_y , thus, $P(s)$ will be larger than the actual set of all plants Π .¹⁰¹ Roughly speaking, Eq. (2.11) represents a better generalized form for identifying and using the nonparametric uncertainty description because Δ is a full matrix. In order to achieve tighter bounds on the uncertainty values in Eq. (2.10), we need to use a parametric uncertainty description with our perturbation structure. Eq. (2.9), given in state-space form, is a parametric uncertainty

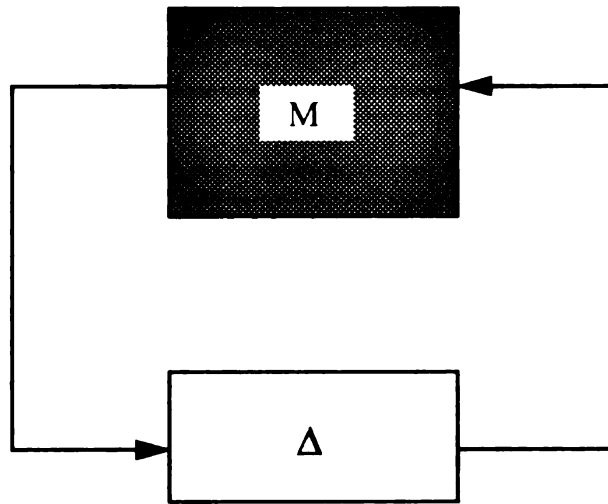


Figure 2.4 - A general block-diagonal bounded perturbation diagram.

description in the time domain. Numerically, these uncertainties can be identified directly, as shown in Eq. (2.10), and written in terms of multiple individual perturbations L_i of real or rational transfer functions. If each individual perturbation L_i satisfies Eq. (2.13) then they can be collected and placed into one large block diagonal perturbation matrix, where $\Delta = \text{diag} \{\Delta_1, \Delta_2, \dots, \Delta_m\}$. If a perturbation structure is implemented, weighting matrices can be used to normalize the uncertainty such that the actual perturbation $L_i(\Delta_i)$ is

$$L_i = W_2 \Delta_i W_1, \quad \bar{\sigma}(\Delta_i) \leq 1 \quad \forall \omega. \quad (2.15)$$

where W_1 and W_2 are rational weighting matrices that must have no poles or zeros in the open right half of the complex plane.^{48, 49}

To analyze the degree of stability for both of these uncertainty descriptions, we construct a block diagram for the system as shown in Fig. 2.4. The matrix M , called the interconnection matrix, is the nominal system model as seen from the various uncertainties. It represents a block-diagonal, bounded perturbation problem.⁴⁹ The nonparametric uncertainty descriptions the

solution to this problem involves a generalization of the ordinary singular value decomposition (SVD).⁴⁸ It is very important to determine the greatest singular value of a matrix, as it is equivalent to the maximal "gain" of the matrix as the input vector varies over all possible directions. The matrix value provides a reliable, nonconservative measure to determine whether the robustness conditions of the model are satisfied. For the parametric uncertainty descriptions, this measure is called the structured singular value (SSV), denoted by μ , which also serves as an essential analysis tool for verifying the robustness conditions.^{36, 48, 49, 101} Since all simultaneous uncertainties can be put into block-diagonal form by merely constructing the associated M matrix, SVD and SSV allow us to nonconservatively analyze the occurrence of uncertainty anywhere in the model.

Now recall that a necessary and sufficient condition for asymptotic stability of a rational transfer function is that all its poles lie in the open left half of the complex plane.¹²⁸ This condition is easily verified for a transfer function, which has a finite number of asymptotic stable terms, and can be extended to a transfer matrix via the Nyquist criterion.^{95, 137} However, if our plant is unstable, meaning it has poles in the right half plane (RHP), we want to retain this degree of stability throughout the modeling process in order to improve performance in the control design. For instance, if we are working with a reduced order model $P(s)$, we make the assumption that all the unstable terms of the full system are included in $P(s)$. Hence, we want to consider the degree of stability of a given transfer matrix to be defined by²⁸

$$\phi^{\text{stability}}(A) \triangleq \max \{ \Re(\pi) \mid \pi \text{ is a pole of } A \}. \quad (2.16)$$

Therefore, the degree of stability of the system must be equivalent for all models in the set. This statement will be verified in the derivation of the robustness conditions on the M - Δ structure.

Consider L to be of the form given in Eq. (2.14), where the perturbation Δ satisfies Eq. (2.13). Now if the nominal system model $P_o(s)$ is stable, M is stable and Δ is a perturbation

which can destabilize the system. However, if the nominal system model $P_o(s)$ is unstable then M is unstable and Δ is a perturbation which can further destabilize the system. The following theorem establishes conditions on M so that the degree of stability is maintained by Δ .

Theorem 2.1

Under the assumption that either all of the perturbations Δ are stable or all the members $P(s)$ of the set Π of possible plants have the same number of RHP poles and if the absence of encirclements of $\det(I - M\Delta)$ about the origin of the Nyquist D contour is necessary and sufficient for robustness, the closed loop system given in Fig. (2.4) is stable and/or the degree of stability is equivalent for all perturbations Δ if and only if the condition

$$\overline{\sigma}(M(i\omega)) < 1, \quad \forall \omega \quad (2.17)$$

is satisfied.^{48, 49, 101}

This theorem states that if Eq. (2.17) is satisfied then no perturbation can destabilize the closed loop $M - \Delta$. Thus, the degree of stability is unaltered by uncertainty. From Theorem 2.1 we can derive the necessary and sufficient conditions for robustness for the different uncertainty perturbation structures given in Eq. (2.14). By comparing Fig. (2.3) with Fig. (2.4), we obtain:

1) Additive uncertainty perturbation

$$M = -l_A(I + P_o)^{-1} \quad (2.18)$$

2) Multiplicative input uncertainty perturbation

$$M = -(I + P_o)^{-1} P_o l_I \quad (2.19)$$

3) Multiplicative output uncertainty perturbation

$$M = -P_o(I + P_o)^{-1} l_O \quad (2.20)$$

4) Multiplicative inverse uncertainty perturbation

$$M = (I + P_o)^{-1} l_E, \quad (2.21)$$

where for the nonparametric uncertainty descriptions, which follow from Eq. (2.13), all perturbation quantities must satisfy

$$\bar{\sigma}(L_k) \leq l_k, \quad k = A, I, O, E. \quad (2.22)$$

When the perturbations Δ are restricted by a specific block diagonal structure, such as in Eq. (2.15), Theorem 2.1 can be, in general, arbitrarily conservative. Therefore, to account for the structure of the perturbations Δ , in order to achieve tight bounds on the uncertainty, let us define the structured singular value (SSV) as an alternative to SVD. The function $\mu(M)$, or SSV, is defined such that $\mu^{-1}(M)$ is equal to the smallest maximum SVD of Δ needed to make $(I - M\Delta)$ singular.^{44, 101} If no Δ exists such that $\det(I - M\Delta) = 0$, then $\mu(M) = 0$. Hence, $\mu^{-1}(M)$ is a function of M and the structure of Δ . An interpretation of this definition in terms of the generalized small gain theorem,⁴⁴ similar to that given in Theorem 2.1, gives the SSV the tightest possible bound on our system M .

The following theorem establishes the necessary and sufficient robustness conditions for the structured or parametric perturbations Δ .

Theorem 2.2^{36, 48, 49}

Under the assumption that either all of the perturbations Δ are stable or all the members $P(s)$ of the set Π of possible plants have the same number of RHP poles and if the absence of encirclements of $\det(I - M\Delta)$ about the origin of the Nyquist D contour is necessary and sufficient for robustness, the closed loop system given in Fig. (2.4) is stable and/or the degree of stability is equivalent for all perturbations Δ if and only if

$$\mu(M(i\omega)) < 1, \quad \forall \omega. \quad (2.23)$$

Much like Theorem 2.1, this Theorem 2.2 states that if Eq. (2.23) is satisfied then no perturbation can destabilize the closed loop $M - \Delta$ and the degree of stability is unaltered by the parametric uncertainty description. Take note that when the perturbations are replaced by a

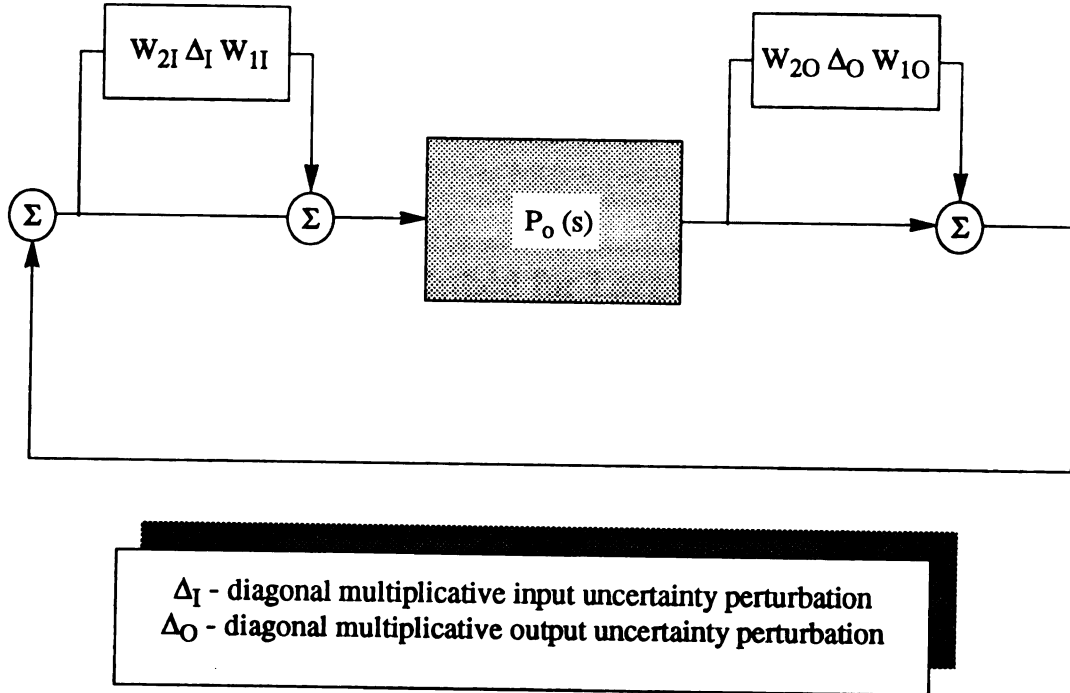


Figure 2.5 - An example of a plant with weighted multiplicative input and output uncertainty.

nonparametric or unstructured description, so that, Δ is a full matrix, then

$$\mu(M) = \bar{\sigma}(M) \quad (2.24)$$

which follows from Theorem 2.1.^{48, 101}

It has been shown that uncertainty can be characterized using parametric and non-parametric uncertainty descriptions. These perturbations can then be applied directly where they occur in the model. For example, if we consider a model that has both actuator and sensor error, we can simultaneously apply weighted multiplicative input and output uncertainty perturbations using a parametric uncertainty description. A schematic of such an uncertainty model is given in Fig. 2.5.

In particular, we may combine these to form a more practical, mixed representation of uncertainty. Where, for instance, unmodelled dynamics could be expressed as a nonparametric

description and uncertainty in the pole locations could be expressed using a parametric uncertainty description. An important point to remember, whether either a nonparametric or parametric description is used, is that uncertainty must be modeled where it occurs, and not where it might be mathematically convenient.

2.2 A Concurrent Modeling Method for Large-Scale Systems

An approach that includes the kind of uncertainty models described in the previous section introduces two specific problems that need to be addressed during modeling: the *analysis problem*, and the *synthesis problem*. The analysis problem is to determine if a given set effectively portrays the system dynamics of the actual process. The evaluation of this problem involves experimental testing, parameter identification, and model testing with all quantitative examinations being limited to setting hard bounds. Specifically, such a procedure may involve overshoot, undershoot, risetime and settling time evaluation, response envelope and input bounding, and an examination of response effects due to disturbances, noise, or actuator operation. The object is to learn as much as possible about the system, its components, and their interactions. The synthesis problem, on the other hand, entails finding a nominal model and an associated uncertainty description that optimally and accurately fits the model set. To evaluate this problem, the fundamental properties discussed in the previous section must be imposed and evaluated. Of course, this usually requires a procedure that can efficiently access all the available information acquired in the preceding problem step in order to limit the decisions in the modeling procedure and the number of iterations. Hence, a concurrent engineering method would be a very practical format in which to make these decisions during the modeling process.

In Figure 2.1, a standardized modeling procedure was presented for large-scale systems analysis.¹²⁹ This procedure is characteristic of typical iterative top-down approaches that rely on highly accurate representations for the system's components. It was shown in the previous

section that such highly accurate representations are not always necessary. In fact, a highly uncertain system can be modeled very efficiently. Innate system uncertainty can be non-conservatively and accurately modeled.¹¹⁸ Undoubtedly, it would be very effective if we could take full advantage of this trade-off between what we know and what we do not know about the system. Moreover, it would be very efficient if we could not only do this, but do it concurrently.

2.2.1 The analysis problem

For large-scale systems, a common difficulty arises with the need to efficiently represent the components and their interconnections. A structure that can simplify these interactions should be hierarchical so that systems can be built from the bottom up.³⁶ Such a structure will permit models and data, which describe a system or a collection of systems, to be incorporated into, and extracted from, a single variable. For instance, such a variable might contain design, performance, and/or input specifications, in addition to the plant model, controller or both. Furthermore, these variables are flexible in that they allow functions to be represented in state-space form, as a transfer function, as polynomials, etc., thereby vastly simplifying user interaction. A general schematic for a controlled structure is given in Fig. 2.6. This structure can be formed using commands in MATLAB's *Robust Control Toolbox*. In Fig. 2.6, the system's components are broken into the respective parts and all their ancillary components, bounds, and specifications are branched accordingly. Consequently, this simplified user interaction allows us to make major or minor modifications and improvements in the branches such that results can be readily observed in the main system tree.

All the different techniques and ways used to obtain a model for the system and its components can usually be classified in terms of either a forward or an inverse problem evaluation. In particular, system identification methods can be categorized as an inverse problem definition, whereas all others tend to fall into the forward problem solving class. Unlike the

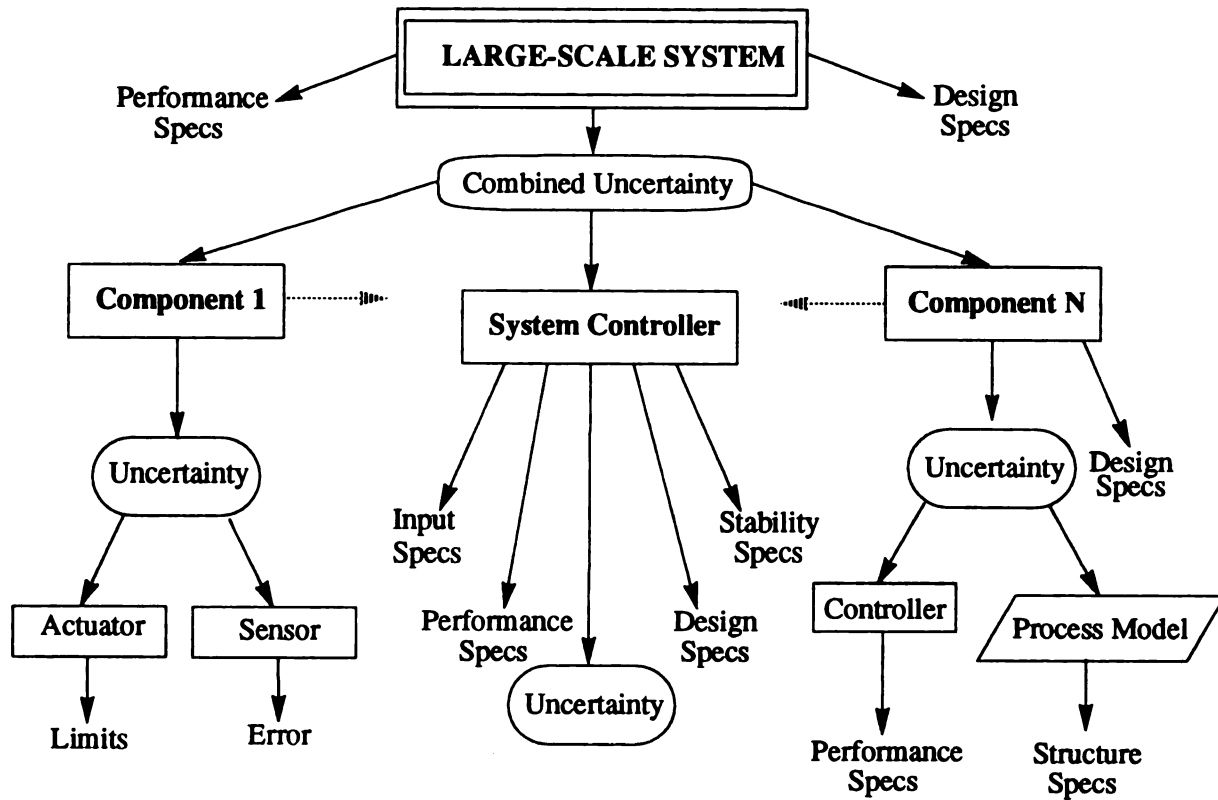


Figure 2.6 - A hierarchical structure for constructing and completing the analysis problem for large-scale systems.

forward problem definition class, system identification techniques are very useful, because models are derived directly from experimental data. These models are used for verifying predicted dynamical models, setting bounds on inputs and parameters, and improving the fidelity of a reduced order model. The details pertaining to the different types of system identification techniques will not be discussed here. However, generally, system identification involves an experimental apparatus of some kind in order to measure, acquire and process data. These data possess measurement uncertainty, in addition to numerical uncertainty in the estimation algorithm, and in conjunction with uncertainty apparent in the reduced or assumed model structure for the system. Nonetheless, for all the uncertainty inherent in the procedure, system identification provides the best methods known for verifying predicted models.^{80, 111} Thus, it is crucial to

couple the inverse problem definition process with the forward definition process in order to obtain all available information and verify a model set.

2.2.2 The synthesis problem

The evaluation of all available information occurs in this portion of the modeling procedure. It is here where models are rejected, and successive iterations may take place before a useful nominal model and its associated uncertainty description are found. Therefore, assuming that the work accomplished in the analysis problem is complete, we can use this information to simultaneously characterize our given model. Regarding model reduction, fitting, and error analysis, it is assumed that these will all take place when using a frequency description of the model. The frequency domain is most useful because it provides the person modeling with some measure of the model's response over all frequency.^{111, 118} This is very important in the steps discussed here because most uncertainty models have limits that vary extensively with frequency and models that must be based on frequency weighted bounds. These uncertainty models are very common. The frequency domain also allows us to investigate frequency dependent parameters and model them accordingly.

A general schematic showing how the synthesis problem may be conducted is given in Fig. 2.7. This diagram takes into consideration the fact that information about a particular component or system can be obtained analytically, numerically, and experimentally. In most cases, analytical methods are highly limited and solutions are usually approximated using numerical techniques. The key in the system identification portion of this procedure is to select a model structure and its order to fit data using an appropriate estimator. Clearly, reduced-order models are highly desirable, thus, the nominal model and identified models should reflect this. Usually, from the identification procedure, enough data can be obtained to develop reasonable nonparametric models. Since nonparametric models are necessarily lumped models, these

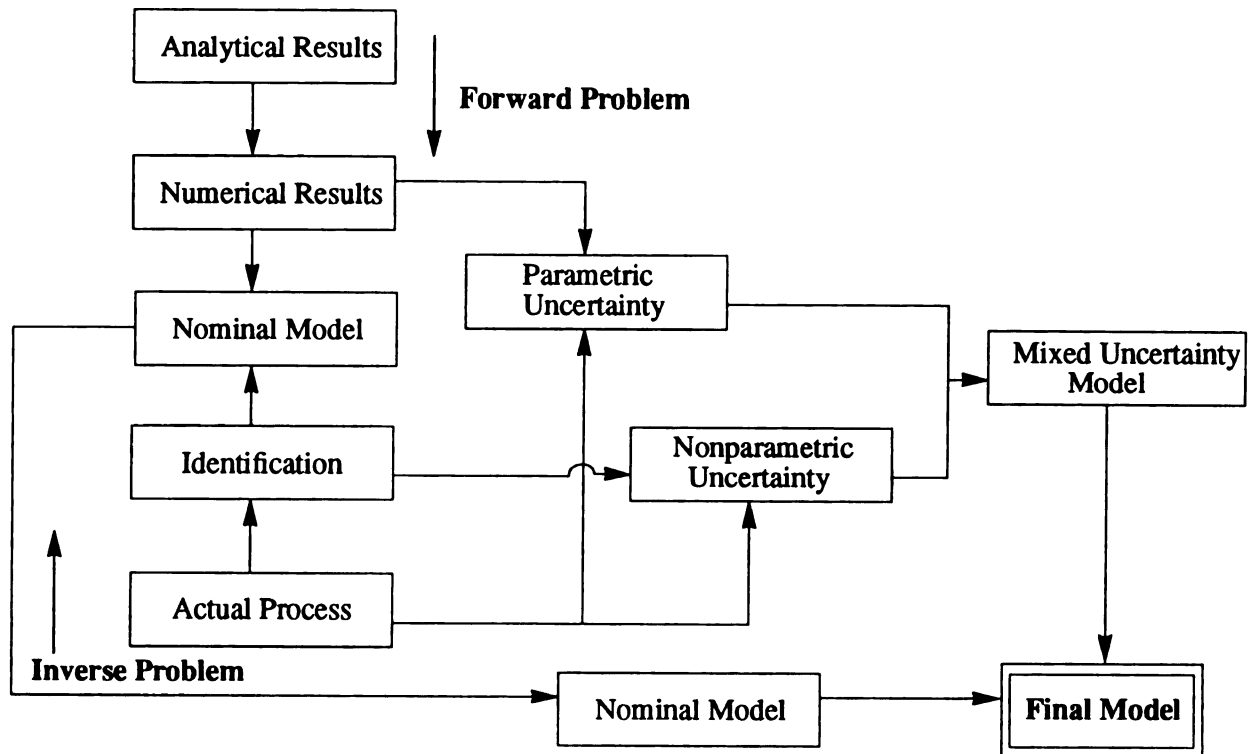


Figure 2.7 - A concurrent scheme for evaluating dynamical system models and uncertainty.

uncertainty descriptions can be readily constructed.¹⁸

Some time after the nonparametric models have been formed, the task of making the uncertainty model less conservative must be executed through a parametric identification. This process is usually conducted by changing parameters in the numerical model and comparing these results with the actual event. In some cases, it may be necessary to add the nonparametric model may need to be added to the numerical model in order to complete this task. However, results will be conservative if proper care is not taken. The difficulty with constructing a parametric uncertainty representation is that a substantial amount of knowledge, understanding, and information about the actual process must be obtained.

Finally, the two representations can be joined to form a mixed representation. Mixed uncertainty representations can take on many different shapes and/or forms. They either can be

written out in a simultaneous manner or in a sequential manner. For example, in a sequential type representation, we allow a parametric uncertainty description to degenerate into a nonparametric description at a particular limiting frequency. This is based on the reasoning that we will probably know more about the model and system behavior in the low frequency range than we know in the high frequency range. After some experimental and/or numerical analysis, a crossover region can be identified where all details about the system's parameters become quite fuzzy. It is this crossover region where the uncertainty model changes from parametric to nonparametric to compensate for such things as unmodelled dynamics, neglected dynamics, etc. The sequential mixed uncertainty representation provides us with the flexibility to tailor our model to give the most nonconservative results.

Discussion about the nominal model has been brief partly because of the need for an optimization procedure to be defined. A general diagram for a model fitting optimization procedure is given in Fig. 2.8. This schematic closely resembles the procedure outlined in Fig. 2.7 with some additional decision making details. The kernel of the optimization procedure is to fit uncertainty sets that have been obtained using numerical, analytical, and experimental results to some predetermined nominal and uncertainty model. Such a method must be able to search along all set boundaries and make very nonconservative fits. For most cases, it follows that a search over all the given sets will involve first finding the center of the set, and second verifying that it is a good representation of that set. Obviously, this center, which can be found using a myriad of numerical techniques, represents the nominal model. Basically, the goal for multiple uncertainty sets is to fit a continuous model through determined center points and minimize conservatism in the uncertainty model given the robustness constraints discussed in the previous sections. Clearly, the rigidity of the procedure outlined in Fig. 2.8 is kept to a minimum because the general formulation of the nominal and uncertainty model is often isolated from that of any common problem because several objectives will often need to be addressed and

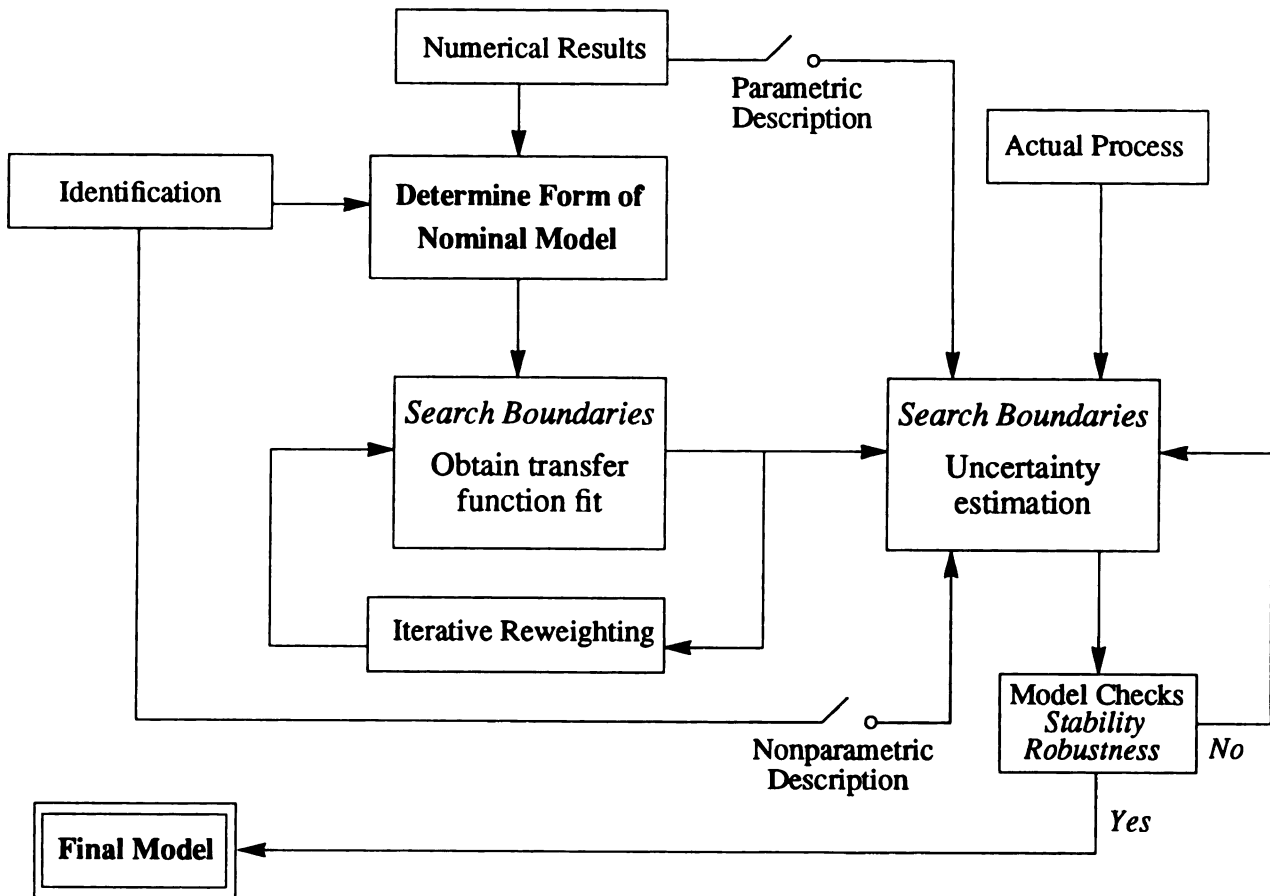


Figure 2.8 - A generalized nominal and uncertainty model optimization procedure.

traded off in some manner. Therefore, requirements for an optimization procedure must enable the model's intentions to be expressed, yet be able to solve the problem and enter preferences into a numerically tractable and realistic procedure.

In a graphical depiction, consider the family Γ of all possible plants represented by an infinite number of uncertain regions in the Nyquist plane, as shown in Fig. 2.9(a). Since an infinite number of uncertain regions are shown, we only see the uncertainty in terms of an upper and lower bound. If we accept a nominal model to be the average of these two bounds, optimization is unnecessary and this problem becomes rather trivial. However, if we have a representation, as shown in Fig. 2.9(b), with a finite number of uncertain regions, the optimization procedure becomes more difficult. This is because we must first determine a point

in

pe

m

in

ea

thi

of

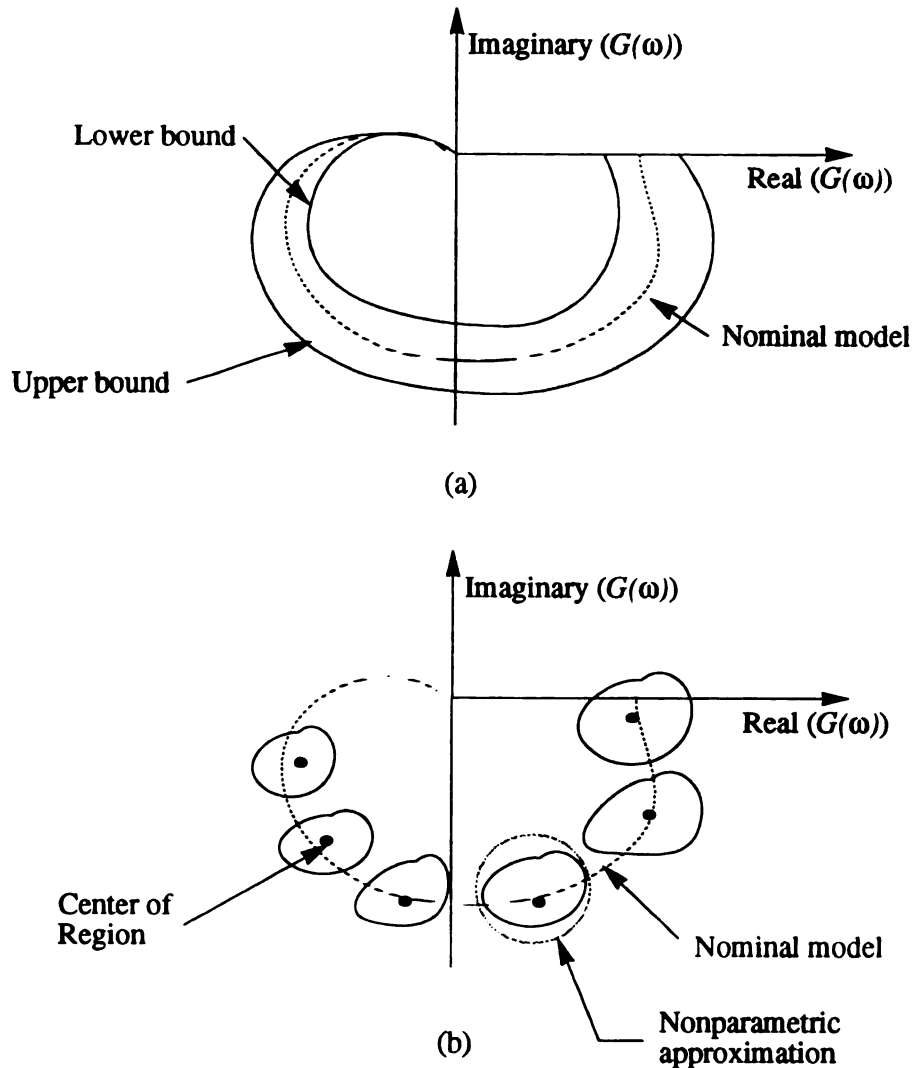


Figure 2.9 - An example of uncertainty regions for a family Γ graphically shown in the Nyquist plane.

inside each region that is at or is near its center, and secondly determine a continuous model that passes through each of these points. Next we optimize the fit for a nonconservative uncertainty model that varies with frequency. If we wanted to approximate each given region of uncertainty in Fig. 2.9(b) with a normed-bound, then we would search for the smallest circle that contains each actual uncertain region of interest and fit it with an additive uncertainty model. Although this gives a very convenient uncertainty representation for numerical purposes, it is at the expense of some conservatism, because it includes regions outside the actual uncertainty.

2.3 A Numerical Example

2.3.1 Analytical analysis formulation

For an example of the technique proposed in the previous section let us consider a simple cantilever beam with a concentrated mass attached to its free-end. We will assume elastic deformation to be small and model the beam using Euler-Bernoulli beam theory. The configuration of the beam and the corresponding notation are given in Fig. 2.10. Using variational principles, an expression for the beam's equation of motion can be written as:

$$EI \frac{\partial^4 w(x, t)}{\partial x^4} + \frac{\partial}{\partial t} [w(x, t)] + \tilde{m} \frac{\partial^2 w(x, t)}{\partial t^2} = -\tilde{m} \frac{\partial^2 w_o(x, t)}{\partial t^2} \quad (2.25)$$

and the corresponding boundary conditions

$$w(0, t) = 0 \quad \frac{\partial w}{\partial x}(0, t) = 0 \quad (2.26)$$

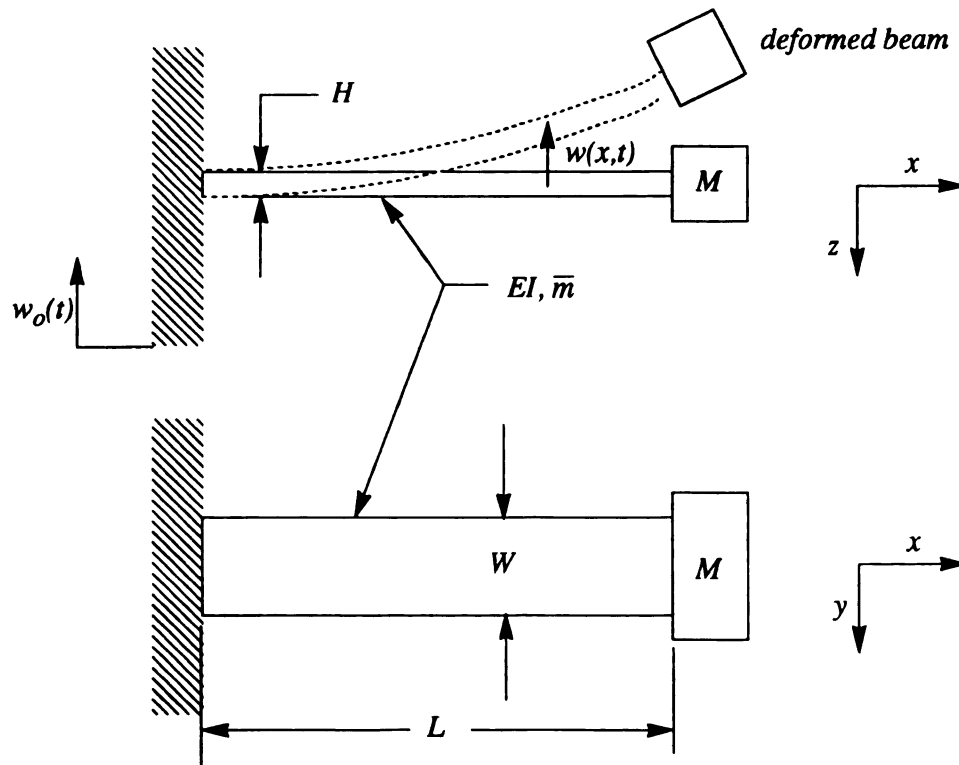


Figure 2.10 - The configuration for the cantilever beam example.

$$EI \frac{\partial^2}{\partial x^2} (w(L, t)) = 0 \quad EI \frac{\partial^3}{\partial x^3} (w(L, t)) = M \frac{\partial^2}{\partial t^2} w(x, t) \quad (2.22)$$

where $w(x, t)$ is the lateral displacement of an arbitrary point on the beam for any given time t , EI is the beam bending stiffness, ν is the damping operator, \tilde{m} is the mass per unit length of the beam, M is the mass of the attached concentrated load, and $w_o(t)$ is a rigid-body external translation applied to the beam. The dimensions of the beam are given in terms of its length L , width W , and height H . Also, M is regarded strictly as a point mass.

To begin the modeling procedure, we initially see that an analytical solution to Eq. (2.25) can be obtained using the separation of variables method.⁹⁵ Assume that the solution can be written as

$$w(x, t) = \sum_{k=1}^{\infty} \phi_k(x) \eta_k(t) \quad (2.28)$$

where $\phi_k(x)$ are the normal mode shapes or eigenfunctions and $\eta_k(t)$ are the time-dependent generalized coordinates. By substituting Eq. (2.28) into Eq. (2.25), we obtain

$$EI \sum_{k=1}^{\infty} \phi_k^{IV}(x) \eta_k(t) + \sum_{k=1}^{\infty} \nu[\phi_k(x)] \dot{\eta}_k(t) + \tilde{m} \sum_{k=1}^{\infty} \phi_k(x) \ddot{\eta}_k(t) = -\tilde{m} \ddot{w}_o \quad (2.29)$$

Now let us assume that the normal modes of the undamped system, as determined by the eigenvalue problem, can be used to uncouple Eq. (2.29). To complete the eigenvalue problem, the damping and the forcing terms in Eq. (2.25) are temporarily excluded and a general solution is easily verified for the free vibration problem to be

$$\phi_k(x) = A' \sin(\lambda_k x) + B' \cos(\lambda_k x) + C' \sinh(\lambda_k x) + D' \cosh(\lambda_k x), \quad k = 1, 2, 3, \dots \quad (2.30)$$

where A' , B' , C' , D' are constants of integration and λ_k are positive variables. By substituting Eq.

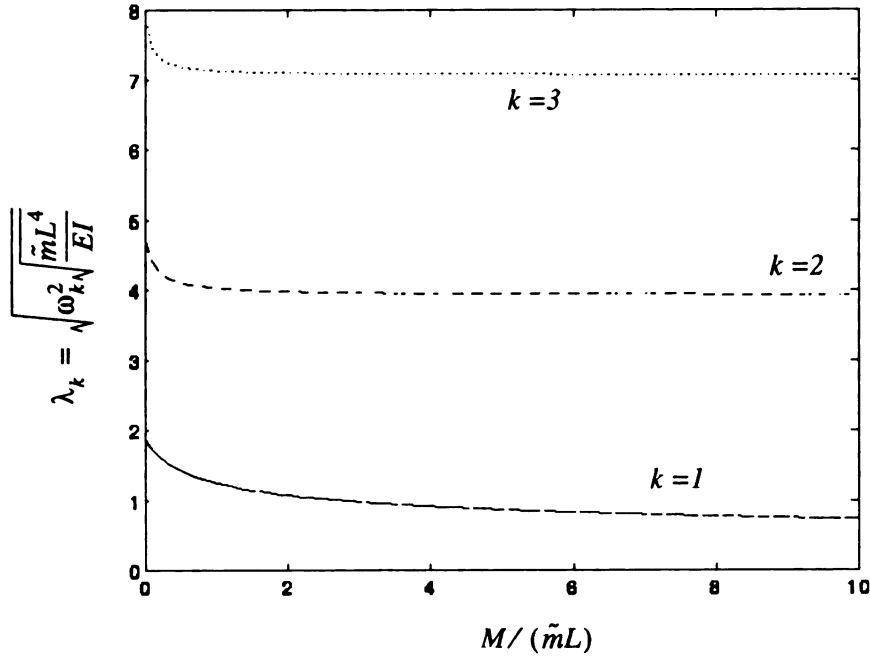


Figure 2.11 - The variation of λ_k with concentrated tip mass ratio.

(2.30) into Eq. (2.25) and applying the boundary conditions, the following equation is yielded:

$$\phi_k(x) = \frac{C'}{(\cos(\lambda_k L) + \cosh(\lambda_k L))} [(\sin(\lambda_k x) - \sinh(\lambda_k x))(\cos(\lambda_k L) + \cosh(\lambda_k L)) - (\sin(\lambda_k L) + \sinh(\lambda_k L))(\cos(\lambda_k x) - \cosh(\lambda_k x))] \quad k = 1, 2, 3, \dots \quad (2.31)$$

where the infinite values for λ_k must be determined numerically from

$$\lambda_k = \frac{-\tilde{m}(\cos(\lambda_k x) \cosh(\lambda_k x) + 1)}{M(\cos(\lambda_k L) \sinh(\lambda_k L) - \cosh(\lambda_k L) \sin(\lambda_k L))} \quad k = 1, 2, 3, \dots \quad (2.32)$$

Once this equation has been solved for λ_k , we can complete the eigenvalue problem by determining the undamped natural frequencies

$$\omega_k^2 = \lambda_k^2 \sqrt{\frac{EI}{\tilde{m}L^4}}, \quad k = 1, 2, 3, \dots \quad (2.33)$$

The resulting values for $k = 1, 2$ and 3 are given in Fig. 2.11 for a large range of tip masses. It is obvious from the diagram that structural variation can be considered quite negligible for masses

five

pon

ing

we

max

whic

damp

[0, L]

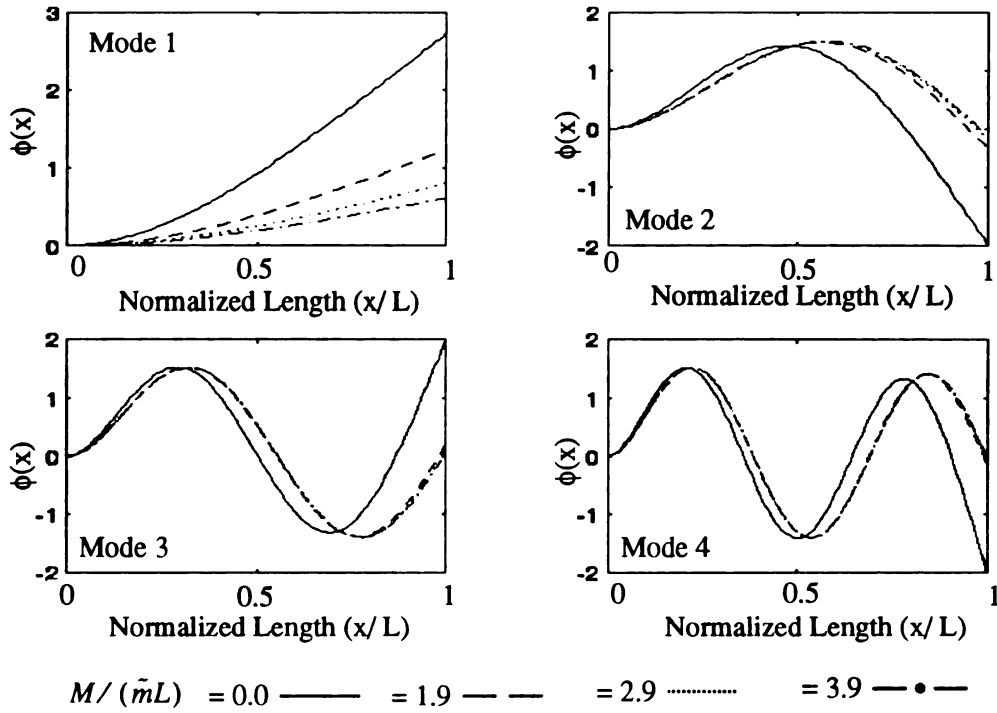


Figure 2.12 - First four normal mode shapes for various concentrated tip mass ratio.

five times as great as the beam. It is important to determine whether the beam can actually support a mass of such magnitude and maintain the specified deflection constraints. The corresponding mode shapes for various tip masses when $k = 4$ are given in Fig. 2.12. Clearly, from Fig. 2.12 we see that when no concentrated mass is added the mode shapes for the first four modes are at a maximum. The effect of adding inertia at the end of the beam suppresses normal mode vibration, which acting in a manner proportional to the square of its natural frequency.

Under the assumption that the normal modes of the undamped system are unaffected by damping, then by multiplying Eq. (2.29) by $\phi_r(x)$ and integrating over the domain of the beam $[0, L]$ we can use the orthogonal relationship to form

$$\ddot{\eta}_k(t) + \sum_{r=1}^{\infty} \nu_{rk} \dot{\eta}_k(t) + \omega_k^2 \eta_k(t) = N_k(t), \quad k = 1, 2, 3, \dots \quad (2.34)$$

2

the

the

with

when

exp

when

solu

initi

After

where

$$v_{rk} = \int_0^L \phi_k(x) v[\phi_r(x)] dx, \quad r, k = 1, 2, 3, \dots \quad (2.34a)$$

and the generalized modal forces are represented by

$$N_k(t) = \int_0^L \phi_k(x) \ddot{w}_o dx \equiv \bar{n}_k \ddot{w}_o, \quad k = 1, 2, 3, \dots \quad (2.34b)$$

Take notice that Eq. (2.34) represents an infinite set of coupled ordinary differential equations, so that, in general, damping produces coupling of the normal coordinates. In order to continue with this analytical solution and obtain values for the response of the beam the assumption will be made that the damping operator is a linear combination of

$$v = \alpha EI \frac{\partial^4}{\partial x^4} + \beta \tilde{m} \quad (2.35)$$

where α and β are constant coefficients. In this case, the equations can be easily decoupled and expressed as

$$\ddot{\eta}_k(t) + 2\xi_k \omega_k \dot{\eta}_k(t) + \omega_k^2 \eta_k(t) = \bar{n}_k \ddot{w}_o, \quad k = 1, 2, 3, \dots \quad (2.36)$$

where ξ_k denotes the modal damping factors of the cantilever beam defined such that $\xi_k < 1$. The solution to Eq. (2.36) can be readily obtained by means of the Laplace transformation. With the initial conditions set to zero, the nonrational transfer function from input to output is

$$G(s) = \sum_{k=1}^{\infty} \left(\frac{\bar{n}_k}{s^2 + 2\xi_k \omega_k s + \omega_k^2} \right) \quad (2.37)$$

After some algebraic manipulation of Eq. (2.37) the response of the beam becomes

$$\eta_k(t) = \frac{1}{\omega_{kd}} \int_0^t N_k(\tau) e^{-\xi_k \omega_k (t-\tau)} \sin(\omega_{kd}(t-\tau)) d\tau, \quad k = 1, 2, 3, \dots \quad (2.38)$$

v

d

th

wh

inp

wh

res

when

where

$$\eta_k(0) = 0 \quad \dot{\eta}_k(0) = 0$$

and ω_{kd} is the natural frequency associated with the damped system, which is simply

$$\omega_{kd} = \omega_k \sqrt{(1 - \xi_k^2)} = \omega_k \sqrt{\left(1 - \left(\frac{\alpha \omega_k^2 + \beta}{2\omega_k}\right)^2\right)} \quad (2.39)$$

The general response for the beam is obtained by inserting Eq. (2.38) into Eq. (2.28), with the result

$$w(x, t) = \sum_{k=1}^{\infty} \phi_k(x) \frac{1}{\omega_{kd}} \int_0^t N_k(\tau) e^{-\xi_k \omega_k (t-\tau)} \sin(\omega_{kd}(t-\tau)) d\tau \quad (2.40)$$

where $\phi_k(x)$ is given by Eq. (2.31) and $N_k(t)$ by Eq. (2.34b). Let us consider the case in which the input has the form

$$\ddot{w}_o = -W_o \zeta(t) \quad (2.41)$$

where W_o is a constant acceleration and $\zeta(t)$ the unit step function. Hence, we arrive at the step response when Eq. (2.41) is substituted into Eq. (2.40) and integrated

$$w(x, t) = \sum_{k=1}^{\infty} \frac{-W_o A'}{B' \omega_k^2 (\cos(\lambda_k L) + \cosh(\lambda_k L))} [(\sin(\lambda_k x) - \sinh(\lambda_k x)) (\cos(\lambda_k L) + \cosh(\lambda_k L)) - (\sin(\lambda_k L) + \sinh(\lambda_k L)) (\cos(\lambda_k x) - \cosh(\lambda_k x))] \left[1 - \frac{1}{\sqrt{(1 - \xi_k^2)}} e^{-\xi_k \omega_k t} \cos(\omega_{kd} t - \theta_k) \right] \quad (2.42)$$

where

$$\theta_k = \arctan\left(\frac{\xi_k}{\sqrt{(1 - \xi_k^2)}}\right) \quad (2.42a)$$

$$A' = \left(\frac{2}{\lambda_k}\right) (\cosh(\lambda_k L) + 1 - \cosh(\lambda_k L) (\cos(\lambda_k L) - 1)) \quad (2.42b)$$

Let

the cons

response

tip mass

the beam

case to c

experime

In F

via Eq. (2,

2. Clearly

denced in

mass, the re

Table 2.1 - Material and geometric properties for the flexible beam configuration.

Property	Specifications
Material	Aluminum Sheet
L	31.2 cm
W	2.60 cm
H	0.1143 cm
E	68.5 GPa
\tilde{m}	0.7133 g/cm
α	0.00124
β	0.001

$$B' = \sqrt{\int_0^L \phi_k^2(x) dx + \frac{M}{\tilde{m}L} \phi_k^2(L)} \quad (2.42c)$$

Let us consider a beam with the material and geometric properties given in Table 2.1. With the constant acceleration W_o set to 1 cm/s², we can use Eq. (2.42) to determine the transient response of the beam's tip ($x = L$) for various conditions. These conditions will include various tip masses, variations in the elastic bending stiffness, various damping factors, and variations in the beam dimensions. It is anticipated that damping will be very small and vary slightly from case to case and mode to mode. Therefore, the damping parameters will need to be bounded experimentally as determined in the proceeding formulation.

In Fig. 2.13, the analytically determined response of the cantilever beam for a step input, via Eq. (2.42) and summed over $k = 1$ through 10, is given for various tip mass ratios of 0, 1, and 2. Clearly, the amplitude of the tip decreases with increasing tip mass, a trend which was evidenced in the eigenvalue results given in Fig. 2.11. Effectively, with infinitely increasing tip mass, the response of our cantilever beam with the free-end boundary condition degenerates into

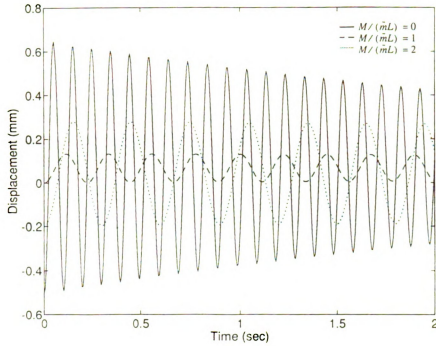


Figure 2.13 - Step input response for various concentrated tip mass ratios.

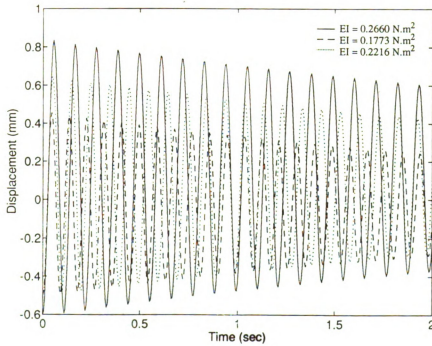


Figure 2.14 - Step input response for various beam bending stiffness.

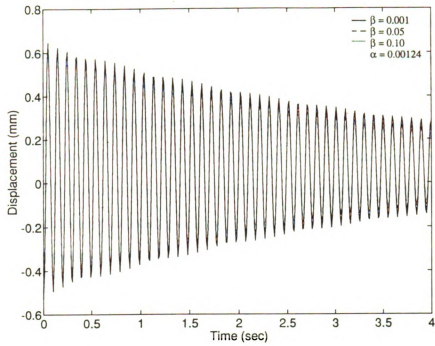


Figure 2.15 - Step input response for various values of β with α constant.

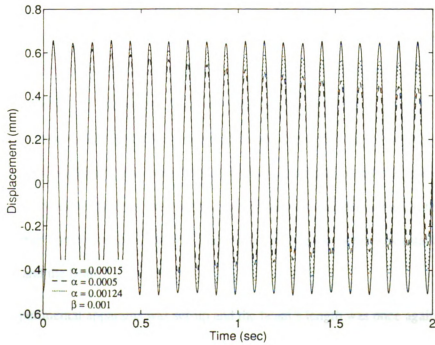


Figure 2.16 - Step input response for various values of α with β constant.

one with a pinned boundary condition, thus tip displacement will approach zero. In Fig. 2.14, beam response is given for variations in the bending stiffness of up to $\pm 20\%$ of the value given in Table 2.1. These results show this parameter significantly contributes to the magnitude of the beam's amplitude. Realistically speaking, 20% is a rather large variation, however, it serves to prove how uncertainty in assumed constant values can alter final results substantially. Figures 2.15 and 2.16 are presentations of a step input response for variations in the constant damping parameters α and β . It is assumed that for convenience, these remain constant for all modes and are innate characteristics of the beam's material. It is evident from Fig. 2.15 and 2.16 that α influence on decay is much greater than β but only over a limited range of values. This is partly because α is proportional to the square of the modal natural frequency, yet it is limited because ξ_k becomes imaginary at various modes when α is greater than 0.00124. We see that having two parameters to adjust, which gives us more freedom when putting bounds on damping.

2.3.2 Experimental analysis formulation

The primary objective for this experimental portion of the analysis problem is to determine bounds on the actual response of the beam. These bounds, in conjunction with the analytical results, will be used to obtain a useful uncertainty model for our final reduced order, linearized system. Accordingly, an Aluminum beam with the same dimensions as given in Table 2.1, and configuration as shown in Fig. 2.10, was utilized in this example. To provide excitation a vibrational shaker was employed. The beam was clamped onto a rigid mount that was attached to this shaker. The concentrated masses used in the experiment were securely attached to the end of the beam via rubber contact cement. It was important that a good bond was established between these masses and the beam.

The experimental apparatus was set-up and the beam's length was once again measured due to variation in the clamping procedure. It was found that the measurement uncertainty was approximately $\Delta L = \pm 1$ mm. This uncertainty was also consistent for the width measurement.

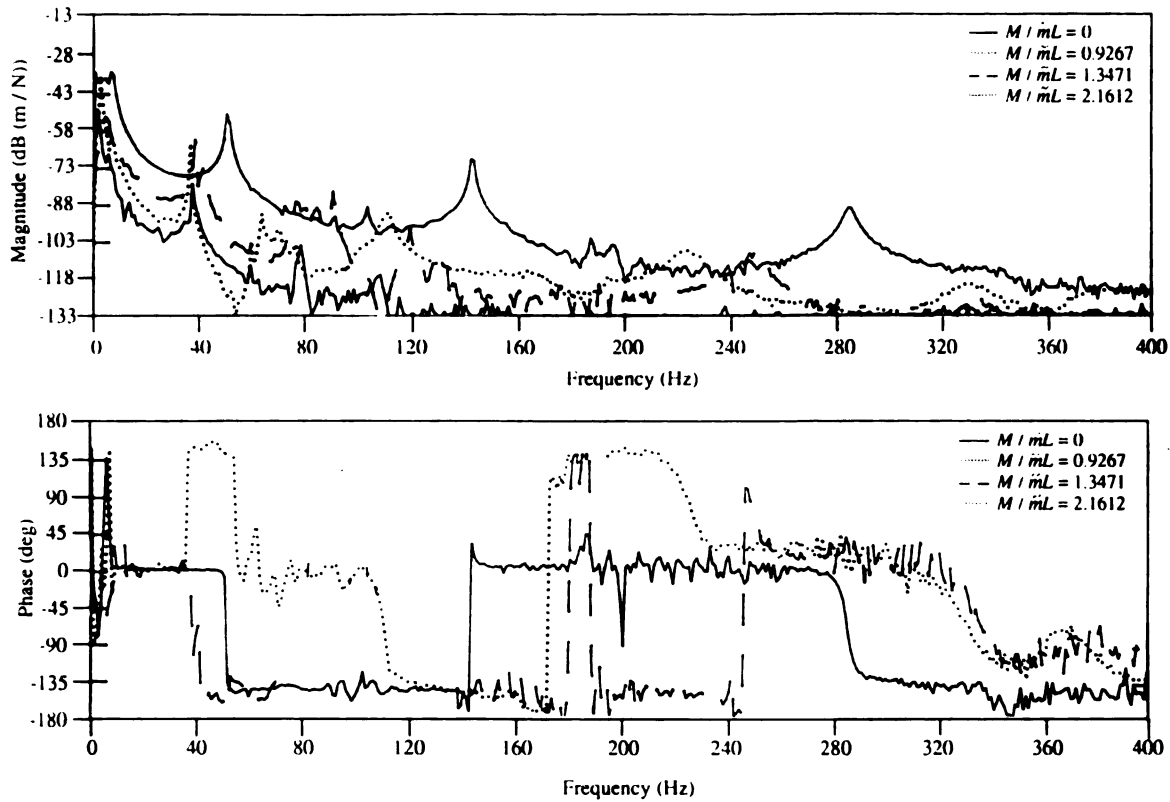


Figure 2.17 - Receptance response for various mass ratios.

Three small aluminum blocks of approximately 20.18 g, 29.98 g and 48.10 g were used for the concentrated tip masses and the mass per unit length of the beam was 0.713 g/cm. The measurement error in these readings were determined to be approximately $\Delta M = \pm 10$ mg. Additional sources of uncertainty were also investigated. Uncertainty attributed to variations in the elastic bending modulus over the length, a non-rigid tip mass attachment, excitations at the natural frequencies of the mounting apparatus, beam warping, and fluctuating conditions of the boundary conditions. Obviously, such uncertainties are not only small, as compared to measurement noise and calibration error, but are difficult to quantify directly. Thus, they can be lumped together in the form of a nonparametric model which will be determined later.

To measure the natural frequencies and damping factors for each mode of interest wideband and narrowband periodic excitations were applied. Over a wideband range of 400 Hz the magnitude and phase of the receptance was measured. Receptance is a measure of the displacement of

Table 2.2 - Measured cantilever beam natural frequencies.

Frequency (Hz)	Concentrated Tip Mass Ratio			
	0	0.9267	1.3471	2.1612
ω_1	9.25	4.25	3.85	2.8754
ω_2	58.625	45.91	38.875	44.25
ω_3	162.10	127.5	120.38	118.125
ω_4	290.75	220.63	213.25	174.25
ω_5	473.25	347.13	325.21	225.75
ω_6	578.63	426.88	428.0	359.15

the structure under a constant input load normalized by that load.¹⁰² For various ratios of tip mass to beam mass, the receptance of the beam at $x = L$ is illustrated in Fig. 2.17. It is easy to see from Fig. 2.17 that phase information contains extreme noise which greatly increases with additional mass. This noise is especially apparent in the very high and very low (rigid-body) frequency regions. With increasing tip mass the resonant peaks decrease and shift to the left as they are dominated by strong regions of anti-resonance. This is also evident in the diagram for the phase also. The greater the mass-dominance the greater the negative slope of the frequency response magnitude.

For purposes of identifying these resonant peaks narrowband excitation was used. The first six natural frequencies for the various tip masses are given in Table 2.2. These values are observed to be in close agreement qualitatively with Fig. 2.11, where a general decrease in magnitude occurs with increasing tip mass. Table 2.3 presents a comparison between the calculated and measured natural frequencies of the beam for $M/\tilde{m}L = 0$ and $M/\tilde{m}L = 2.1612$. As seen from these results the analytical data provides an upper bound and the measured values provide the lower bound on ω_n . The difference can be attributed to damping and energy losses through excitation of the out-of-plane and torsional modes. Moreover, friction at the clamped boundary inter-

Frequency (Hz)	$M/\bar{m}L = 0$		$M/\bar{m}L = 2.1612$	
	Calculated	Measured	Calculated	Measured
ω_1	10.132	9.25	3.023	2.8754
ω_2	63.50	58.625	45.621	44.25
ω_3	175.81	162.10	145.28	118.125
ω_4	347.43	290.75	301.74	174.25
ω_5	575.98	473.25	515.07	225.75
ω_6	860.42	578.63	785.29	359.15

Table 2.3 - A comparison between measured and calculated cantilever beam natural frequencies.

face may add to these losses. Of course, this type of time-dependent boundary condition would be very difficult to model.

The damping ratios were obtained from Fig. 2.17 using the half-power point method.¹⁰² This method is convenient and used here because it is valid for small damping. Results were determined for various mass ratios and are given in Table 2.4. We see that damping tends to remain fairly consistent with increasing beam mass but decrease with increasing mode number.

Table 2.4 - Measured cantilever beam damping ratios.

Damping Ratio	Concentrated Tip Mass Ratio			
	0	0.9267	1.3471	2.1612
ξ_1	0.0204	0.0204	0.0209	0.0205
ξ_2	0.0173	0.0185	0.0193	0.0195
ξ_3	0.0096	0.0099	0.0102	0.0101
ξ_4	0.0088	0.0091	0.0095	N/A
ξ_5	0.0071	0.0054	N/A	N/A
ξ_6	0.0008	N/A	N/A	N/A

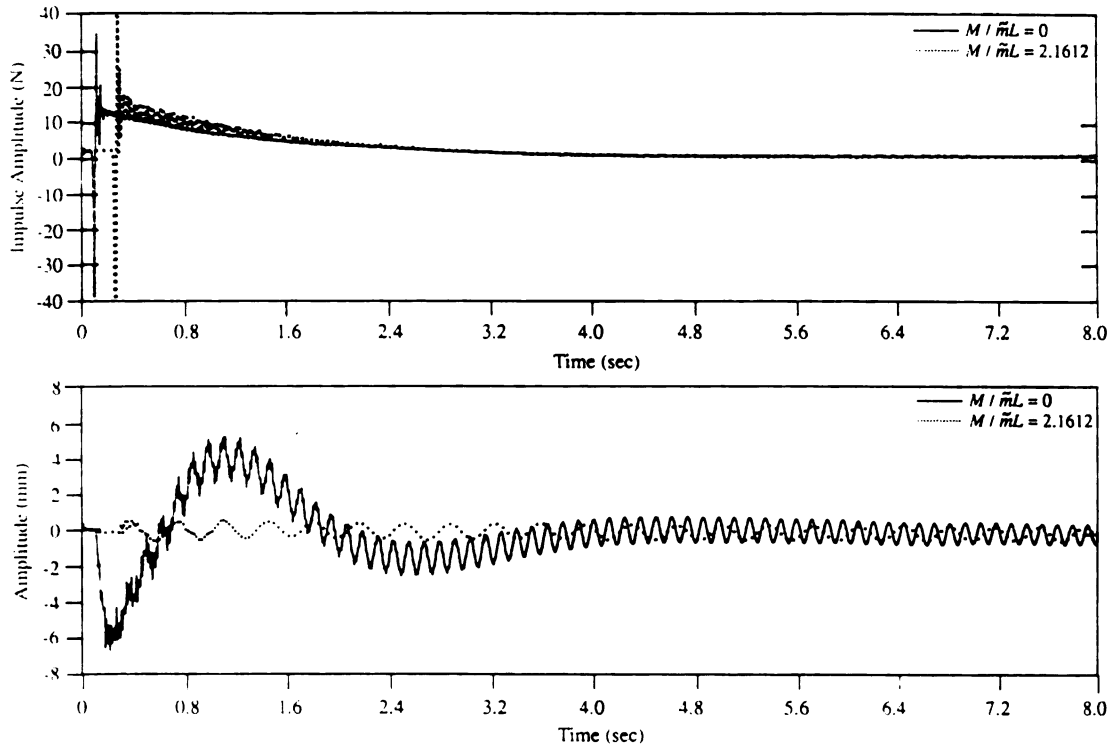


Figure 2.18 - Transient impulse response of the beam tip for two mass ratios.

At the higher modes for the larger masses damping ratios were indeterminable. The results for the modes greater than $k = 3$ are uncertain because the measurement signal was very weak. Hence, further calculations will be based on the assumption that damping ratios remain constant for $k \geq 3$.

Experimentally determined transient responses were obtained for both an impulse and step input. These responses were completed for tip mass ratios of 0 and 2.16, respectively. The object here was to set bounds on the overshoot, undershoot, and settling time for a pre-selected range of tip masses. Figure 2.18 is a depiction of the transient response due to an impulse of approximately 30 N. The vast differences between the two cases are apparent, where tip displacement for the 0 mass cases has an overshoot of about 6 mm and an undershoot of -2 mm. When a mass is attached to the tip, displacement is greatly reduced. As seen in these results, since oscillations are still occurring even after 8 seconds, damping must be very small. It took approximately 12 to 15 seconds for the tip to settle to its original position.

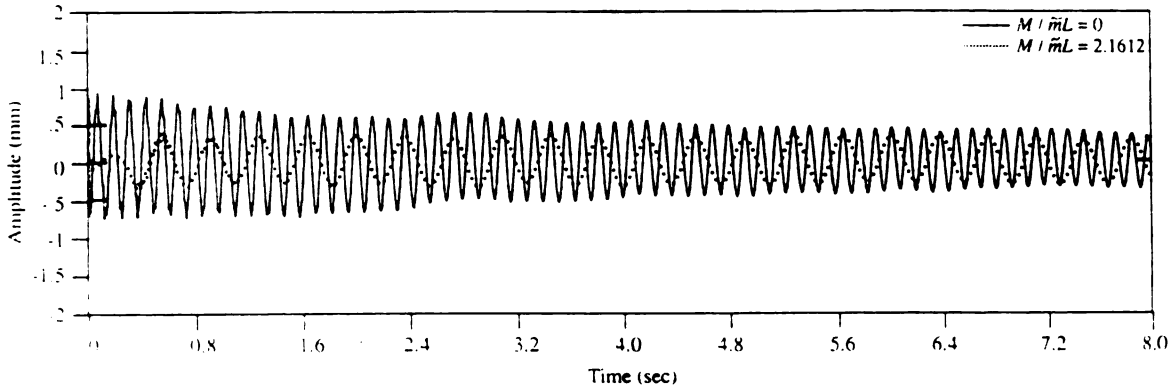


Figure 2.19 - Transient step response of the beam tip for two mass ratios.

In Fig. 2.19 the transient response of the beam is given for a step input of magnitude equivalent to W_0 in the previous section. Results from this experiment are very close to the analytical results presented in Fig. 2.13. By comparing the two cases using a linear systems approach, we find that the 0 mass ratio case has a period of $T_s = 0.1204$ seconds and a damping ratio of approximately 0.0087. The 2.16 mass ratio case has a period of $T_s = 0.3704$ seconds and a damping ratio of approximately 0.0097. If we assume the first mode to be the primary mode that dictates the beam's response, we see that the damping factors obtained from Fig. 2.19 are much less than those given in Table 2.4. However, these values are within a particular range when modes 1 through 3 are considered. This difference may be attributed to the averaging of the measurements that was used to obtain the receptance results illustrated in Fig. 2.17. The period gives us some indication of what response should be expected from a reduced order model. Also, since the natural frequencies and damping factors associated with each tip mass are different, the goal of the synthesis problem will be to construct a nominal model that can be used to reflect the general response of the model. We want to develop a nominal model that is able to accommodate uncertainty in the tip mass. The motivation for this is similar to that used when formulating a model for

Mode	Natural Frequency (Hz)		Damping Ratio	
	ω_k^L	ω_k^U	ξ_k^L	ξ_k^U
1	2.75	10.0	0.008	0.025
2	44.0	64.0	0.008	0.020
3	115.0	175.0	0.008	0.015
4	174.0	300.0	0.008	0.015
5	220.0	475.0	0.008	0.015
6	355.0	560.0	0.008	0.015

Table 2.5 -Physical bounds on model parameters.

a single-link robot arm where the mass of the object being grasped is known only within a specified range.

The conclusion of the analysis formulation involves evaluating the above information. After an examination of the analytical and experimental results we can set bounds that reflect the actual dynamics of the beam. Two specific sources of uncertainty need to be interpreted. These relate to general uncertainty in the dynamic model and specific uncertainty in its parameters. Essentially, because this example is rather simple, and it has been determined that the first mode is the primary mode that dictates the beam's response, we do not have to account for neglected dynamics. However, modeling errors in the high frequency dynamics cannot easily be neglected.. These errors, which are apparent in the analytical model, are attributed to the assumptions made regarding small deflections. To accurately model higher frequency modes, we would have to abandon Euler-Bernoulli beam theory for the more complex Timoshenko theory.¹¹⁹ Hence, it will be necessary to fit our model with a frequency weighted lumped perturbation.

The second source of uncertainty occurs due to variations in the model parameters. Since we identified several parameters earlier, such as tip mass uncertainty, measurement uncertainty, and material specification uncertainty, these parameters will be considered. However, because the

2.3.3 Synthesis problem formulation

$$\begin{aligned}\dot{x} &= Ax + Bu \\ y &= Cx\end{aligned}\tag{2.43}$$
$$\underline{x} = \{\eta_o, \dot{\eta}_o, \eta_1, \dot{\eta}_1, \dots, \eta_k, \dot{\eta}_k\} \quad \underline{x}(0) = \{\underline{x}_o\} \quad (2.43a)$$

$$\underline{w} = \{w_o\} \quad (2.43b)$$

$$\underline{y} = \{w(L, t)\} \quad (2.43c)$$

$$A = \begin{bmatrix} 0 & 1 & 0 & 0 & 0 & 0 \\ 0 & 0 & 0 & 1 & 0 & 0 \\ 0 & 0 & -\omega_1^2 & -2\xi_1\omega_1 & 0 & 0 \\ 0 & 0 & 0 & 0 & 0 & 0 \\ 0 & 0 & 0 & 0 & 0 & 0 \\ 0 & 0 & 0 & 0 & 0 & 0 \end{bmatrix} \quad (2.43d)$$

$$B = \begin{bmatrix} 0 & 1 & 0 & \bar{n}_1 & \dots & 0 & \bar{n}_k \end{bmatrix}^T \quad (2.43e)$$

$$C = \begin{bmatrix} L & 0 & \phi_1(L) & 0 & \dots & \phi_k(L) & 0 \end{bmatrix} \quad (2.43f)$$

and \mathbf{x}_o is a vector of initial conditions, and $\eta_o, \dot{\eta}_o$ represent rigid body motion of the beam. Equation (2.43) resembles the general form of the LTI system given in Eq. (2.7) with the exception that it is not finite-dimensional because it contains an infinite number of modes, all of which cannot be modeled. In order to continue this formulation, a truncated model will be derived using only four of the modes identified in the analysis. It is assumed that this primary mode model includes all characteristics in the residual modes of the beam's dynamics. We then have a four mode model a state vector containing 8 modal elements and two rigid-body elements. Also, take note that this problem is single-input single-output (SISO), since we are only interested in tip displacement for prescribed base motion.

If we assume that Eq. (2.9) is a valid representation for our uncertain system, then Eq. (2.43) can be rewritten as a nominal model with bounded perturbations on its matrices. Let us consider parametric model uncertainty. From Eq. (2.43e), we see that the tip mass directly affects the system matrices both as a parameter and through the system's eigenvalues. In order to model this system so that all variations in tip mass are accounted for, we need to select some nominal operating conditions. It has been determined that tip mass ranges between a bounded mass ratio of 0 and 2.25, therefore, calculated primary mode eigenvalues must range between [1.875, 1.0233]. For simplicity, we can determine a nominal operating condition by finding the mean of this range and substituting it into Eq. (2.32) to obtain a nominal mass ratio. The mean for the eigenvalue range was found to be 1.4491, which corresponded to a nominal mass ratio of 0.4421. Therefore, after substituting this value into Eq. (2.43), we see that nominal matrices B_o and C_o are easily established based solely on this nominal operating condition assumption.

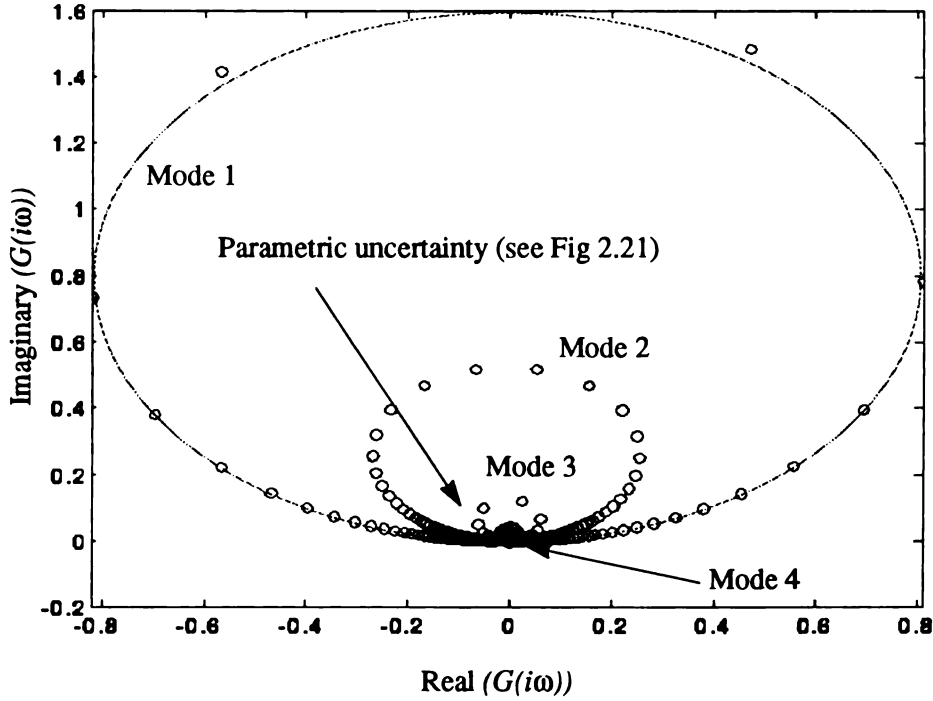


Figure 2.20 - Fuzzy Nyquist diagram associated with plant set.

Prior to constructing the nominal model, we transformed our state space model into a sum of four transfer functions, as given in Eq. (2.37), for the nominal operating condition. The transfer functions were used to get a physical understanding of the uncertainty region topology over a desired wideband frequency range of 0 to 400 Hz. This was accomplished by mapping the uncertain transfer functions to the Nyquist plane. The parametric in the modal natural frequencies and damping ratios is represented by the fuzzy Nyquist diagram in Fig. 2.20. From Fig. 2.20 we see that our plant set is open loop stable by the Nyquist criterion.²⁹ It is also evident that the gain margin for all possible plants and all modes is infinite, which is consistent with the experimental data in Fig. 2.17. The resolution of Fig. 2.20 does not specifically show the parametric uncertainty over the desired frequency range. To better observe the uncertainty regions, a local Nyquist plot was constructed and is given in Fig. 2.21. This plot graphically shows the effect of parametric uncertainty by nine individual fuzzy regions located at $\omega = [.01, 400]$.

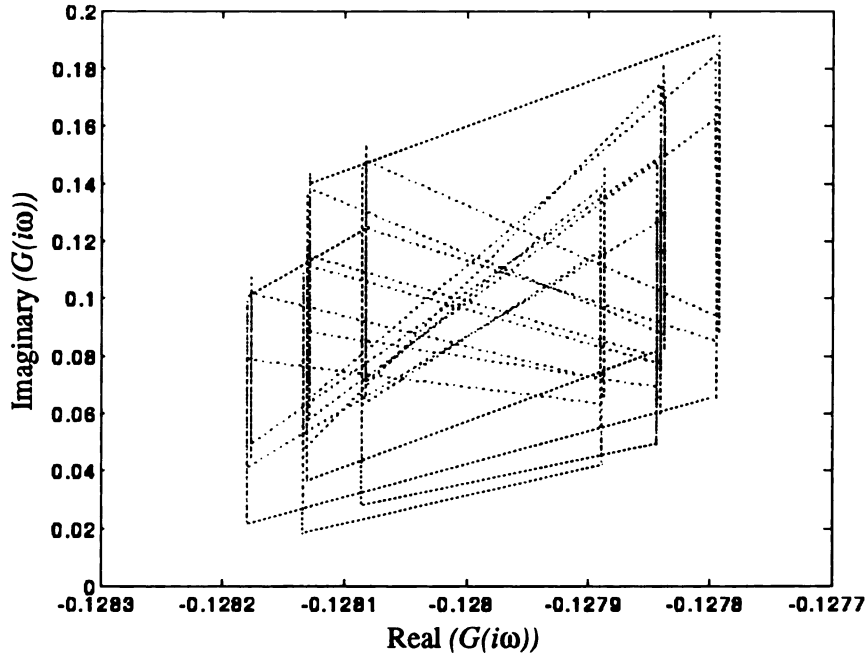


Figure 2.21 - Local fuzzy Nyquist diagram showing parametric uncertainty.

Now looking closely at matrix A reveals that it is composed of the two uncertain parameters. By focussing on the system matrix A the nominal model can be easily constructed by simply using the averages of the upper and lower bounds given in Table 2.5. In most cases, however, an assumption of this kind could lead to unwanted model error in critical frequency ranges. To avoid introducing more error than what already exists, two additional models were constructed for comparative evaluation. The first nominal model is based on an average of the individual poles and zeros in the model set transfer function. The second nominal model is an average of the individual elements in the A matrix. These two nominal models are referred to as 1 and 3, respectively, and the parameter averaged model as nominal model 2.

Fig 2.22 is an illustration of the fuzzy pole-zero map for this system, which has four stable poles and three zeros. The uncertainty regions associated with the zeros and poles are represented by the dotted and dashed lines, respectively. It is clear from this map that our uncertain system includes several nonminimum phase plants. Uncertainty descriptions that include RHP zeros must be carefully examined and constructed.¹⁰¹ Figure 2.23 is a detailed representation of the

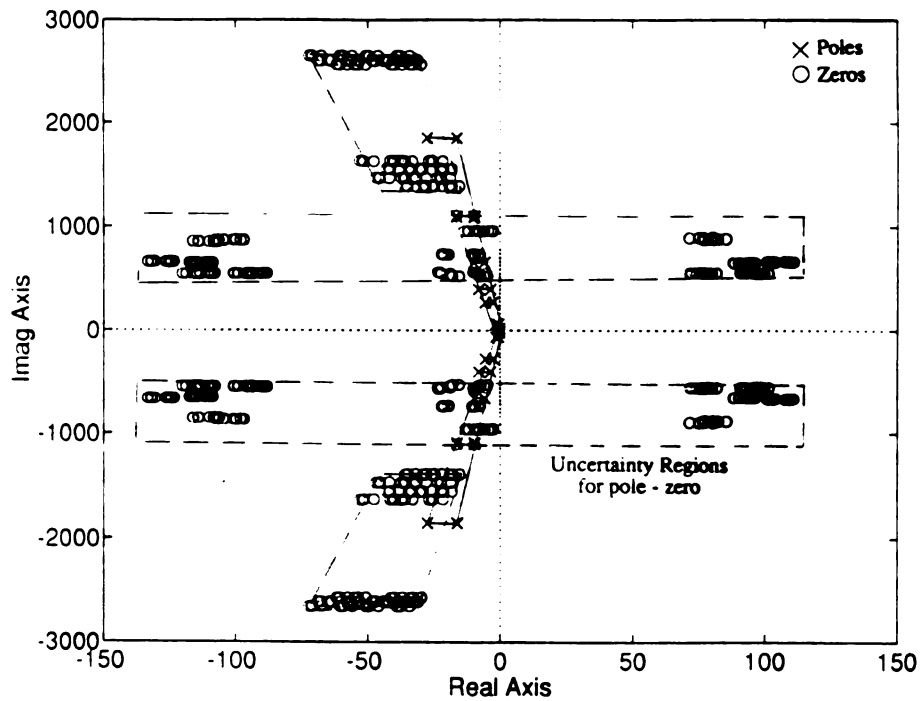


Figure 2.22 - A pole-zero map outlining global uncertainty regions included in the plant set.

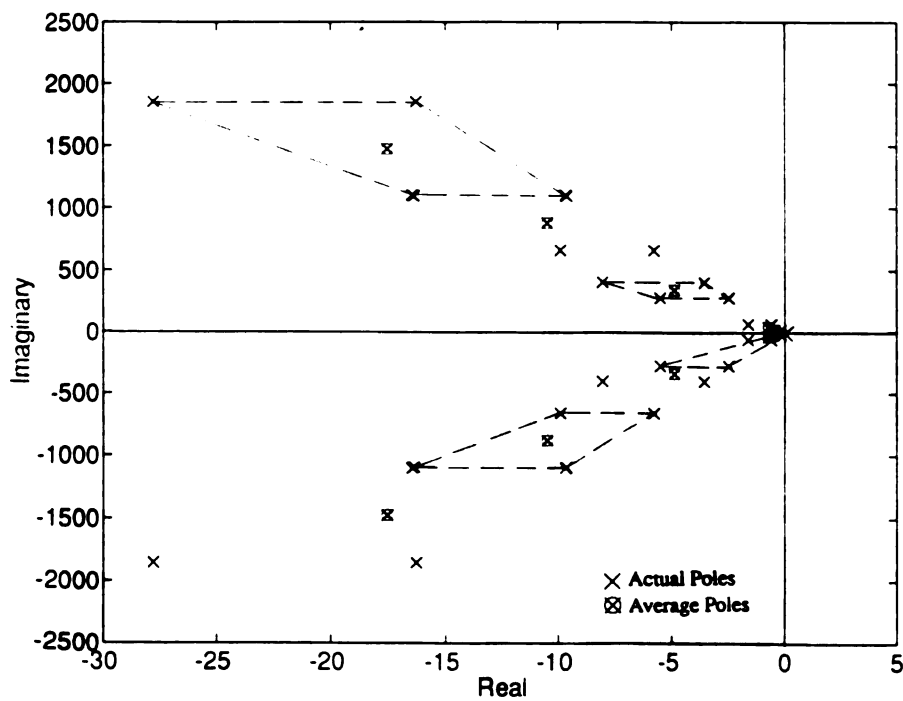


Figure 2.23 - Pole map showing averaged poles and their associated uncertainty regions.

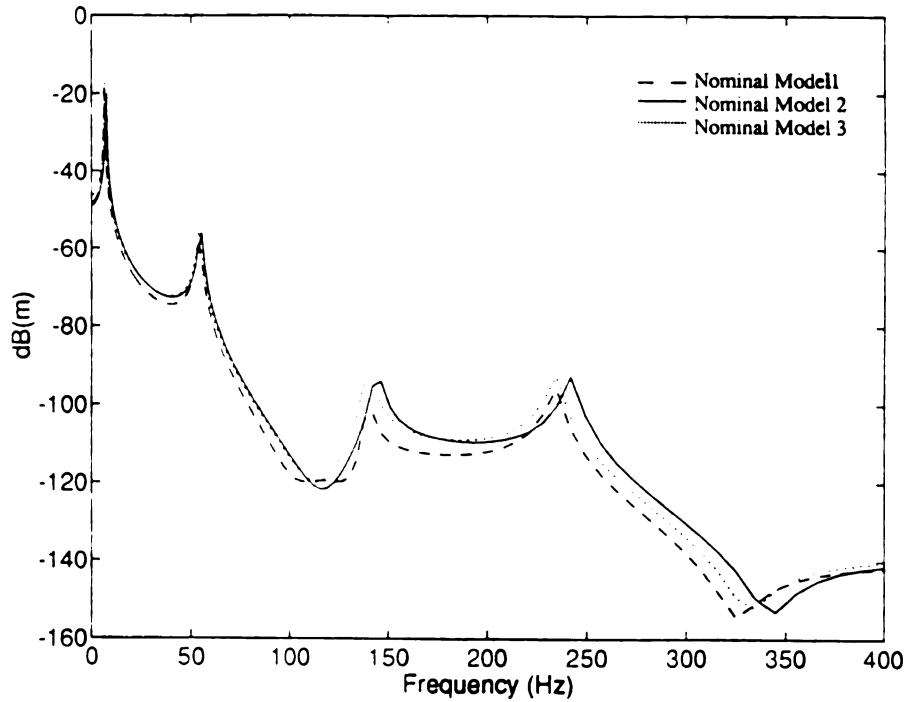


Figure 2.24 - Bode plots for the three 4 mode nominal models.

pole uncertainty and of the location of the averaged poles. Note that rigid-body mode causes one open loop pole to exist at the origin. Bode plots of the three four mode nominal models are illustrated in Fig. 2.24. Close agreement between the three models is apparent in the range between the first two primary modes. However, the difference between model 2 and models 1 and 3 becomes significant with increasing frequency. Models 1 and 3 are fairly consistent over the spectrum because they represent averages for the entire plant set. These results are also qualitatively consistent with the receptance plot given in Fig. 2.17. It follows from these results that model 3 will be adopted for the 4th order nominal model.

Now that the plant set has been bounded and the nominal model defined, consider modeling parametric uncertainty in detail. To include parametric uncertainty in the model, we need to formulate the plant using the block diagram in Fig. 2.4. Rewriting the uncertain equation (2.43) to fit this structure requires the perturbation ΔA be placed into the following form

$$\max_{A \in \Omega_A} |A - A_n| = \Delta A = W_2 \Delta W_1 \quad (2.44)$$

where matrices W_1 and W_2 play the roles of placing the parametric uncertainty block Δ into the diagonal structure given in Eq. (2.15). By substituting Eq. (2.44) into the uncertain version of Eq. (2.43) we are able to write the following state space equations that are associated with the M - Δ structure:

$$\begin{aligned}\dot{x} &= A_o x + B_o u + W_2 z \\ y &= C_o x \\ z &= \Delta W_1 x \\ \Delta &= \text{diag} \{ \Delta_{\omega_1^2}, \Delta_{\omega_2^2}, \dots, \Delta_{2\xi_1\omega_1}, \Delta_{2\xi_2\omega_2}, \dots \}\end{aligned}\quad (2.45)$$

where the subscript o refers to the nominal model. To obtain a diagonal matrix for Δ , the singular-value decomposition (SVD) can be applied to ΔA . As a result, SVD provides two unitary matrices which can be made equivalent to W_1 and W_2 such that the product of $W_2 \Delta W_1^T$ is identically ΔA . From Eq. (2.45), the overall augmented plant matrix and system matrix M written in state space form becomes

$$G(\Delta, s) \equiv \begin{bmatrix} A_o & B_o & W_2 \\ C_o & 0 & 0 \\ W_1 & 0 & 0 \end{bmatrix} = M \quad (2.46)$$

$$A = [A_o] \quad B = [B_o \ W_2] \quad C = [C_o \ W_1]^T \quad D = \begin{bmatrix} 0 & 0 \\ 0 & 0 \end{bmatrix}$$

This form is a linear fractional transformation of Eq. (2.43). It is used to represent the transfer function M “seen” by the uncertainty blocks as a transfer function from y to z .³⁶

Two step responses for an input of 1 cm/sec^2 were conducted for the upper (maximum ΔA) and lower (minimum ΔA) perturbations in the A matrix. The simulation results, illustrated in Fig. 2.25, are compared to the step response for the nominal model. The strong influence of the small damping and high natural frequency in the lower bound response is similar to the experimental results depicted in Fig. 2.19. In comparison to the nominal model and upper bound, we must also note the large amplitude of oscillation about 1.4 mm in the upper bound. These large values inevitably show that the physical bounds on the uncertainty perturbations are large as compared to the nominal model, possibly including more plant sets than are necessary. To determine the relative

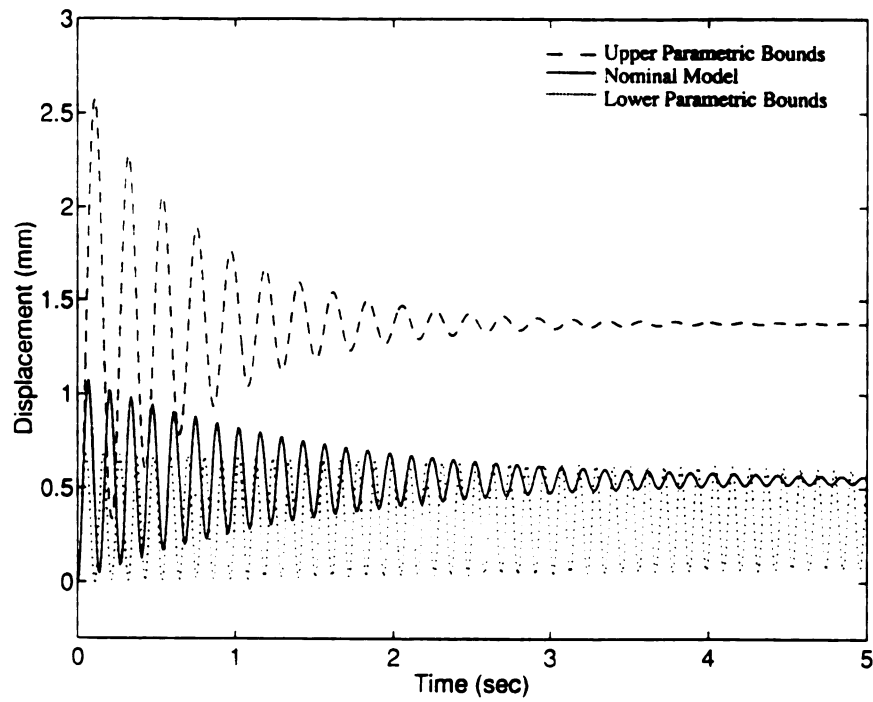


Figure 2.25 - Step response of the lower and upper parametric uncertainty bounds.

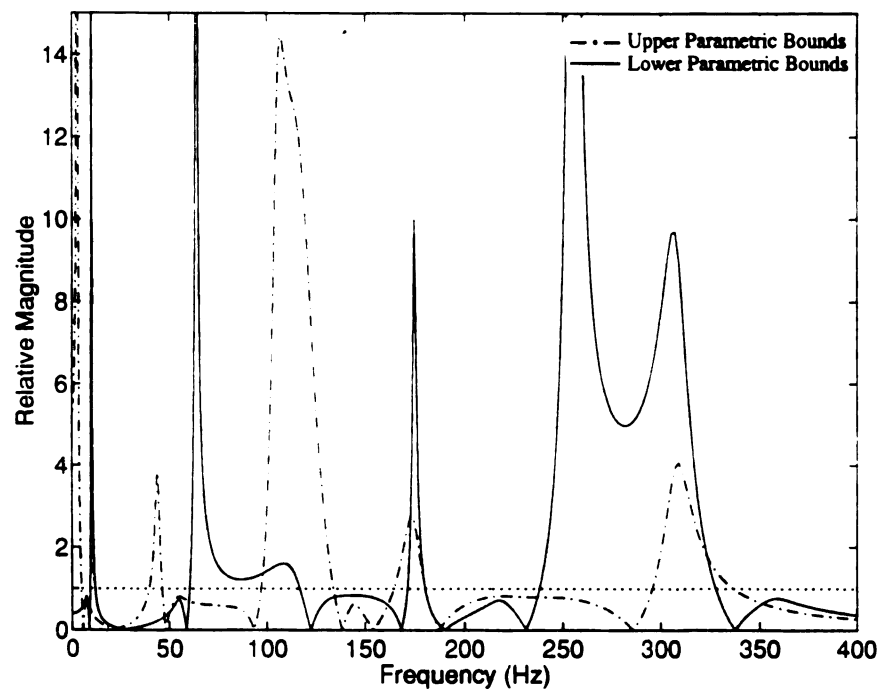


Figure 2.26 - Multiplicative uncertainty for both lower and upper perturbations on A.

magnitude of these additive perturbations the multiplicative form of uncertainty, given in Eq. (2.11), was generated. Results for the upper and lower bounds are presented in Fig. 2.26. These results verify the observations made in Fig. 2.25. Notice that both relative magnitudes exceedingly cross unity at or near every mode past the first two modes. This is because our model describes well the steady-state and low frequency behavior, but becomes highly inaccurate for high frequency inputs. Furthermore, since we have included zeros crossing and located in the RHP in the uncertainty description, we see $|r| \geq 1$ at these modes, which implies that the phase is completely unknown. The very sharp peak in the lower bound near the origin is caused by the presence of the rigid-body mode. Since the rigid-body mode is located at the origin in the Nyquist plane, it causes $|r| = \infty$. This is unsuitable because rigid-body motion for this structure is typically known, so that uncertainty at or near D.C. should be negligible. Consequently, these results leave us two choices, to either go back and reformulate the physical parametric uncertainty bounds, or to reduce the effect of the perturbation through the use of weighting matrices. The second path is chosen for interest.

The results from Figures 2.25 and 2.26 suggest excessively large perturbations from the nominal model. To evaluate stability robustness of the model due to these perturbations, we employ the singular value method (SV or SVD) and the structured singular value method (SSV). Figure 2.27 depicts upper SV and SSV bounds on M , normalized with beam length L and generated over a range of 0 to 400 Hz. It is evident from this diagram that the SV gives a slightly more conservative upper bound than does the SSV. This is expected since SSV gives the tightest possible bound on M .^{47, 101} Figure 2.27 also indicates an upper bound greater than 0 for both methods. Thus, the magnitude of the perturbation causes the condition for stability robustness, as given in *Theorem 2.2*, to not be satisfied for all $\Delta \leq 1$. Earlier, it was determined that this model set is stable for all parametric variation, thus $\phi^{stability}(G(s)) = 0$. However, because the magnitude of the perturbations include more plants in the set than were intended, we see that M is fully destabilized by Δ , as determined by the conservative SV results and partially destabilized using SSV.

Theor

applie

were

weight

depend

LAB.

of the

the pt

reduc

resent

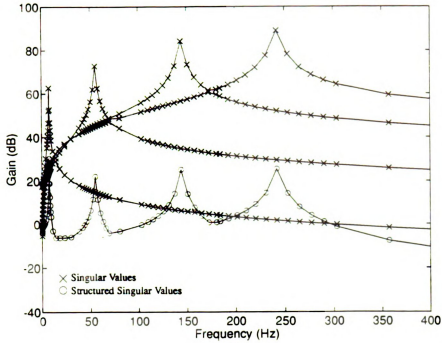


Figure 2.27 - A comparison of the SV and SSV representations for M .

Since it is undesirable to make our system unstable by adding uncertainty, in order to satisfy *Theorem 2.2* and to reduce the relative magnitude of the perturbations weighting matrices must be applied to M . Three different weighting matrices were imposed on the uncertainty model, and were compared. For convenience the same weight was applied to all Δ_i . Included in these three weighting matrices were a constant valued model, a frequency dependent model, and a frequency dependent multiplier scaled model that was obtained using the SSV subroutine provided by MATLAB.³⁶

The constant valued model was able to reduce the upper bound only for values below 10% of the initial ΔA , as shown in Fig.2.28. Obviously, the use of this model would demand that either the physical parametric bounds given in Table 2.5 be reformulated, or that the nominal model be reduced to a lesser number of modes and complemented with a large additive nonparametric representation. The frequency dependent model is given by the equation:

$$D(s) = \frac{0.144s + 2880}{2s + 5600}, \quad s = i\omega \quad (2.47)$$

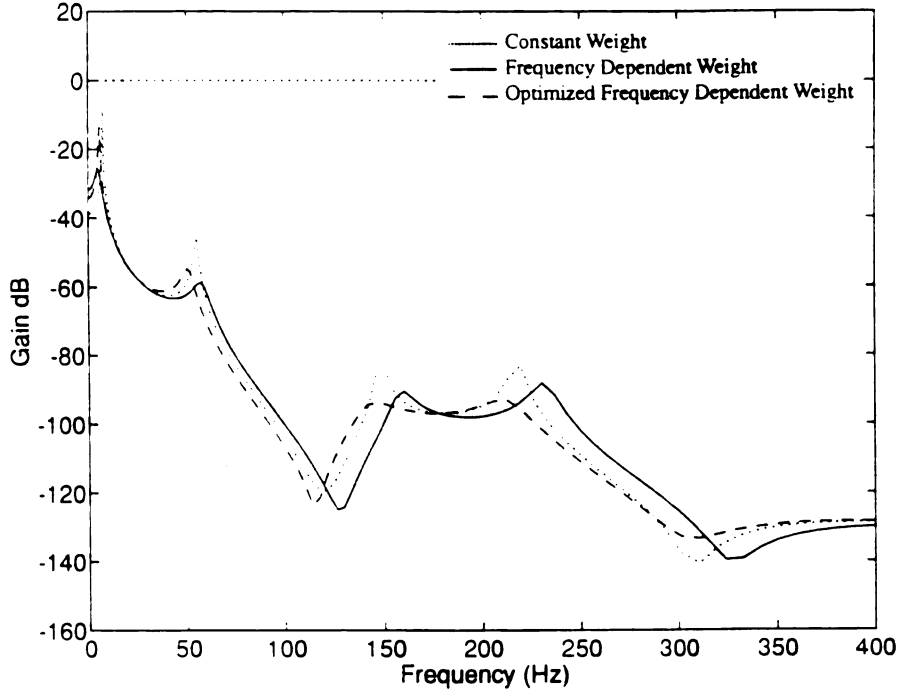


Figure 2.28 - SSV stability evaluation for the parametric uncertainty model.

This model imposes a weight of about 40% of the initial ΔA in the low frequency range (first two modes), which gradually increases with frequency and rolls-off at approximately 65 Hz to reach a final value of 65% of ΔA . As seen from Fig. 2.28 this model provides a much better uncertainty representation because it reduces conservatism in the peaks. The weighting strategy allows us to take advantage of what we know, such as the dynamics in the low frequency range. We see a gradual increase in uncertainty of up to 200 Hz, approximately of the same frequency at which experimental error caused poor results.

The third model is based on a multiplier method that uses convex optimal diagonal scaling to accurately predict system robustness. Ideally, if M is diagonalized by a real positive matrix D such that

$$\mu(M) \leq \bar{\sigma}(DMD^{-1}) \quad \forall D \in \Omega_d \quad (2.48)$$

then $\|DMD^{-1}\|_{\infty}$ can be made much smaller than $\|M\|_{\infty}$ to provide very tight bounds and accurate predictions of the system robustness.^{36, 101} From Fig. 2.28 it is apparent that this model

gives the tightest possible bound on parameter uncertainty, and not at the expense of physical accuracy. However, one disadvantage with this method is that it is computationally demanding to determine a new D at each frequency over the desired range.

Notice in Fig. 2.28 that the SSV for all three weighted cases decreases for frequencies past 225 Hz. This shows that uncertainty perturbations in this frequency range are highly attenuated by the system dynamics. However, from our experimentally measured response we know that two more natural frequencies exist between 220 and 400 Hz. Although these modes were not included in the model, their presence cannot be overlooked. In addition, the uncertainty that was identified as a result of the small deflection assumption, the assumed boundary conditions, and other small errors, is investigated here using lumped uncertainty perturbations.

To accomplish this we employ a nonparametric uncertainty description. In Fig. 2.3, four perturbation structures for representing nonparametric uncertainty are given. Here we will investigate and compare the additive and multiplicative output perturbation structures. The additive structure is appropriate for modeling uncertainty due to unmodelled dynamics and uncertain RHP zeros. On the other hand, the multiplicative structure is more appropriate for modeling neglected high frequency dynamics and input or output errors. For additive uncertainty, the following weighted perturbation was applied

$$L_A(s) = \frac{5.5s^2 + 1408s + 1.377e^6}{s^2 + 1001s + 2.114e^6} \Delta(s), \quad \forall s = i\omega \quad (2.49)$$

and for the multiplicative uncertainty the following weighted perturbation was applied

$$L_M(s) = \frac{12.95s + 0.7}{4s^2 + 3.4s + 8.34} \Delta(s), \quad \forall s = i\omega \quad (2.50)$$

such that Δ satisfied Eq. 2.13. Both uncertainty weights were determined by fitting continuous stable minimum phase state-space realizations through selected data based on percentages of the nominal model. For instance, in the low frequency region where only small variations are

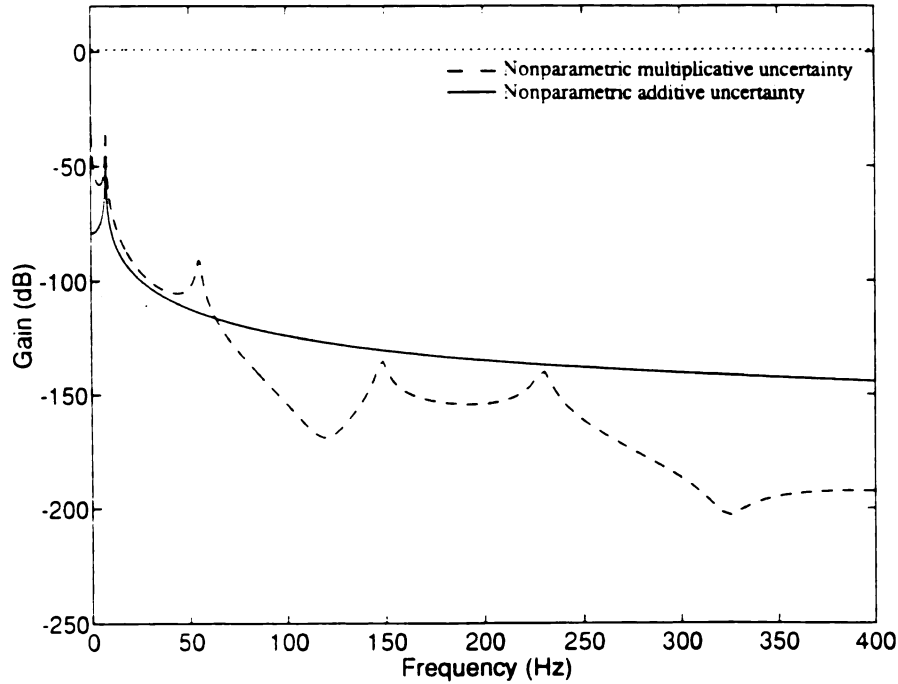


Figure 2.29 - SSV stability evaluation for the nonparametric uncertainty models.

expected, less weight is needed. In the high frequency region, error and uncertainty are typically large, thus, system response can be relaxed using more conservative models, i.e., models that contain more plants in the set. A suitable model was then fit so that uncertainty increased from 10% to 65% in the crossover region between 100 and 200 Hz. Subsequently, the order of these weighted models was reduced to the form given in Eq. (2.49) and Eq. (2.50).

The results from the nonparametric uncertainty evaluation are depicted in Fig. 2.29. It is clear from these results that both models meet the stability bound given in *Theorem 2.1*. According to the multivariable stability margin,³⁶ the primary resonance peak of the multiplicative uncertainty model can tolerate a 29.2% perturbation before instability occurs, whereas the additive model can only be as large as 26.7%. This may occur because the weighted additive uncertainty model greatly relaxes the response beyond the fundamental natural frequency. On the one hand, it does this at the expense of increasing the order of the model from eight to ten. On the other hand, the reason for the large conservatism in the multiplicative model is because uncer-

tainty is lumped together with perturbations that are relative to the nominal model. Although frequency weighting slightly improves this situation, it cannot account for all the unnecessary plants admitted to the model set. The additive model directly affects nominal system response as opposed to being relative to the nominal system. This idea follows the parametric uncertainty representation where additive perturbations were applied to the system A matrix.

The results from the structured and unstructured uncertainty descriptions give some indication of the need for a mixed uncertainty model. We see that tight bounds are achieved in the low and mid-frequency ranges using the parametric uncertainty description, which was formulated from actual bounds on physical parameters. On the other hand, we find the nonparametric uncertainty description advantageous for relaxing the nominal model in the high frequency range. By combining these two models in a sequential manner we can construct a very realistic description of the model uncertainty.

For the sake of completeness, let us consider a sequential approach for the mixed uncertainty model instead of the simultaneous approach. For the sequential mixed uncertainty we must impose a bound on the parametric description such that,

$$G(s) = \begin{cases} G(\Delta, s) & \forall \omega < \omega_t \\ G(s) & \forall \omega \geq \omega_t \end{cases} \quad s = i\omega \quad (2.51)$$

where ω_t denotes the parametric bounding frequency. It is at this frequency where the parametric uncertainty model fully transforms into the nonparametric uncertainty model. Prior to ω_t all RHP zeros must be constrained to the LHP. This will ensure that all primary modes are properly damped out. At ω_t and beyond all RHP poles that exist in the parametric uncertainty description must be constrained to the LHP. This ensures that our plant is stable at high frequency. For plants with truncated or unmodeled dynamics this statement is important to the stability of the entire model. It follows that at ω_t the nonparametric uncertainty description must be limited by

$$\max_{A \in \Omega_A} \left\| \lim_{\omega \rightarrow \infty} |G(\Delta, s)| \right\| \equiv \frac{k_h}{\omega^e} \quad (2.52)$$

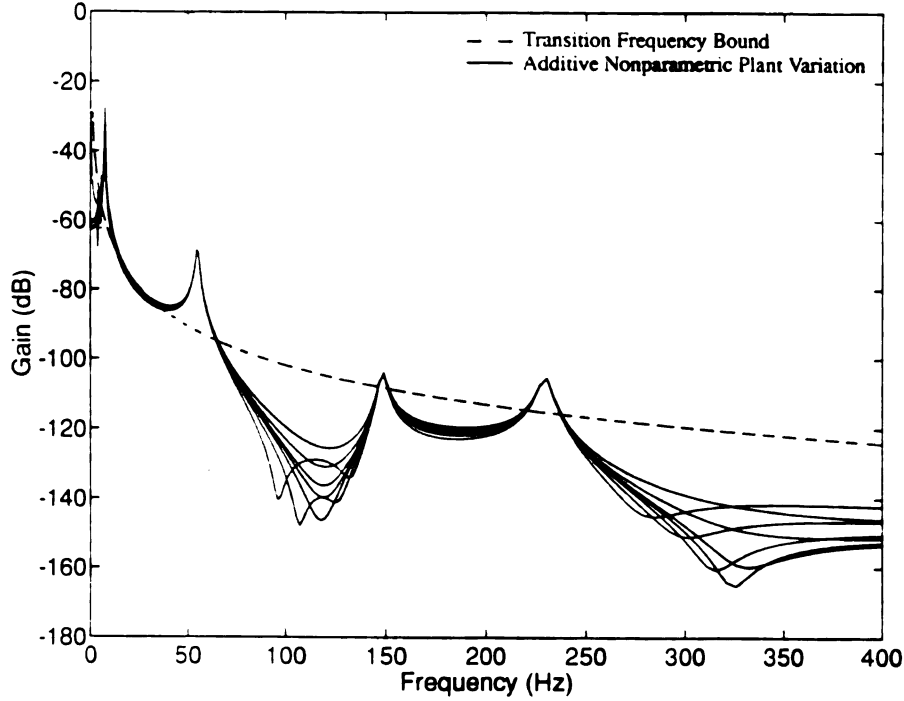


Figure 2.30 - Variation of additive nonparametric uncertainty and frequency bound.

where k_h is the high-frequency gain of the plant and e is the excess of poles to zeros of $G(\Delta, s)$. Equation (2.52) signifies the lower limit of the parametric uncertainty description as ω approaches infinity. Therefore, for $G(s) \in \Gamma$ to smoothly transition from $G(\Delta, s) \in \Gamma$, it must be bounded by the following relation

$$\max_{\Delta \in \Omega_\Gamma} \|G(i\omega)\| \leq \left| \frac{k_h}{\omega^e} \right| \quad \forall \omega \geq \omega_t \quad (2.53)$$

where Ω_Γ is the set containing all nonparametric plants $G(s)$.

In this example, k_h/ω approaches a gain of -37.47 dB/decade as ω goes to infinity for a pole-zero excess of unity. In Fig. 2.30, the variations of the perturbed nominal model for the additive nonparametric model is shown with the bound given by Eq. (2.53). We see that the final intersection of the gain limit and the bound occurs at 237.8 Hz. If we select this frequency as the transition frequency our additive nonparametric uncertainty model satisfies Eq. (2.53). Hence, the transition is smooth between the parametric and nonparametric uncertainty descriptions. It is also

evident from Fig. 2.31 that if the bound on the right side of Eq. (2.53) was imposed a large amount of conservatism would be included in the nonparametric model. As our nonparametric model shows this large amount of conservatism is unnecessary and can be limited. Of course, in a realistic problem we probably would move the transition frequency to the intersection after the second primary mode. This would be most useful, as a practical problem would most likely be reduced to include two primary modes instead of four.

2.4 Chapter Summary

In this chapter a procedure for modeling large-scale structural systems was introduced and applied. This procedure is practical because it captures all aspects of the system while translating them into an appropriate working model. We find that there is no one standard or simple way of doing this because models are unique to the problem at hand. Thus, the method proposed here assumes and treats the system as a set of models instead of a single system. This calls for a nominal model to describe the typical behavior of the system and an uncertainty model to describe perturbations from the nominal model. Modeling systems in the presence of uncertainty have been shown through introduction of a general mathematical framework. It is also shown that this procedure is very compatible with concurrent engineering. For example, during initial design, parameters are very uncertain and imprecise. We can develop uncertainty models that gradually improve as the design matures and the amount of imprecision and uncertainty subsides. In this regard, a model is simultaneously developed through each stage of the design process. Finally, our procedure is applied to a cantilever beam example. Using results from experimental and analytical analysis, a nominal model and parametric and nonparametric uncertainty models were developed. These uncertainty models were then combined to form a single, mixed uncertainty model. This example gives conclusive evidence of the usefulness and efficiency of mixed uncertainty models and the concurrent design procedure.

Chapter 3

EXPERIMENTAL ANALYSIS FORMULATION FOR A DISTRIBUTED-PARAMETER STRUCTURE

3.0 Introduction

In the field of structural control, the need for good models to support robust control system design has been indicated.^{18, 82, 111} Experimental system identification is one way to achieve this goal. It can be used either to observe certain aspects of predicted dynamics or to verify the reduced-order mathematical models needed to establish controller designs. Thus, through carefully controlled experiments, reduced-order models of relatively high fidelity can be attained. Such experiments would be designed to determine ranges for specific material, structural, or input parameters, to estimate nonlinear system component bounds, or to verify fully-assembled mathematical models. Therefore, we see that experimental system identification is a useful way to provide the valuable information needed in the analysis problem of the concurrent modeling procedure. However, system identification of distributed-parameter structures poses a unique challenge for experiment design.^{33, 124} The highly resonant dimensionality of the structure imposes limits that are attributed to noise, deficiencies in model-order selection, and poor correlation of higher frequency modes.¹⁸ All experimental techniques have some random variation or error which must be assessed to establish the significance of the results. If the models obtained from identification are to serve as descriptive references for simulations, it is

very important to minimize as well as investigate uncertainty. This is particularly important when there is no general agreement on the physical mechanism of the observed behavior, nor on the properties of the structure. In this case, poorly designed identification experiments will have little effect on any derived mathematical model and uncertainty may be too large to accurately quantify or bound. On the one hand, if the problem is the selection of a constitutive equation that accurately describes the relationship between a structure and its properties under certain conditions, this can be resolved by fitting data to several different constitutive equations and by making some comparative measurements.¹⁵ On the other hand, if the problem concerns the interaction of the system's components with its surroundings, many models need to be evaluated and/or fit before accurate conclusions can be drawn and bounds can be determined.

For the electrorheological (ER) fluid structure considered in this study, a combination of many aspects make any identification process cumbersome. The dearth of reliable and repeatable testing methods for ER fluids has hindered attempts to formulate a collective mechanical property database.¹³⁹ Since simple, quick, and convenient test methods are not currently available, imperfections in the different models used for ER fluids make comparative conclusions difficult. Thus, ER fluids must first be individually tested and fit to an appropriate rheological model in most cases. Secondly, the integration of the ER fluid within the structure imposes certain restrictions on the identification measurements. Assumptions must be made with care so that the salient features of the system's behavior are addressed in detail. It is plausible to assume that only through an analytical and experimental identification, and a numerical correlation, will critical sources of error be revealed.

The objective of this chapter is to begin the analysis problem in the mathematical modeling procedure with an experimental formulation. This will entail an identification of the behavior of free-edged plates composed of an ER fluid actuator core. In order to provide an accurate description and bounds on parameters, a mathematical model for the ER fluid actuator is

developed. These descriptions will facilitate the analytical and numerical portions of this investigation. A review of the ER fluid mechanism begins this chapter. Then a mathematical model of the actuator is constructed to accommodate analytical and finite-element methods. A numerical example of the actuator model is presented in order to demonstrate its capabilities. Finally, a nonparametric experimental identification procedure is conducted for two ER fluid actuated plates with rectangular and square geometries. Identification will involve an evaluation of the dynamic response of the structure for zero electrical potential and while undergoing various time-dependent voltage excitations. In conclusion, responses for the electrical and dynamic behavior of the ER fluid are also considered.

3.1 Electrorheological Fluids

3.1.1 Rheology of suspensions

When a large concentration of solid particles, called the solute, is dissolved in an insulatory liquid solvent, and the size of the particles are much larger than the molecules of the liquid, the admixture is defined as a sol suspension.⁵⁵ In a suspension, three kinds of forces coexist to various degrees. These forces are of colloidal origin due to the electrical interaction between the particles, the ever-present Brownian force, or (thermal) randomization of the particles, and the local viscous forces acting on the particles.¹⁵ Thus, the presence of the solid phase alone markedly affects the rheological properties of the original solvent to give the suspension unique qualities of its own.

If we impose an identical deformation to the solvent and then the suspension, a significant difference will be apparent between their measured stresses.^{22, 43, 51} These differences are attributed to the remarkable changes in viscosity, deformation, and rate of deformation as a result of the solid-solid and solid-fluid phase interaction. A viscosity versus shear rate curve for a

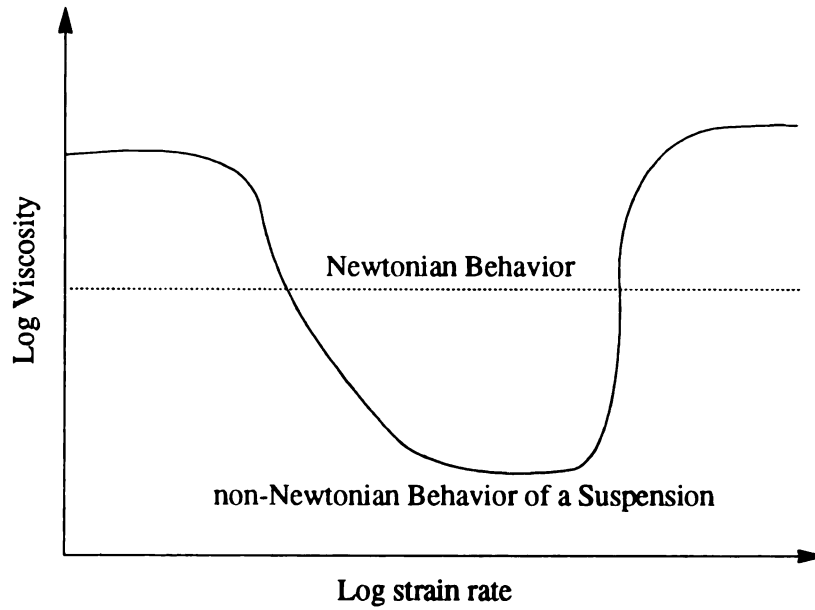


Figure 3.1 - A strain rate versus viscosity curve for a typical suspension.

typical suspension is given in Fig. 3.1. As compared to the common Newtonian fluid in the schematic, the suspension shows a non-Newtonian decrease in effective viscosity which is known as shear thinning. Shear thinning results from the aggregation and separation of solid particles during steady shearing. At high and low shear rates, the suspension displays the Newtonian fluid characteristics of the solvent as evidenced by the two plateaus. Of course, such factors as concentration of the solute, temperature, pressure, particle size and particle surface quality all have considerable effect on the suspension viscosity, as well as its response to deformation.

At rest, the suspension assumes a state of equilibrium where the particles tend to form a structure that possesses minimal energy transfer. An innate characteristic of these fluid systems is that the particles always arrange themselves so that the net forces are in mutual equilibrium.¹⁵ This arrangement can vary according to the dominance of the three interacting forces. On the one hand, if the particles are very small, forces acting on the particles are largely of Brownian nature and the particles arrange themselves to form a thermodynamic equilibrium. On the other hand, when the particles are large, forces are of colloidal form and the equilibrium arrangement

is either electrically attractive, or repulsive. Thus, when colloidal forces are electrically attractive the structural arrangement can vary from near-spherical flocs to individual pearl-like strings. When the colloidal forces are repulsive, the particles distance themselves from one another to form a dispersion or a more structured pseudo-lattice dispersion.^{15, 43}

Upon deformation, particle energy transfer in a dispersion increases as an uninterrupted sequence of structure disassembly and arrangement occurs. Clearly, the rheological properties of the suspension are strongly dependent on these considerations, as shown by Fig. 3.1. Therefore, any modification of the suspension, either by adsorption of surfactant materials onto the surface of the particles, presence of an activator phase, or the introduction of an electrical potential across the fluid, will have direct consequences on the response of the particle structure, and, the suspension's rheological properties.

Essentially, ER fluids represent a class of sol suspensions that exhibit large modifications in particulate structure when subjected to an electric potential. In general, ER fluids consist of a particle constituent, a dielectric fluid component, a surfactant, and, in some cases, an activator phase.¹³⁹ Observations of ER fluids at rest give indication of a dispersion, since repulsive colloidal forces dominate particle interaction.^{24, 26, 127} When an electrical field is applied to the dispersion, the particles readily become attracted to one another as a result of polarization. Simultaneously, as particles polarize and become charged dipoles, the dispersed solid phase re-orient, re-structures or flocs to form column-like strings or bridges between the electrodes. These strings define a new structure and equilibrium state that has very different and unique rheological properties as compared to the original suspension.¹⁰⁰

3.1.2 The electrical behavior of ER fluids

Conventional electrostatic theory indicates the existence of a uniform field between two electrodes separated by a dielectric medium, Yet as shown by Felici,⁵⁰ when a dielectric suspension is

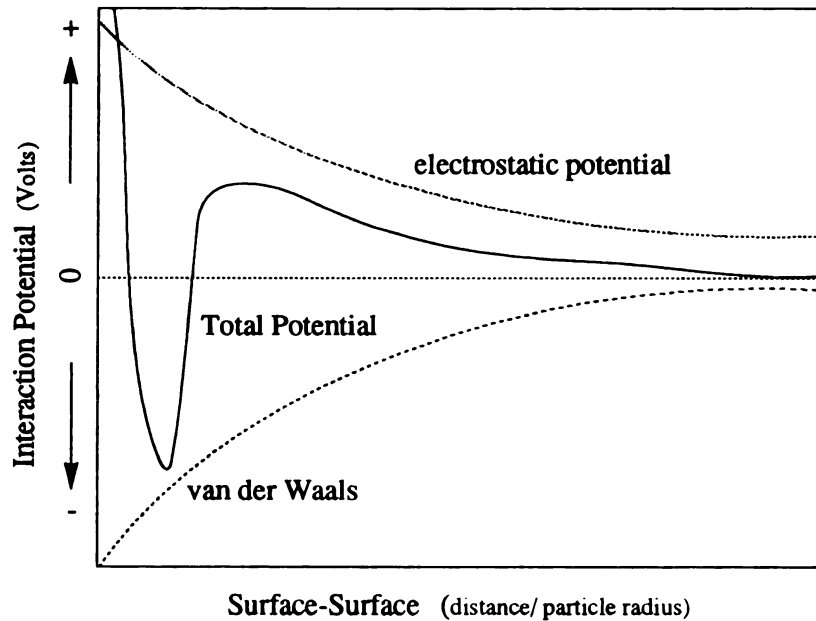


Figure 3.2 - Representative colloidal interaction potential over particle surface separation.

inserted between two electrodes, the electric field is complicated by numerous local non-uniformities. Such local non-uniformities in the suspension affect particle polarization and conduction, and cause field warping and very large particle motion. Furthermore, local non-uniform field effects can continue for several minutes after the imposition of a steady-state global voltage.¹⁰⁰ We find that the local non-uniformities in the electric field contribute to the mechanism that governs the behavior of an ER fluid and the formation pearl-like particle strings that are held together by strong inter-particle forces.

To predict the behavior of the dispersion and its structure, accurate information about particle interaction is required. Two of the most important colloidal forces in a dispersion at rest are the van der Waals potential, which is derived from the attractive molecular forces existing at the atomic level, and the electrostatic potential. Comparatively, the former potential is strongly attractive, whereas the later is effectively repulsive. In Fig. 3.2, the balance between these interactive potentials is given for a dispersion at rest. This balance determines the apparent

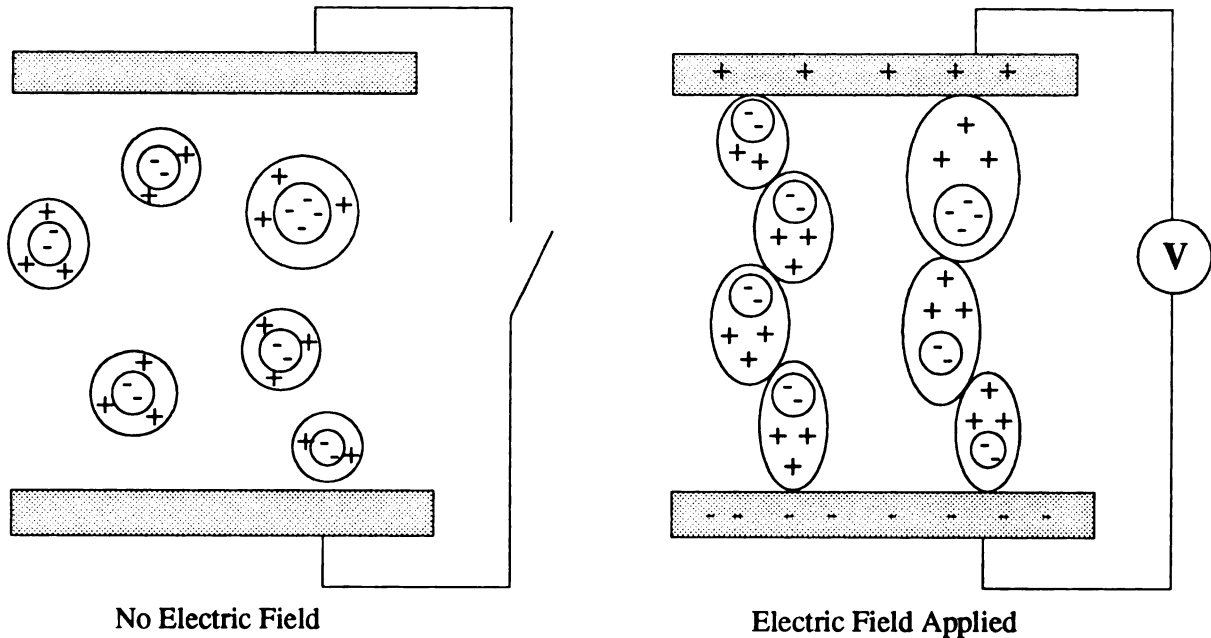


Figure 3.3 - Double-electric layer theory for ER fluids.

pseudo-structure behavior of the ER fluid. For instance, a large repulsive electrostatic potential causes the particles to form a stable-ordered lattice structure due to the disassociation of ionic groups on the particle surfaces or the adsorption of ions from the solvent.^{24, 113, 132} Conversely, a large van der Waals potential stimulates agglomeration, and, in highly concentrated suspensions, promotes aggregation to form a very disordered flocs.⁵⁹ In Fig. 3.2 the strong attractive minimum of the total energy can lead to agglomeration, however, a repulsive maximum will retard this attraction causing particles to separate. This gives qualitative indication of the random, disordered and dispersed behavior of a dispersion and the properties of the ER effect.

It is generally accepted that the electrorheological phenomenon originates from particle polarization induced by an electric field.^{15, 100, 120, 113} Currently, most models that describe particle polarization can be categorized into three specific theories: i) a distorted double-layer theory, ii) a water surfactant theory, and iii) an exclusive particle polarization theory. These three

interpretations have been summarized in a paper by Weiss, *et al.*¹³⁹ Only for completeness, will each theory be discussed here in brief.

The double-layer theory is graphically shown in Fig. 3.3. This theory involves the distortion of an ionic layer surrounding each particle, causing each particle to align itself in a direction of opposing charge. The water surfactant theory proposed by Stangroom,¹²³ suggests that the minimum requirements needed by a material to exhibit the ER effect include a hydrophobic liquid, hydrophilic and porous particle, and moisture. The moisture acts as a bridge between particles, where ions in the water shift the amount of water surrounding the particle to act as a "glue".¹³⁹ Although water may be important for some ER fluid systems, recently, several anhydrous fluid systems have been developed suggesting that the mechanism for ER activity may be inherently attributed to the chemistry of the fluid constituents and not the apparent moisture content of the solid phase. Treasurer, *et al.*,¹³² suggests that this mechanism is dependent on the intrinsic polyelectrolyte chemistry of the dispersed particle. The final theory is based on the detailed theory of polarization⁵ to explain the five different stages of columbic particle attraction.

The importance of permittivity on the ER fluid dispersion subjected to an electric field must be stressed. The very large difference apparent between the permittivities of the particles and of the fluid solvent is responsible for polarization and structure formation within the ER fluid.¹³⁶ Both structure and polarization are dependent on the electrostatic potential between particles and on the non-uniformity of the electric field. Electrostatic potential is dependent on the magnitude of the particles' surface charge and dielectric constant of the solvent. The adsorption of conducting surfactants on the non-conducting dispersion permit particle polarization. Upon application of an electric field, the surface carries a charge introducing a formation of the dipole moments of the disperse particles. For a structure and orientation of the dispersion to exist, the particles must have a relative dielectric constant of sizable difference as compared to the surrounding base fluid. This large difference between the two dielectric constants enables the

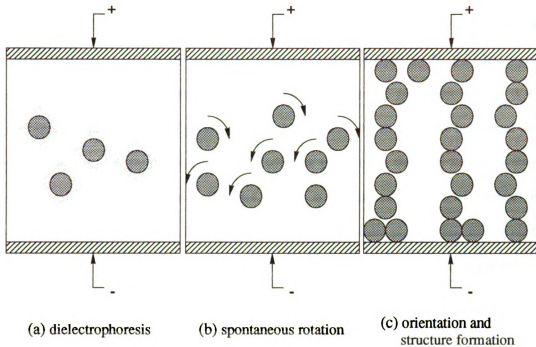


Figure 3.4 - Changes in the structure as a result of dielectric polarization of the suspension

particles to move towards regions of higher field strength, severely straining the interfacial layer formed around the dispersed particles. The observed structures in the ER fluid originate due to the induced separation of the charges on the surface of the structure. Origination is determined by the interface of the necessary double electric, hydrate, or adsorption layers.^{43, 100, 139}

At the macroscopic level, observations of an ER fluid in the presence of an electrical field show the ability of the solid phase to create a strong structural skeleton or bridge between the electrodes. This structural skeleton is manifest by particle electrocoagulation which is caused by several varying mechanisms of particle migration. The polarization of the particles plays a very important role in the structure formation and orientation as illustrated in Fig. 3.4. First, the neutral particles are polarized. As a result, they experience torques while remaining stationary, not being impelled to translate in a direction toward either electrode. Next, the dipoles tend to

2
C
C
R
P
C
A
A
fu
be
de
w
se
3.
An
sh
ber
rel
cha
vis
beh
of t
fluid
mani
field

align themselves to achieve a state of minimum energy in the electric field. This is called dielectrophoresis. Dielectrophoresis, as shown in Fig. 3.4 (a), occurs as a result of field effects on the translational motion of the neutral or weakly polarizable particles.¹⁰⁰ Simultaneously, as more particles polarize, individual particle rotation is observed, as shown in Fig. 3.4 (b). Finally, once the particle layer is polarized by ion adsorption, the strain on an individual particle creates an electrostatic dipolar force between adjacent particles as they are forced to form the aggregate bridge structure shown in Fig. 3.4 (c). It is this increase in the interacting dipolar forces that results in an increase in the relative motion of the solid phase while new bridges are being formed. Consequently, the continuous motion of the particles during aggregate bridge destruction and reformation results in noticeable rheological property changes of the ER fluid with changing electrical field. Rheological behavior of an ER fluid is discussed in the next section.

3.1.3 The rheological behavior of ER fluids

An arbitrary material containing particle suspensions of colloidal dimensions, may, in some cases, show viscoelastic behavior, and in other cases show viscoplastic behavior.^{23, 77, 87} The differences between the two materials are quite large, especially in terms of their respective mathematical relations for stress, strain, strain rate, and viscosity. ER fluids, on the other hand, show characteristic features of both types of behavior. They encompass linear and non-linear viscoelasticity in certain areas of low electric field intensity and strain rate, and viscoplastic behavior in regions of high stress and strain rate. It is because of this complex inter-dependency of the rheological parameters on the external electric field that the mechanism by which an ER fluid can be modeled is severely altered. Therefore, a complete rheological model will be manifest by the range of the corresponding ER fluid's application, and will depend on electric field as well as deformation rate and magnitude, and thermodynamic effects.³⁸

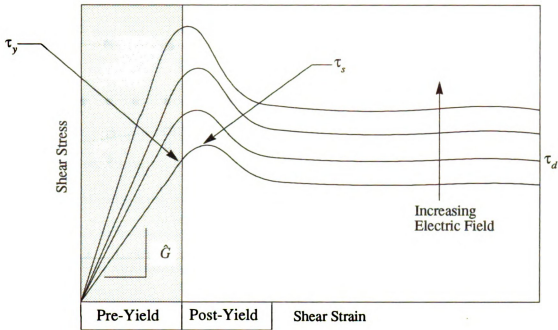


Figure 3.5 - A schematic of observed shear stress/strain behavior of an ER fluid.

ER fluids behave in a slightly Newtonian manner only in the absence of an electric field. When thus activated, the rheological properties of an ER fluid show non-Newtonian behavior such as shear-dependent viscosity and a yield stress.^{24, 43, 55, 77} Unlike Newtonian fluids, an ER fluid can support a stress with no flow. Thus the minimum stress required to cause an ER fluid to flow is termed the static yield stress. This maximum stress has been demonstrated in numerous experiments clarifying that it must be a non-zero value.^{24, 26, 124, 127} In Fig. 3.5, a hypothetical representation of the shear stress-strain curve is given for quasi-static deformation of an ER fluid subjected to various uniform electric potentials. Illustrated here is the elastic-limit yield stress, τ_y , the static shear stress, τ_s , and the dynamic yield stress, τ_d which is equivalently the stress in the limit of zero shear rate.^{26, 38} The dynamic yield stress is observed as a dynamic equilibrium between the processes of structure destruction and formation. With increasing

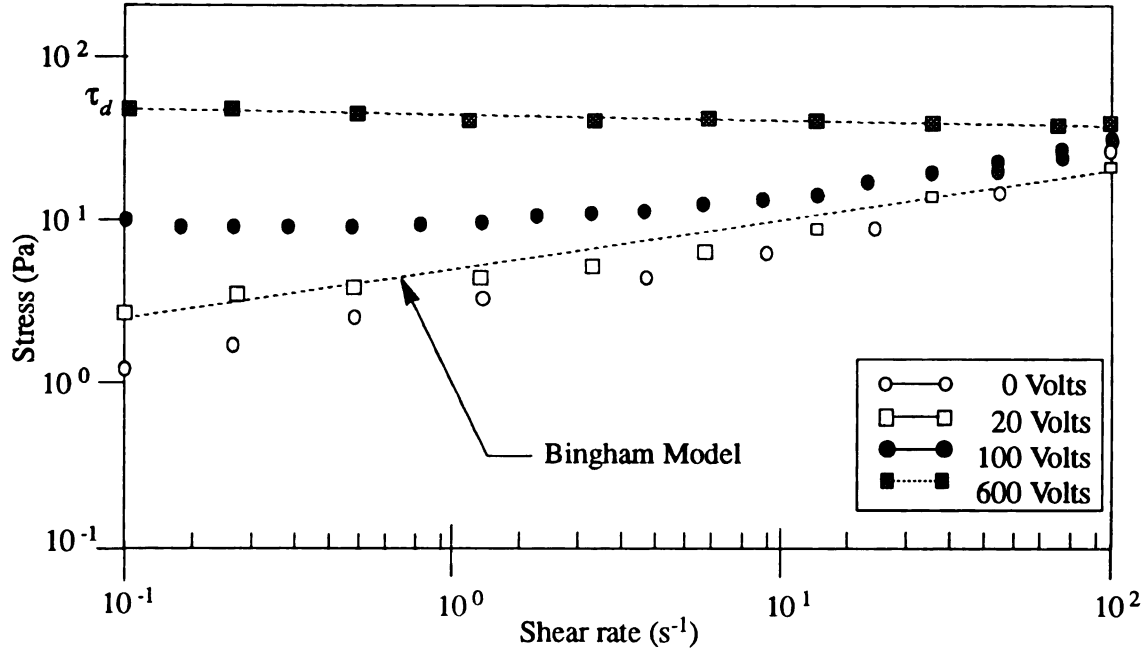


Figure 3.6 - A figurative description of the shear stress versus shear-rate Bingham model

electrical field intensity these parameters also increase with the most noticeable change occurring in the static and dynamic yield stresses. In solid mechanics we find that for a complete removal of a stress exceeding τ_y , the material never recovers and suffers a permanent strain, γ_e , where this strain signifies the elastic-plastic transition of the material. For ER fluids, this transition has been defined as a 1% offset yield from an observed linear region.¹³⁹ Evidence has been given that this behavior is representative of most ER fluid materials,^{26, 120, 127} however, it is possible that these pre- and post-static yield stresses may not occur in this exact order if they exist at all.

An ER fluid behavior can be described by the two regimes of pre and post-yield. Over the past few decades, the post-yield regime has received the majority of attention. A schematic of this rheological constitutive behavior during post-yield is given in Fig. 3.6. The Bingham model,^{22, 23} is the simplest model that provides a sufficient description of this viscoplastic behavior

$$\tau = \tau_d(V) + \mu_B \dot{\gamma} \quad (3.1)$$

where μ_B is the Bingham viscosity or plastic viscosity of the fluid and V signifies the applied

el

of

be

ve

nu

str

reg

inv

sim

a m

the

but

yield

for

moi

maj

5%

com

mois

recog

reduc

or dr

basic

electric field. The Bingham model recognizes that the yield stress defining the onset of flow is observed to change with an increase in electric field. Although, we cannot generalize the behavior of all ER fluids by Eq. (3.1) since it is only an idealized representation, it has proven very useful in the development of specific post-yield applications.^{55, 125}

The response of ER fluids in the pre-yield regime has been a subject only of a limited number of investigations.¹³⁹ The pre-yield regime, depicted in Fig. 3.5, is defined by a yield strain and static yield stress, τ_e , and a complex shear modulus \hat{G} . In Fig. 3.5, the pre-yield regime is shown as a simple representation of a linear viscoelastic material. However, several investigations have concluded that a viscoelastic representation of an ER fluid would not be simple to model using linear viscoelasticity.^{76, 120, 143} In accordance with linear viscoelastic theory, a material is linear, provided its complex shear modulus is dependent on frequency alone and not the shear amplitude.⁵¹ An ER fluid's complex shear modulus is not only dependent on frequency but also on strain amplitude, thus it acts like a highly nonlinear viscoelastic material during pre-yield. Moreover, an ER fluid displays such behavior over a limited range of deformation, and for a moderate range of frequencies.^{53, 69, 76, 87, 143}

The kind of applications that research has focussed on have shown that temperature and moisture content play a large role in the rheological properties during ER activity. For a majority of dispersions, the ER effect only occurs if a conductive additive, such as water, (over 5%) is adsorbed onto the surface of non-conductive solid particles.^{43, 55, 136} ER fluids of this composition are hydrous mixtures and are usually termed wet fluids. For wet fluids, although moisture plays an important role in the polarization and structure formation, it has been recognized that a characteristic disadvantage of all hydrous fluid systems is their substantial reduction in ER activity upon heating. Consequently, the principle motivation behind anhydrous or dry fluid research has been requirements for higher temperature applications. The concepts basic to wet fluids also apply to dry fluids, however, the present knowledge is quite premature.

3.2 Constitutive Model for the Actuator

One inherent physical limitation of an ER fluid is that its operating conditions dictate the use of two embed electrodes of opposing polarity. This characteristic imposes important and obvious restrictions on a prospective active control design by requiring that the structure have either negligible electrical conductivity or some type of insulatory material containing the fluid between the two electrodes. It follows from this observation that a structure with negligible electrical conductivity would be an ideal candidate for ER fluid embedment. However, for structures with electrical conductivity, or structures composed of various compartmentalized fluid actuators, the inclusion of insulation within the structural domain is necessary. Insulation would be used to constrain the fluid within or restrain the fluid from interacting with portions of the structure. Hence, the insulation is an important material to be considered in the actuator design because it interacts so closely with the fluid. It is not the goal of this section to develop a new constitutive model for an electrorheological fluid, but to develop a mathematical model for the ER fluid/insulatory actuator.

3.2.1 Preliminary considerations

Unfortunately, the models developed in this thesis have some limitations that exclude them from being totally general and applicable to all ER fluid structures. These limitations are a result of the lack of knowledge associated with the complex behavior of the materials. Since we seek equations that accurately describe material behavior for specific conditions, and with a minimal number of parameters, empirical models will be developed to address these needs. Empirical models are quite useful for this situation because materials can be significantly affected by such variables as shear rate, temperature, pressure, concentration, and time of shearing. When specific variables are fixed in a controlled experiment, the data collected should accurately reflect behavior for such conditions. The disadvantage here is that the functionality and versatility of the mathematical relation has been limited.

The

by l

form

ticu

of 5

eval

The

450)

for th

an a

heat-

repre

the m

and c

consi

quene

in the

effecti

model

shear r

where,

The materials identified in this section will include an ER fluid and an insulatory material. The insulatory material used throughout is a natural sheet rubber elastomer that was manufactured by Dana Corporation. Elastomers possess a unique combination of physical, electrical, and performance characteristics that make them good materials for a broad range of applications. In particular, they can be classified as nonconductors, since most have volume resistivities on the order of 5×10^{10} ohms-cm.¹³⁸ In this application, the electrical parameters were researched in order to evaluate specific losses within the structure due to the high voltages applied across electrodes. The dielectric constant for an operating frequency of 1kHz is 8, and it has a dielectric strength of 450 volts /mm.¹³⁸ The possibility of power loss through capacitance was considered, however, for the size of insulator materials included here these losses are quite negligible. Nevertheless, in an actual structure these parameters may have long term effects such as dielectric breakdown, heat-aging resistance, current-arc resistance, and hygroscopic induced electrical effects.

The material properties of the elastomer are considered to be linear viscoelastic and readily represented by a storage modulus, loss modulus, and loss factor. The most important effects on the material properties of the elastomer are temperature, frequency, dynamic load, static preload, and chemical contact.¹⁰² However, for this isothermal analysis, only the effects of frequency are considered since the modulus of an elastomeric rubber always increases with increasing frequency.^{51, 138} Material data for the insulate in simple shear is given in Fig. 3.7. Normal stresses in the rubber will be determined by a constant Young's Modulus given by $\hat{E} = 1.225$ MPa. An effective range of temperature will assumed to exist at 20°-25° Celsius. Given this information, a model can be empirically fit for the shear and loss modulus to yield an expression for the complex shear modulus:

$$\hat{G}(\omega) = G'(\omega) (1 + j\eta'(\omega)) \quad (3.2)$$

where, the shear modulus G' and the loss modulus η' are,

$$G'(\omega) = 461.9129 + 8.4685\omega - 0.0021\omega^2 \quad (3.2a)$$

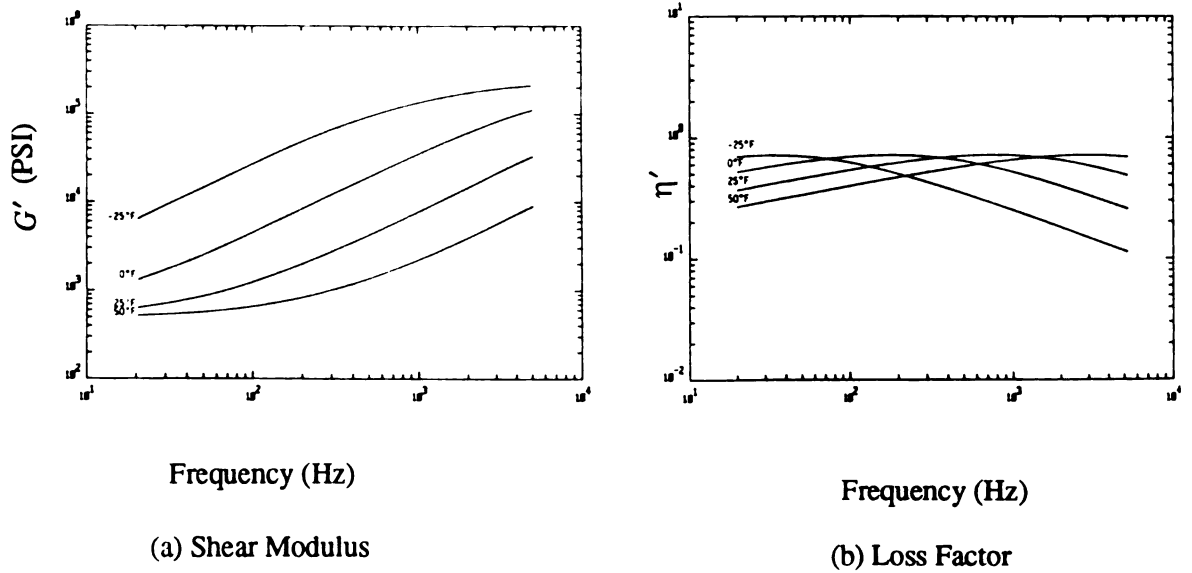


Figure 3.7 - Isothermal shear modulus for the insulate material.

$$\eta'(\omega) = \frac{1}{100} (22.571767\omega - 0.3277812) \quad (3.2b)$$

The least-square parameter fit in Eq. (3.2a) for the shear modulus data that was presented in Fig. 3.7 is given in Fig. 3.8. The density of the insulator, ρ_{in} , is approximately 1376.62 kg/m³.

3.2.2 Identification of an electrorheological fluid

Of the diverse selection of ER fluids available, a model will be developed for a simple hydrous fluid. This suspension comprises a weight-per-weight fraction of 45 percent Argo cornstarch and 55 percent vacuum silicone oil manufactured by Dow Corning and has a density, ρ_{fl} , of 970.0 kg/m³. Experimental rheological data for the ER fluid were recorded in a previous investigation that employed a Rheometric 800 mechanical spectrometer that was outfitted for high voltage applications.⁵⁵ Steady shear measurements were conducted at temperatures ranging from 24 to 29 degrees Celsius for shear rates spanning $0.1 \frac{1}{s}$ to $100 \frac{1}{s}$. The non-Newtonian viscosity of the fluid is given in Fig. 3.9. These data effectively represent anticipated behavior of suspensions. In the

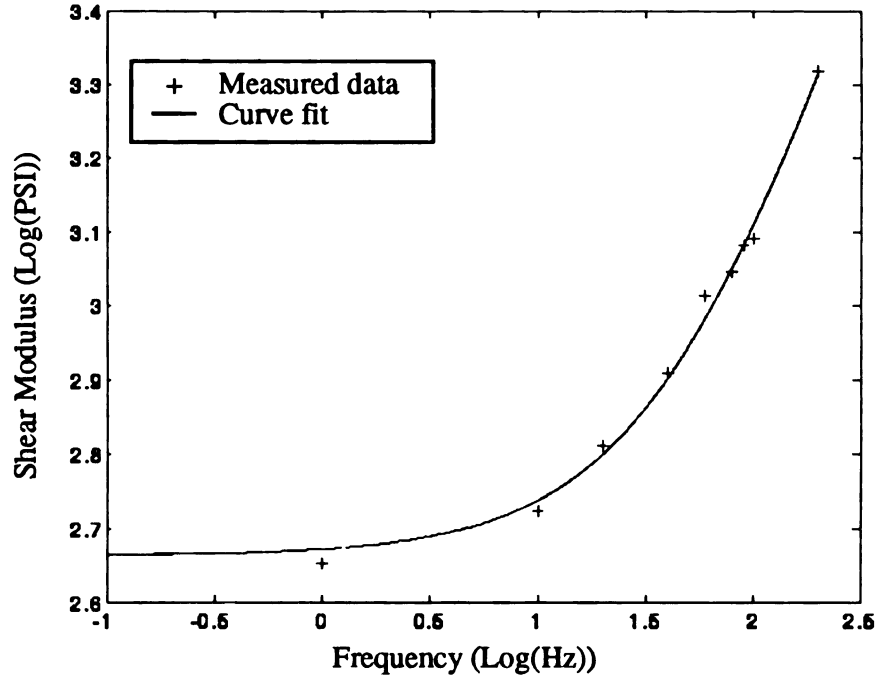


Figure 3.8 - Shear modulus curve fit for the insulate material data at 25 °C.

case of an ER fluid, this behavior is illustrated for a range of various measured electrical potentials. The upper region at low shear rate is followed by a shear-thinning region, which is then followed by a flattening-out region, where near constant values beyond $100 \frac{1}{s}$ are expected. The small range of shear rates demonstrates the limited scope of these previous experiments. Steady shear measurements of the shear stress were also made for shear rates spanning $0.1 \frac{1}{s}$ to $100 \frac{1}{s}$. These experimentally determined shear stress versus strain rate data are given in Fig. 3.10. Clearly, the particles in the fluid become more difficult to separate with increasing voltage, as is evidenced by the larger shear stresses. Moreover, at low shear rates, observations lead us to believe that the stress of the fluid is independent of shear rate.⁵⁵ This is indicative of the previous discussions pertaining to the apparent yield stress possessed by the ER fluid.

A least-squares fit that minimized the L_2 norm of the difference between the experimental data presented in Fig. 3.9 and Fig. 3.10 and the curve fits was completed. Over the given range of shear rates the following functions for the viscosity and shear rate were determined

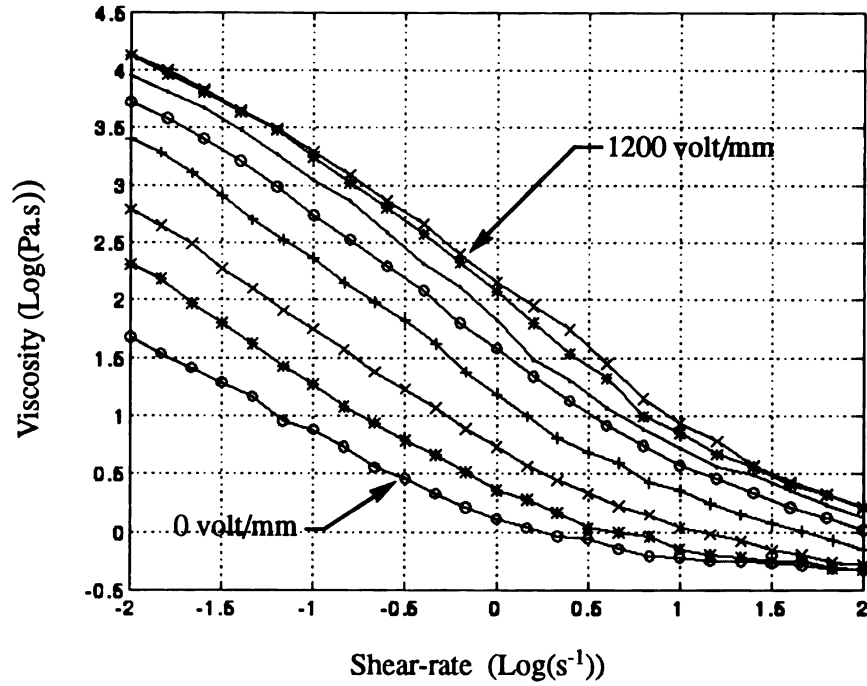


Figure 3.9 - Experimentally determined non-Newtonian viscosity for a hydrous ER fluid.

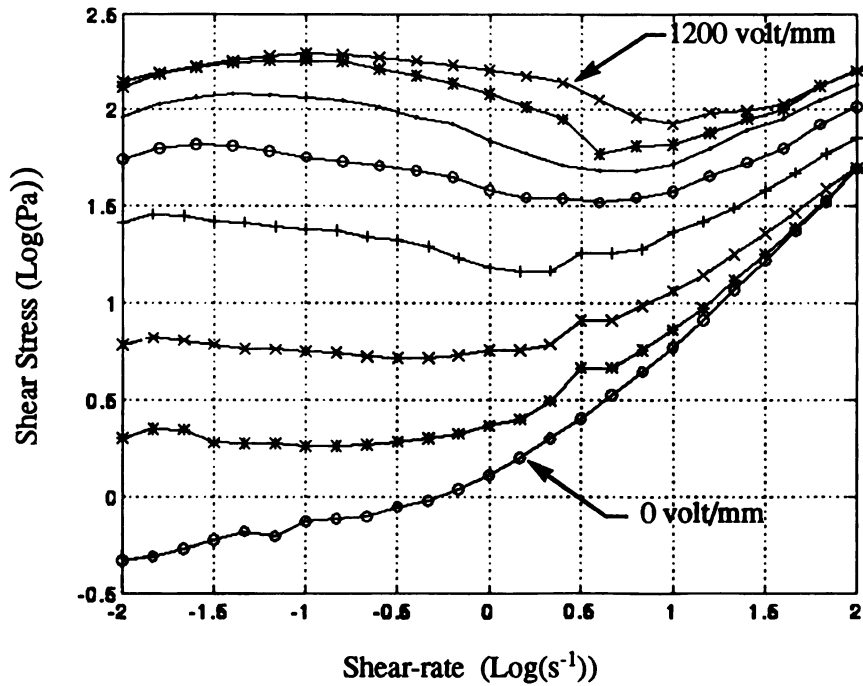


Figure 3.10 - Experimentally determined shear stress for a hydrous ER fluid.

$$\eta = A_1 \dot{\epsilon}^3 + A_2 \dot{\epsilon}^2 + A_3 \dot{\epsilon} + A_4 \dot{\epsilon}^3 V + A_5 \dot{\epsilon}^3 V^2 + A_6 \dot{\epsilon}^3 V^3 + A_7 \dot{\epsilon}^2 V^3 + A_8 \dot{\epsilon} V^3 + A_9 \dot{\epsilon}^2 V + A_{10} \dot{\epsilon}^2 V^2 + A_{11} \dot{\epsilon} V^2 + A_{12} \dot{\epsilon} V + A_{13} V + A_{14} V^2 + A_{15} V^3 \quad (3.3)$$

$$\sigma = S_1 \dot{\epsilon}^3 + S_2 \dot{\epsilon}^2 + S_3 \dot{\epsilon} + S_4 \dot{\epsilon}^3 V + S_5 \dot{\epsilon}^3 V^2 + S_6 \dot{\epsilon}^3 V^3 + S_7 \dot{\epsilon}^2 V^3 + S_8 \dot{\epsilon} V^3 + S_9 \dot{\epsilon}^2 V + S_{10} \dot{\epsilon}^2 V^2 + S_{11} \dot{\epsilon} V^2 + S_{12} \dot{\epsilon} V + S_{13} V + S_{14} V^2 + S_{15} V^3 \quad (3.4)$$

where the A 's and S 's denote constant parameters, $\dot{\epsilon}$ is the strain rate, and V represents the applied voltage or electric field. The resulting fits for both ER fluid parameters are given in Fig. 3.11 and Fig. 3.12. To note here, the fine mesh represents the curve fit and the coarse mesh denotes the experimental data that is given in Fig. 3.9 and Fig. 3.10.

The transient electrical behavior of an ER fluid is very important for power consumption analysis and time response estimates. Since ER fluids consist of conductive particles surrounded by a dielectric medium, they essentially function as leaky capacitors.¹³⁹ Although, it is the leak-

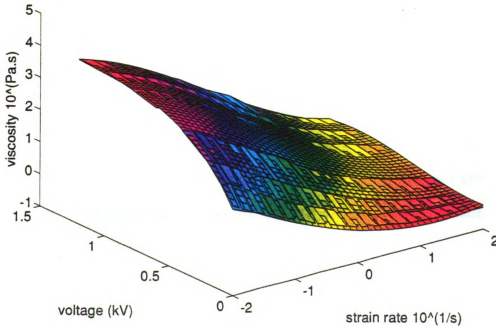


Figure 3.11 - Curve fit comparison for the non-Newtonian viscosity of the ER fluid.

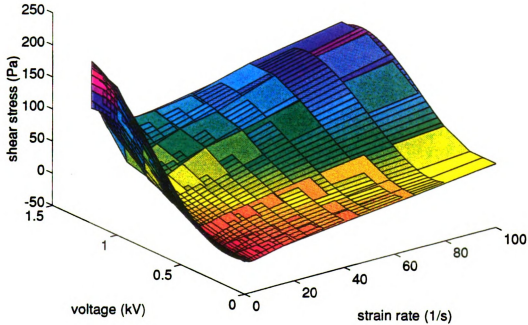


Figure 3.12 - Curve fit comparison for the shear stress of the ER fluid.

age of charge between particles that results in the measurement of an electrical current through the ER material. To model this behavior, an assumed equivalent linearized lumped resistor-capacitor circuit, such as the one illustrated in Fig. 3.13, can be used. This approach has been used by several authors,¹²¹ to define a current-voltage law for the fluid using identification techniques. Here, voltage measurements were taken using a 0.018 inch probe placed between two flat plate electrodes located 1.36 mm apart. The hydrous ER fluid detailed in the previous section was contained between the two electrodes. With one of the electrodes designated as a ground, a high voltage electric field ranging from 1 to 2 kV was applied to the other. Voltage measurements were then made in real-time using an HP dynamic signal analyzer.

Initially, a short experiment was conducted to determine if the assumed circuit representation provided a valid description for the ER fluid's electrical behavior during dynamic excitation. In Fig. 3.14, results for three different cases are presented: (i) voltage measurements for the fluid

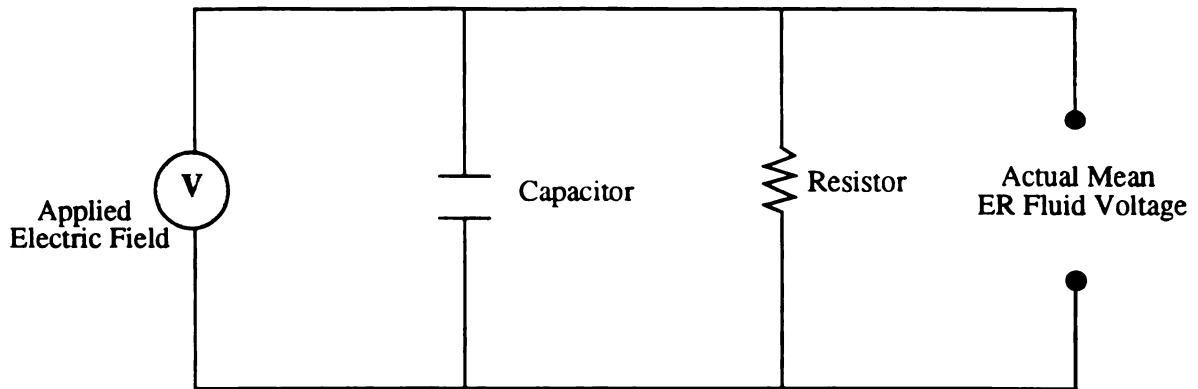


Figure 3.13 - Equivalent transient electrical behavior for an ER fluid.

highly agitated with a dynamic excitation, (ii) the fluid thirty minutes after excitation, and (iii) the fluid one hour after agitation. As shown in the illustration, there is not much difference between the three cases, however, measurements taken prior to the experiment with the fluid at rest were approximately ten times less than these data. The results give us evidence to conclude that the equivalent ER fluid electrical circuit depicted in Fig. 3.13 is a valid representation for the transient electrical response during and after dynamic excitation.

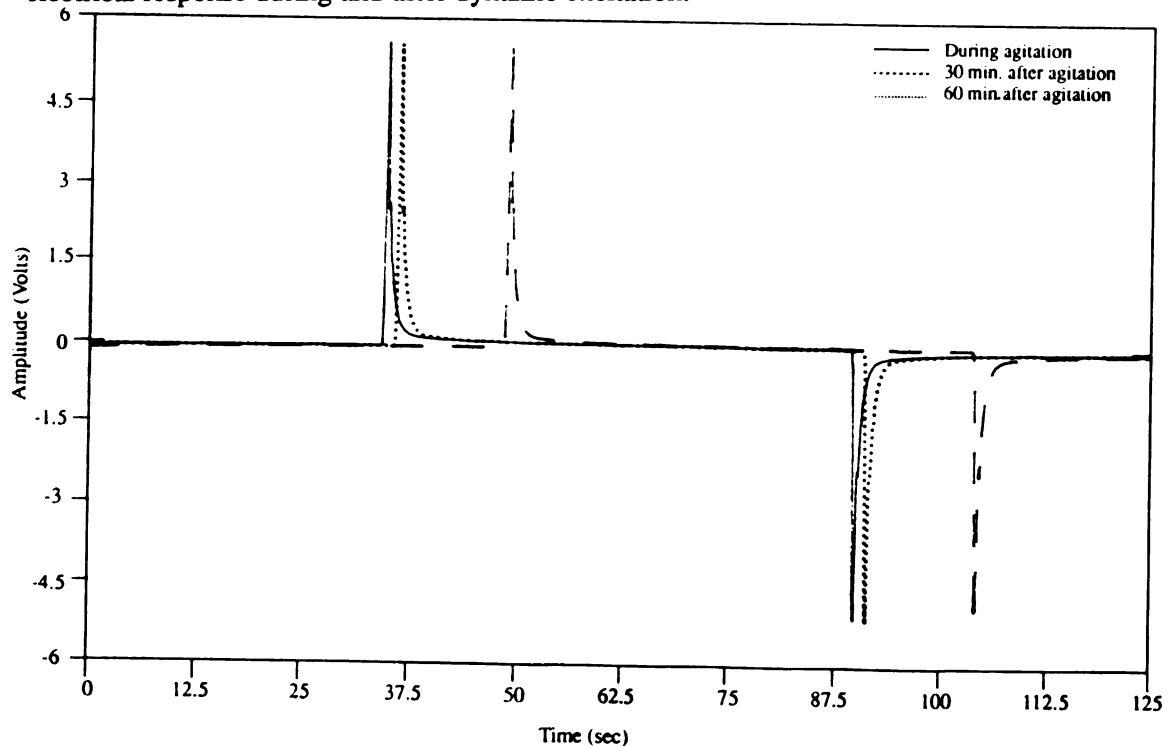


Figure 3.14 - Actual voltage of the ER fluid medium for an applied electric field of 2 kV.

To identify reasonable parameters for the resistor and the capacitor in the circuit, an iterative identification routine was implemented using MATLAB. This routine employs a fourth and fifth order Runge-Kutta ordinary differential equation solver to integrate the two following equations used to characterize the circuit given in Fig. 3.13:

$$RC \frac{dV}{d\tau} + V = Ri \quad (3.5)$$

$$R \frac{dq}{d\tau} + \frac{q}{C} = V \quad (3.6)$$

where R and C denote the resistor and capacitor, respectively, τ is the time variable, i is the current, V is the voltage, and q is the Coulombic charge of the ER fluid. A comparison between the simulated results and the experimental results are given in Fig. 3.15. Using values of $R = 64.1 \text{ k}\Omega$ and $C = 10.3 \text{ nF}$, we see that the simulated results give a time constant of $T_c = 11.56 \text{ msec}$, whereas the experimental results give a time constant of approximately $T_c = 10.38 \text{ msec}$.

The electrostatic distribution inside the ER fluid structure can be determined by considering an electric field E as a potential problem in the three-dimensional dielectric medium Ω . If we let $\Phi(x, y, z, t)$ represent the time-dependent scalar electric potential, then the field is given as,

$$\nabla \Phi = E \quad (3.7)$$

and the governing equation for the three-dimensional domain Ω is:

$$\frac{\partial}{\partial x} \left(\epsilon_p \frac{\partial \Phi}{\partial x} \right) + \frac{\partial}{\partial y} \left(\epsilon_p \frac{\partial \Phi}{\partial y} \right) + \frac{\partial}{\partial z} \left(\epsilon_p \frac{\partial \Phi}{\partial z} \right) + \sigma^s = 0 \quad (3.8)$$

together with the associated boundary conditions,

$$\Phi = \phi_o(x, y, t) \quad \text{on} \quad \Gamma_1 \quad (3.9a)$$

$$\epsilon_p \frac{\partial \Phi}{\partial x} + \epsilon_p \frac{\partial \Phi}{\partial y} + \epsilon_p \frac{\partial \Phi}{\partial z} = F^s \quad \text{on} \quad \Gamma_2 \quad (3.9b)$$

where $\epsilon_p(x, y, z)$ is the effective permittivity for the ER fluid medium, σ^s is the surface charge density, F^s is the electrical flux or displacement, and Γ_1, Γ_2 are portions of the surface Γ from the domain Ω . For this analysis, Γ_1 represents the top and bottom surfaces of the fluid element and Γ_2

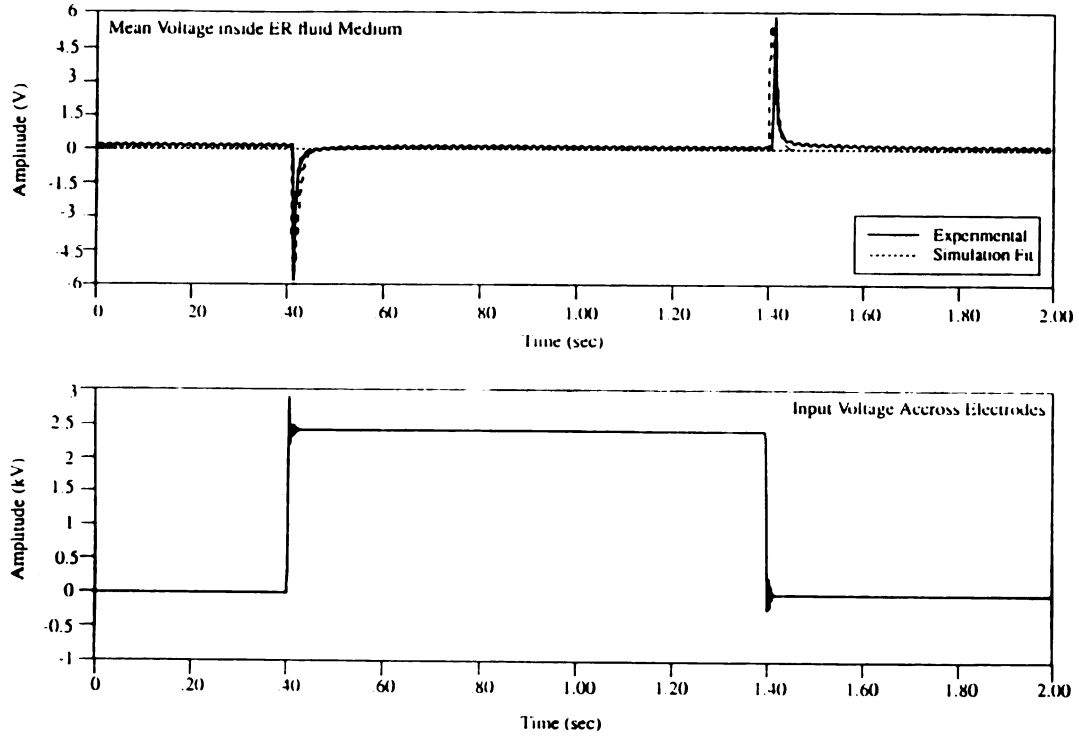


Figure 3.15 - Comparison between experimental and simulated voltages for the ER fluid medium.

represents the four sides of the ER fluid element. The series solution for the problem given in Eq. (3.8) can be written as

$$\Phi(x, y, z, t) = \sum_{m=1}^{\infty} \sum_{n=1}^{\infty} A_{mn} \cos\left(\frac{m\pi x}{a}\right) \cos\left(\frac{n\pi y}{b}\right) (e^{-\pi w^{mn} z} - e^{\pi w^{mn} z}) \quad (3.10)$$

where

$$A_{mn} = \frac{4}{ab} \int_0^b \cos\left(\frac{n\pi y}{b}\right) \int_0^a \phi_o(x, y, t) \cos\left(\frac{m\pi x}{a}\right) dx dy \quad (3.10a)$$

and

$$w^{mn} = \sqrt{\frac{m^2}{a^2} + \frac{n^2}{b^2}} \quad (3.10b)$$

For the small distances between electrodes, this electrostatic distribution will be almost negligible.

3.2.3 A model for the actuator

In this section we consider the result of incorporating the insulatory material and ER fluid into a

single functional unit of a composite actuator. The insulate, besides restraining the ER fluid and insulating the structure, also has the function of transferring some of the applied loads. Thus, it is of great importance to be able to predict the properties of the composite actuator, given the component properties and their geometric arrangement. For this analysis, the rule of mixtures will be utilized to accomplish this for a given generic geometrical configuration of the actuator. The rule of mixtures provides a rough solution of the properties, because it considers the composite properties as volume-weighted averages of the component properties.^{32, 68} Nevertheless, a very accurate description is not necessary here because the ratios of insulate-to-ER fluid are anticipated to be rather small.

Accordingly, the material model for the actuator will be based on the following assumptions:

Assumption (3.1)

- i) There is no inter-conversion of mass and both constituents are chemically inert to each other (no fluid to solid transmission),
- ii) The insulatory solid is assumed to be linearly viscoelastic and incompressible,
- iii) The electrorheological fluid is assumed to be ideal and incompressible,
- iv) The actuator is homogeneous with all normal stresses in the fluid negligible.

Consider the unit cell geometry, taken from the infinitely large composite actuator, of thickness d , depicted in Fig. 3.16. Fig. 3.16 illustrates a compartmentalized geometry for the actuator. Such a geometry might be useful for limiting actuator effort to discrete portions of the structure, or employing different ER fluids. Essentially, the unit cell is the smallest geometric entity that, when repeated, will reconstruct the entire geometry. Here, the unit cell is idealized to be a parallelepiped consisting of insulate material edges with an ER fluid core. Its orientation is defined by an x - y - z Cartesian coordinate system. Use of the property of volume additivity allows us to define the density of the actuator. Volume additivity is an intrinsic property that states that the total volume of the aggregate components is equivalent to the sum of the respective volumes of the superimposed continua at any time or deformation state.⁵⁶ If we then consider the insulate mass m_{in}

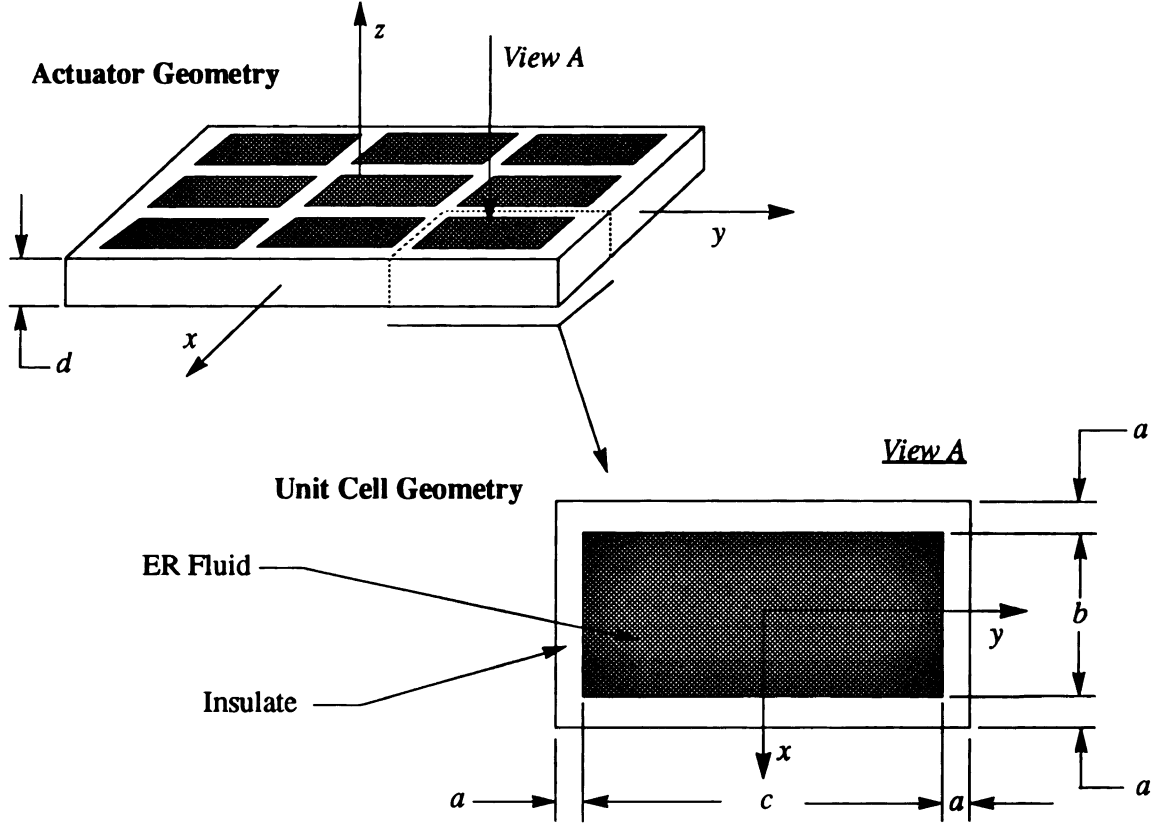


Figure 3.16 - Geometric configuration of the actuator and its unit cell.

and volume ∇_{in} , and the ER fluid's mass m_{fl} and volume ∇_{fl} , the total mass and volume for the actuator are given by the expressions,

$$m^A = m_{fl} + m_{in} \quad (3.11)$$

$$\nabla^A = \nabla_{fl} + \nabla_{in} = bcd + 2ad(2a + b + c) \quad (3.12)$$

According to the rule of mixtures the actuator mass density ρ^A is given by

$$\tilde{\rho}_A = \frac{m_{fl} + m_{in}}{\nabla^A} = \frac{\nabla_{fl} \rho_{fl} + \nabla_{in} \rho_{in}}{\nabla^A} = v_{fl} \rho_{fl} + v_{in} \rho_{in} \quad (3.13)$$

where v_{fl} and v_{in} denote the volume fractions of the fluid and insulatory material, respectively.

Now, let us apply a small-amplitude oscillatory shear strain to the upper and lower surfaces of the unit cell given in Fig. 3.16 in a direction parallel to the y axis. The rule of mixtures

approach will be used to determine the mechanical properties of the actuator. It has been assumed that the insulate behaves like a linear viscoelastic material, such that in oscillatory shear, it obeys the following isotropic constitutive equation for the shear stress and normal stress^{15, 51}

$$\tau = \hat{G}(\omega) (\varepsilon + \dot{\varepsilon}) \quad (3.14a)$$

$$\sigma = \hat{E}(\omega) (\varepsilon + \dot{\varepsilon}) \quad (3.14b)$$

where the dotted quantity denotes differentiation with respect to time. However,, the ER fluid has a constitutive behavior that is dependent on the strain rate and electric field potential as given in Eq. (3.4). Now, if the two components adhere perfectly and have an identical Poisson ratio, each will undergo an identical shear strain, ε^A .^{32, 68} This assumption holds since the ER fluid will take on the shape of the enclosed cavity during deformation.^{54, 127} Therefore, according to the rule of mixtures the constitutive law for the actuator assumes the form

$$\sigma^A = v_{in} G'(\omega) \varepsilon^A + (v_{in} G'(\omega) \eta'(\omega) \dot{\varepsilon}^A + v_{fl} f(\dot{\varepsilon}^A, V)) \quad (3.15)$$

where the dynamic stress of ER fluid actuator is now characterized by a simplified nonlinear viscoelastic model that is dependent on frequency of oscillation, strain rate, and electric field. To note, all pre-yield effects of the ER fluid are considered negligible because sufficient information and data were not available to consider this phenomena.

3.2.4 Numerical comparisons

In order to verify the material model derived in the previous section, a simple numerical comparative study was conducted. To verify the material model, a FORTRAN subroutine was written for use with the finite element software ABAQUS.¹ This enables us to physically model the nonlinear material behavior of the actuator. The objective here is to compare and contrast the response of the combined insulate/ER fluid actuator model given in Eq. (3.15) with experimental data, and also with an actual unit cell geometry having separate insulate and ER fluid domains. A schematic of the geometries for the two models with identical uniform shear loading conditions is given in Fig. 3.17. As seen from Fig. 3.17, model (1) represents the actual unit cell geometry, and

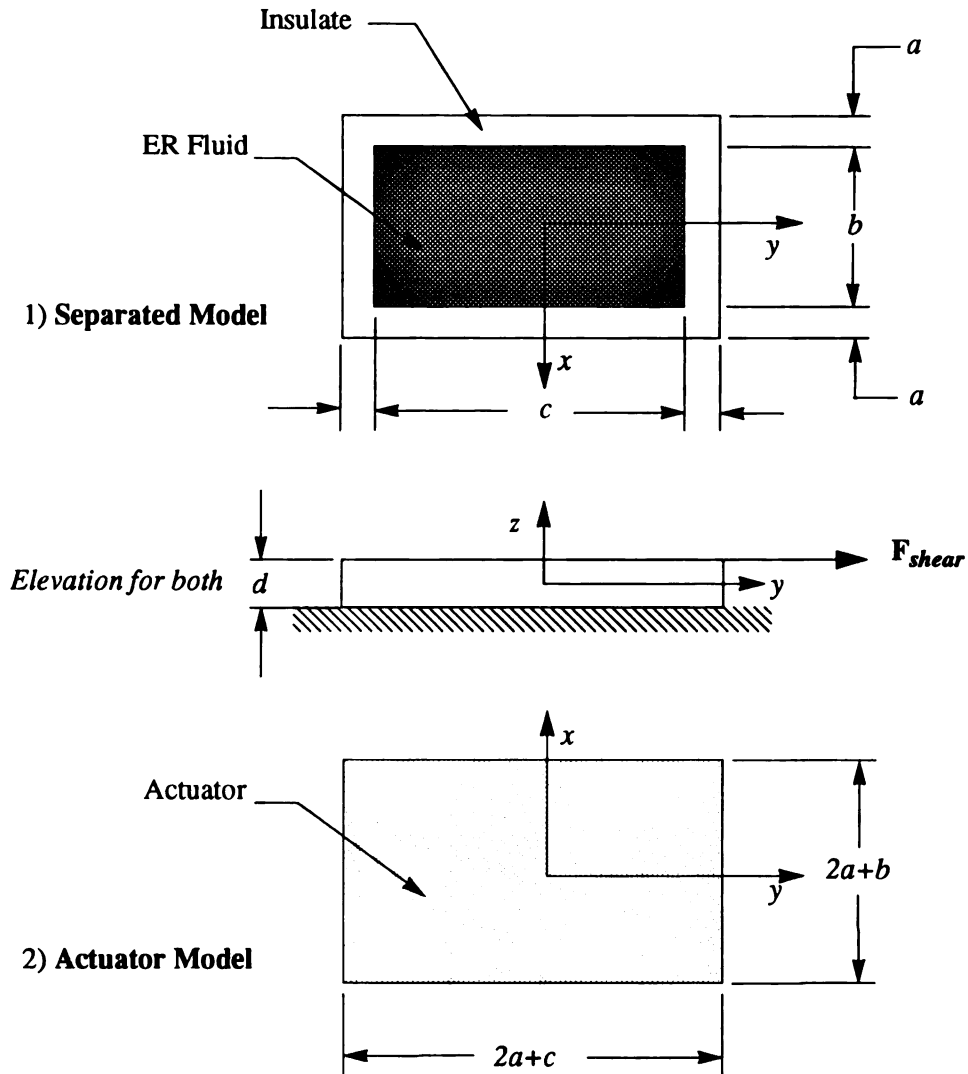


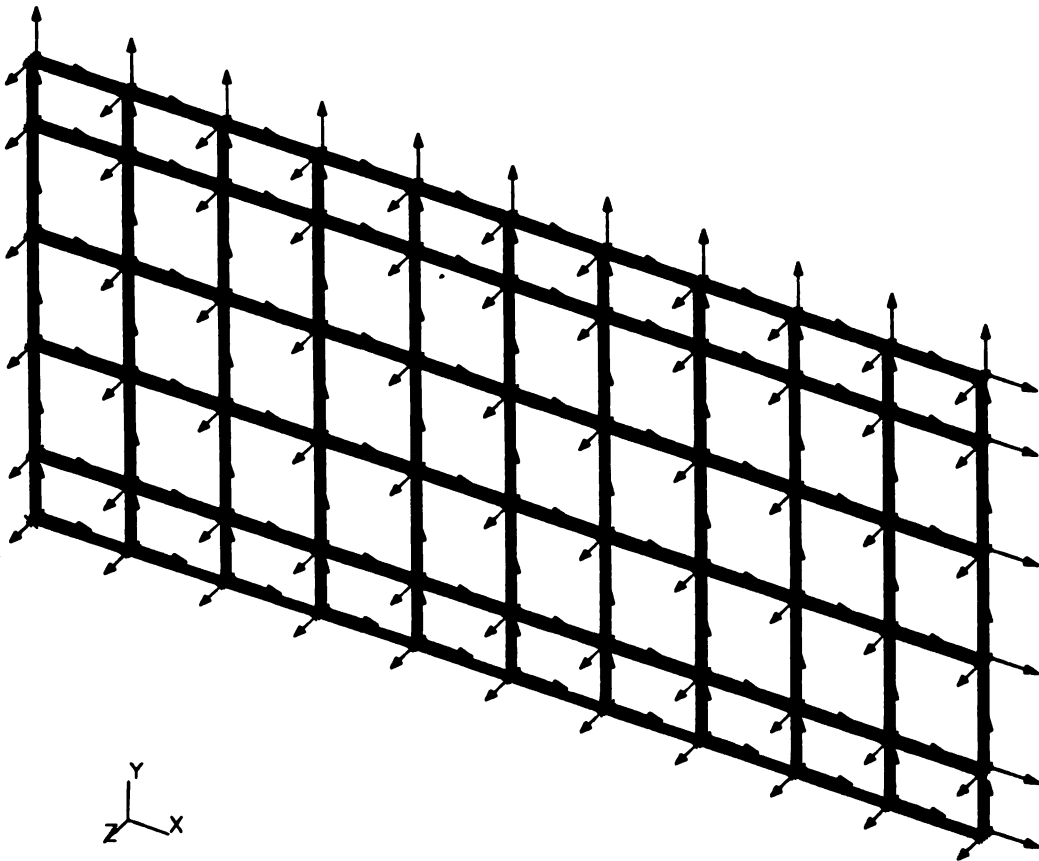
Figure 3.17 - Geometric configuration and loading of the actuator models.

model (2) represents the geometry associated with the actuator model. It is very important that the orientation of the local Cartesian coordinate system shown in Fig. 3.17 is used for all element and material axes. The actuator model and its mechanical properties are highly dependent on geometry. Although the insulation is isotropic, the actuator acts orthotropic in the presence of an electric potential, due to the ER fluid.. This observation holds only for parallel electrode geometries.

For these two models, the geometry of the unit cell was discretized as shown in Fig. 3.18. The associated dimensions for the unit cell are given in Table 3.1. The unit cell was discretized

Table 3.1 - Dimensions for the two actuator models.

Dimension (cm)	Models	
	1	2
<i>a</i>	0.7	0.7
<i>b</i>	3.6	3.6
<i>c</i>	8.6	8.6
<i>d</i>	0.16	0.16

**Figure 3.18 - Discretized geometry for the two models.**

into four layers of 50 hybrid solid elements. The hybrid element is especially useful for applications with incompressible or nearly incompressible materials as displacement and pressure are represented as independent variables.¹ The same discretized model was used for both cases, and as illustrated by the smaller elements included around the edges in Fig. 3.18, accommodations were made for the separated model, or model 1.

The material model for the actuator was incorporated into ABAQUS as follows.¹ The integration operator that was used for Eq. (3.15) is the simple, stable central difference operator:

$$\dot{\zeta}_{\tau + \frac{1}{2}\Delta\tau} = \frac{\Delta\zeta}{\Delta\tau} \quad (3.16)$$

$$\zeta_{\tau + \frac{1}{2}\Delta\tau} = \zeta_{\tau} + \frac{\Delta\zeta}{2}, \quad (3.17)$$

where ζ is some function, ζ_{τ} is its value at the beginning of the increment, $\Delta\zeta$ is the change in the function over the increment, and $\Delta\tau$ is the time increment. Applying this to the constitutive equation given in Eq. (3.15) gives

$$\Delta\sigma_{xz}^A = \frac{2}{\Delta\tau} \left[(A\Delta\tau + B) \Delta\epsilon_{xz}^A + C\Delta\tau f\left(\frac{\Delta\epsilon_{xz}^A}{\Delta\tau}, V\right) + \Delta\tau (A\epsilon_{xz}^A - \sigma_{xz}^A) \tau \right] \quad (3.18)$$

$$\Delta\sigma_{yz}^A = \frac{2}{\Delta\tau} \left[(A\Delta\tau + B) \Delta\epsilon_{yz}^A + C\Delta\tau f\left(\frac{\Delta\epsilon_{yz}^A}{\Delta\tau}, V\right) + \Delta\tau (A\epsilon_{yz}^A - \sigma_{yz}^A) \tau \right] \quad (3.19)$$

where

$$\begin{aligned} A &= v_{in} G'(\omega) \\ B &= v_{in} G'(\omega) \eta'(\omega) \\ C &= v_{fl} \end{aligned}$$

Then the Jacobian matrix has the following terms

$$\frac{\partial}{\partial \Delta\epsilon_{xz}^A} (\Delta\sigma_{xz}^A) = \frac{2}{\Delta\tau} \left[(A\Delta\tau + B) + C\Delta\tau \frac{\partial}{\partial \Delta\epsilon_{xz}^A} f\left(\frac{\Delta\epsilon_{xz}^A}{\Delta\tau}, V\right) \right] \quad (3.20)$$

$$\frac{\partial}{\partial \Delta\epsilon_{yz}^A} (\Delta\sigma_{yz}^A) = \frac{2}{\Delta\tau} \left[(A\Delta\tau + B) + C\Delta\tau \frac{\partial}{\partial \Delta\epsilon_{yz}^A} f\left(\frac{\Delta\epsilon_{yz}^A}{\Delta\tau}, V\right) \right] \quad (3.21)$$

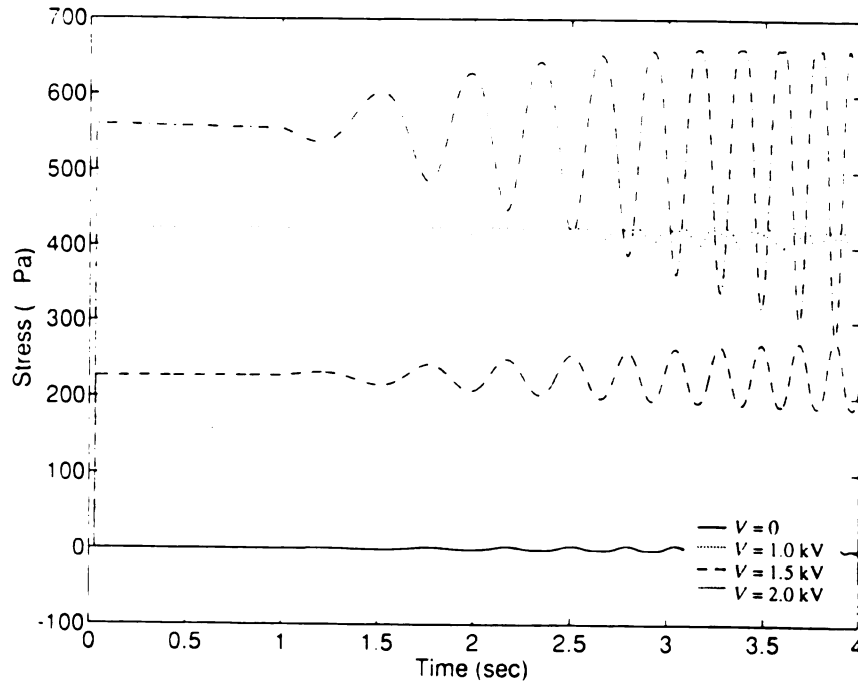


Figure 3.19 - Time response of the ER fluid model under periodic excitation.

since the normal and inplane stresses are neglected only these two components reside in this matrix.

A periodic excitation which varied in frequency from 0.001 Hz to 120 Hz over a range of 10 seconds was imposed on the models. This excitation was in the form of a harmonic shear

$$\epsilon^A = \epsilon_o \cos(\omega t) \quad (3.22)$$

where ϵ_o is the shearing amplitude and ω is the circular frequency of oscillation. Results were first obtained in the time domain and then mapped to the frequency domain for further analysis using a discrete fast Fourier transform. Data in the frequency spectrum were passed through a Hanning window and averaged over several simulations to improve resolution.

Initially, the ER fluid model was investigated singularly to compare its response with the experimental results presented in the previous section. Figure 3.19 shows the response of the ER fluid during harmonic shearing with an amplitude of $\epsilon_o = 20\%$ and for constant input voltages of

0, 1 kV, 1.5 kV, and 2 kV, respectively. It is evident from these results that ER fluid is capable of supporting a definite yield stress which is indicative of the dynamic yield stress in ER fluids. This increases with increasing voltage input, or until ER fluid breakdown occurs between the electrical polarization of the particles, as shown in Fig. 3.5. It is also seen in Fig. 3.19 that the excitation imposed on the ER fluid causes the stress to oscillate about this mean yield stress, with its magnitude dependent on the particular voltage input. The amplitude of these oscillations are highly dependent on the frequency of oscillation, and is representative of the high stresses that are encountered in the low shear-rate region of Fig. 3.12.

Effectively, limitations of the ER fluid model are apparent as a result of the approximations made outside regions where experimental data were taken. Because the response is of a dynamical nature, the innate inertial characteristics of the particles within the fluid and the fluid itself must be considered at high frequency. Eventually, the motion of the fluid will be such that very little aggregate structure formation will be possible. This observation puts large doubt in our model at high frequency.

The results depicted in Fig. 3.19 were mapped to the frequency domain to obtain a discrete representation of the power spectral density. Power spectral density is a measure of the power transmitted at various frequencies prescribed by some $|P(\omega)|$, where $P(\omega)$ is the Fourier transformed frequency response function. These data are illustrated in Fig. 3.20 over a range of 0 to 100 Hz. Although the diagram is very unclear due to the limited number of discrete simulation data, three distinct peaks are apparent. The peaks represent the amount of power entering the system for all the frequency components of an excitation lying in an infinitesimal band between ω and $\omega + d\omega$. For $V = 0$ these peaks are recognized at 24.7 Hz, 52.3 Hz, and 78.4 Hz, respectively. With increasing voltage, only the latter two peaks are apparent, with the middle becoming more defined. This information tells us that between 50-56 Hz, and 75-82 Hz, we should expect minimal power dissipation from the ER fluid model regardless of input voltage magnitude.

To make comparisons between model 1 and model 2, the same procedure above was

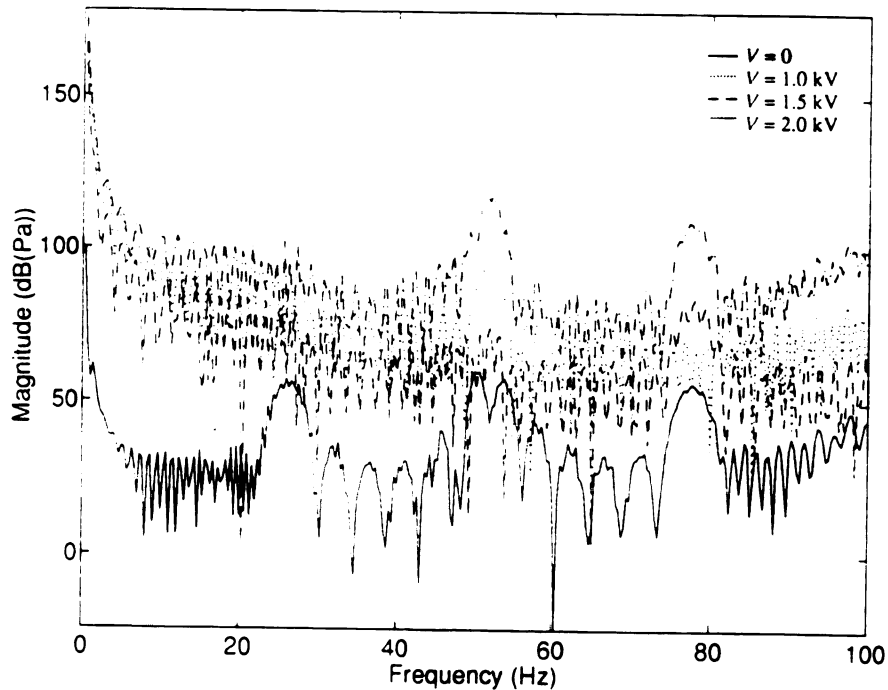


Figure 3.20 - Power spectral density of the ER fluid model for various constant voltage inputs.

repeated. Using a steady-state option provided by ABAQUS, the mean stress response for both models was obtained over a frequency range of 0 to 100 Hz. Figure 3.21 shows a comparison between these results for zero voltage input. Moreover, the results for the 2 kV case were qualitatively identical. With the addition of the insulate material, the stresses in the unit cell for both model jumps by a magnitude of ten. It is evident that the mean stress decreases with increasing frequency for both cases. However, the actuator model seems to under predict the actual geometry by almost 100 Pa at low frequency, where in fact, the rule of mixtures model should be more accurate. Intuitively, the close agreement in the high frequency range must be due to approximation error in the linear solver routine. This error may be attributed to the large differences between the constitutive laws for the ER fluid and the insulate. Surely, a more accurate description of the unit cell would be necessary to compensate for these errors. Thus, the model obtained through the rule of mixtures approach should be considered conservative for accurate modeling of

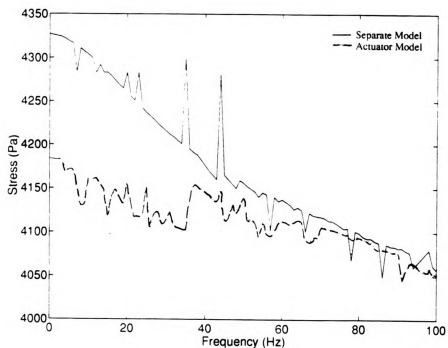


Figure 3.21 - Steady-state comparison between models 1 and 2 for zero voltage input.

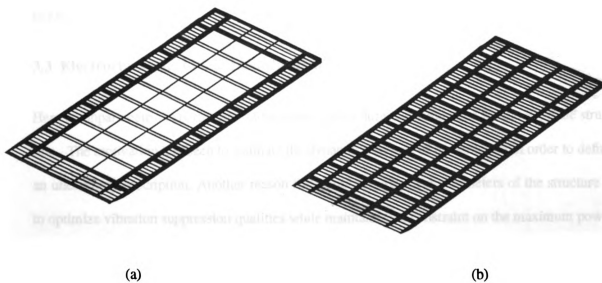


Figure 3.22 - Deformed configurations for: (a) model 1, and (b) model 2 for zero voltage input.

the actuator. The associated deformed configurations for both models, which were determined at a frequency of oscillation of 15 Hz, are given in Fig. 3.22. These two models are very similar in appearance.

Figure 3.23 shows the response of the actuator during harmonic shearing. The actuator has a unit cell geometry with the volume ratios of $v_{in} = 0.2808$ and $v_{fl} = 0.7192$, which are obtained using Eq. (3.12) and the data in Table 3.1. For a constant amplitude of $\epsilon_0 = 10\%$, and for constant input voltages of 0, 2 kV, and 4 kV, these results show how voltage directly affects the response of the actuator. Clearly, the small change in amplitude reflects the small effect that the ER fluid will have on the dynamic response of a large structure. Hence, the ER fluid is severely limited when drastic stiffness is necessary. The associated power density spectrum analysis for the actuator model under various voltage inputs is given in Fig. 3.24. The results depicted in this response spectrum demonstrate characteristics similar to those described in Fig. 3.20, however, the larger peak near 80 Hz has disappeared. By using the solid zero voltage line as a reference we see a small shift in the peaks is apparent for increasing voltage. Consequently, this observation gives us some indication of what direction a structure's frequency response will shift during excitation.

3.3 Electrorheological Plate Identification

Here a nonparametric experimental identification procedure was conducted for the ER plate structure. The motivation has been to estimate the dynamic response of the structure in order to define an uncertainty description. Another reason for identifying physical parameters of the structure is to optimize vibration suppression qualities while maintaining a constraint on the maximum power consumption of the ER fluid actuator. Stevemns, *et al.*,¹²⁵ investigated time-dependent excitation of an ER fluid clutch and concluded that it was possible to reduce power consumption by more than 50% using excitation in the form of voltage pulses. However, the ER effect diminishes with increasing frequency.¹³⁶ Clearly, there are advantages if ER fluid actuator excitation can be opti-

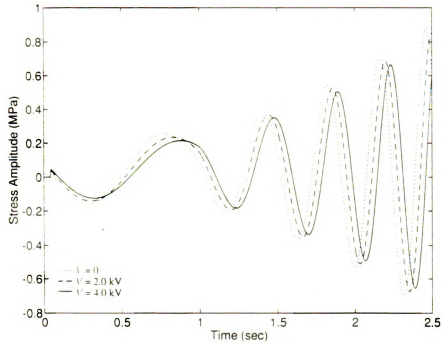


Figure 3.23 - Time response of the actuator model under periodic excitation.

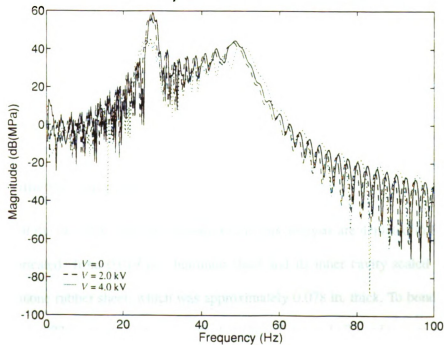


Figure 3.24 - Power spectral density of the actuator model for various constant voltage inputs.

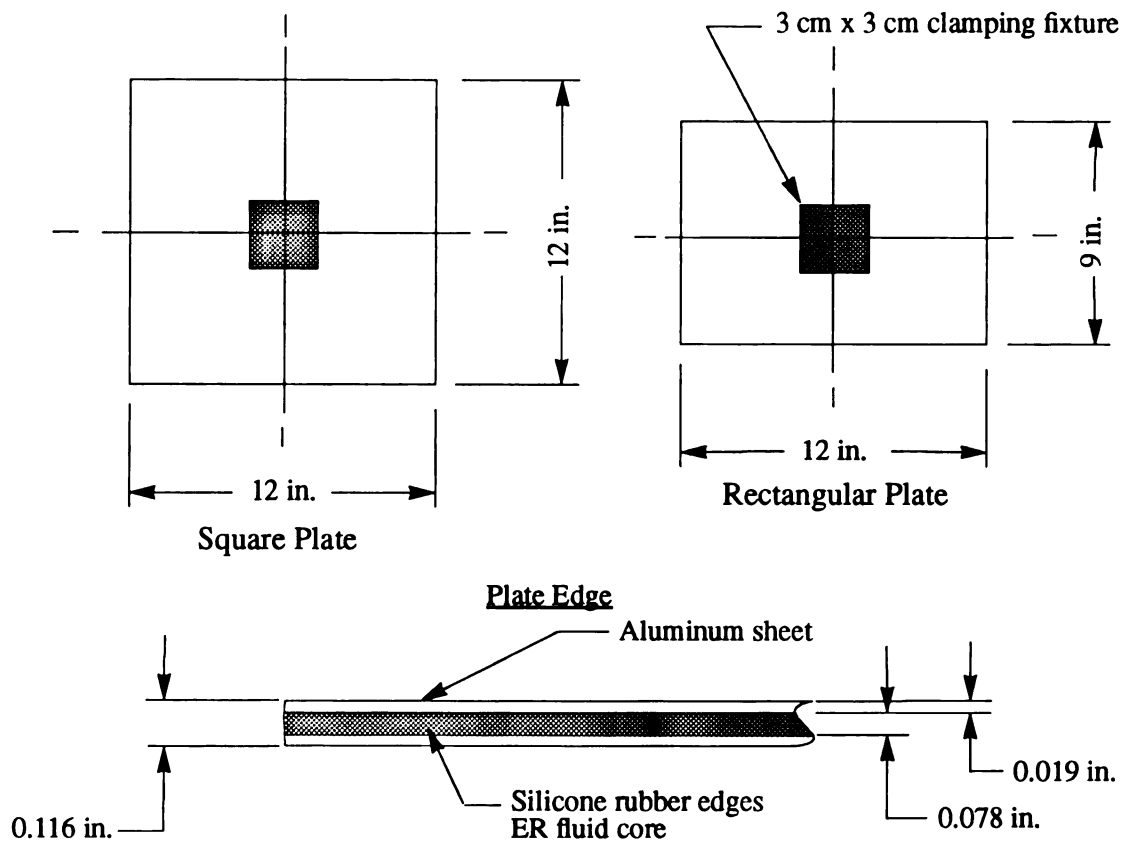


Figure 3.25 - Schematic of the two plate specimens.

mized using a voltage supply containing variable waveform, amplitude, frequency, and phase characteristics. Such optimization has been mentioned briefly in previous experimental investigations.^{121, 136}

3.3.1 Experimental apparatus

A schematic of the two plate specimens employed in this analysis are depicted in Fig. 3.25. Each plate was fabricated from 0.019 in. aluminum sheet and its inner cavity sealed with a 50 DA durometer silicone rubber sheet, which was approximately 0.078 in. thick. To bond these components, a silicone RTV rubber agent was applied to all surfaces and allowed to cure for a minimum of 24 hours at room temperature. After cure, each plate was punctured with a needle through the insulate and the cavity was injected with the ER fluid.

The experimental arrangement utilized in this study permitted a forced excitation and dynamic response analysis of an Er fluid embedded plate with free-edge support conditions. The corresponding instrumentation and experimental arrangement utilized in this investigation is depicted in Fig. 3.26. Each plate was mounted to an aluminum fixture that was firmly attached to a Brüel & Kjær shaker unit via a small 3 cm square clamping fixture. The external forcing imposed on the plate was supplied by an HP dynamic signal analyzer, and the time-dependent voltage excitation was supplied by a programmable arbitrary function generator. In addition, a Brüel & Kjær force transducer was included to determine the mobility and receptance frequency response measurements. The amplitude of excitation was maintained at minimal levels to reduce nonlinear and other parasitic effects on each plate.

3.3.2 Plate modal analysis

Prior to determining the plate response for the voltage excitations, the first six resonant frequencies and associated mode shapes of each plate were experimentally identified. In order to determine these dynamic characteristics, one quarter of each plate was discretized as illustrated in Fig. 3.27. In Fig. 3.27, each black dot signifies a point of measurement. By using the HP signal analyzer as an excitation source and data acquisition system, receptance and mobility responses were obtained. These responses were determined by imposing deterministic (sine-dwell) and random (stochastic) forced excitations on each plate. For improved signal-to-noise ratio, the Hanning window was used for random excitation, and all data were exponentially averaged over time.

The plate resonant frequencies were identified from transfer and point receptance and mobility frequency responses taken at discrete points. The receptance response for both the rectangular and square plates is depicted in Fig. 3.28. In Fig. 3.28 it is apparent that the frequency response of each plate is relatively mass dominated, as evidenced by the large decrease with increasing frequency. Mass dominance, as opposed to stiffness dominance, is also supported by the existence of a resonance after each anti-resonance. Receptance response results were verified

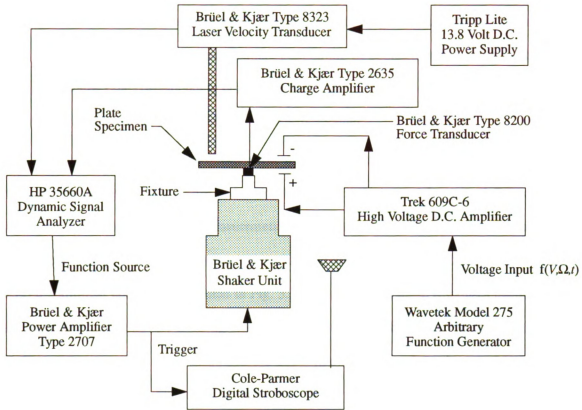


Figure 3.26 - Experimental arrangement and instrumentation.

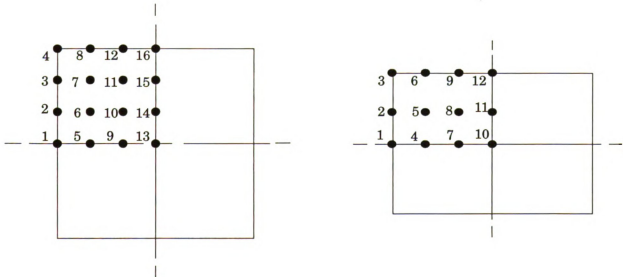


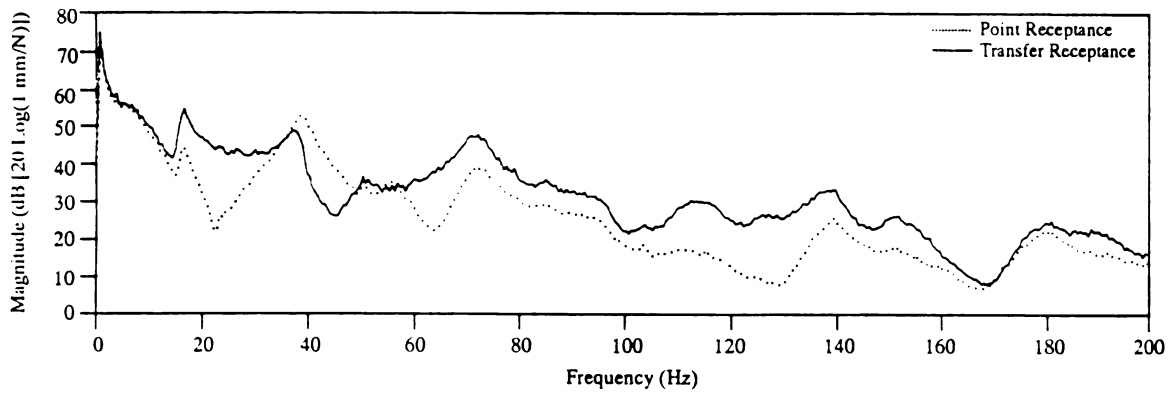
Figure 3.27 - Experimental plate discretization.

using a wide-band random excitation. This permitted an estimate of the frequency response function at the measurement point of interest in terms of both magnitude and phase. These results were then divided by the input force frequency spectrum, as depicted in Fig. 3.29 and Fig. 3.30. Phase plots depict the corresponding changes with resonance and anti-resonance and were used to determine gain insight on the approximate resonance values.

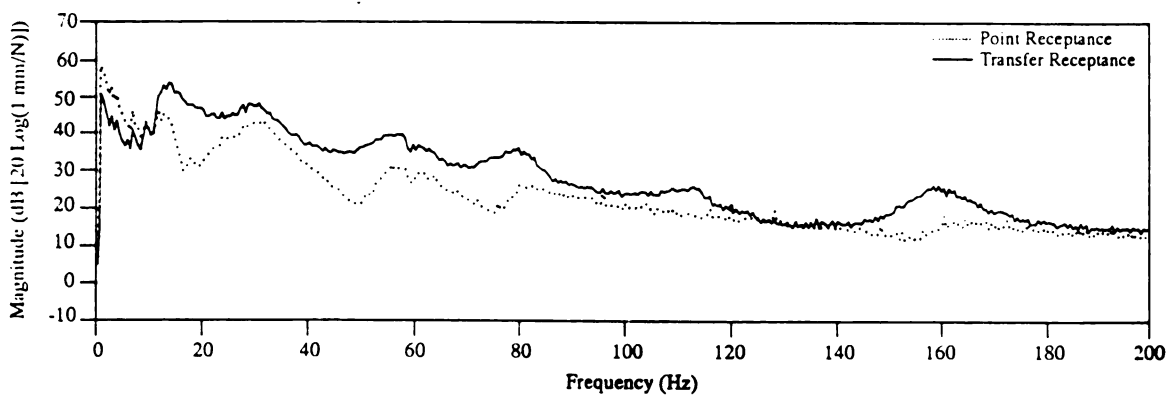
For purposes of identifying questionable resonant frequencies, this procedure was repeated using narrowband random and pure sinusoidal excitations and repeated for several different points of measurement. Multiple point measurements were averaged together using sinusoidal profiles to ensure accuracy. For comparison purposes only, the magnitude of the mobility responses from several additional points are presented in Fig. 3.31. As expected, those responses taken from the square plate are in relatively close agreement due to symmetry. However, the responses at point 16 from the rectangular plate illustrates the beam-like influence of the longer side. Thus, as expected, a resonance is noticed near every $k \omega_n$ along the frequency spectrum where k is the mode number.

The damping ratios were obtained from Fig. 3.28-3.31 using the half-power point method introduced in Chapter 2.¹⁰² Results from the various measurement points are given in Table 3.2. We see that damping tends to remain fairly consistent in the domain of each plate, and increase with increasing mode number. The large damping ratios in both plates for $V = 0$ kV can be attributed to both the insulate material that bonds the two aluminum electrodes together and the contribution of the fluid inertia. It is evident that these damping ratios are much larger than the structural damping ratios of aluminum alone. At the higher modes the results have large uncertainty because the measurement signal was very weak.

Mode shapes for each plate were also identified visually by triggering the digital stroboscope laser velocity transducer simultaneously to measure the displacement of the plate at each discretized point. Data were then compiled, normalized with respect to the input, and graphically plotted using a curve fitting routine. The results from this procedure are presented in Fig. 3.32



(a)



(b)

Figure 3.28 - Receptance for: (a) square plate, and (b) rectangular plate at $V = 0$ kV.

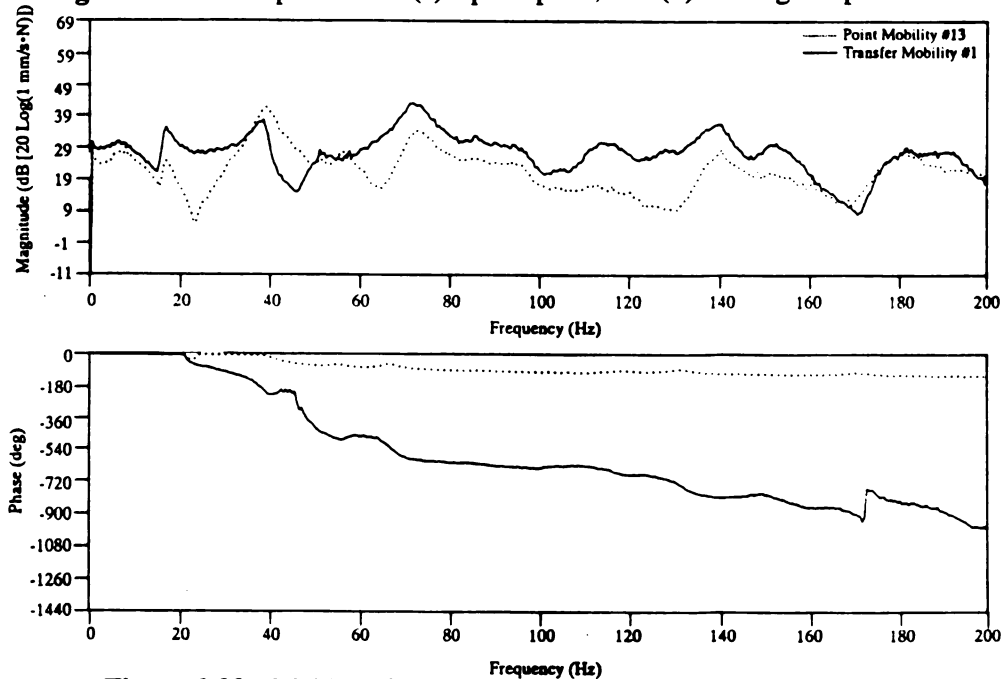


Figure 3.29 - Mobility frequency response for the square plate at $V = 0$ kV.

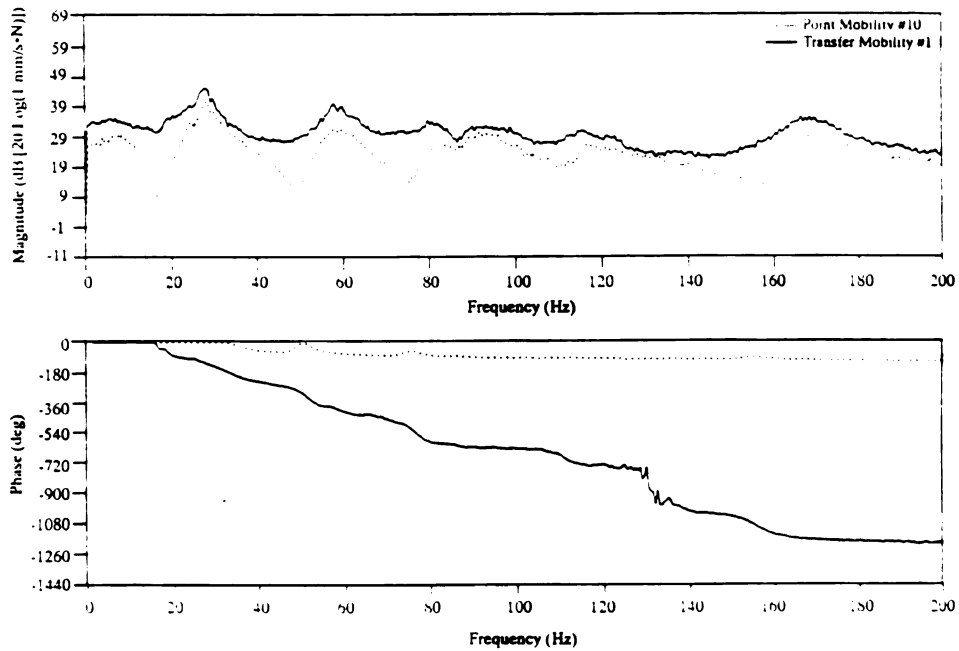


Figure 3.30 - Mobility frequency response for the rectangular plate at $V = 0$ kV.

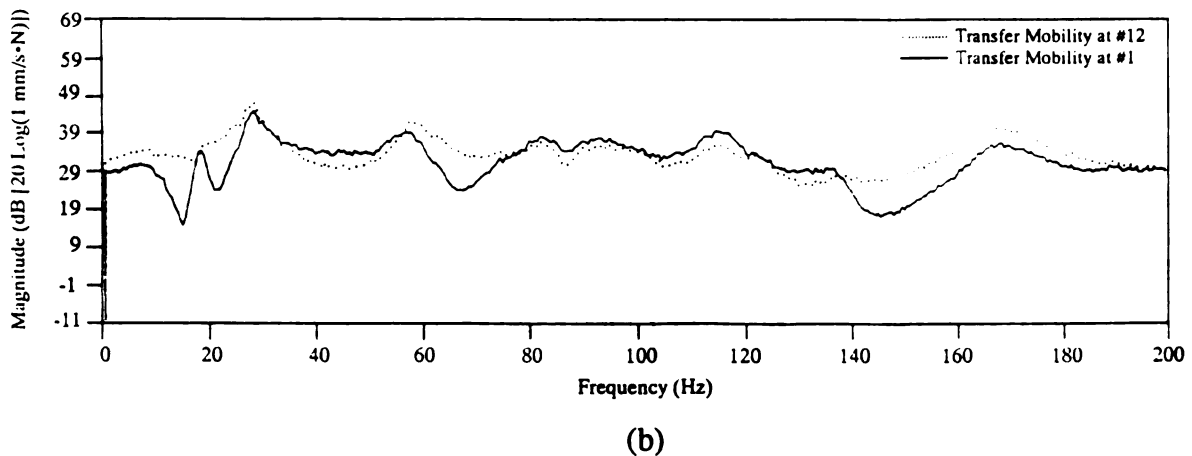
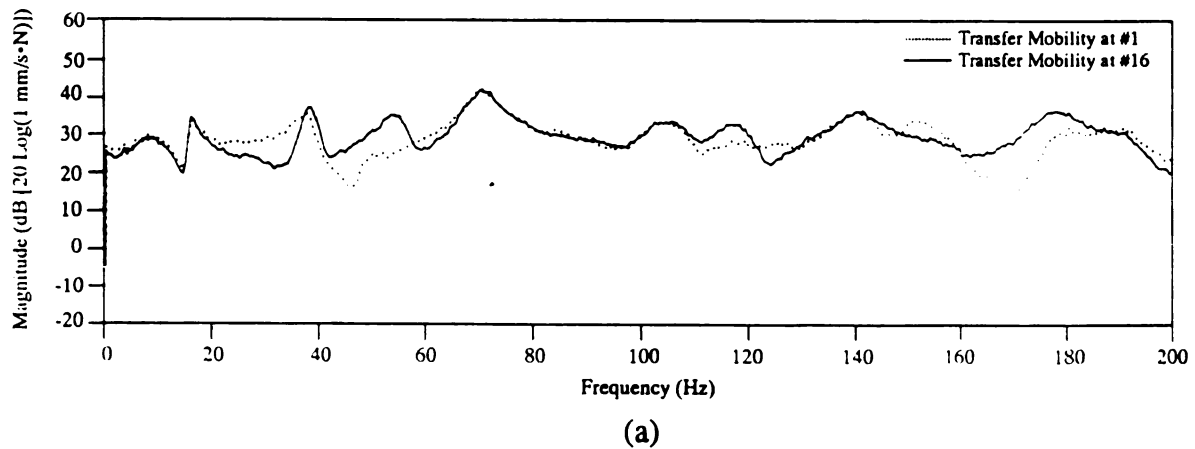


Figure 3.31 - Mobility responses for the (a) square, and (b) rectangular plates at $V = 0$ kV.


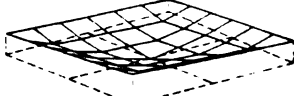

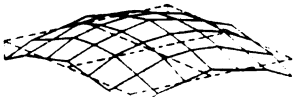

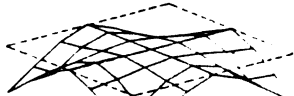
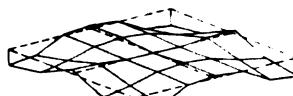

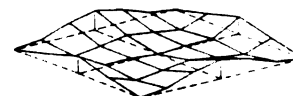

Mode Shape Identification	
Rectangular Plate	Square Plate
 Mode 1	 Mode 1
 Mode 2	 Mode 2
 Mode 3	 Mode 3
 Mode 4	 Mode 4
 Mode 5	 Mode 5

Figure 3.32 - Mode shape identification results for both plates at $V = 0$ kV.

Frequency Response Point		Plate Damping Ratios					
		ξ_1	ξ_2	ξ_3	ξ_4	ξ_5	ξ_6
Square Plate	#1	0.01	0.015	0.015	0.015	0.016	0.0191
	#13	0.009	0.011	0.013	0.0135	0.015	0.0194
	#16	0.0112	0.0131	0.011	0.014	0.0156	0.021
Rectangular Plate	#1	0.011	0.015	0.019	0.012	0.016	0.0185
	#10	0.008	0.016	0.015	0.0146	0.0171	0.0187
	#12	0.009	0.012	0.011	0.0164	0.0167	0.019

Table 3.2 - Experimentally determined damping ratios for $V = 0$ kV.

and the first six resonant frequencies of each plate are tabulated in Table 3.3. Beyond six resonant peaks the signal-to-noise ratio was too weak to identify further values.

3.3.3 Input verification

Each plate was subjected to simple voltage inputs and response measurements were taken in both the time and frequency domains. The simple periodic voltage waveforms included alternating (reversed polarity) sinusoidal, triangular, and square inputs. The frequency of the voltage input is given by Ω . To conduct the time domain measurements, a continuous narrowband periodic exci-

Table 3.3 - Experimentally determined plate natural frequencies.

Mode	Square Plate	Rectangular Plate
frequency (Hz)		
1	19.50	15.52
2	37.87	31.36
3	64.56	53.15
4	118.3	76.35
5	138.7	111.5
6	181.8	155.6

tation was imposed on the plate and transient response was monitored. Results for the sinusoidal and square inputs, taken at measurement point 1 for the rectangular plate, are depicted in Fig. 3.33 and 3.34. It is apparent in these diagrams that the ER fluid actuator has the largest effect on plate vibration at peak voltages. The amplitude of the plate was greatly reduced for each voltage waveform, however, the greatest reduction is evidenced with the square voltage input. It is also important to note the time lag associated with vibration suppression. This observation is important when time-dependent voltages are considered and will be addressed later.

The final investigation included a square voltage pulse imposed on each plate. These results are presented in Fig. 3.35 and Fig. 3.36, in which we see that the pulse input results in the greatest reduction in plate amplitude, especially for low frequency excitation. The amplitude response of the square plate is much less than the rectangular plate, and it is more stable. Although, as illustrated in Fig. 3.31, the square plate is an inherently stiffer structure than the rectangular plate.

From these results, it is evident that the alternating voltage inputs have one advantage over the pulse input in that they are better suited for low frequency steady-state excitations. For example, in the case of suppressing a continuous amplitude disturbance, an in-phase sinusoidal voltage input would be much better than a pulse input. This is because they apply the greatest amplitude reduction over the excitation with the least consumption of power. The square voltage input would be an exclusion because it is only undergoing a change in polarity rather than a change in amplitude. Hence, the amount of power necessary to produce this potential is almost identical to that of a constant voltage. Nevertheless, to compare the constant to the square voltage input in terms of stiffness and damping improvement, the constant input would surpass because the alternating square input tends to weaken dipolar bonding of the ER fluid particles.¹²⁵ In transient conditions, the most feasible of these four waveforms would be the pulse input. Since transient conditions will contain a large spectrum of frequencies, the pulse input would provide the greatest reduction in amplitude. Although, the reduction will come at the expense of power and a time lag

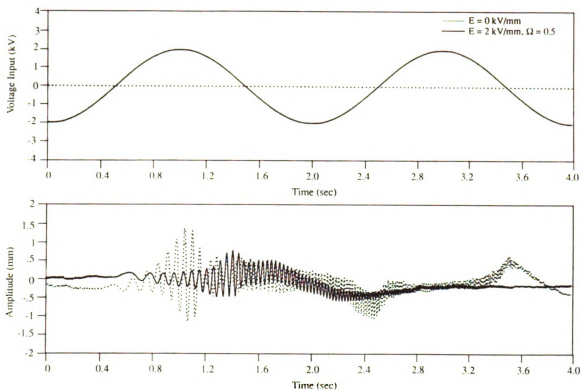


Figure 3.33 - Transient response of the rectangular plate for $V = 2$ kV and $\Omega = 0.5$ Hz.

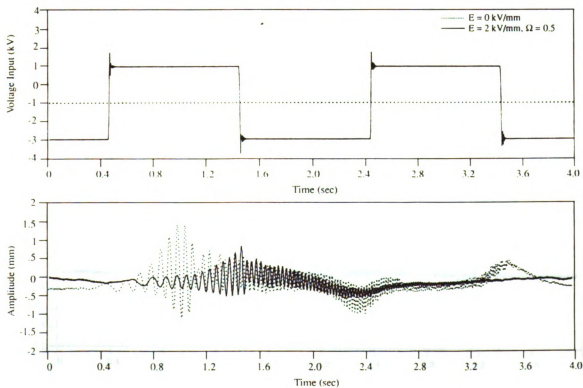


Figure 3.34 - Transient response of the rectangular plate for $V = 2$ kV and $\Omega = 0.5$ Hz.

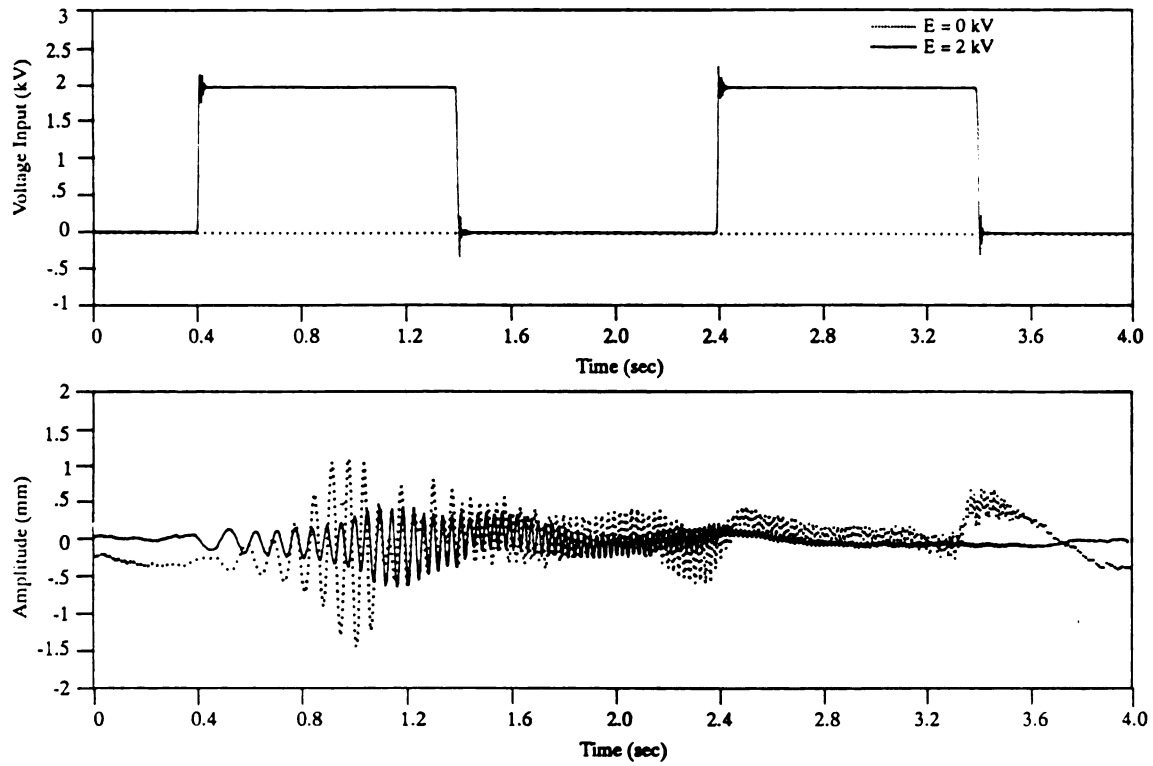


Figure 3.35 - Transient response of the rectangular plate for $V = 2$ kV and $\Omega = 0.5$ Hz.

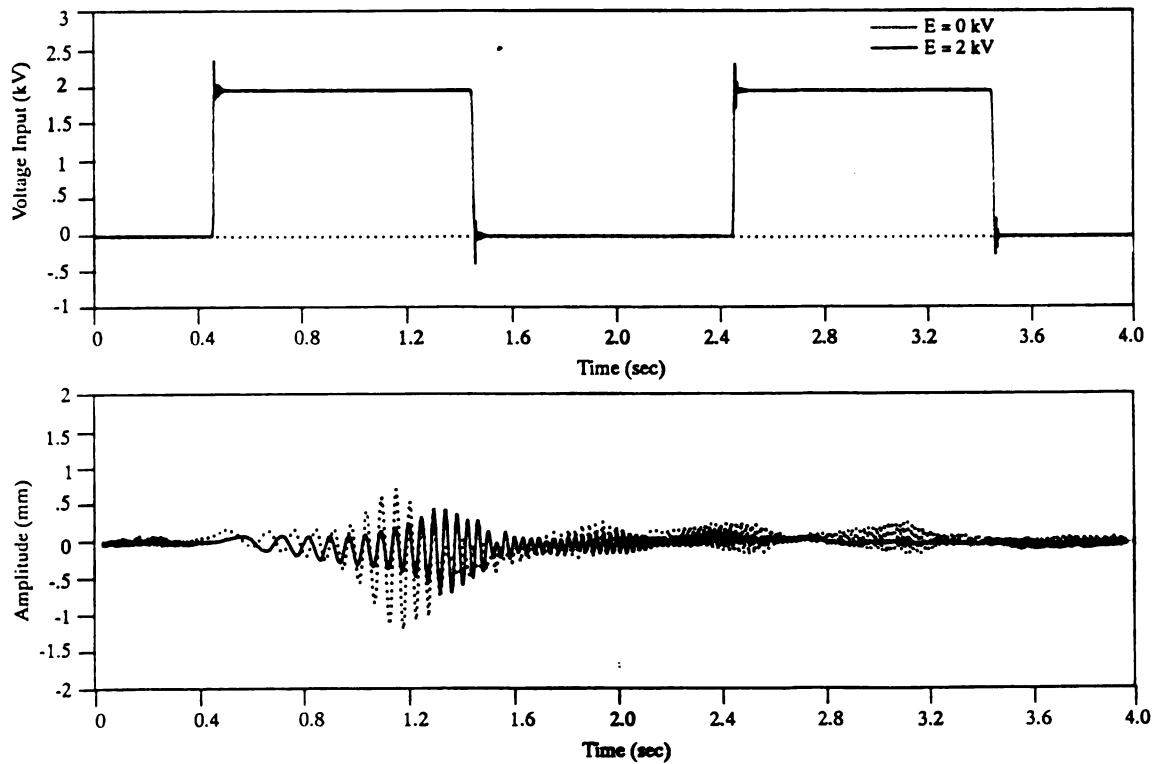


Figure 3.36 - Transient response of the square plate for $V = 2$ kV and $\Omega = 0.5$ Hz.

induced by the selection of an optimal pulse length and frequency.

To further investigate the effect of time-dependent voltages over a large spectrum of excitations, frequency responses were generated for both plates. For convenience, the same waveforms and measurement points were used. A random narrowband forced excitation was imposed on each plate, and the corresponding magnitude and phase descriptions were recorded. These data represent the plate frequency response for voltage input amplitudes of 2 kV and frequencies of 0, 1, 10, and 50 Hz, respectively. Square and rectangular plate response is illustrated in Figures 3.37-3.42 for sinusoidal, square, and pulse voltage inputs. The triangular input has not been shown because of its similarity to the sinusoidal input. We can conclude that the ER fluid effect diminishes with increasing voltage frequency for all waveforms due to response consistency with previous results.. As expected, we see the largest reduction in amplitude over the largest frequency range in the pulse input responses. It is also seen in this response that only small changes in magnitude resulted from large changes in voltage input frequency. This is unlike the alternating input results, which show increases with increasing frequency. We must conclude that for small pulse lengths, a dynamic electrical and rheological coupling takes place, induced by dynamic agitation. This coupling must cause stiffness and damping to decay at a rate proportional to the length of exposure time to the potential. Since the ER fluid changes from its liquid-to-solid phase rather rapidly, it must take longer to return to a liquid, thereby retaining its salient properties for some time.

Using a constant frequency of 1 Hz, results were obtained for different voltage input amplitude. Magnitude results from these experiments are depicted in Fig. 3.43 and Fig. 3.44 for the rectangular and square plate, respectively. For clarity, the phase representations corresponding to each plot have been excluded, although each phase was identical to the results in Figures 3.37-3.42. We see from Fig. 3.43 and Fig. 3.44 that a change in amplitude, as well as change in frequency of the input voltage, has the capability of inducing a frequency response shift. It is clear that the ER effect due to a 1 kV amplitude voltage input reduces overall plate vibration almost as

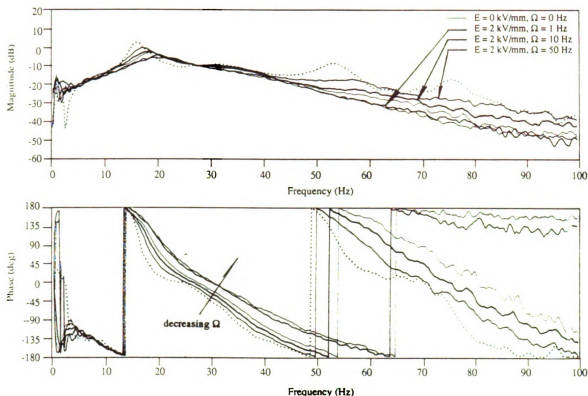


Figure 3.37 - Frequency response of the rectangular plate for a sinusoidal input of $V = 2$ kV.

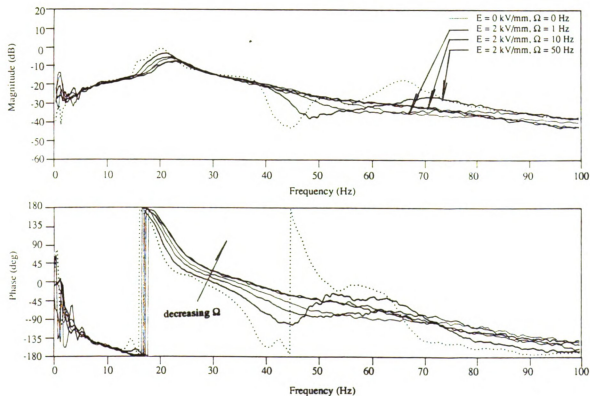


Figure 3.38 - Frequency response of the square plate for a sinusoidal input of $V = 2$ kV.

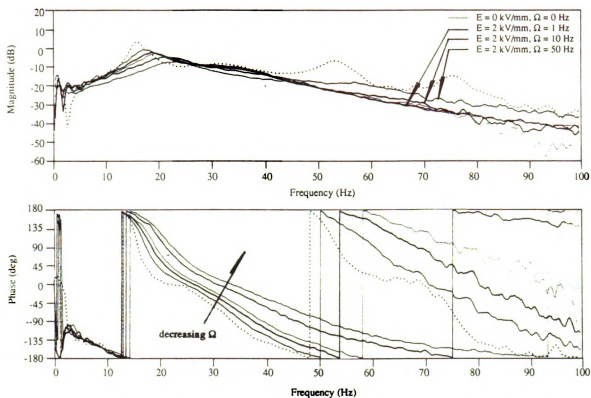


Figure 3.39 - Frequency response of the rectangular plate for a square input of $V = 2$ kV.

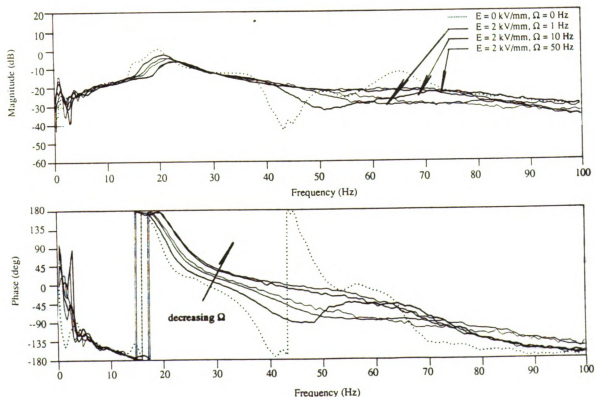


Figure 3.40 - Frequency response of the square plate for a square input of $V = 2$ kV.

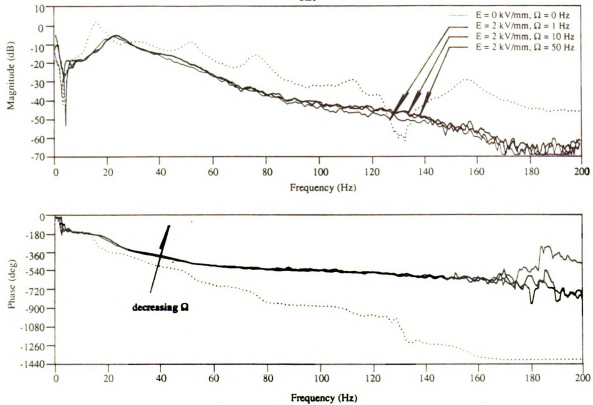


Figure 3.41 - Frequency response of the rectangular plate for a pulse input of $V = 2$ kV.

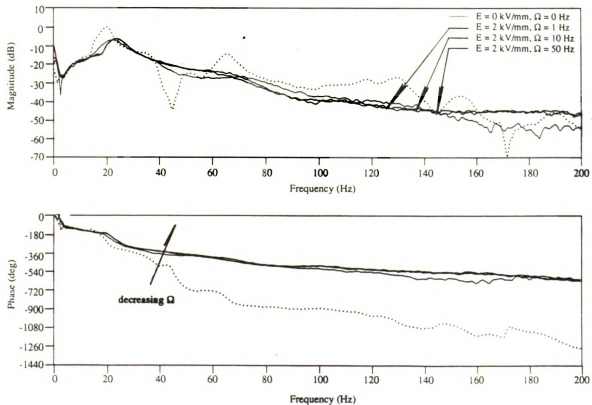
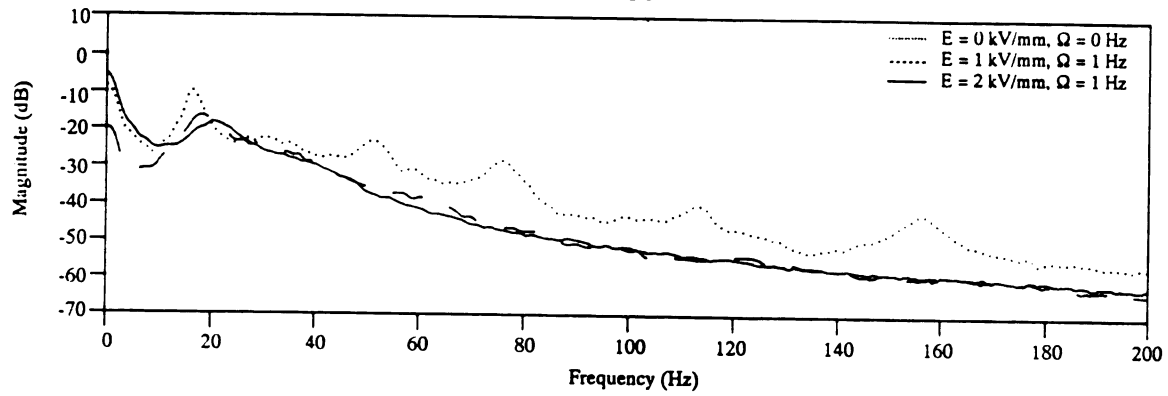
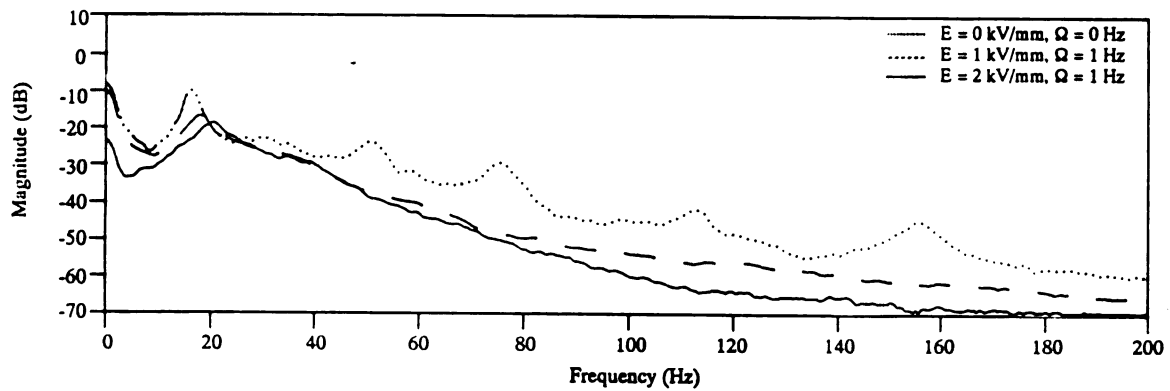


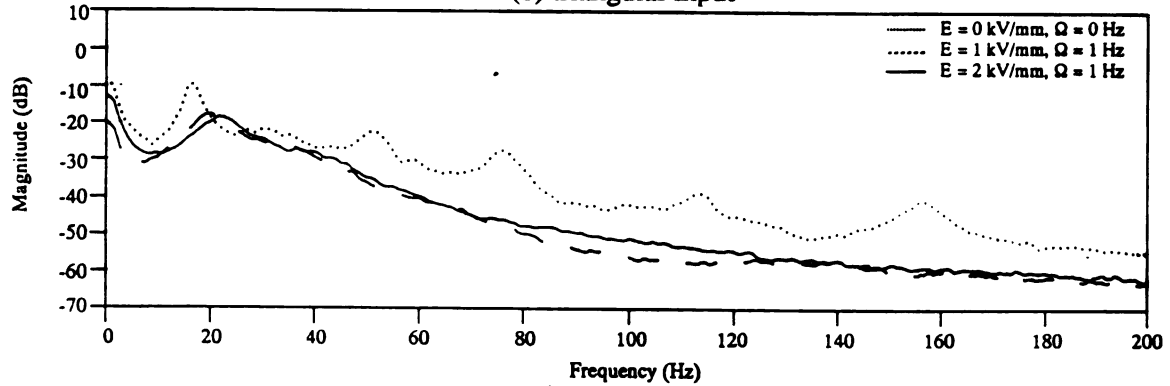
Figure 3.42 - Frequency response of the square plate for a pulse input of $V = 2$ kV.



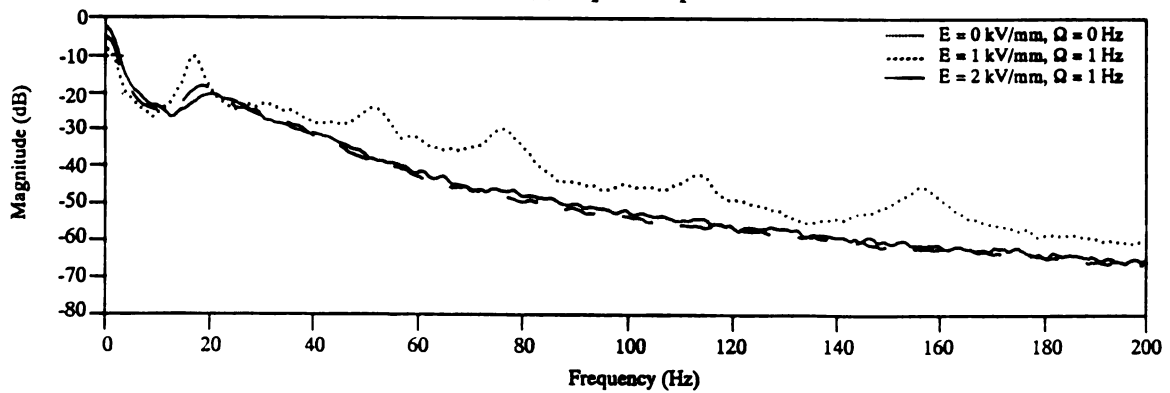
(a) sinusoidal input



(b) triangular input

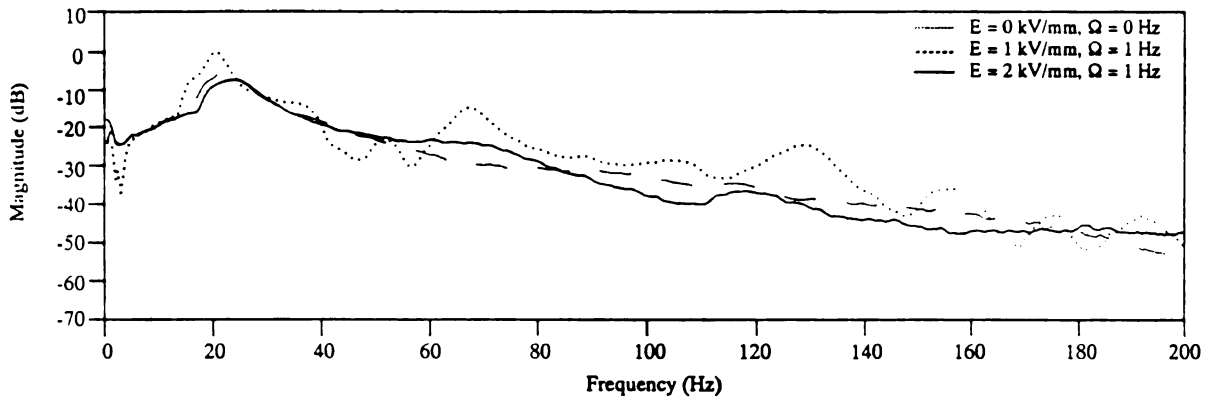


(c) square input

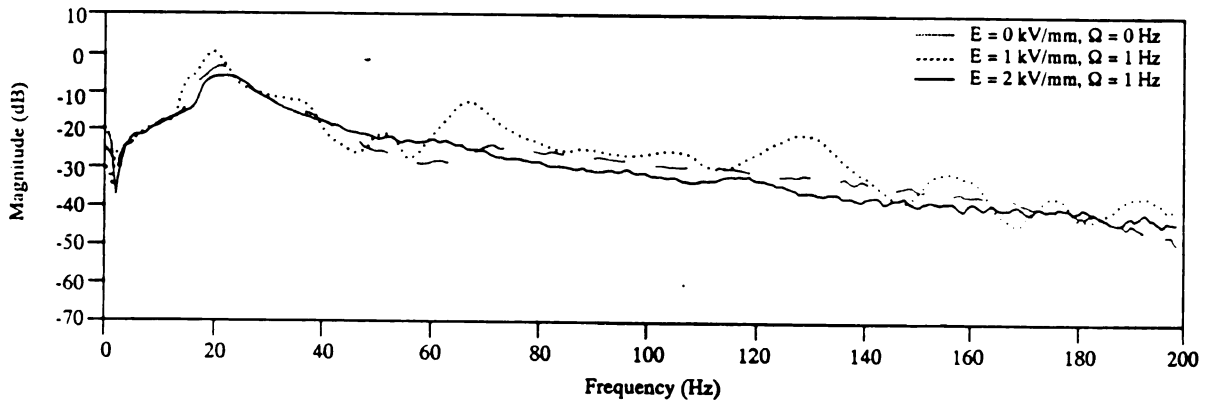


(d) pulse input

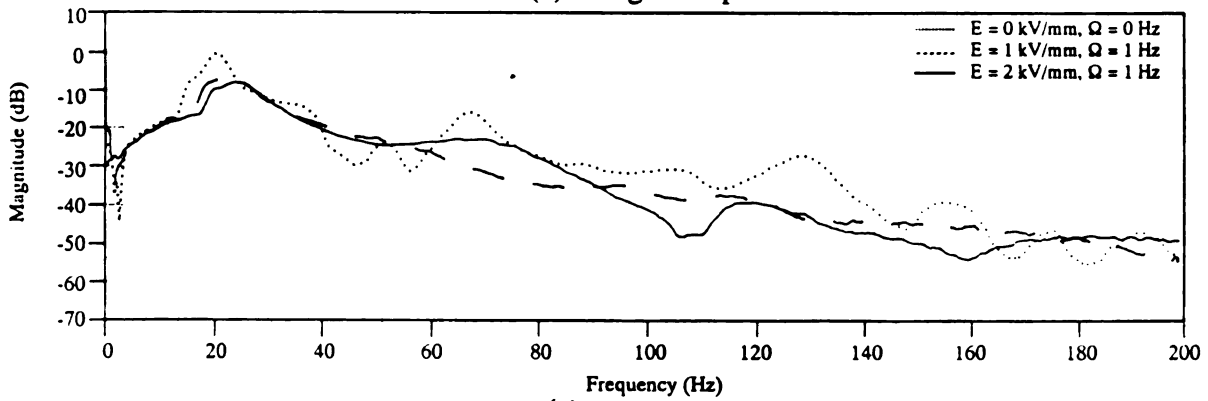
Figure 3.43 - Frequency response of the rectangular plate for different voltage inputs at $\Omega = 1$ Hz.



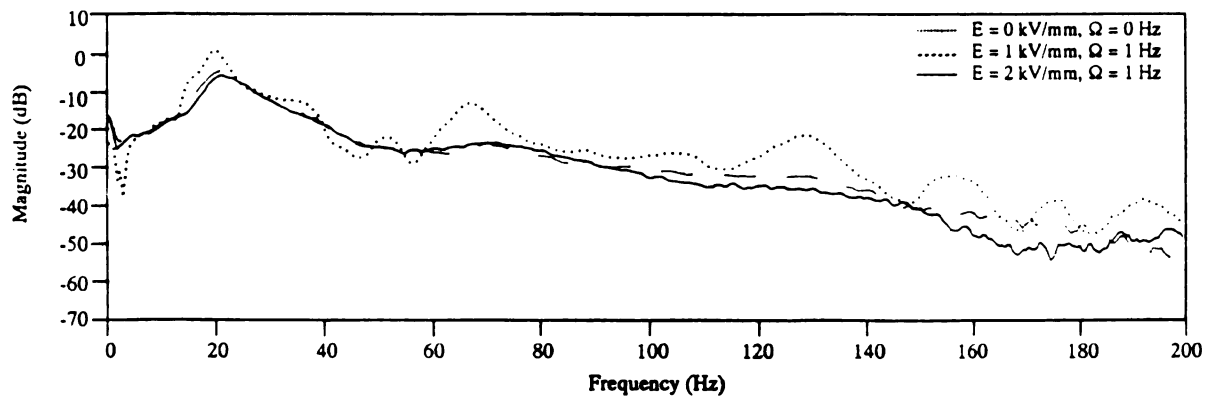
(a) sinusoidal input



(b) triangular input



(c) square input



(d) pulse input

Figure 3.44 - Frequency response of the square plate for different voltage inputs at $\Omega = 1 \text{ Hz}$.

much as the ER effect resulting from a 2 kV amplitude voltage input for the alternating waveforms. This is evident in the rectangular plate response for sinusoidal and pulse inputs beyond the first natural frequency. It is in this frequency range that the response from the two different amplitudes becomes almost identical. However, the most notable response change in both plates due to voltage amplitude occurs with the triangular voltage input. Here, use of a 2 kV amplitude only reduced overall plate response by 10% for frequencies above 60 Hz, whereas a 1 kV amplitude reduced overall plate response by over 18% beyond 85 Hz. Moreover, we see that the square input contributes to the largest shift in the natural frequencies.

From the square plate response in Fig. 3.44, all three alternating voltage inputs had relatively the same affect on the plate's response. One possible reason for this is the larger innate stiffness of the square plate. Observations conclude that the 1 kV amplitude performs much better than the 2 kV amplitude for several voltage input cases. For instance, in the frequency range between 40 and 80 Hz for a sinusoidal voltage input, plate vibration is reduced by over 12% due to a 1 kV amplitude input and only 7% due to a 2 kV amplitude input. A possible explanation for this exists with the attainable level of damping. When the ER fluid is charged with a 2 kV input, the stiffness of the plate becomes greater, however, this effect does not guarantee that the level of damping also becomes greater. In fact, at a level of 1 kV, we achieve almost the same level of stiffness as we do for the 2 kV amplitude input if observe the slopes of the frequency response, yet with an increase in damping, as depicted in Fig. 3.44 (c). This occurs around the second natural frequency in all cases. It must follow that the amount of random particle breaking and aligning at 1 kV is greater than at 2 kV. Consequently, this increases structural damping rather than structural stiffening, which is more apparent in the fundamental natural frequency.

Finally, it is obvious that the ER effect has negligible influence on rigid body motion or vibration below the first natural frequency. It is also observed from the plate frequency responses that significant reduction in plate vibration occurs in a limited narrowband range between the first and second natural frequencies. From these results it can be concluded that the ERE is fairly con-

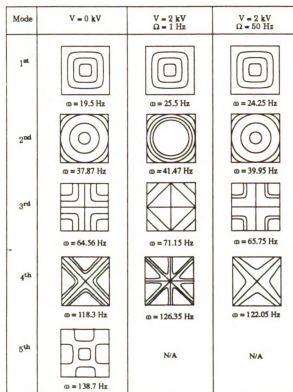


Figure 3.45 - Mode shape identification for the square plate activated with a square pulse voltage input at various frequency.

sistent over wideband frequencies for both plates when excited by a pulse voltage input. However, the results from the other alternating voltage inputs give conclusive evidence of their narrowband potential. It follows that a higher-power pulse voltage input would be acceptable to damp transient plate vibration, whereas the sinusoidal or triangular voltage inputs would be better for narrowband low-power steady-state plate vibration reduction.

To investigate the effect that time-dependent inputs have on the ER fluid structures, several experiments were conducted using variable frequency and amplitude pulse voltage inputs to activate the ER fluid. In a manner similar to that performed earlier, the first five mode shapes were identified for different values of pulse voltage input frequency. Figures 3.45 and 3.46 show the results of the experimentally observed mode shapes for the rectangular and square plates, respectively. Due to large damping and low measurement signals at high frequencies, several mode shapes were too difficult to identify. In Figs. 3.45 and 3.46, the corresponding shift in the plate

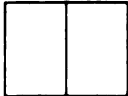


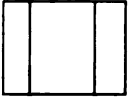

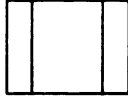



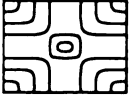
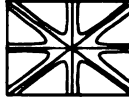
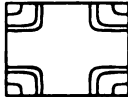

Mode	V = 0 kV	V = 2 kV $\Omega = 1$ Hz	V = 2 kV $\Omega = 60$ Hz
1 st	 $\omega = 15.52$ Hz	 $\omega = 24.53$ Hz	 $\omega = 23.95$ Hz
2 nd	 $\omega = 31.36$ Hz	 $\omega = 35.76$ Hz	 $\omega = 34.21$ Hz
3 rd	 $\omega = 53.15$ Hz	 $\omega = 55.45$ Hz	 $\omega = 54.3$ Hz
4 th	 $\omega = 76.35$ Hz	 $\omega = 135.1$ Hz	 $\omega = 132.5$ Hz
5 th	 $\omega = 111.45$ Hz	N/A	N/A

Figure 3.46 - Mode shape identification for the rectangular plate activated with a square pulse voltage input at various frequency.

resonance peaks, as a result of the ERE, is evident. The most noticeable change is the apparent modification of the mode shapes associated with the higher modes. For the square plate, this modification occurs at the 3rd mode, and for the rectangular plate, this occurs at the 4th mode. These changes exist as a result of the alternating stiffnesses, which in turn are due to the pulsing effect which couples the zero voltage and nonzero voltage responses.

3.3.4 Electrical and rheological dynamic coupling

At some point during the design of ER fluid structures, it will be necessary to optimize the pulse waveform for minimal power consumption. With the pulse waveform, we have the capability of tailoring the pulse length and amplitude. As observed earlier, when a potential is imposed across the plate, the response is relatively fast. However, at the termination of the potential, we see that the dissipation of the ERE is very dependent on the length of the potential. From this reasoning, a high frequency (long pulse length) voltage input would be able to maintain a fairly constant level

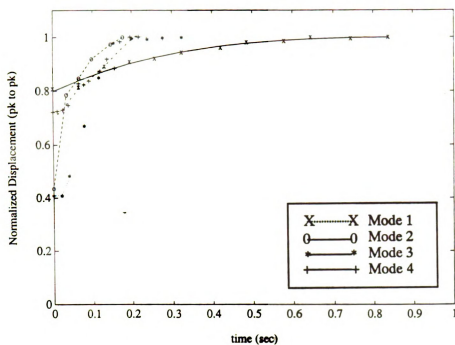


Figure 3.47 - Reduction of the ER effect with time for a pulse length of 10 msec.

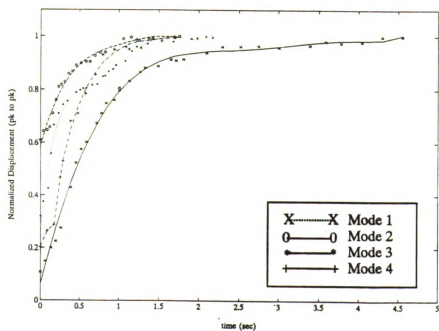


Figure 3.48 - Reduction of the ER effect with time for a pulse length of 500 msec.

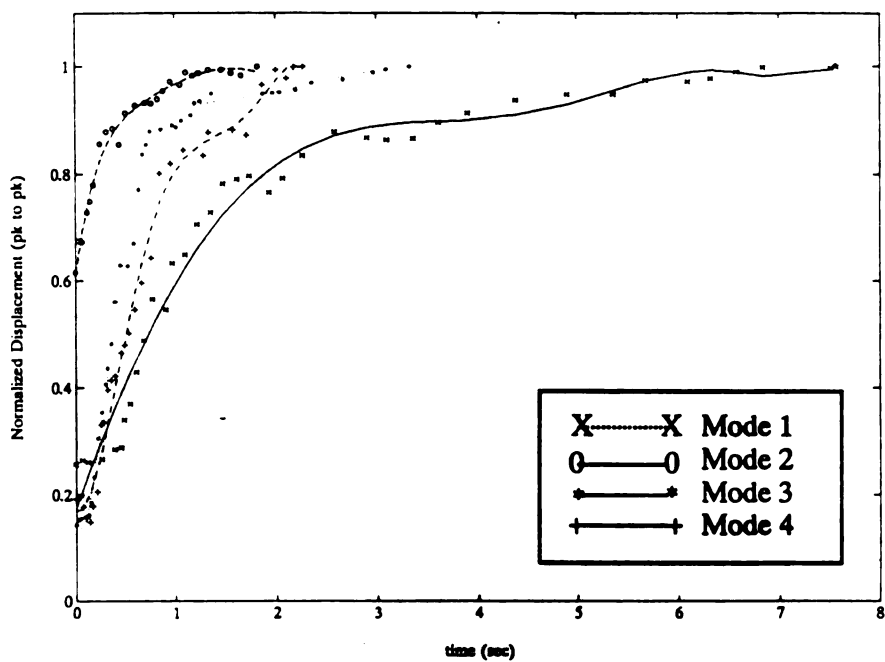


Figure 3.49 - Reduction of the ER effect with time for a pulse length of 1 second.

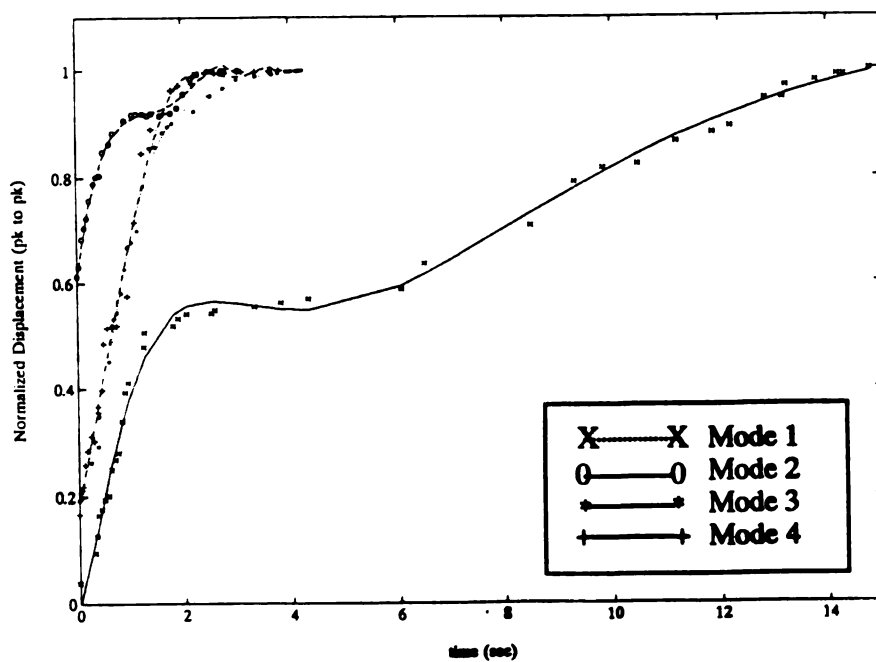


Figure 3.50 - Reduction of the ER effect with time for a pulse length of 5 seconds.

of stiffness and damping over time, whereas the low frequency (short pulse length) would fluctuate from a large reduction in vibration to large amplitudes, depending. Without a loss of generality, we will call this phenomena the “capacitance effect” of the ER fluid. This effect is not new, but has been indirectly acknowledged in several experimental investigations.^{120, 143}

For this identification experiment, a single pulse voltage input of 2 kV was imposed on the rectangular plate as it underwent a forced sinusoidal excitation with an amplitude of 5 mm. After imposing a voltage on the plate, the transient decay of the ER fluid effect was monitored for steady-state conditions until plate amplitude returned to the original zero voltage value.

The results from this procedure are shown in Figs. 3.47-3.50. Peak-to-peak plate amplitude was normalized using the zero voltage value for each associated mode. To identify values from these results, data was fit using a Nelder-Meade simplex curve-fitting routine, as shown by the solid line in Figures 3.47-3.50. The following equation was used to fit the data

$$y(x, t) = \sum_{i=1}^5 C_i \left(1 - \exp\left(-\frac{\tau}{\phi_i}\right)\right) \quad (3.23)$$

where C_i are constants and ϕ_i are time constants. The routine was repeated to minimize the least-square error. These results provide evidence for the conclusions made about the influence of the ERE over the first few modes. We see that this influence is large and that the greatest vibration reduction occurs in the first mode for each case. Figures 3.47-3.50 also resemble that of typical first-order response.

When approaching the coupling between the electrical and rheological dynamics using a linear systems perspective, it is clear that there is an increase in time constant for increased pulse length. Hence, these results give conclusive evidence that an optimal pulse length exists to meet power consumption constraints.

3.4 Chapter Summary

A brief discussion of ER fluids and the physical mechanism behind the ERE was presented. This discussion included sections on the rheology of suspensions, the electrical, and the rheological

behavior of an ER fluid. Following this introduction, a constitutive model for the ER fluid actuator was developed. It was shown that the ER fluid and actuator model, which were based on empirical data, were comparative to available experimental data during low frequency shearing. In steady-state, the actuator model provided marginal results of up to 25% difference between actuator geometries at low frequency. This shows that estimated portions of the model need further experimental verification. Finally, a detailed description of the experimental apparatus and ER plate identification was given. Dynamic performance was evaluated for two plate configurations. These results show the innate complexity of the ER fluid structure.

Chapter 4

ANALYTICAL AND NUMERICAL ANALYSIS FORMULATIONS FOR A DISTRIBUTED-PARAMETER STRUCTURE

4.0 Introduction

The use of active control as a method for providing damping for large flexible structures has been of particular significance in recent years. In most cases, these flexible structures are composed of various subsystems that interact with the main structure to yield a very complex dynamic system. Nonetheless, to provide effective control over the assembled main structure a sufficient amount of knowledge about the interaction of the system's ancillary components is required in order to formulate a mathematical description of its dynamical behavior. Analyzing the main structure as a complete unit is very difficult because of the computational intensity and time necessary to determine and solve for the system response. One approach that can be applied to these complex structures, and yield a more tractable analysis, is substructuring. Substructure synthesis is a technique where the main structure is subdivided into various, discrete elastic subsystems that are described separately with good accuracy, and reassembled to act as a single structure by imposing certain geometric compatibility constraints on the individual subsystem's boundaries.^{62, 95, 119} Since large flexible structures are actually a complex assembly of conventional beams, plates, or thin shells, a mathematical model for the full structure can be constructed of any combination of impedance, stiffness, and/or transfer matrices. Hence, each subsystem

model is an input-output relation that can be conveniently assembled to establish a linearized dynamic model of the main structure. When numerical methods are applied to the linearized model, e.g., finite-element analysis, relatively good approximations can be obtained for active control design of the main structure.

This chapter is dedicated to the development and analysis of conventional plates that are fabricated with embedded electrorheological (ER) fluid actuators. Since the behavior associated with these distributed parameter systems is very complex, it would be extremely difficult to mathematically describe them assembled in a large system. Actuated systems reduced to beams and plates are ideal candidates to model since they are critical to the response of a flexible controlled structure. Following, with our concurrent approach, it is the goal of this chapter to obtain an analytical model for distributed parameter plates and beams that could be implemented in a practical active control design by fitting certain parameters using numerical and/or system identification methods.

The general configuration of the plate is one composed of alternating layers of ER actuator material embedded between host layers of structural material. The constitutive material models for the two structures are generalized to accommodate a diverse species of ER fluid actuators and structural materials. The assumptions used to derive both models are based on fundamental sandwich structure theory^{89, 90, 140} and constrained layer theory,¹⁶ and the governing equations of motion are derived using Hamilton's principle. Sandwich structure analysis is useful here because it gives us the freedom to include shearing effects and core displacements independently but within a logical manner, where all interfacial boundary conditions are satisfied. Hence, through-the-thickness stresses are continuous and single-valued when the equilibrium equations are used. Comparative results for the static and dynamic response of the plate is given. Our objective here is to quantitatively contrast a simple case with previous published and experimental results in order to accurately verify our model its applicability.

4.1 Structural Kinematics

The analytical model presented here focuses on multi-ply structures consisting of alternating layers of various structural and actuator materials. Since it is not the intent of this study to consider the failure modes for these structures it will be assumed that perfect bonding exists between all layers. This assumption is quite acceptable according to Kim and Hong,⁷³ as long as bonding stiffness does not drop below a certain critical level. To formulate the governing equations of motion, a displacement approach is used where all strains and rotations are considered small as compared to unity, and in-plane elastic deformation is assumed to occur about the cross-sectional midplane of the structure.

Let us consider the structure composed of N layers of bonded actuator and structural layers and of uniform height H , as shown in the cross-sectional schematic in Fig. 4.1. We see from Fig. 4.1 that N must be an odd number so that all actuator layers are structurally constrained. Properties for an individual layer are identified by the subscript i , and the thickness of a layer is identified by

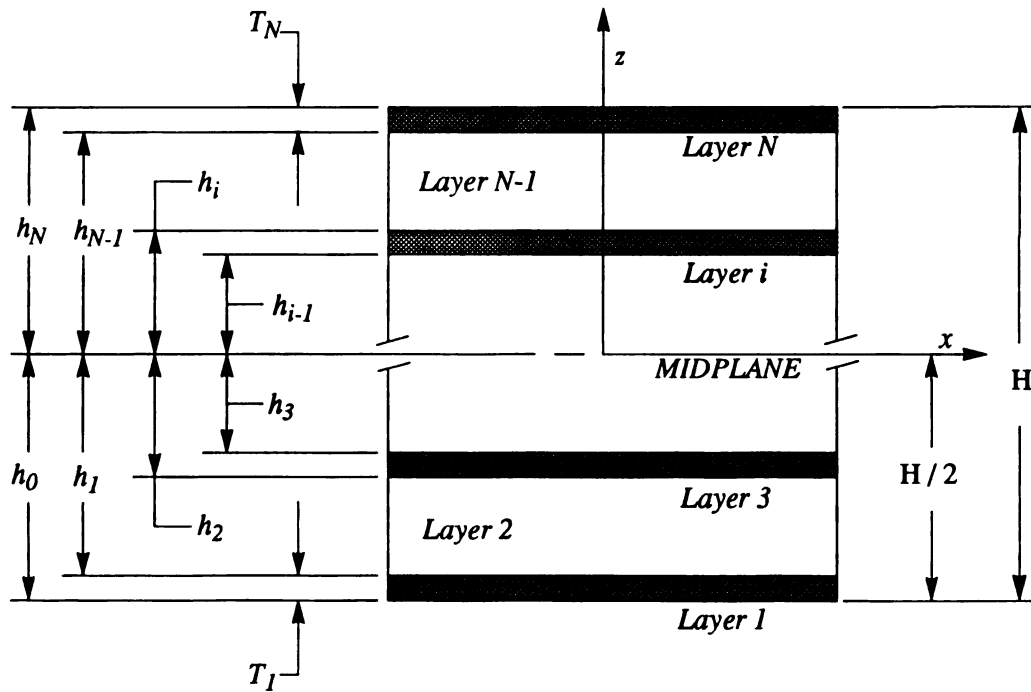


Figure 4.1 - Cross-section in the x - z plane of a distributed-parameter composite structure.

T_i . The coordinate system adopted for this model is a Cartesian system that consists of the longitudinal coordinate x , the in-plane lateral coordinate y , and the transverse out-of-plane coordinate z , where the x - y plane is coincident with the midplane surface of the structure, also shown in Fig. 4.1. The displacement field chosen for this model is based on the higher-order shear deformation theory proposed by Reddy.¹¹² This theory accounts for the transverse shear strain and the stress-free conditions at the surfaces. Given the following assumed displacement field:

$$\begin{aligned} u(x, y, z, \tau) &= u^o(x, y, \tau) + z\gamma_x(x, y, \tau) + z^2\zeta_x(x, y, \tau) + z^3\xi_x(x, y, \tau) \\ v(x, y, z, \tau) &= v^o(x, y, \tau) + z\gamma_y(x, y, \tau) + z^2\zeta_y(x, y, \tau) + z^3\xi_y(x, y, \tau) \\ w(x, y, z, \tau) &= w(x, y, \tau) \end{aligned} \quad (4.1)$$

where u^o and v^o represent the in-plane displacements of a point (x, y) on the midplane surface of the structure, γ_x and γ_y define the rotations of all normals to the midplane about the y and x axes, ζ_x , ζ_y , ξ_x and ξ_y are the higher-order functions that will be determined using the imposed boundary conditions, and τ is the time variable. Eq. (4.1) yields the minimum number of variables necessary to describe the field for a simple laminated composite. Thus, the following assumptions are necessary to continue the kinematic description for the structure in Fig. 4.1:

Assumption (4.1)

- i. In-plane deformation of the actuator layers vary linearly through-the-thickness,
- ii. In-plane deformation of the outer structural layers, $i = 1$ and N , vary linearly through-the-thickness, and their rotation is independent of the equivalent core,
- iii. In-plane deformation of the inner structural layers, $i = 3$ through $N-2$, vary linearly through-the-thickness, however, their rotations are identical,
- iv. Rotatory inertia in the structural layers is considered to be negligible,
- v. Transverse displacement for the structure is independent of the z -coordinate,
- vi. In-plane stiffnesses in the actuator layers will not contribute to the in-plane stiffness.

The application of this displacement field requires that the actual multi-layered configuration in Fig. 4.1 be simplified according to *Assumption (4.1)*. To accomplish this, we represent the inner structural layers, i.e., between $i=1$ and N , by a lumped configuration that resembles the

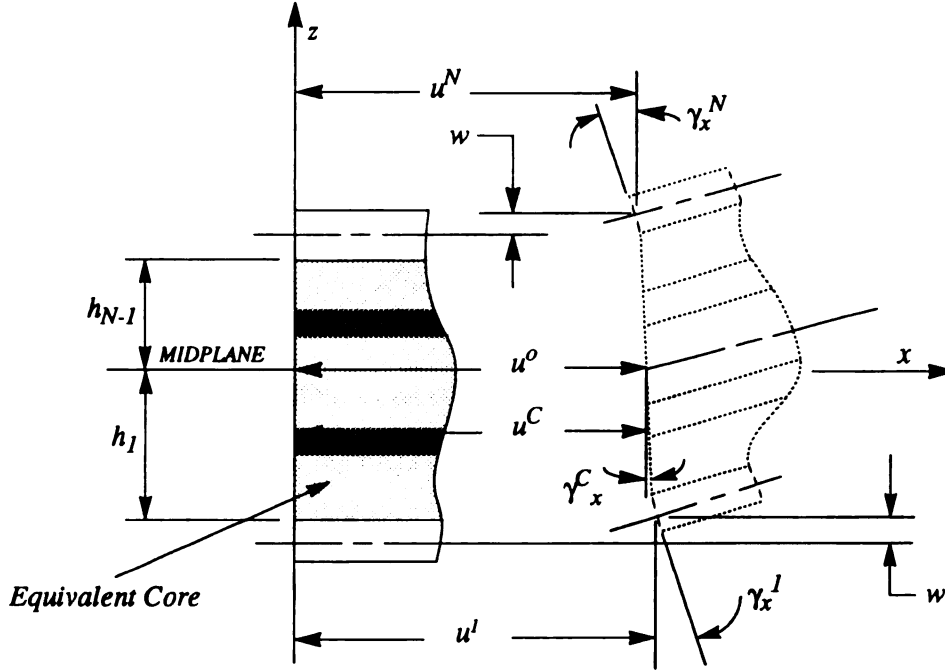


Figure 4.2 - Cross-section in the x - z plane of the displacement pattern for the structure.

three-layered classical sandwich structure used in constrained layer theory.¹⁶ The simplified configuration is illustrated in Fig. 4.2. Since the thickness of the inner structural layers is assumed to be much smaller in magnitude than the actuator layers, it is possible to describe the rotation of the inner structure by a single equivalent rotation. This simplification eliminates the need to represent each inner i th layer by an independent rotation, thus reducing the total number of rotations in the model to three. In addition, the equivalent core permits the evaluation of the necessary transverse stresses through-the-thickness of the structure, without imposing severe discontinuities in the analytical model. This is important because the inner structural layer's contribution to the overall structure's stiffness in shear is much greater than their contribution in bending.

Equation (4.1) can be modified for the structure in Fig. 4.2 and written as:

$$\begin{aligned}
 u^I &= u^o + h_1 (\gamma_x^I - \gamma_x^C) + z\gamma_x^I + z^2\zeta_x^I + z^3\xi_x^I \\
 u^C &= u^o + z\gamma_x^C + z^2\zeta_x^C + z^3\xi_x^C \\
 u^N &= u^o + h_{N-1} (\gamma_x^C - \gamma_x^N) + z\gamma_x^N + z^2\zeta_x^N + z^3\xi_x^N
 \end{aligned} \tag{4.2a}$$

$$\begin{aligned}
v^1 &= v^o + h_1 (\gamma_y^1 - \gamma_y^C) + z\gamma_y^1 + z^2\zeta_y^1 + z^3\xi_y^1 \\
v^C &= v^o + z\gamma_y^C + z^2\zeta_y^C + z^3\xi_y^C \\
v^N &= v^o + h_{N-1} (\gamma_y^C - \gamma_y^N) + z\gamma_y^N + z^2\zeta_y^N + z^3\xi_y^N \\
w^1 &= w^C = w^N = w
\end{aligned} \tag{4.2b}$$

$$w^1 = w^C = w^N = w \tag{4.2c}$$

where γ_x^C and γ_y^C define the rotations of all core normals to the midplane about the y and x axes, respectively, and the superscript C represents all quantities relating to the equivalent core. The displacement field can be further simplified by applying the appropriate boundary conditions to each of the layers. The boundary conditions imply that the transverse shear stresses must be continuous through-the thickness and vanish on the surfaces of the structure, also the displacements must be continuous across the interfaces. If we make the assumption that the structural layers are orthotropic sheets in plane stress, and impose the following boundary conditions,

$$\begin{aligned}
\sigma_{xz}^i(x, y, \pm \frac{H}{2}) &= \sigma_{yz}^i(x, y, \pm \frac{H}{2}) = 0 & i = 1, N \\
\sigma_{xz}^1(x, y, h_1) &= \sigma_{xz}^C(x, y, h_1) & \sigma_{xz}^1(x, y, h_{N-1}) &= \sigma_{xz}^C(x, y, h_{N-1}) \\
\sigma_{yz}^C(x, y, h_1) &= \sigma_{yz}^N(x, y, h_1) & \sigma_{yz}^C(x, y, h_{N-1}) &= \sigma_{yz}^N(x, y, h_{N-1}) \\
u^1(x, y, h_1) &= u^C(x, y, h_1) & u^C(x, y, h_{N-1}) &= u^N(x, y, h_{N-1}) \\
v^1(x, y, h_1) &= v^C(x, y, h_1) & v^C(x, y, h_{N-1}) &= v^N(x, y, h_{N-1})
\end{aligned} \tag{4.3}$$

we can form a set of twelve equations with twelve unknowns. The solutions for the twelve higher-order functions in Eq. (4.2) are given as

$$\begin{aligned}
\zeta_j^1 &= \frac{5h_{N-1}(\gamma_j^1 - \gamma_j^N)}{3H(2h_{N-1} + H)} + \frac{h_{N-1}(\gamma_j^1 - \gamma_j^C)}{15h_1(2h_{N-1} + H)} + \frac{Hh_{N-1}(\gamma_j^C - \gamma_j^1)}{4h_1^2(2h_{N-1} + H)} \\
&\quad - \frac{5h_1^2(\gamma_j^N - \gamma_j^C) + 3H(\gamma_j^1 - \gamma_j^C)}{15h_1^2(2h_{N-1} + H)} + \frac{H(\gamma_j^C - \gamma_j^1)}{4h_{N-1}(2h_{N-1} + H)}
\end{aligned} \tag{4.4a}$$

$$\xi_j^1 = \frac{4(\gamma_j^C - \gamma_j^N)(5\gamma_j^N + \gamma_j^1)}{27H^2(2h_{N-1} + H)^2} - \frac{60h_1^2 \frac{\partial w}{\partial j}}{45H^2 h_1^2} - \frac{h_{N-1}^2(4Hh_1(\gamma_j^C - \gamma_j^1) + 15H^2(\gamma_j^1 - \gamma_j^C))}{45H^2 h_1^2 h_{N-1}(2h_{N-1} + H)} - \frac{20Hh_1^2(\gamma_j^N - \gamma_j^C + 3\gamma_j^1) + 12H^2 h_1(\gamma_j^C - \gamma_j^1)}{45H^2 h_1^2(2h_{N-1} + H)} \quad (4.4b)$$

$$\zeta_j^C = \frac{h_{N-1}^2(-20h_1^2(\gamma_j^N + \gamma_j^1) + 4Hh_1(\gamma_j^C - \gamma_j^1) + 3H^2(\gamma_j^C - \gamma_j^1))}{12H^2 h_1^2 h_{N-1}(2h_{N-1} + H)} + \frac{-4h_{N-1}(5\gamma_j^N + \gamma_j^C) + 3H(\gamma_j^N - \gamma_j^C)}{12Hh_{N-1}(2h_{N-1} + H)} \quad (4.4c)$$

$$\xi_j^C = \frac{(60(2h_{N-1}^2 + Hh_{N-1})\frac{\partial w}{\partial j} + 20h_{N-1}^2(5\gamma_j^N + \gamma_j^1))(\gamma_j^C - \gamma_j^N)}{135H^2 h_{N-1}(2h_{N-1} + H)^2} - \frac{h_{N-1}^2(4Hh_1(\gamma_j^C - \gamma_j^1) + 3H^2(\gamma_j^1 - \gamma_j^C))}{45H^2 h_1^2 h_{N-1}(2h_{N-1} + H)} - \frac{20h_1^2(\gamma_j^N - \gamma_j^C + 3\gamma_j^1) + 12Hh_1(\gamma_j^C - \gamma_j^1) + 9H^2(\gamma_j^C - \gamma_j^1)}{45Hh_1^2(2h_{N-1} + H)} \quad (4.4d)$$

$$\zeta_j^N = \frac{h_{N-1}(20h_1^2(\gamma_j^1 - \gamma_j^N) + 4Hh_1(\gamma_j^C - \gamma_j^1) + 3H^2(\gamma_j^C - \gamma_j^1))}{60H^2 h_1^2(2h_{N-1} + H)} + \frac{20h_{N-1}(5\gamma_j^N - \gamma_j^C) + 15H(\gamma_j^N - \gamma_j^C)}{60Hh_{N-1}(2h_{N-1} + H)} \quad (4.4e)$$

$$\xi_j^C = -\frac{(20h_{N-1}(5\gamma_j^N - \gamma_j^1) - 60h_{N-1}\frac{\partial w}{\partial j})(\gamma_j^C - \gamma_j^N)}{135H^2h_{N-1}(2h_{N-1} + H)^2}$$

$$- \frac{h_{N-1}^2(4Hh_1(\gamma_j^C - \gamma_j^1) + 3H^2(\gamma_j^1 - \gamma_j^C))}{45H^2h_1^2h_{N-1}(2h_{N-1} + H)} - \frac{80h_1^2(\gamma_j^N - \gamma_j^C + 3\gamma_j^1) + 15Hh_1(\gamma_j^C - \gamma_j^1)}{45Hh_1^2(2h_{N-1} + H)}$$
(4.4f)

where,

$$j = x, y$$

Accordingly, by substituting Eq. (4.4) into Eq. (4.3), the strains can be evaluated for the above displacement field and expressed as:

$$\begin{aligned}\epsilon_j^1 &= e_j^1 + z\kappa_j^1 + z^2\lambda_j^1 + z^3\mu_j^1 \\ \epsilon_j^C &= e_j^C + z\kappa_j^C + z^2\lambda_j^C + z^3\mu_j^C \\ \epsilon_j^N &= e_j^N + z\kappa_j^N + z^2\lambda_j^N + z^3\mu_j^N\end{aligned}\quad j = x, y, xy \quad (4.5a)$$

and

$$\begin{aligned}\epsilon_{jz}^1 &= e_{jz}^1 + z\kappa_{jz}^1 + z^2\lambda_{jz}^1 \\ \epsilon_{jz}^C &= e_{jz}^C + z\kappa_{jz}^C + z^2\lambda_{jz}^C \\ \epsilon_{jz}^N &= e_{jz}^N + z\kappa_{jz}^N + z^2\lambda_{jz}^N\end{aligned}\quad j = x, y \quad (4.5b)$$

$$\epsilon_z^1 = \epsilon_z^C = \epsilon_z^N = 0 \quad (4.5c)$$

where,

$$\begin{aligned}e_j^1 &= \epsilon_j^o + h_1(\kappa_j^1 - \kappa_j^C) & e_{lz}^1 &= \gamma_l^1 + \frac{\partial w}{\partial l} \\ e_j^C &= \epsilon_j^o & e_{lz}^C &= \gamma_l^C + \frac{\partial w}{\partial l} \\ e_j^N &= \epsilon_j^o + h_{N-1}(\kappa_j^C - \kappa_j^N) & e_{lz}^N &= \gamma_l^N + \frac{\partial w}{\partial l}\end{aligned}$$

$$j = x, y, xy \quad l = x, y \quad (4.5d)$$

and the midplane strains are defined as,

$$\epsilon_x^o = \frac{\partial u^o}{\partial x} \quad \epsilon_y^o = \frac{\partial v^o}{\partial y} \quad \epsilon_{xy}^o = \frac{\partial u^o}{\partial y} + \frac{\partial v^o}{\partial x} \quad (4.5e)$$

the curvatures for the structure are,

$$\begin{aligned} \kappa_x^i &= \frac{\partial \gamma_x^i}{\partial x} & \kappa_y^i &= \frac{\partial \gamma_y^i}{\partial y} & \kappa_{xy}^i &= \frac{\partial \gamma_x^i}{\partial y} + \frac{\partial \gamma_y^i}{\partial x} \\ \kappa_{xz}^i &= 2\zeta_x^i & \kappa_{yz}^i &= 2\zeta_y^i \end{aligned} \quad i = l, C, N \quad (4.5f)$$

and the higher-order terms,

$$\begin{aligned} \lambda_x^i &= \frac{\partial \zeta_x^i}{\partial x} & \lambda_y^i &= \frac{\partial \zeta_y^i}{\partial y} & \lambda_{xy}^i &= \frac{\partial \zeta_x^i}{\partial y} + \frac{\partial \zeta_y^i}{\partial x} & \lambda_{xz}^i &= 3\zeta_x^i & \lambda_{yz}^i &= 3\zeta_y^i \\ \mu_x^i &= \frac{\partial \xi_x^i}{\partial x} & \mu_y^i &= \frac{\partial \xi_y^i}{\partial y} & \mu_{xy}^i &= \frac{\partial \xi_x^i}{\partial y} + \frac{\partial \xi_y^i}{\partial x} \end{aligned} \quad (4.5g)$$

$i = l, C, N$

To find the rate of traverse shear of deformation in the core we differentiate Eq. (4.5b) with respect to the time variable to give

$$\dot{\epsilon}_{xz}^C = \frac{d\epsilon_{xz}^C}{d\tau} = \frac{d\gamma_x^C}{d\tau} + \frac{\partial \dot{w}}{\partial x} + 2z \frac{d\zeta_x^C}{d\tau} + 3z^2 \frac{d\xi_x^C}{d\tau} \quad (4.6)$$

$$\dot{\epsilon}_{yz}^C = \frac{d\epsilon_{yz}^C}{d\tau} = \frac{d\gamma_y^C}{d\tau} + \frac{\partial \dot{w}}{\partial y} + 2z \frac{d\zeta_y^C}{d\tau} + 3z^2 \frac{d\xi_y^C}{d\tau} \quad (4.7)$$

where the dotted quantities, such as (\dot{u}) , denote with respect to time and the higher-order terms become

$$\frac{d\zeta_x^C}{d\tau} = \frac{h_{N-1}^2 (4Hh_1 + 3H^2) \frac{d\gamma_x^C}{d\tau} + 4Hh_1^2 h_{N-1} \frac{d\gamma_x^C}{d\tau} - 3h_1^2 H^2 \frac{d\gamma_x^C}{d\tau}}{12Hh_1^2 (Hh_{N-1} + 2h_{N-1}^2)} \quad (4.6a)$$

$$\begin{aligned} \frac{d\xi_x^C}{d\tau} = & -\frac{4(2h_{N-1}^2 + Hh_{N-1})\frac{d\dot{w}}{dx}}{3H(Hh_{N-1} + 2h_{N-1}^2)} - \frac{h_{N-1}^2(4Hh_1 + 3H^2)\frac{d\gamma_x^C}{d\tau}}{45Hh_1^2(Hh_{N-1} + 2h_{N-1}^2)} + \\ & \frac{h_{N-1}(20Hh_1^2 - 12H^2h_1 - 9H^3)\frac{d\gamma_x^C}{d\tau} - 15\frac{d\gamma_x^C}{d\tau}H^2h_1^2}{45Hh_1^2(Hh_{N-1} + 2h_{N-1}^2)} \end{aligned} \quad (4.6b)$$

and

$$\frac{d\xi_y^C}{d\tau} = \left(\frac{(h_{N-1}^2(4Hh_1 + 3H^2) + 4Hh_1^2h_{N-1} - 3h_1^2H^2)}{12Hh_1^2(Hh_{N-1} + 2h_{N-1}^2)} \right) \frac{d\gamma_y^C}{d\tau} \quad (4.7a)$$

$$\begin{aligned} \frac{d\xi_y^C}{d\tau} = & -\frac{4(2h_{N-1}^2 + Hh_{N-1})\frac{d\dot{w}}{dy}}{3H(Hh_{N-1} + 2h_{N-1}^2)} - \frac{h_{N-1}^2(4Hh_1 + 3H^2)\frac{d\gamma_y^C}{d\tau}}{45Hh_1^2(Hh_{N-1} + 2h_{N-1}^2)} \\ & + \left(\frac{h_{N-1}(20Hh_1^2 - 12H^2h_1 - 9H^3) - 15H^2h_1^2}{45Hh_1^2(Hh_{N-1} + 2h_{N-1}^2)} \right) \frac{d\gamma_y^C}{d\tau} \end{aligned} \quad (4.7b)$$

Now differentiating Eq. (4.3) with respect to time yields the velocities for the i th structural layer

$$\begin{aligned} \dot{u}^1 &= \frac{du^o}{d\tau} - h_1 \frac{d\gamma_x^C}{d\tau} & \dot{v}^1 &= \frac{dv^o}{d\tau} - h_1 \frac{d\gamma_y^C}{d\tau} \\ \dot{u}^C &= \frac{du^o}{d\tau} + z \frac{d\gamma_x^C}{d\tau} + z^2 \frac{d\xi_x^C}{d\tau} + z^3 \frac{d\xi_x^C}{d\tau} & \dot{v}^C &= \frac{dv^o}{d\tau} + z \frac{d\gamma_y^C}{d\tau} + z^2 \frac{d\xi_y^C}{d\tau} + z^3 \frac{d\xi_y^C}{d\tau} \\ \dot{u}^N &= \frac{du^o}{d\tau} + h_{N-1} \frac{d\gamma_x^C}{d\tau} & \dot{v}^N &= \frac{dv^o}{d\tau} + h_{N-1} \frac{d\gamma_y^C}{d\tau} \\ \dot{w} &= \frac{dw}{d\tau} \end{aligned} \quad (4.8)$$

where the time derivatives of the structural layer rotations and their higher-order terms in Eq. (4.2) can be neglected based on *Assumption (4.1.iv)*.

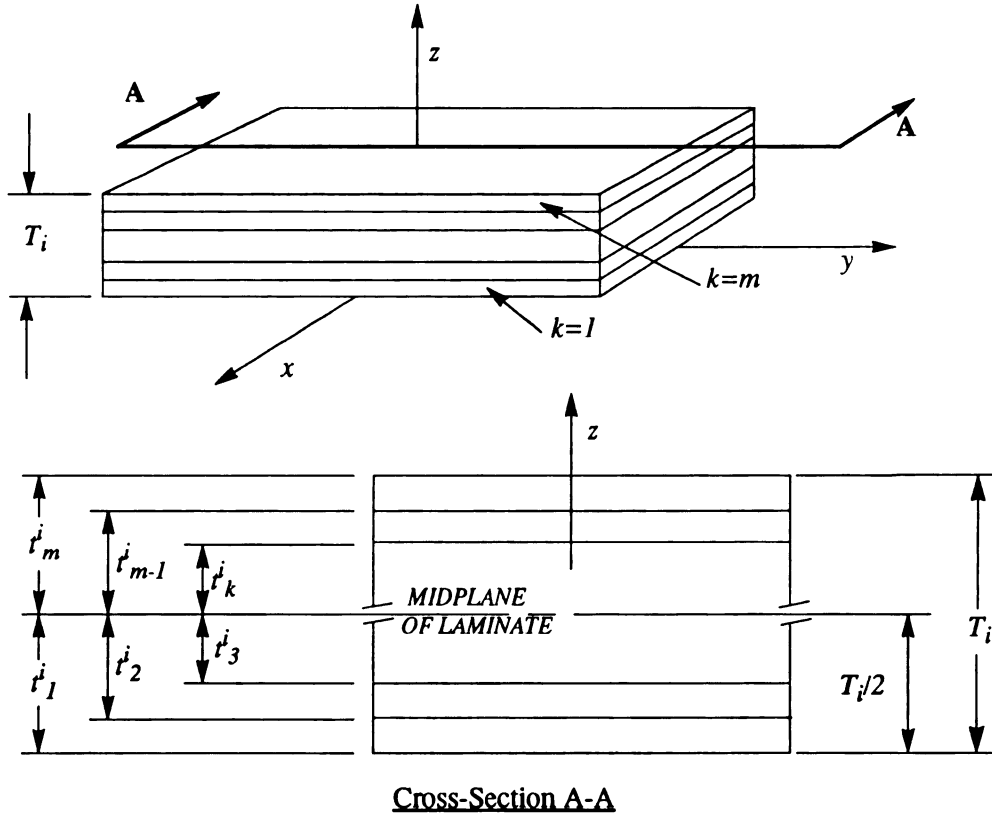


Figure 4.3 -A single structural layer fabricated as a composite laminate.

4.2 Constitutive Equations

The constitutive relationship sought for this structure is derived to accommodate layers of isotropic, orthotropic laminated unidirectional, laminated quasi-isotropic, or viscoelastic composite materials. The assumptions made pertaining to the material model are listed below.

Assumption (4.2)

- i. The material model for the structural layers are symmetric composite laminates constructed from homogeneous and orthotropic lamina,
- ii. For a viscoelastic structural material the moduli are modeled to follow linear viscoelasticity and can be treated using the linear complex modulus approach.

Let us consider a single structural layer of thickness T_i fabricated as a symmetric laminated composite comprised of m stacked and rigidly bonded laminae, as shown in Fig. 4.3. Here, a lamina is an orthotropic sheet in plane stress. In Fig. 4.3, we see that each k th lamina is located at a

vertical distance t_k^i from its midplane surface. Now consider a material coordinate system for a lamina, with the principle axes 1, 2 and 3. The principle material axes for a lamina are oriented such that the 1 axis is parallel to the fiber direction, the 2 axis is transverse to the fiber direction in the surface of the lamina, and the 3 axis is normal to the lamina surface. Under *Assumption (4.2.i)*, each lamina possesses a plane of elastic symmetry parallel to the 1-2 plane, so that the constitutive equations for the k th lamina, of the i th structural layer, can be written as:

$$\begin{bmatrix} \sigma_1^{(k)} \\ \sigma_2^{(k)} \\ \sigma_{12}^{(k)} \end{bmatrix}^{(i)} = \begin{bmatrix} \bar{Q}_{11}^{(k)} & \bar{Q}_{12}^{(k)} & 0 \\ \bar{Q}_{12}^{(k)} & \bar{Q}_{22}^{(k)} & 0 \\ 0 & 0 & \bar{Q}_{66}^{(k)} \end{bmatrix}_{(k)}^{(i)} \begin{bmatrix} \epsilon_1^{(k)} \\ \epsilon_2^{(k)} \\ \epsilon_{12}^{(k)} \end{bmatrix}^{(i)}$$

$$\begin{bmatrix} \sigma_{13}^{(k)} \\ \sigma_{23}^{(k)} \end{bmatrix}^{(i)} = \begin{bmatrix} \bar{Q}_{44}^{(k)} & 0 \\ 0 & \bar{Q}_{55}^{(k)} \end{bmatrix}_{(k)}^{(i)} \begin{bmatrix} \epsilon_{13}^{(k)} \\ \epsilon_{23}^{(k)} \end{bmatrix}^{(i)} \quad (4.9)$$

where $\bar{Q}_{ij}^{(k)}$ are the k th plane stress reduced elastic constants in the material axes of the k th lamina, and the overbar signifies that the quantities are referenced to the material axes of that lamina. In addition, σ_1 is the normal stress in the fiber direction, σ_2 is the normal stress perpendicular to the fiber direction, and σ_{12} , σ_{13} and σ_{23} represent the shear stresses in their respective planes. Similarly, the ϵ_{ij} denote the strains in their respective directions. The correspondence between the reduced elastic constants and the usual engineering constants is:

$$\begin{aligned} \bar{Q}_{11} &= \frac{E_1}{1 - \nu_{12}\nu_{21}} \\ \bar{Q}_{12} &= \frac{E_2\nu_{12}}{1 - \nu_{12}\nu_{21}} = \frac{E_1\nu_{21}}{1 - \nu_{12}\nu_{21}} \\ \bar{Q}_{22} &= \frac{E_2}{1 - \nu_{12}\nu_{21}} \end{aligned} \quad (4.10a)$$

$$\begin{aligned}
\bar{Q}_{44} &= G_{13} \\
\bar{Q}_{55} &= G_{23} \\
\bar{Q}_{66} &= G_{12}
\end{aligned} \tag{4.10b}$$

In Eq. (4.10), E_1 and E_2 represent the Young's modulus in directions 1 and 2, G_{12} , G_{23} , and G_{13} are the shear moduli for the lamina, and ν_{21} and ν_{12} denote the Poisson ratio when the lamina is strained in either the 1 or 2 directions, respectively.

If the (x,y,z) system denotes the standard basis directions for the i th structural layer, then, to construct each lamina's contribution to the stiffness, the k th lamina must be rotated to this system. With arbitrary fiber orientation, the variation of the k th reduced stiffness matrix can be obtained by transforming the generally orthotropic $[\bar{Q}]_k$ to the specifically orthotropic reduced stiffness matrix $[Q]_k$. This transformation relates the mechanical properties of the k th lamina in the material system to the geometrical (x,y,z) system through a simple rotation θ that is positive counter-clockwise. The stress-strain relation in Eq. (4.9) is transformed using the equation

$$\begin{aligned}
\begin{bmatrix} \sigma_x^{(k)} \\ \sigma_y^{(k)} \\ \sigma_{xy}^{(k)} \end{bmatrix}^{(i)} &= [S]^{-1} [\bar{Q}]_{(k)}^{(i)} [S] \begin{bmatrix} \epsilon_x^{(k)} \\ \epsilon_y^{(k)} \\ \epsilon_{xy}^{(k)} \end{bmatrix}^{(i)} = [Q]_{(k)}^{(i)} \begin{bmatrix} \epsilon_x^{(k)} \\ \epsilon_y^{(k)} \\ \epsilon_{xy}^{(k)} \end{bmatrix}^{(i)} \\
\begin{bmatrix} \sigma_{xz}^{(k)} \\ \sigma_{yz}^{(k)} \end{bmatrix}^{(i)} &= [\hat{S}]^{-1} [\bar{Q}]_{(k)}^{(i)} [\hat{S}] \begin{bmatrix} \epsilon_{xz}^{(k)} \\ \epsilon_{yz}^{(k)} \end{bmatrix}^{(i)} = [Q]_{(k)}^{(i)} \begin{bmatrix} \epsilon_{xz}^{(k)} \\ \epsilon_{yz}^{(k)} \end{bmatrix}^{(i)}
\end{aligned} \tag{4.11}$$

where $[S]$ and $[\hat{S}]$ are the transformation matrices given by,

$$[S] = \begin{bmatrix} c^2 & s^2 & cs \\ s^2 & c^2 & -cs \\ -2cs & 2cs & (c^2 - s^2) \end{bmatrix} \tag{4.12a}$$

$$[\hat{S}] = \begin{bmatrix} c & -s \\ s & c \end{bmatrix} \quad (4.12b)$$

and

$$\begin{aligned} c &= \cos(\theta) \\ s &= \sin(\theta) \end{aligned} \quad (4.12c)$$

To arrive at the constitutive relations for the structure, we must define the section force and moment resultants per unit length in the geometric basis directions. Referring back to *Assumption (4.1)* and Fig. 4.1, and employing the fundamental relationships for these quantities from classical plate theory,^{32, 68} we can write for the first-order stress resultants,

$$(N_x, N_y, N_{xy}) = \int_{-H/2}^{H/2} (\sigma_x, \sigma_y, \sigma_{xy}) dz \quad (4.13)$$

$$(M_x, M_y, M_{xy}) = \int_{-H/2}^{H/2} (\sigma_x, \sigma_y, \sigma_{xy}) z dz \quad (4.14)$$

$$(Q_x, Q_y) = \int_{-H/2}^{H/2} (\sigma_{xz}, \sigma_{yz}) dz \quad (4.15)$$

and write for the following higher-order terms,

$$(P_x, P_y, P_{xy}) = \int_{-H/2}^{H/2} (\sigma_x, \sigma_y, \sigma_{xy}) z^2 dz \quad (4.16)$$

$$(Y_x, Y_y, Y_{xy}) = \int_{-H/2}^{H/2} (\sigma_x, \sigma_y, \sigma_{xy}) z^3 dz \quad (4.17)$$

and,

$$R_x = \int_{-H/2}^{H/2} \sigma_{xz} z dz \quad (4.18)$$

$$R_y = \int_{-H/2}^{H/2} \sigma_{yz} z dz \quad (4.19)$$

$$S_x = \int_{-H/2}^{H/2} \sigma_{xz} z^2 dz \quad (4.20)$$

$$S_y = \int_{-H/2}^{H/2} \sigma_{yz} z^2 dz \quad (4.21)$$

where N_x, N_y, N_{xy} are the stress resultants, M_x, M_y, M_{xy} are the moment resultants, Q_x, Q_y are the section shear stress resultants, and P_j, Y_j, R_j and S_j signify the appropriate higher-order contributions to these terms.

In Eq. (4.13), Eq. (4.14) and Eq. (4.15) we see that the inplane stress resultants are found by integrating over the structural layers only, therefore, when Eqs (4.13-4.17) are integrated over the domain depicted in Fig. 4.2 we have

$$(N_x, N_y, N_{xy}) = \int_{h_0}^{h_1} (\sigma_x^1, \sigma_y^1, \sigma_{xy}^1) dz + \sum_{i=3}^{N-3} \int_{h_{2i}}^{h_{2i+1}} (\sigma_x^C, \sigma_y^C, \sigma_{xy}^C) dz + \int_{h_{N-1}}^{h_N} (\sigma_x^N, \sigma_y^N, \sigma_{xy}^N) dz \quad (4.22)$$

$$(M_x, M_y, M_{xy}) = \int_{h_0}^{h_1} (\sigma_x^1, \sigma_y^1, \sigma_{xy}^1) z dz + \sum_{i=3}^{N-3} \int_{h_{2i}}^{h_{2i+1}} (\sigma_x^C, \sigma_y^C, \sigma_{xy}^C) z dz + \int_{h_{N-1}}^{h_N} (\sigma_x^N, \sigma_y^N, \sigma_{xy}^N) z dz \quad (4.23)$$

$$(P_x, P_y, P_{xy}) = \int_{h_0}^{h_1} (\sigma_x^1, \sigma_y^1, \sigma_{xy}^1) z^2 dz + \sum_{i=3}^{N-3} \int_{h_{2i}}^{h_{2i+1}} (\sigma_x^C, \sigma_y^C, \sigma_{xy}^C) z^2 dz + \int_{h_{N-1}}^{h_N} (\sigma_x^N, \sigma_y^N, \sigma_{xy}^N) z^2 dz \quad (4.24)$$

$$(Y_x, Y_y, Y_{xy}) = \int_{h_0}^{h_1} (\sigma_x^1, \sigma_y^1, \sigma_{xy}^1) z^3 dz + \sum_{i=3}^{N-3} \int_{h_{2i}}^{h_{2i+1}} (\sigma_x^C, \sigma_y^C, \sigma_{xy}^C) z^3 dz + \int_{h_{N-1}}^{h_N} (\sigma_x^N, \sigma_y^N, \sigma_{xy}^N) z^3 dz \quad (4.25)$$

Now if we substitute the total inplane strains in Eq. (4.5) into the constitutive equation in (4.11), and then substitute the resulting inplane stresses from Eq. (4.11) into the resultants in equations (4.22-4.25) we obtain the following relationship for the i th structural layer

$$\begin{bmatrix} \{N_x, N_y, N_{xy}\}^T \\ \{M_x, M_y, M_{xy}\}^T \\ \{P_x, P_y, P_{xy}\}^T \\ \{Y_x, Y_y, Y_{xy}\}^T \end{bmatrix}^{(i)} = \begin{bmatrix} A & B & D & E \\ & D & E & F \\ & & F & J \\ \text{symm} & & & K \end{bmatrix}^{(i)} \begin{bmatrix} \{e_x, e_y, e_{xy}\}^T \\ \{\kappa_x, \kappa_y, \kappa_{xy}\}^T \\ \{\lambda_x, \lambda_y, \lambda_{xy}\}^T \\ \{\mu_x, \mu_y, \mu_{xy}\}^T \end{bmatrix}^{(i)} \quad (4.26)$$

where

$$i = I, C, N$$

and $A_{ln}^{(i)}$, $B_{ln}^{(i)}$, $D_{ln}^{(i)}$, etc. are the structure's stiffnesses for the i th structural layer. The relation in Eq. (4.26) consists of two twelve element vectors and a twelve-by-twelve symmetric matrix. The matrix is defined by the following expressions:

$$(A_{ln}^1, B_{ln}^1, D_{ln}^1, E_{ln}^1, F_{ln}^1, J_{ln}^1, K_{ln}^1) = \sum_{k=1}^m \int_{t_{k-1}^1}^{t_k^1} [Q_{ln}]_{(k)}^{(1)} (1, z, z^2, z^3, z^4, z^5, z^6) dz \quad (4.27)$$

$$(A_{ln}^C, B_{ln}^C, D_{ln}^C, E_{ln}^C, F_{ln}^C, J_{ln}^C, K_{ln}^C) = \sum_{i=1}^{\frac{N-3}{2}} \sum_{k=1}^m \int_{t_{k-1}^i}^{t_k^i} [Q_{ln}]_{(k)}^{(2i+1)} (1, z, z^2, z^3, z^4, z^5, z^6) dz \quad (4.28)$$

$$(A_{ln}^N, B_{ln}^N, D_{ln}^N, E_{ln}^N, F_{ln}^N, J_{ln}^N, K_{ln}^N) = \sum_{k=1}^m \int_{t_{k-1}^N}^{t_k^N} [Q_{ln}]_{(k)}^{(N)} (1, z, z^2, z^3, z^4, z^5, z^6) dz \quad (4.29)$$

$$l, n = I, 2, 6$$

To obtain the constitutive relations for the transverse portion of the structure we rewrite Eq.

(4.15) and Eqs. (4.18-4.20) as follows

$$(Q_x, Q_y) = \sum_{i=1}^{N+1} \int_{h_{2i-2}}^{h_{2i-1}} (\sigma_{xz}^{2i-1}, \sigma_{yz}^{2i-1}) dz + \sum_{j=1}^{N-1} \int_{h_{2j-1}}^{h_{2j}} (\sigma_{xz}^{2j}, \sigma_{yz}^{2j}) dz \quad (4.30)$$

$$(R_x, R_y) = \sum_{i=1}^{N+1} \int_{h_{2i-2}}^{h_{2i-1}} (\sigma_{xz}^{2i-1}, \sigma_{yz}^{2i-1}) z dz + \sum_{j=1}^{N-1} \int_{h_{2j-1}}^{h_{2j}} (\sigma_{xz}^{2j}, \sigma_{yz}^{2j}) z dz \quad (4.31)$$

$$(S_x, S_y) = \sum_{i=1}^{N+1} \int_{h_{2i-2}}^{h_{2i-1}} (\sigma_{xz}^{2i-1}, \sigma_{yz}^{2i-1}) z^2 dz + \sum_{j=1}^{N-1} \int_{h_{2j-1}}^{h_{2j}} (\sigma_{xz}^{2j}, \sigma_{yz}^{2j}) z^2 dz \quad (4.32)$$

Equations (4.30-4.32) are equivalent to Eq. (4.15) and Eqs (4.18-4.21), yet, they are divided into their respective actuator and structural layer components. By substituting Eq. (4.5) into the constitutive equations in (3.15) and (4.11), and, then substituting these resulting transverse stresses into equations (4.30-4.32) we establish the relations,

$$\begin{bmatrix} \{Q_x, Q_y\}^T \\ \{R_x, R_y\}^T \\ \{S_x, S_y\}^T \end{bmatrix}^{(i)} = \begin{bmatrix} A & B & D \\ & D & E \\ \text{symm} & & F \end{bmatrix}^{(i)} \begin{bmatrix} \{e_{xz}, e_{yz}\}^T \\ \{\kappa_{xz}, \kappa_{yz}\}^T \\ \{\lambda_{xz}, \lambda_{yz}\}^T \end{bmatrix}^{(i)} \quad i = 1, N \quad (4.33)$$

and for the core

$$\begin{bmatrix} \{Q\} \\ \{R\} \\ \{S\} \end{bmatrix}^{(C)} = \begin{bmatrix} A & B & D \\ & D & E \\ \text{symm} & & F \end{bmatrix}^{(CS)} \begin{bmatrix} \{e\} \\ \{\kappa\} \\ \{\lambda\} \end{bmatrix}^{(C)} + \begin{bmatrix} \{(h_2 - h_1)f^{(2)} + (h_4 - h_3)f^{(4)} + \dots\} \\ \left\{\frac{(h_2^2 - h_1^2)f^{(2)}}{2} + \frac{(h_4^2 - h_3^2)f^{(4)}}{2} + \dots\right\} \\ \left\{\frac{(h_2^3 - h_1^3)f^{(2)}}{3} + \frac{(h_4^3 - h_3^3)f^{(4)}}{3} + \dots\right\} \end{bmatrix} \quad (4.34)$$

where the superscript CS refers to the structural layers, and f is used to represent the function

$$f^{(i)} = f(\epsilon^C, \dot{\epsilon}^C, \omega, V), \quad i = 2, 4, 6, \dots \quad (4.35)$$

which is a generalized description of Eq. (3.15) for the i th actuator layer in the core. Then the stiffnesses for the i th structural layers are written as

$$(A_{ln}^1, B_{ln}^1, D_{ln}^1, E_{ln}^1, F_{ln}^1) = \sum_{k=1}^m \int_{t_{k-1}^1}^{t_k^1} [Q_{ln}]_{(k)}^{(1)} (1, z, z^2, z^3, z^4) dz \quad (4.36)$$

$$(A_{ln}^{CS}, B_{ln}^{CS}, D_{ln}^{CS}, E_{ln}^{CS}, F_{ln}^{CS}) = \sum_{i=1}^{\frac{N-3}{2}} \sum_{k=1}^m \int_{t_{k-1}^{2i}}^{t_k^{2i+1}} [Q_{ln}]_{(k)}^{(2i+1)} (1, z, z^2, z^3, z^4) dz \quad (4.37)$$

$$(A_{ln}^N, B_{ln}^N, D_{ln}^N, E_{ln}^N, F_{ln}^N) = \sum_{k=1}^m \int_{t_{k-1}^N}^{t_k^N} [Q_{ln}]_{(k)}^{(N)} (1, z, z^2, z^3, z^4) dz \quad (4.38)$$

$$l, n = 4, 5$$

Since Eq. (4.35) is dependent on strain, strain rate, voltage, and frequency of oscillation the actuator layers stiffness is nonlinear and cannot be formulated in the same manner as Eq. (4.37). Thus, it will be left as a function throughout the analysis and only dealt with for special cases.

4.3 Governing Equations

Here Hamilton's principle is applied to derive the governing equations of motion for a plate and beam. Since Hamilton's principle is only applicable to conservative systems, the structure must be initially treated as a fully elastic system, hence, the derivation of the equations of motion will exclude damping. Once the energy functional is minimized for this provisional system, damping in the structure can be introduced by invoking the correspondence principle.⁵¹ The notation throughout this section will be such that the superscripts denote information pertaining to the individual layers of the plate, respectively.

The configuration of the plate is depicted in Fig. 4.4. The plate is of uniform width W , total length L , and uniform height H . Each layer is identified by the subscript i , and the thickness of an individual layer is identified by t_i . The total number of structural and actuator layers in the plate N must also be odd so that the actuator layers are constrained. A similar Cartesian coordinate system that consists of the global coordinates x , y and z is adopted for this model, where the x - y plane of this system is referenced so that $z=0$ at the midplane surface of the plate cross-section, as shown in Fig. 4.4. For this analytical model of the plate we assume that *Assumption (4.1)* and *Assumption (4.2)* holds true.

We turn toward the evaluation of the various energies involved in order to be able to express the Lagrangian function in terms of our plate variables. From Eq. (4.2), there are a total of seven displacements which are functions of three midplane deformations and six rotations.

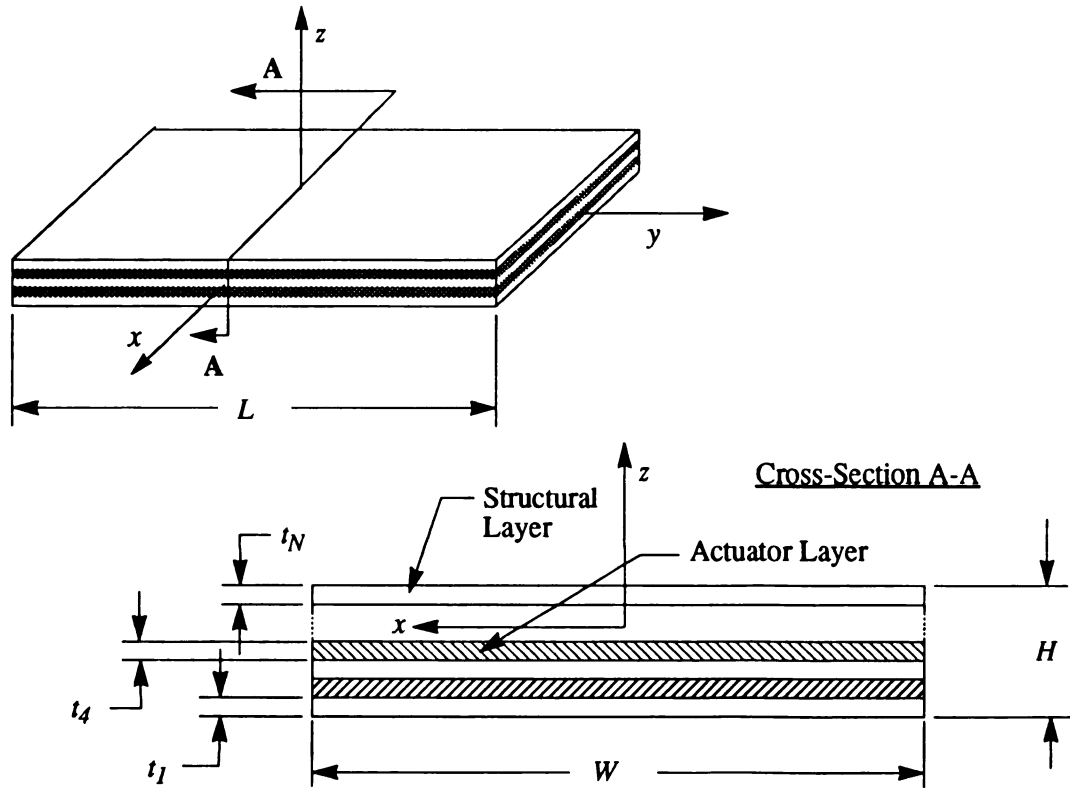


Figure 4.4 - Configuration of the distributed-parameter plate.

When we consider the kinetic energy T we have:

$$T = \frac{1}{2} \iint_R \tilde{m} \int_{-\frac{H}{2}}^{\frac{H}{2}} [(\dot{u}^I)^2 + (\dot{u}^C)^2 + (\dot{u}^N)^2 + (\dot{v}^I)^2 + (\dot{v}^C)^2 + (\dot{v}^N)^2 + w^2] dz dA \quad (4.39)$$

where \tilde{m} is the mass per unit area of the plate and is given by

$$\tilde{m}^p = \sum_{i=1}^N \rho^i (h_i - h_{i-1}) \quad (4.40)$$

Substituting Eq. (4.8) into Eq. (4.39) and integrating with respect to z we get

$$T = \frac{1}{2} \iint_R \tilde{m} H \left(3 \left((\dot{u}^o)^2 + (\dot{v}^o)^2 + \left(\frac{\dot{w}}{3} \right)^2 \right) + \left(h_1^2 + \frac{H^2}{12} + h_{N-1}^2 \right) [(\dot{\gamma}_x^C)^2 + (\dot{\gamma}_y^C)^2] \right. \\ \left. + 2(h_{N-1} - h_1) [\dot{u}^o (\dot{\gamma}_x^C)^2 + \dot{v}^o (\dot{\gamma}_y^C)^2] \right) dA \quad (4.41)$$

The elastic strain energy for the structure is given by

$$U = \frac{1}{2} \iint_R \int_{-\frac{H}{2}}^{\frac{H}{2}} \{ \sigma_x \epsilon_x + \sigma_y \epsilon_y + \sigma_z \epsilon_z + \sigma_{xy} \epsilon_{xy} + \sigma_{xz} \epsilon_{xz} + \sigma_{yz} \epsilon_{yz} \} dz dA \quad (4.42)$$

Here we see that the triple integration is performed over the volume of the structure, where dA denotes a small surface element of the structure in the x - y plane. Now, if we take into account the assumptions made in the previous section and substitute Eq. (4.11) into Eq. (4.42), we find the strain energy for the i th layer is

$$U^{(i)} = \frac{1}{2} \iint_R \left(Q_{11}^{(i)} (\epsilon_x^{(i)})^2 + Q_{22}^{(i)} (\epsilon_y^{(i)})^2 + Q_{66}^{(i)} (\epsilon_{xy}^{(i)})^2 + Q_{44}^{(i)} (\epsilon_{yz}^{(i)})^2 \right. \\ \left. + Q_{55}^{(i)} (\epsilon_{xz}^{(i)})^2 + 2Q_{12}^{(i)} \epsilon_x^{(i)} \epsilon_y^{(i)} + 2Q_{16}^{(i)} \epsilon_x^{(i)} \epsilon_{xy}^{(i)} + 2Q_{26}^{(i)} \epsilon_y^{(i)} \epsilon_{xy}^{(i)} + 2Q_{45}^{(i)} \epsilon_{yz}^{(i)} \epsilon_{xz}^{(i)} \right. \\ \left. + Q_x^{(i)} e_{xz}^{(i)} + R_x^{(i)} \kappa_{xz}^{(i)} + S_x^{(i)} \lambda_{xz}^{(i)} + Q_y^{(i)} e_{yz}^{(i)} + R_y^{(i)} \kappa_{yz}^{(i)} + S_y^{(i)} \lambda_{yz}^{(i)} \right) dz dA$$

$$i = I, C, N \quad (4.43)$$

Subsequently, when the strain-displacement relationship in (4.2) and the constitutive relationships in (3.15), (4.26), (4.33) and (4.34) are substituted into Eq. (4.43), integrated with respect to z , and then summed, the following equation can be written for the total strain energy of the plate.

$$\begin{aligned}
U = \iint_R \{ & \frac{\partial u^o}{\partial x} (N_x^1 + N_x^C + N_x^N) + \frac{\partial v^o}{\partial x} (N_y^1 + N_y^C + N_y^N) + (\frac{\partial v^o}{\partial x} + \frac{\partial u^o}{\partial y}) (N_{xy}^1 + N_{xy}^C + N_{xy}^N) + \\
& \frac{\partial \gamma_x^C}{\partial x} (N_x^N h_{N-1} - N_x^1 h_1) + \frac{\partial \gamma_y^C}{\partial y} (N_y^N h_{N-1} - N_y^1 h_1) + (\frac{\partial \gamma_x^C}{\partial y} + \frac{\partial \gamma_y^C}{\partial x}) (N_{xy}^N h_{N-1} - N_{xy}^1 h_1) + \\
& h_1 (N_x^1 \frac{\partial \gamma_x^1}{\partial x} + N_y^1 \frac{\partial \gamma_y^1}{\partial y} + N_{xy}^1 (\frac{\partial \gamma_x^1}{\partial y} + \frac{\partial \gamma_y^1}{\partial x})) - h_{N-1} (N_x^N \frac{\partial \gamma_x^N}{\partial x} + N_y^N \frac{\partial \gamma_y^N}{\partial y} + N_{xy}^N (\frac{\partial \gamma_x^N}{\partial y} + \frac{\partial \gamma_y^N}{\partial x})) + \\
& \frac{\partial w}{\partial x} (Q_x^1 + Q_x^C + Q_x^N) + \frac{\partial w}{\partial y} (Q_y^1 + Q_y^C + Q_y^N) + M_x^1 \frac{\partial \gamma_x^1}{\partial x} + M_x^C \frac{\partial \gamma_x^C}{\partial x} + M_x^N \frac{\partial \gamma_x^N}{\partial x} + M_y^1 \frac{\partial \gamma_y^1}{\partial y} + M_y^C \frac{\partial \gamma_y^C}{\partial y} + \\
& M_y^N \frac{\partial \gamma_y^N}{\partial y} + M_{xy}^1 (\frac{\partial \gamma_x^1}{\partial y} + \frac{\partial \gamma_y^1}{\partial x}) + M_{xy}^C (\frac{\partial \gamma_x^C}{\partial y} + \frac{\partial \gamma_y^C}{\partial x}) + M_{xy}^N (\frac{\partial \gamma_x^N}{\partial y} + \frac{\partial \gamma_y^N}{\partial x}) + Q_x^1 \gamma_x^1 + Q_y^1 \gamma_y^1 + \\
& Q_x^C \gamma_x^C + Q_y^C \gamma_y^C + Q_x^N \gamma_x^N + Q_y^N \gamma_y^N + P_x^1 \frac{\partial \zeta_x^1}{\partial x} + P_y^1 \frac{\partial \zeta_y^1}{\partial y} + P_{xy}^1 (\frac{\partial \zeta_x^1}{\partial x} + \frac{\partial \zeta_y^1}{\partial x}) + P_x^C \frac{\partial \zeta_x^C}{\partial x} + P_y^C \frac{\partial \zeta_y^C}{\partial y} + \\
& P_{xy}^C (\frac{\partial \zeta_x^C}{\partial x} + \frac{\partial \zeta_y^C}{\partial x}) + P_x^N \frac{\partial \zeta_x^N}{\partial x} + P_y^N \frac{\partial \zeta_y^N}{\partial y} + P_{xy}^N (\frac{\partial \zeta_x^N}{\partial x} + \frac{\partial \zeta_y^N}{\partial x}) + Y_x^1 \frac{\partial \xi_x^1}{\partial x} + Y_y^1 \frac{\partial \xi_y^1}{\partial y} + \\
& Y_{xy}^1 (\frac{\partial \xi_x^1}{\partial x} + \frac{\partial \xi_y^1}{\partial x}) + Y_x^C \frac{\partial \xi_x^C}{\partial x} + Y_y^C \frac{\partial \xi_y^C}{\partial y} + Y_{xy}^C (\frac{\partial \xi_x^C}{\partial x} + \frac{\partial \xi_y^C}{\partial x}) + Y_x^N \frac{\partial \xi_x^N}{\partial x} + Y_y^N \frac{\partial \xi_y^N}{\partial y} + Y_{xy}^N (\frac{\partial \xi_x^N}{\partial x} + \frac{\partial \xi_y^N}{\partial x}) + \\
& 2 (R_x^1 \zeta_x^1 + R_y^1 \zeta_y^1) + 2 (R_x^C \zeta_x^C + R_y^C \zeta_y^C) + 2 (R_x^N \zeta_x^N + R_y^N \zeta_y^N) + 3 (S_x^1 \xi_x^1 + S_y^1 \xi_y^1) + \\
& 3 (S_x^C \xi_x^C + S_y^C \xi_y^C) + 3 (S_x^N \xi_x^N + S_y^N \xi_y^N) \} dA
\end{aligned} \tag{4.44}$$

where the nonlinear section shear stress resultants for the core are

$$Q_x^C = Q_x^C(\epsilon^C, \dot{\epsilon}^C, \omega, V) \tag{4.44a}$$

$$R_x^C = R_x^C(\epsilon^C, \dot{\epsilon}^C, \omega, V) \tag{4.44b}$$

$$S_x^C = S_x^C(\epsilon^C, \dot{\epsilon}^C, \omega, V) \tag{4.44c}$$

Equation (4.44) is more tractable when only symmetric composite laminates are used. Hence, the terms B_{ij} , E_{ij} , and J_{ij} are identically zero. Moreover, when the plate structure is symmetric the B_{ij} , E_{ij} terms for the core layers are also zero.

The total potential energy for the plate can be formed by considering transverse and inplane loading. For transverse bending, we are concerned with loads generated by normal tractions applied to the top and bottom surface of the plate which leads to the following expression for the potential energy

$$W = - \iint_R q w dA \quad (4.45)$$

where q is equivalent to

$$q = \sigma_z^i \left(\frac{H}{2} \right) - \sigma_z^i \left(-\frac{H}{2} \right) \quad (4.46)$$

For inplane loading,

$$V = \frac{1}{2} \iint_R \left[F_x \left(\frac{\partial w}{\partial x} \right)^2 + F_y \left(\frac{\partial w}{\partial y} \right)^2 + 2F_{xy} \left(\frac{\partial w}{\partial x} \frac{\partial w}{\partial y} \right) \right] dA \quad (4.47)$$

which have been taken directly from Whitney.¹⁴⁰ In Eq. (4.47), F_x , F_y and F_{xy} denotes the initial inplane force resultants applied to the pre-buckled state.

From Hamilton's principle the governing equations of motion and the proper boundary conditions for the plate are determined by substituting (4.41), (4.44), (4.45), and (4.47) into the variational equation and integrating over an arbitrary time interval

$$\delta I = \int_{\tau_0}^{\tau_1} (\delta T - \delta U - \delta V - \delta W) d\tau = 0 \quad (4.48)$$

Integrating the expressions in Eq. (4.48) by parts, and collecting the coefficients of δu^o , δv^o , δw , $\delta \gamma_x^I$, $\delta \gamma_x^C$, $\delta \gamma_x^N$, $\delta \gamma_y^I$, $\delta \gamma_y^C$, and $\delta \gamma_y^N$, we obtain the following equilibrium equations:

$$\begin{aligned} \delta u^o: & \quad \frac{\partial}{\partial x} (N_x^I + N_x^C + N_x^N) + \frac{\partial}{\partial y} (N_{xy}^I + N_{xy}^C + N_{xy}^N) \\ & = \tilde{m}^P H \left[(h_1 - h_{N-1}) \frac{d^2 u^o}{d\tau^2} - \frac{d^2 \gamma_x^C}{d\tau^2} (h_{N-1}^2 + h_1^2 + \frac{H^2}{12}) \right] \end{aligned} \quad (4.49a)$$

$$\delta v^o: \quad \frac{\partial}{\partial x}(N_{xy}^1 + N_{xy}^C + N_{xy}^N) + \frac{\partial}{\partial y}(N_y^1 + N_y^C + N_y^N) \\ = \tilde{m}^p H \left[(h_1 - h_{N-1}) \frac{d^2 v^o}{d\tau} - \frac{d^2 \gamma_y^C}{d\tau} (h_{N-1}^2 + h_1^2 + \frac{H^2}{12}) \right] \quad (4.49b)$$

$\delta w:$

$$\left(\frac{\partial^2}{\partial x^2} (Y_x^1 + Y_x^C + Y_x^N) + \frac{\partial^2}{\partial y^2} Y_y^1 + Y_y^C + Y_y^N + 4 \frac{\partial^2}{\partial x \partial y} (Y_{xy}^1 + Y_{xy}^C + Y_{xy}^N) \right. \\ \left. - 3 \frac{\partial}{\partial x} (S_x^1 + S_x^C + S_x^N) - 3 \frac{\partial}{\partial y} (S_y^1 + S_y^C + S_y^N) \right) \left(\frac{4}{3H^2} \right) + \\ \frac{\partial}{\partial x} (Q_x^1 + Q_x^C + Q_x^N) + \frac{\partial}{\partial y} (Q_y^1 + Q_y^C + Q_y^N) + F_x \frac{\partial^2 w}{\partial x^2} + F_y \frac{\partial^2 w}{\partial y^2} + 2F_{xy} \frac{\partial^2 w}{\partial x \partial y} + q = 2H \frac{d^2 w}{d\tau^2} \quad (4.49c)$$

and the curvatures about the y axis,

$\delta \gamma_x^I:$

$$\frac{h_1^2 h_{N-1}^2 (4H - 20) \left(\frac{\partial}{\partial x} (Y_x^1 + Y_x^C + Y_x^N) + \frac{\partial}{\partial y} (Y_{xy}^1 + Y_{xy}^C + Y_{xy}^N) \right) + 9H^3 h_{N-1} \left(\frac{\partial Y_x^C}{\partial x} + \frac{\partial Y_{xy}^C}{\partial y} \right)}{90H^2 h_1^2 h_{N-1}^2 + 45H^3 h_1^2 h_{N-1}} + \\ \frac{h_{N-1} (12H^2 h_1 - 60H h_1^2) \left(\frac{\partial}{\partial x} (Y_x^1 + Y_x^C) + \frac{\partial}{\partial y} (Y_{xy}^1 + Y_{xy}^C) \right) + 3H^2 h_{N-1}^2 \frac{\partial}{\partial y} (Y_{xy}^C - 5Y_{xy}^1 + Y_{xy}^N)}{90H^2 h_1^2 h_{N-1}^2 + 45H^3 h_1^2 h_{N-1}} + \\ \frac{3H^2 h_{N-1}^2 \left(\frac{\partial}{\partial x} (Y_x^C + Y_x^N - 5Y_x^1) \right) + h_{N-1}^2 (S_x^1 + S_x^C + S_x^N) (60H h_1 - 12h_1^2)}{90H^2 h_1^2 h_{N-1}^2 + 45H^3 h_1^2 h_{N-1}} + \\ \frac{3H^2 h_{N-1}^2 (5S_x^1 - S_x^C - S_x^N) + (S_x^1 + S_x^C) (180H h_1^2 h_{N-1} - 36H^2 h_1 h_{N-1}) - 27H^3 h_{N-1} S_x^C}{90H^2 h_1^2 h_{N-1}^2 + 45H^3 h_1^2 h_{N-1}} \\ - Q_x^1 + h_1 \left(\frac{\partial N_x^1}{\partial x} + \frac{\partial N_{xy}^1}{\partial y} \right) + \frac{\partial M_x^1}{\partial x} + \frac{\partial M_{xy}^1}{\partial y} = 0 \quad (4.49d)$$

and,

$\delta\gamma_x^C$:

$$\begin{aligned}
& \frac{-h_{N-1}^2 (4Hh_1 + 3H^2) \left(\frac{\partial}{\partial x} (Y_x^1 + Y_x^C + Y_x^N) + \frac{\partial}{\partial y} (Y_{xy}^1 + Y_{xy}^C + Y_{xy}^N) \right) - 9H^3 h_{N-1} \left(\frac{\partial Y_x^C}{\partial x} + \frac{\partial Y_{xy}^C}{\partial y} \right)}{90H^2 h_1^2 h_{N-1}^2 + 45H^3 h_1^2 h_{N-1}} + \\
& \frac{h_{N-1} (15H^2 h_1 - 60Hh_1^2) \left(\frac{\partial}{\partial x} (Y_x^1 + Y_x^C) + \frac{\partial}{\partial y} (Y_{xy}^1 + Y_{xy}^C) \right) + 15H^2 h_{N-1}^2 \frac{\partial}{\partial y} (Y_{xy}^1 - Y_{xy}^C + Y_{xy}^N)}{90H^2 h_1^2 h_{N-1}^2 + 45H^3 h_1^2 h_{N-1}} + \\
& \frac{15H^2 h_1^2 \left(\frac{\partial}{\partial x} (Y_x^N - Y_x^C - Y_x^1) \right) + h_{N-1}^2 (S_x^1 + S_x^C + S_{xy}^N) (36Hh_1 - 9h_1^2)}{90H^2 h_1^2 h_{N-1}^2 + 45H^3 h_1^2 h_{N-1}} + \\
& \frac{3H^2 h_{N-1}^2 (5S_x^1 - S_x^C - S_x^N) + (S_x^1 + S_x^C) (45Hh_1^2 h_{N-1} - 60H^2 h_1 h_{N-1}) - 27H^3 h_{N-1} S_x^C}{90H^2 h_1^2 h_{N-1}^2 + 45H^3 h_1^2 h_{N-1}} + \\
& -Q_x^C + h_1 \left(\frac{\partial N_{xy}^1}{\partial y} - \frac{\partial N_x^1}{\partial x} \right) + h_{N-1} \left(\frac{\partial N_{xy}^N}{\partial y} - \frac{\partial N_x^N}{\partial x} \right) + \frac{\partial M_x^C}{\partial x} + \frac{\partial M_{xy}^C}{\partial y} = 2H (h_{N-1} - h_1) \frac{d^2 u^o}{d\tau}
\end{aligned} \tag{4.49e}$$

$\delta\gamma_x^N$:

$$\begin{aligned}
& \frac{h_1^2 h_{N-1}^2 (20H - 120) \left(\frac{\partial}{\partial x} (Y_x^1 + Y_x^C + Y_x^N) + \frac{\partial}{\partial y} (Y_{xy}^1 + Y_{xy}^C + Y_{xy}^N) \right) + 45H^3 h_{N-1} \left(\frac{\partial Y_x^C}{\partial x} + \frac{\partial Y_{xy}^C}{\partial y} \right)}{90H^2 h_1^2 h_{N-1}^2 + 45H^3 h_1^2 h_{N-1}} + \\
& \frac{h_{N-1} (4H^2 h_1 - 30Hh_1^2) \left(\frac{\partial}{\partial x} (Y_x^1 + Y_x^C) + \frac{\partial}{\partial y} (Y_{xy}^1 + Y_{xy}^C) \right) + 15H^2 h_{N-1}^2 \frac{\partial}{\partial y} (Y_{xy}^C - 5Y_{xy}^1 + Y_{xy}^N)}{90H^2 h_1^2 h_{N-1}^2 + 45H^3 h_1^2 h_{N-1}} + \\
& \frac{45H^2 h_{N-1}^2 \left(\frac{\partial}{\partial x} (Y_x^C + Y_x^N - 5Y_x^1) \right) + h_{N-1}^2 (S_x^1 + S_x^C + S_{xy}^N) (3Hh_1 - 45h_1^2)}{90H^2 h_1^2 h_{N-1}^2 + 45H^3 h_1^2 h_{N-1}} + \\
& \frac{4H^2 h_{N-1}^2 (25S_x^1 - S_x^C - S_x^N) + (S_x^1 + S_x^C) (135Hh_1^2 h_{N-1} - 72H^2 h_1 h_{N-1}) - 9H^3 h_{N-1} S_x^C}{90H^2 h_1^2 h_{N-1}^2 + 45H^3 h_1^2 h_{N-1}} \\
& -Q_x^1 + h_1 \left(\frac{\partial N_x^1}{\partial x} + \frac{\partial N_{xy}^1}{\partial y} \right) + \frac{\partial M_x^1}{\partial x} + \frac{\partial M_{xy}^1}{\partial y} = 0
\end{aligned} \tag{4.49f}$$

and the curvatures about the x axis,

$\delta\gamma_y^I$:

$$\begin{aligned}
& \frac{h_1^2 h_{N-1}^2 (4H - 20) \left(\frac{\partial}{\partial x} (Y_{xy}^1 + Y_{xy}^C + Y_{xy}^N) + \frac{\partial}{\partial y} (Y_y^1 + Y_y^C + Y_y^N) \right) + 9H^3 h_{N-1} \left(\frac{\partial Y_{xy}^C}{\partial x} + \frac{\partial Y_y^C}{\partial y} \right)}{90H^2 h_1^2 h_{N-1}^2 + 45H^3 h_1^2 h_{N-1}} + \\
& \frac{h_{N-1} (12H^2 h_1 - 60H h_1^2) \left(\frac{\partial}{\partial x} (Y_{xy}^1 + Y_{xy}^C) + \frac{\partial}{\partial y} (Y_y^1 + Y_y^C) \right) + 3H^2 h_{N-1}^2 \frac{\partial}{\partial y} (Y_y^C - 5Y_y^1 + Y_y^N)}{90H^2 h_1^2 h_{N-1}^2 + 45H^3 h_1^2 h_{N-1}} + \\
& \frac{3H^2 h_{N-1}^2 \left(\frac{\partial}{\partial x} (Y_{xy}^C + Y_{xy}^N - 5Y_{xy}^1) \right) + h_{N-1}^2 (S_y^1 + S_y^C + S_y^N) (60H h_1 - 12h_1^2)}{90H^2 h_1^2 h_{N-1}^2 + 45H^3 h_1^2 h_{N-1}} + \\
& \frac{3H^2 h_{N-1}^2 (5S_y^1 - S_y^C - S_y^N) + (S_y^1 + S_y^C) (180H h_1^2 h_{N-1} - 36H^2 h_1 h_{N-1}) - 27H^3 h_{N-1} S_y^C}{90H^2 h_1^2 h_{N-1}^2 + 45H^3 h_1^2 h_{N-1}} \\
& - Q_y^1 + h_1 \left(\frac{\partial N_{xy}^1}{\partial x} + \frac{\partial N_y^1}{\partial y} \right) + \frac{\partial M_{xy}^1}{\partial x} + \frac{\partial M_y^1}{\partial y} = 0
\end{aligned} \tag{4.49g}$$

and,

$\delta\gamma_y^C$:

$$\begin{aligned}
& \frac{-h_{N-1}^2 (4H h_1 + 3H^2) \left(\frac{\partial}{\partial x} (Y_{xy}^1 + Y_{xy}^C + Y_{xy}^N) + \frac{\partial}{\partial y} (Y_y^1 + Y_y^C + Y_y^N) \right) - 9H^3 h_{N-1} \left(\frac{\partial Y_{xy}^C}{\partial x} + \frac{\partial Y_y^C}{\partial y} \right)}{90H^2 h_1^2 h_{N-1}^2 + 45H^3 h_1^2 h_{N-1}} + \\
& \frac{h_{N-1} (15H^2 h_1 - 60H h_1^2) \left(\frac{\partial}{\partial x} (Y_{xy}^1 + Y_{xy}^C) + \frac{\partial}{\partial y} (Y_y^1 + Y_y^C) \right) + 15H^2 h_{N-1}^2 \frac{\partial}{\partial y} (Y_y^1 - Y_y^C + Y_y^N)}{90H^2 h_1^2 h_{N-1}^2 + 45H^3 h_1^2 h_{N-1}} + \\
& \frac{15H^2 h_1^2 \left(\frac{\partial}{\partial x} (Y_{xy}^N - Y_{xy}^C - Y_{xy}^1) \right) + h_{N-1}^2 (S_y^1 + S_y^C + S_y^N) (36H h_1 - 9h_1^2)}{90H^2 h_1^2 h_{N-1}^2 + 45H^3 h_1^2 h_{N-1}} + \\
& \frac{3H^2 h_{N-1}^2 (5S_y^1 - S_y^C - S_y^N) + (S_y^1 + S_y^C) (45H h_1^2 h_{N-1} - 60H^2 h_1 h_{N-1}) - 27H^3 h_{N-1} S_y^C}{90H^2 h_1^2 h_{N-1}^2 + 45H^3 h_1^2 h_{N-1}} + \\
& - Q_y^C + h_1 \left(\frac{\partial N_y^1}{\partial y} - \frac{\partial N_{xy}^1}{\partial x} \right) + h_{N-1} \left(\frac{\partial N_y^N}{\partial y} - \frac{\partial N_{xy}^N}{\partial x} \right) + \frac{\partial M_{xy}^C}{\partial x} + \frac{\partial M_y^C}{\partial y} = 2H (h_{N-1} - h_1) \frac{d^2 v^o}{d\tau}
\end{aligned}$$

(4.49h)

and finally,

$\delta\gamma_y^N$:

$$\begin{aligned}
& \frac{h_1^2 h_{N-1}^2 (20H - 120) \left(\frac{\partial}{\partial x} (Y_{xy}^1 + Y_{xy}^C + Y_{xy}^N) + \frac{\partial}{\partial y} (Y_y^1 + Y_y^C + Y_y^N) \right) + 45H^3 h_{N-1} \left(\frac{\partial Y_x^C}{\partial x} + \frac{\partial Y_y^C}{\partial y} \right)}{90H^2 h_1^2 h_{N-1}^2 + 45H^3 h_1^2 h_{N-1}} + \\
& \frac{h_{N-1} (4H^2 h_1 - 30H h_1^2) \left(\frac{\partial}{\partial x} (Y_{xy}^1 + Y_{xy}^C) + \frac{\partial}{\partial y} (Y_y^1 + Y_y^C) \right) + 15H^2 h_{N-1}^2 \frac{\partial}{\partial y} (Y_y^C - 5Y_y^1 + Y_y^N)}{90H^2 h_1^2 h_{N-1}^2 + 45H^3 h_1^2 h_{N-1}} + \\
& \frac{45H^2 h_{N-1}^2 \left(\frac{\partial}{\partial x} (Y_{xy}^C + Y_{xy}^N - 5Y_{xy}^1) \right) + h_{N-1}^2 (S_y^1 + S_y^C + S_y^N) (3H h_1 - 45h_1^2)}{90H^2 h_1^2 h_{N-1}^2 + 45H^3 h_1^2 h_{N-1}} + \\
& \frac{4H^2 h_{N-1}^2 (25S_y^1 - S_y^C - S_y^N) + (S_y^1 + S_y^C) (135H h_1^2 h_{N-1} - 72H^2 h_1 h_{N-1}) - 9H^3 h_{N-1} S_y^C}{90H^2 h_1^2 h_{N-1}^2 + 45H^3 h_1^2 h_{N-1}} \\
& - Q_y^1 + h_1 \left(\frac{\partial N_{xy}^1}{\partial x} + \frac{\partial N_y^1}{\partial y} \right) + \frac{\partial M_{xy}^1}{\partial x} + \frac{\partial M_y^1}{\partial y} = 0
\end{aligned} \tag{4.49i}$$

The boundary conditions are of the following form:

$$\begin{aligned}
& u^{(i)} n_x + v^{(i)} n_y \quad \text{or} \quad N_x^{(i)} n_x^2 + N_y^{(i)} n_y^2 + 2N_{xy}^{(i)} n_x n_y \\
& -u^{(i)} n_x + v^{(i)} n_y \quad \text{or} \quad (N_y^{(i)} - N_x^{(i)}) n_x n_y + N_{xy}^{(i)} (n_x^2 - n_y^2) \\
& w \quad \text{or} \quad (Q_x^{(i)} - R_x^{(i)}) n_x + (Q_y^{(i)} - R_y^{(i)}) n_y - \frac{4H^2 h_{N-1}^2 - 3H^2 h_1 h_{N-1}}{90H^2 h_1^2 h_{N-1}^2 + 45H^3 h_1^2 h_{N-1}} \\
& \quad \left((n_x \frac{\partial}{\partial y} - n_y \frac{\partial}{\partial x}) ((Y_y^{(i)} - Y_x^{(i)}) n_x n_y + Y_{xy}^{(i)} (n_x^2 - n_y^2)) \right) \\
& \frac{\partial w}{\partial x} n_x + \frac{\partial w}{\partial y} n_y \quad \text{or} \quad Y_x^{(i)} n_x^2 + Y_y^{(i)} n_y^2 + 2Y_{xy}^{(i)} n_x n_y \\
& \gamma_x^{(i)} n_x + \gamma_y^{(i)} n_y \quad \text{or} \quad \left(M_x - \frac{12H h_{N-1}^2 - H^2 h_1 h_{N-1}}{90H^2 h_1^2 h_{N-1}^2 + 45H^3 h_1^2 h_{N-1}} Y_x^{(i)} \right) n_x^2 \\
& \quad + \left(\left(M_y - \frac{5H h_{N-1} - 20H^2 h_1 h_{N-1}^2}{90H^2 h_1^2 h_{N-1}^2 + 45H^3 h_1^2 h_{N-1}} Y_y^{(i)} \right) n_y^2 + n_x n_y \right) \\
& \quad 2 \left(M_{xy} - \frac{H h_{N-1} - H^2 h_1^2 h_{N-1}}{90H^2 h_1^2 h_{N-1}^2 + 45H^3 h_1^2 h_{N-1}} Y_{xy}^{(i)} \right)
\end{aligned} \tag{4.50}$$

$i = 1, C, N$

4.4 Comparative Results

4.4.1 Static results

To demonstrate how this distributed-parameter plate theory compares to existing results, let us consider the plate given in Fig. 4.4 to be simply supported and subjected to the following static surface load

$$q = q_o \sin\left(\frac{\pi x}{W}\right) \sin\left(\frac{\pi y}{L}\right) \quad (4.51)$$

Accordingly, with the plate being simply supported, the boundary conditions are

$$\begin{aligned} w\left(x, \frac{-L}{2}\right) &= w\left(x, \frac{L}{2}\right) = w\left(\frac{-W}{2}, y\right) = w\left(\frac{W}{2}, y\right) = 0 \\ Y_y^{(i)}\left(x, \frac{-L}{2}\right) &= Y_y^{(i)}\left(x, \frac{L}{2}\right) = Y_x^{(i)}\left(\frac{-W}{2}, y\right) = Y_x^{(i)}\left(\frac{W}{2}, y\right) = 0 \\ M_y^{(i)}\left(x, \frac{-L}{2}\right) &= M_y^{(i)}\left(x, \frac{L}{2}\right) = M_x^{(i)}\left(\frac{-W}{2}, y\right) = M_x^{(i)}\left(\frac{W}{2}, y\right) = 0 \\ \gamma_y^{(i)}\left(x, \frac{-L}{2}\right) &= \gamma_y^{(i)}\left(x, \frac{L}{2}\right) = \gamma_x^{(i)}\left(\frac{-W}{2}, y\right) = \gamma_x^{(i)}\left(\frac{W}{2}, y\right) = 0 \end{aligned} \quad (4.52)$$

$$i = 1, C, N.$$

Use of the Naiver approach described by Whitney¹⁴⁰ permits us to solve Eq. (4.49). For simplicity, consider the plate to be composed of three layers, i.e. $N = 3$, where the actuator layer is sandwiched between two identical face aluminum sheets with constant thickness. Table 4.1 provides the assumed properties for the plate.

For this case, Eq. (4.49) is greatly reduced because all time derivatives are set to zero and several of the plate stiffnesses are identically zero. From Table 4.1 the following stiffnesses fall into this category

$$\begin{aligned} B_{lk} &= E_{lk} = J_{lk} = 0 & l, k &= 1, 2, 4, 5, 6 \\ A_{16}^{(i)} &= A_{26}^{(i)} = D_{16}^{(i)} = D_{26}^{(i)} = F_{16}^{(i)} = F_{26}^{(i)} = K_{16}^{(i)} = K_{26}^{(i)} = 0 \end{aligned} \quad (4.53)$$

Table 4.1 - Material and geometric properties for the plate configuration.

Structural Layers		Actuator Layers	
Property ($i = 1,3$)	Specifications	Property ($i = 2$)	Specifications
Material	Aluminum Sheet	G'	1.225 MPa
L	31.2 cm	ν (<i>Poisson</i>)	0.45
W	31.2 cm	ν_{in} (<i>volume</i>)	0.15
H	0.1143 cm	ν_{fl} (<i>volume</i>)	0.85
$E^{(i)}$	68.5 GPa	ρ	1224.1 kg /m ³
ρ	2714.3 kg /m ³	$E^{(i)}$	1.225 MPa
$\nu^{(i)}$ (<i>Poisson</i>)	0.334	q_o	1 N
$h^{(i)}$	0.50 mm	W	31.2 cm

$$A_{45}^{(i)} = D_{45}^{(i)} = F_{45}^{(i)} = 0$$

$$i = 1, C, N \quad (4.53\text{con't})$$

and using Eq. (3.15) the core stiffness reduces to

$$\sigma_{xz}^C = \nu_{in} G' (0) \epsilon_{xz}^C \quad (4.54a)$$

$$\sigma_{yz}^C = \nu_{in} G' (0) \epsilon_{yz}^C \quad (4.54b)$$

Following the Naiver procedure, we assume a solution which satisfies Eq. (3.52) and is of the following form

$$w = \sum_{m,n=1}^{\infty} W_{mn} \sin\left(\frac{\pi x}{W}\right) \sin\left(\frac{\pi y}{L}\right)$$

$$\gamma_x^{(i)} = \sum_{m,n=1}^{\infty} X_{mn}^{(i)} \cos\left(\frac{\pi x}{W}\right) \sin\left(\frac{\pi y}{L}\right)$$

$$\gamma_y^{(i)} = \sum_{m,n=1}^{\infty} Y_{mn}^{(i)} \sin\left(\frac{\pi x}{W}\right) \cos\left(\frac{\pi y}{L}\right)$$

$$i = 1, C, N \quad (4.55)$$

where W_{mn} , $X_{mn}^{(i)}$ and $Y_{mn}^{(i)}$ are unknown constants to be determined. By substituting Eq. (4.55) into Eq. (4.49), these seven constants can be solved for algebraically. For brevity the equations are not shown.

Results for the maximum nondimensionalized deflections, \bar{w} , of the plate are given in Table 4.2 for various values of W/H , hence various actuator thicknesses. Note that the length-to-thickness ratios used in this section would not be practical for this type of structure, but are only used for comparison purposes. Below, these results are compared to an exact three-dimensional elasticity solution obtained by Pagano.¹⁰⁸ It shows from these results that good agreement between this theory and exact solutions are obtained over a wide range of aspect ratios. However, for large aspect ratios, ER plate deflection is slightly higher than the elasticity solution. This is expected because the three dimensional effects occurring in this model have been neglected. Also, because this theory has been based on sandwich plate theory and constrained layer theory, the in-plane stresses in the core have been assumed to vary linearly through-the-thickness. This means that for all plate aspect ratios, this theory will greatly over-predict the true shearing stresses unless shear correction factors are used.¹¹² It would be highly effective to use shear correction factors, espe-

Nondimensionalized Deflections		
W/H	Pagano ¹⁰⁸	ER Plate
4	0.682	0.49128
10	0.2191	0.16537
50	0.9761	1.05721
100	0.0951	0.09684
$\bar{w} = 10 \left(\frac{wH^3 E^{(1)}}{q_o W^4} \right) \quad w(0,0)$		

Table 4.2 - Nondimensionalized deflections for two three-layer sandwich plates.

cially when integrating the shear stresses for this plate, because good predictions are necessary due to the nature of the actuator and its dependence on the shear rate.

4.4.2 Dynamic results

A finite element analysis of the distributed-parameter plate was conducted to obtain results for its dynamic behavior. Square and rectangular plate configurations were investigated, both had the same dimensions and geometries as the plates given in Fig. 3.25. The nonlinear rule-of-mixtures material model developed in Chapter 3 was implemented for the actuator. For simplicity, the same actuator material is always sandwiched between structural faces of identical geometry and material properties. Furthermore, all structures are symmetric about their midplanes. An examination of the frequency response for steady-state excitations was conducted for free-edge and fixed-edge boundary conditions in order to compare with experimental results in Chapter 3. Modal natural frequencies and damping factors were estimated for both cases and for various constant voltages to set bounds on physical parameter uncertainty.

The plates were discretized using 200 reduced integration, eight-node, second order shell elements with thick shell control. In ABAQUS, the shell element has several unique qualities that make it a good candidate for these structures. Its shell elements are provided with a composite material option that allows us to select the number of integration points through-the-thickness. The number was set to 3 integration points for the structural layers and 5 for the actuator layers. The shell element also includes a transverse shear option that permits the use of shear correction factors. For the sandwich structures considered here these factors are evident in the following equation

$$(Q_x, Q_y) = \int_{-H/2}^{H/2} (k_5 \sigma_{xz}, k_6 \sigma_{yz}) dz \quad (4.56)$$

where k_5 and k_6 are the shear correction factors about the y and x axes, respectively. For these structures $k_5 = 0.4098$ and $k_6 = 0.6915$, which are reasonable for sandwich structures.¹⁴⁰ Finally,

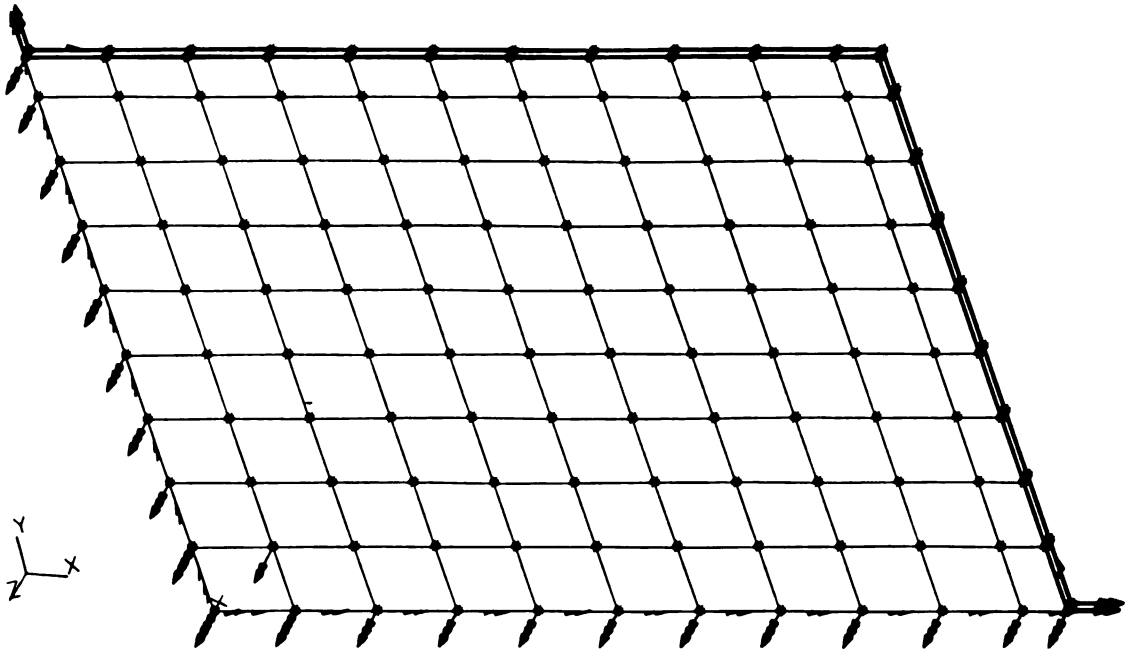


Figure 4.5 - Discretized geometry for a quarter of the distributed-parameter rectangular plate.

the thick shell element used here is able to accommodate full six degree-of-freedom models, whereas the solid brick element would be limited to the three displacements, and would not include the necessary nodal rotations experienced by such a low stiffness structure. An illustration of one quarter of the discretized rectangular plate, shown as a solid model, is presented in Fig. 4.5. Notice that the aspect ratio around the edges was reduced to obtain better solution convergence due to three dimensional free-edge effects.

Figure 4.6 is an illustration of several zero voltage displaced mode shapes for the identical three-layered structures used in the experimental analysis. These mode shapes were computed using a linear subspace routine available in ABAQUS.¹ The flat area in the center of both plates represents the 3 cm square clamping fixture used to attach the plate to the shaker. Due to the magnification of the modes, its appearance seem to have a large effect on the results. We see many similarities between the experimentally observed results in Fig. 3.33 and these results. However, one disadvantage in making the experimental observations is that very close mode shapes of low

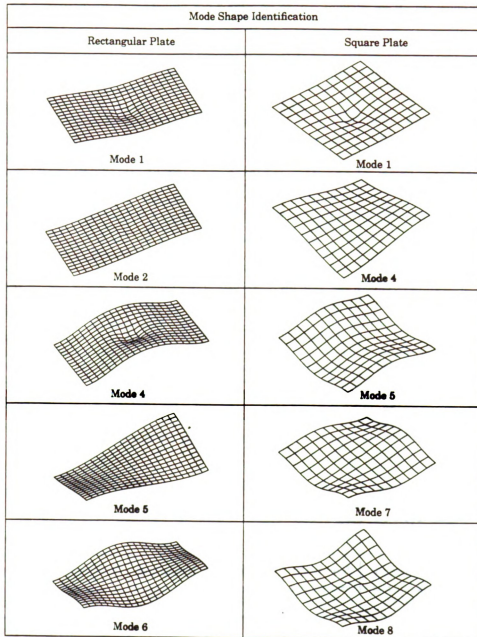


Figure 4.6 - Mode shape results for both plates at $V = 0$ kV.

Table 4.3 - Comparison of measured and computed natural frequencies for the square plate.

Square Plate Response for Constant Voltage Inputs						
Natural Frequency (Hz)	V = 0 kV		V = 1 kV		V = 2 kV	
	measured	computed	measured	computed	measured	computed
ω_1	19.50	19.699	22.06	21.53	23.94	22.96
ω_2		25.525		28.25		29.923
ω_3		25.525		28.25		29.923
ω_4	37.87	41.556	41.47	44.76	63.50	47.036
ω_5	64.56	60.585	71.15	65.58	72.28	69.92
ω_6		70.821		78.072		82.821
ω_7		70.821		78.072		82.821
ω_8	118.3	93.574	126.35	105.48	129.065	113.54

Table 4.3 - Comparison of measured and computed natural frequencies for the rectangular plate.

Rectangular Plate Response for Constant Voltage Inputs						
Natural Frequency (Hz)	V = 0 kV		V = 1 kV		V = 2 kV	
	measured	computed	measured	computed	measured	computed
ω_1	15.52	15.073	19.76	22.45	24.53	25.062
ω_2		17.9		24.85		28.595
ω_3	31.36	29.21	33.21	36.763	35.76	45.763
ω_4	53.15	53.34	54.3	55.914	55.45	56.020
ω_5		68.095		70.577		74.971
ω_6		83.223		83.223		88.663
ω_7	76.35	87.576	132.12	102.76	135.11	111.15
ω_8		104.25		111.025		127.29

magnitude were indeterminable. For this reason, several modes have been omitted in order to compare the two sets of analysis results. It appears that ABAQUS has no problem computing mode shapes that reside only fractions of a frequency apart. In Tables 4.3 and 4.4, natural frequencies for both plates are given for the identified mode shapes in Fig. 3.3 and Fig. 4.6. These mode shapes were matched up and compared to computed shapes then their associated natural frequencies were tabulated. The blank entries in Table 4.3 and 4.4 signify computed values for modes that were not observed in the experimental results. For instance, the results for modes 2 and 3 for the square plate occur at the same frequency and are very small as compared to the fundamental and second observed mode shapes. It is evident here that ABAQUS provides good results for the fundamental and second observed modes for all input voltage cases considered. Although, beyond two modes it was very difficult to determine a match for the experimental values because the natural frequencies are very close to one another. This situation was not encountered experimentally, where all mode shapes seemed to be separated over larger ranges.

Table 4.5 - Material properties for the composite structural layers.

Composite Structural Layers	
Property ($k = 1,2$)	Specifications
Material	Graphite / Epoxy
$t_k^{(i)}$	0.025 mm
$E_{11}^{(i)}$	135 kN /mm ²
$E_{22}^{(i)}$	13 kN /mm ²
$G_{12}^{(i)}$	0.641 kN /mm ²
$G_{13}^{(i)}$	0.641 kN /mm ²
$G_{23}^{(i)}$	0.434 kN /mm ²
$\nu_{12}^{(i)}$	0.38
$\nu_{21}^{(i)}$	0.38
ρ	1553.98 kg /m ³

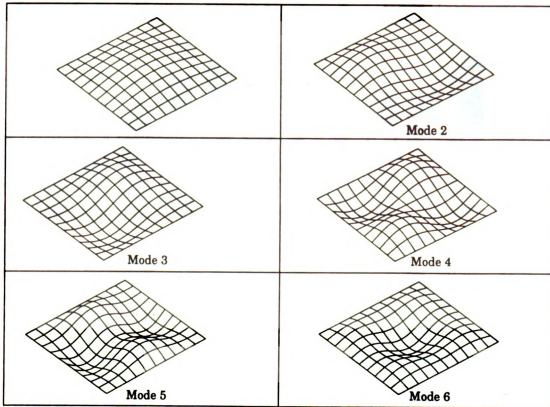


Figure 4.7 - Modes shapes for the clamped-edge square plate.

Good results for the mode shapes and natural frequencies of the first two observed mode shapes permitted an investigation of the variation of natural frequency with the clamped edge boundary condition. Results were obtained for a square clamped-edge plate with the same width and length geometry as given in Table 4.1. However, two specific structural material cases were investigated for $V = 0$ kV. The first case was a plate composed of aluminum structural layers and the second case was a plate composed of a cross-ply, $[0^\circ/90^\circ]$, graphite/epoxy composite. Material data for the plate with the composite structural layers is given in Table 4.5. The mode shapes associated with the first six modes of both plates are given in Fig. 4.7. These mode shapes were identical for both clamped edge cases. It is evident from Fig. 4.7 that modes 2 and 3 must occur at the same natural frequency because mode 3 is just a generalized coordinate shift of mode 2. We also see that the number of node lines increases with $2n$ for this boundary condition

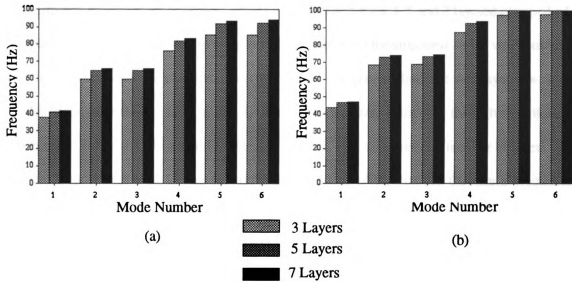


Figure 4.8 -Natural frequencies for a multi-layered square clamped-edge (a) aluminum plate, and (b) composite plate for $V = 0$ kV.

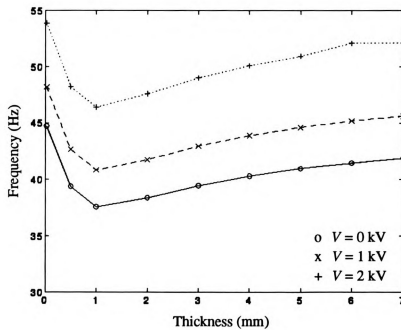


Figure 4.9 -Natural frequencies for a three-layer square clamped-edge aluminum plate with varying actuator layer thickness and $V = 0, 1$ and 2 kV.

Results given in Fig. 4.8 are from an investigation of the variation of natural frequencies with different total number of layers. Values were obtained for a 3, 5 and 7 layered clamped-edge composite and aluminum plate. In each case, the thickness of the structural layers was constant so that the total thickness H changed. For the 5 layer composite plate, the 3rd layer, $i = 3$, was divided into two cross-ply lamina, $k = 4$, in order to maintain symmetry through-the-thickness. As observed in Fig. 4.8, the natural frequency increases with an increasing number of layers. This increase is most significant in Fig. 4.8 (a) for the aluminum plate, although the natural frequencies for the composite plate are larger. In Fig. 4.9, results are shown for a three layer clamped edge aluminum plate with different actuator thicknesses and different voltages. It is apparent that the natural frequency increases with increasing voltage, which is in agreement with experimentally observed results. However, as $h^{(2)}$ increases the natural frequencies begin to approach an asymptotic value. This occurs because bending stiffness is not increasing as rapidly as total plate thickness since structural layer thickness is kept constant. In addition, we see the natural frequencies increasing as $h^{(2)}$ decreases for the converse reason. These values approach the natural frequency of the plate when $h^{(2)} = 0$.

4.5 Chapter Summary

Both analytical and numerical analysis formulations were conducted in this chapter. An analytical model was derived based on a higher-order plate theory. This was further complemented with assumptions from classical sandwich theory and constrained layer theory. Next, the Hamiltonian was used to arrive at the governing equations of motion and associated boundary conditions. It was shown for static loading conditions, using the Navier approach, that close agreement with previously published results was possible. Time constraints did not permit a full dynamic investigation of the analytical model. Numerical results were presented with the use of a commercial finite-element code. Frequency response results were generated for the two plate configurations considered in Chapter 3. Once again time did not permit a full time-dependent dynamic input

voltage investigation. These computed results showed many similarities between experimentally determined results. Natural frequencies for the first two modes for all voltage inputs are in close agreement despite some difficulty determining whether observed natural frequencies matched with computed values. With the actuator model and structure partially verified, the response of the square plate was examined for various materials, actuator thicknesses, and total number of layers. These results were then compared and contrasted.

Due to the large uncertainty in this analysis it was too difficult to accurately set physical bounds for the distributed-parameter plate considered in this analysis formulation. Uncertainty exists as a result of numerous sources, including: i) inertial damping of the fluid, ii) non-rigid bonding conditions between layers, and iii) the replication of the experimental plate boundary conditions. In fact, uncertainty in this case can be a result of objective and subjective causes. In a subjective manner, uncertainty is introduced due to the extreme variations in the operating conditions and the actuator material. Uncertainty introduced objectively is a result of the inability to replicate the boundary conditions in the experiment to the computer model. These two sources of uncertainty must be reduced in order to set bounds on the structure. One possible way of reducing subjective uncertainty is to use narrowband excitation and determine experimental values for the constitutive model of the actuator. This would allow us to experimentally identify a material model for better comparative purposes. Secondly, to reduce objective uncertainty, we could use simply-supported or clamped-edge boundary conditions instead of the free-edge conditions. Although simply-supported conditions are difficult to completely replicate, they would allow a much better comparison than the free-edge boundary conditions that were used.

Chapter 5

CONCLUDING REMARKS AND RECOMMENDATIONS FOR FUTURE WORK

A generalized outline for a mathematical modeling procedure has been established in the spirit of concurrent engineering. Essentially, this procedure has been developed for evaluating a variety of large-scale system modeling problems that exist at the preliminary and initial stages of design. However, in this study, only a certain class of problems involving smaller scale controlled flexible structures has been considered. The reason being that a large-scale assembly can often be decomposed into conventional beams, plates, and shell structures. These problems in structural control have been addressed by exploiting the highly acclaimed methods of robust control theory and uncertain linear systems analysis and combining them with the salient features of concurrent or simultaneous engineering design and development.

Specifically, this concurrent modeling procedure assumes and treats a mathematical model not as a single and precise model but rather as a set, inside of which the actual system lies. This framework calls for two specific models: (i) a nominal model, and (ii) an uncertainty model. In this procedure, it is taken into consideration that tight time constraints would typically limit the construction of two models during the design process. However, instead of deriving each model in series, both models can be derived concurrently as long as applicable physical laws, assumptions, and equations are available to effectively describe the actual process. Thus, by

using this procedure in the design process, one is able to improve the accuracy of the mathematical model simply by improving the accuracy of the uncertainty model. Therefore, over the course of the product or design development program, and as parameters become more precise, uncertainty models should gradually mature with the structural design and its control system.

In Chapter 2, discussion focussed on how the modeling procedure can be divided into two specific problems: (i) the analysis problem, and (ii) the synthesis problem. In this study, the modeling procedure has been applied to a cantilever beam example and plates containing a distributed-parameter actuator. Both analysis and synthesis problems have been investigated in detail for the cantilever beam, however, only the analysis problem has been completed for the plates. In particular, our results show that this procedure provides models that can be very useful for locating and identifying bounds where the actual system lies. This procedure does have some drawbacks due to its "very" generalized form. Experience plays a large role in selecting uncertainty models, extracting correct analytical and experimental information, and fitting this information to an appropriate model in a judicious manner. For example, throughout the cantilever beam example, it is evident that neither parametric nor nonparametric models can fully satisfy full model uncertainty. Clearly, the very conservative nature of the parametric model at high frequencies severely limits its applicability. To include a parametric model at these frequencies will cause higher modes to become unstable for high controller gains. For this reason, a sequential mixed uncertainty model was chosen because it effectively represents the uncertainty over the selected frequency spectrum. Although, as a consequence, much of this decision-making for choosing a transition frequency was based on prior experience.

Now, the actuator used in the plate analysis formulation is an electrorheological (ER) fluid. Its electrical and rheological properties have been investigated in order to formulate phenomenological equations that would be useful in numerical and analytical analysis. Due to its innate

complexity, an empirical model was developed to describe its rheological properties. This model accounts for the global damping and stiffness properties under the influence of electrical potentials. It has been shown through experimental, numerical, and analytical formulations, that extreme coupling between the electrical and rheological properties produces a "dynamic capacitance" effect that is very difficult to model. Consequently, this characteristic excluded consideration of time-dependent voltage inputs and transient vibration. However, steady-state vibration was investigated and good correlations between the experimental and numerical results were obtained for the first two observed natural frequencies at all voltage levels. Damping was not computed nor looked at in detail because of the limitations of the numerical software. Therefore, uncertainty bounds could not be established for this analysis.

In conclusion, this thesis has been an exposition of a concurrent modeling procedure. Two useful applications have been considered with varying degrees of difficulty. Results from these two models have shown that the procedure is highly dependent on the experience of the person modeling and the complexity of the problem at hand. Despite these disadvantages the framework of this modeling procedure, which is based on uncertain linear systems analysis and robust control theory, yields good practical controllers. Thus, future work will include the full integration of this procedure within a process that can accommodate simultaneous structure and controller design and optimization.

BIBLIOGRAPHY

BIBLIOGRAPHY

1. **ABAQUS User's Manual**, Version 5.2, Hibbitt, Karlsson, and Sorenson, Providence, Rhode Island, 1992.
2. Al-Saggaf, U. and Bettayeb, M., "Techniques in Optimized Model Reduction for High Dimensional Systems," *Control and Dynamic Systems*, Vol. 55, Part 1 of 2, 1993, pp. 51-110.
3. Anderson, B.D., Bose, N.K., and Jury, E.I., "Output Feedback Stabilization and Related Problems - Solution Via Decision Methods," *IEEE Transactions on Automatic Control*, AC-20, 1976, pp. 53-66.
4. Anderson, B.D.O. and Liu, Y., "Controller Reduction: Concepts and Approaches," *IEEE Transactions on Automatic Control*, Vol. 34, No. 8, Aug. 1989, pp. 802-812.
5. Anderson, J.C., *Dielectrics*, Reinhold Publishing, New York, 1964.
6. Arockiasamy, M., Neelakanta, P.S., and Sreenirasan, G., "Vibration Control of Beams with Embedded Smart Composite Materials," *Journal of Aerospace Engineering*, Vol. 5, No. 4, 1992, pp. 492-498.
7. Bailey, T. and Hubbard, J.E., "Distributed Piezoelectric-Polymer Active Vibration Control of a Cantilever Beam," *AIAA Journal of Guidance and Control*, Vol. 6, No. 5, 1985, pp. 605-611.
8. Balas, M.J., "Enhanced Modal Control of Flexible Structures Via Innovations Feedthrough," *International Journal of Control*, Vol. 32, No. 6, 1980, pp. 983-1003.
9. Balas, M.J., "Feedback Control of Flexible Systems," *IEEE Transactions on Automatic Control*, AC-23, 1978, pp. 673-679.

10. Balas, M.J., "Trends in Large Space Structure Control Theory: Fondest Hopes, Wildest Dreams," *IEEE Transactions on Automatic Control*, Vol. AC-27, No. 3, 1982, pp. 522-535.
11. Balas, M.J., "Active Control of Flexible Systems," *Journal of Optimization Theory and Applications*, Vol. 25, No. 3, 1978, pp. 415-436.
12. Banks, H.T., Fang, W., Silcox, R.J., Smith, R.C., "Approximation Methods for Control of Structural Acoustics with Piezoceramic Actuators," *Journal of Intelligent Material Systems and Structures*, Vol. 4, No. 1, 1993, pp. 98-116.
13. Bar-kana, I. and Kaufman, H., "Some Applications of Direct Adaptive Control to Large Structural Systems," *AIAA Journal of Guidance, Control, and Dynamics*, Vol. 7, No. 6, 1984, pp. 717-724.
14. Barker, D.S. and Jacquot, R.G., "Spillover Minimization in the Control of Self-Adjoint Distributed Parameter Systems," *Journal of Astronautical Sciences*, Vol. 34, No. 2, 1986, pp. 133-146.
15. Barnes, H.A., Hutton, J.F., and Walters, K., *An Introduction to Rheology*, Rheology, Series No. 3, Elsevier, New York, 1989.
16. Barrett, D.J., "The Effect of Compliant Layering on Damped Beams," *Proceedings of Damping '91*, Vol. 1, Feb 13-15, San Diego, California, 1991, pp. BBB-1-19.
17. Bauchau, O.A., "A Beam Theory for Anisotropic Materials," *Journal of Applied Mechanics*, Vol. 52, No. 2, 1985, pp. 416-422.
18. Bayard, D., Yam, Y., Mettler, E., Hadaegh, F., Milman, M., and Scheid, R., "Automated On-Orbit Frequency Domain Identification for Large Space Structures," *NASA Tech Briefs*, Vol. 16, No. 5, Item #99.
19. Baz, A. and Poh, S., "Optimum Vibration Control of Flexible Beams by Piezoelectric Actuators," *NASA CR-180209*.
20. Belknap, F.M. and Kosmatka, J.B., "Vibration Suppression of Thin-Walled Composite Tubes Using Embedded Viscoelastic Layers," *Proceedings of Damping '91*, Vol. 2, Feb 13-15, San Diego, California, 1991, pp. HAC-1-16.

21. Ben-Arich, D., "Modeling and Control of Discrete Manufacturing Systems using Graphical Concurrent Modeling Language," *Control and Dynamic Systems*, Vol. 48, Part 4 of 5, 1991, pp. 47-74.
22. Bingham, E.C., *Fluidity and Plasticity*, McGraw-Hill, New York, 1922.
23. Bird, R.B., Doi, G.C., and Yarusso, B.J., "The Rheology and Flow of Viscoplastic Materials," *Reviews in Chemical Engineering*, Vol. 1, 1983, pp. 1-70.
24. Block, H. and Kelly, J.P., "Electro-Rheology," *Journal of Physics Digest*, Vol. 21, 1988, pp. 1661-77.
25. Bollough, W.A. and Foxon, M.B., "A Proportionate Coulomb and Viscously Damped Isolation System," *Journal of Sound and Vibration*, Vol. 56, No. 1, 1978, pp. 35-44.
26. Bonnecaze, R.T. and Brady, J.F., "Yield Stresses in Electrorheological Fluids," *Journal of Rheology*, Vol. 36, No. 1, January 1992, pp. 73-115.
27. Borthroyd, G. and Dewhurst, P., "Path to Concurrent Engineering," *Design News*, Vol. 48, No. 16, August 24, 1992, pg. 98.
28. Boyd, S.P. and Barratt, C.H., *Linear Controller Design*, Prentice-Hall, Englewood-Cliffs, New Jersey, 1991.
29. Brogan, W.L., *Modern Control Theory*, Quantum Publishers, New York, 1974.
30. Bruch, J.C., Sloss, J.M., Adali, S., and Sadek, I.S., "Orthotropic Plates with Shear Rotation Subject to Optimal Open-Closed Loop Control," *The Journal of the Astronautical Sciences*, Vol. 38, No. 1, 1990, pp. 105-119.
31. Cannon, R.H., Jr., and Schmitz, E., "Precise Control of Flexible Manipulators," *Robotics Research*, 1984, pp. 841-861.
32. Chawla, K.K., *Composite Materials*, Springer-Verlag, New York, 1987.
33. Chen, J. and Fanson, J., "System Identification Test Using Active Members," *NASA Tech Brief*, Vol. 16, No. 6, Item #75, June 1992.

34. Chen, Y.H. and Chen, J.S., "Adaptive Robust Control of Uncertain Systems," *Control and Dynamic Systems*, Vol. 50, Part 1 of 2, 1992, pp. 175-221.
35. Chiang, C.K., Gray, Jr., C.E., and Mei, C., "Finite Element Large Amplitude Free and Forced Vibrations of Rectangular Thin Composite Plates," *Vibration and Behavior of Composite Structures*, eds. C. Mei, H.F. Wolfe, and I. Elishakoff, ASME-AD-Vol. 14, American Society of Engineering, Dec. 1989, pp. 53-64.
36. Chiang, R.Y. and Safonov, G., *Robust-Control Toolbox User's Guide*, The MathWorks, South Natick, Massachusetts, 1988.
37. Conrad, H., Sprecher, A.F., Choi, Y., and Chen, Y., "The Temperature Dependence of the Electrical Properties and Strength of Electrorheological Fluids," *Journal of Rheology*, Vol. 35, No. 7, October 1991, pp. 1393-1410.
38. Coulter, J.P. and Duclos, T.G., "Applications of Electrorheological Materials in Vibration Control," *Electrorheological Fluids*, Proceedings of the Second International Conference of ER Fluids, J.D. Calson, A.F. Sprecher, and H. Conrad, eds., Raleigh, North Carolina, August 7-9, 1989, pp. 300-325.
39. Crawley, E.F. and de Luis, J., "Use of Piezoelectric Actuators as Elements of Intelligent Structures," *AIAA Journal*, Vol. 25, No. 10, 1987, pp. 1373-1385.
40. Creedon, J.F. and Lindgren, A.G., "Control of the Optical Surface of a Thin, Deformable Primary Mirror with Application to An Orbiting Astronomical Observatory," *Automatica*, Vol. 6, 1970, pp. 643-660.
41. Curtain, R.F., "Pole Assignment for Distributed Systems by Finite-Dimensional Control," *Automatica*, Vol. 21, 1985, pp. 57-67.
42. Davison, E.J., "A Method for Simplifying Linear Dynamic Systems," *IEEE Transactions on Automatic Control*, Vol. AC-11, No. 1, 1966, pp. 93-101.
43. Deinega, Y.F. and Vinogradov, G.V., "Electric Fields in the Rheology of Disperse Systems," *Rheologica Acta*, Vol. 23, No. 6, 1984, pp. 636-651.
44. Desoer, C.A. and Vidyasagar, M., *Feedback Systems: Input-Output Properties*, Academic, New York, 1975.

45. Dimitriadis, E.K., Fuller, C.R., and Rogers, C.A., "Piezoelectric Actuators for Distributed Vibration Excitation of Thin Plates," *Journal of Vibrations and Acoustics*, Vol. 113, No. 1, 1991, pp. 100-107.
46. Dowell, E.H. and Yan, M.J., "Governing Equations for Vibrating Constrained-Layer Damping Sandwich Plates and Beams," *Journal of Applied Mechanics*, Vol. 39, No. 4, 1972, pp. 1081-86.
47. Doyle, J.C., Wall, J.E., and Stein, G., "Performance and Robustness for Structured Uncertainty," *IEEE Transactions on Automatic Control*, Vol. AC-26, No. 1, pp. 629-636.
48. Doyle, J.C. and Stein, G., "Multivariable Feedback Design: Concepts for a Classical/Modern Synthesis," *IEEE Transactions on Automatic Control*, AC-26, No. 4, 1981.
49. Fanson, J.L. and Chen, J.C., "Structural Control by the Use of Piezoelectric Members," Proceedings of NASA/DOD Control-Structures Interaction Conference, NASA CP-2447, Part II.
50. Felici, N.J., *Reviews in General Electricity*, Vol. 76, 1967, p. 786.
51. Flügge, W., *Viscoelasticity*, Blaisdell Publishing Co., Waltham, Massachusetts, 1975.
52. Gamota, D.R. and Filisko, F.E., "Dynamic Mechanical Studies of Electrorheological Materials: Moderate Frequencies," *Journal of Rheology*, Vol. 35, No. 3, April 1991, pp. 399-427.
53. Gamota, D.R. and Filisko, F.E., "High Frequency Dynamic Mechanical Study of an Aluminosilicate Electrorheological Material," *Journal of Rheology*, Vol. 35, No. 7, October 1991, pp. 1411-15.
54. Gandhi, M.V., Thompson, B.S., Choi, S.B., and Shakir, S., "Electro-Rheological-Fluid-Based Articulating Robotic Systems," *Journal of Mechanisms, Transmissions, and Automation in Design*, Vol. 111, No. 3, Sept. 1989, pp. 328-336.
55. Gandhi, M.V. and Thompson, B.S., *Smart Materials and Structures*, Chapman & Hall, London, 1992.

56. Gandhi, M.V. and Usman, M., "Equilibrium Characterization of Fluid-Saturated Continua and An Interpretation of the Saturation Boundary Condition Assumption for Solid-Fluid Mixtures," *International Journal of Engineering Science*, Vol. 27, No. 5, 1989, pp. 539-548.
57. Gibson, J.S., "An Analysis of Optimal Modal Regulation: Convergence and Stability," *SIAM Journal on Control and Optimization*, Vol. 19, No. 5, 1981, pp. 686-707.
58. Goh, C.J. and Caughey, T.K., "On the Stability Problem Caused by Finite Actuator Dynamics in the Collocated Control of Large Space Structures," *International Journal of Control*, Vol. 41, No. 3, 1985, pp. 787-802.
59. Goh, C.J. and Caughey, T.K., "A Quasi-Linear Vibration Suppression Technique for Large Space Structures Via Stiffness Modification," *International Journal of Control*, Vol. 41, No. 3, 1985, pp. 803-811.
60. Goldstein, H. *Classical Mechanics*, 2nd ed., Addison-Wesley Publishing Co., Massachusetts, 1980.
61. Greeley, S.W. and Hyland, D.C., "Reduced Order Compensation: LQG Reduction Versus Optimal Projection Using A Homotopic Continuation Method," Proceedings of the 26th IEEE Conference on Decision and Control, Los Angeles, CA, 1987, pp. 742-747.
62. Hagedorn, P. Kelkel, K. and Wallaschek, J., *Vibrations and Impedance of Rectangular Plates with Free Boundaries*, Springer-Verlag Lecture Notes in Engineering, eds. C.A. Brebbia and S.A. Orszay, No. 23, 1986.
63. Harel, D. and Pnoeli, A., "On the Development of Reactive Systems," ed. by K.R. Apt, *Logic and Models of Concurrent Systems*, Springer-Verlag, New York, 1985, pp. 477-498.
64. Hughes, P.C., "Space Structure Vibration Modes: How Many Exist? Which Ones are Important?," *IEEE Control Systems Magazine*, Feb. 1987, pp. 22-28.
65. Hyland, D.C. and Bernstein, D.S., "The Optimal Projection Equations for Fixed-Order Dynamic Compensation," *IEEE Transactions on Automatic Control*, Vol. AC-29, 1985, pp. 1034-1037.
66. Im, S. and Atluri, S.N., "Effects of a Piezo-Actuator on a Finitely Deformed Beam Subjected to General Loading," *AIAA Journal*, Vol. 27, No. 12, 1989, pp.1439-1445.

67. Johnson, C.D., Kienholtz, D.A., and Rogers, L.C., "Finite Element Prediction of Damping in Beams with Constrained Viscoelastic Layers," *Shock and Vibration Bulletin*, No. 51, May 1981, pp. 71-81.
68. Jones, R.M., *Mechanics of Composite Materials*, Scripta Book Co., Washington DC, 1975.
69. Jordan, T.C., Shaw, M.T., and McLeish, T.C.B., "Viscoelastic Response of Electrorheological Fluids. II. Field Strength and Strain Dependence," *Journal of Rheology*, Vol. 36, No. 1, January 1992, pp. 441-463.
70. Joshi, S.M., "Robustness Properties of Collocated Controllers for Flexible Spacecraft," *AIAA Journal of Guidance, Control, and Dynamics*, Vol. 9, No.1, 1986, pp. 85-91.
71. Khot, N.S., Eastep, F.E., and Venkaya, V.B., "Simultaneous Optimal Structural/ Control Modifications to Enhance the Vibrational Control of A Large Flexible Structure," *Proceedings of the AIAA Guidance, Navigation, and Control Conference*, 1985, pp. 459-466.
72. Killian, J.W. and Lu, Y.P., "A Finite Element Modeling Approximation for Damping Material Used in Constrained Damped Structures," *Journal of Sound and Vibration*, Vol. 97, No. 2, 1984, pp. 352-354.
73. Kim, C-G and Hong, C-S, "Viscoelastic Sandwich Plates with Cross-Ply Faces," *Journal of Structural Engineering*, Vol. 114, No. 1, January 1988, pp. 150-164.
74. Kirk, D.E., *Optimal Control Theory*, Prentice-Hall, Englewood-Cliffs, New Jersey, 1970.
75. Klass, D.L. and Martinek, T.W., "Electroviscous fluids: I. Rheological properties; II. Electrical properties." *Journal of Applied Physics*, Vol. 38, 1967. p. 67.
76. Korobko, E.V. and Shulman, Z.P., "Viscoelastic Behaviour of Electrorheological Fluids," *Electrorheological Fluids*, *Proceedings of the Second International Conference of ER Fluids*, J.D. Calson, A.F. Sprecher, and H. Conrad, eds., Raleigh, North Carolina, August 7-9, 1989, pp. 3-13.
77. Kraynik, A.M., "Comments on ER Fluid Rheology," *Electrorheological Fluids*, *Proceedings of the Second International Conference of ER Fluids*, J.D. Calson, A.F. Sprecher, and H. Conrad, eds., Raleigh, North Carolina, August 7-9, 1989, pp. 445-455.

78. Lall, A.K., Asnani, N.T., and Nakra, B.C., "Damping Analysis of Partially Covered Sandwich Beams," *Journal of Sound and Vibration*, Vol. 123, No. 2, 1988, pp. 247-259.
79. Larson, R.G. and Monroe, K., "The BKZ as an Alternative to the Wagner Model for Fitting Shear and Elongation Flow Data of an LDPE Melt," *Rheologica Acta*, Vol. 23, No. 6, 1984, pp. 10-13.
80. Lee, A. and Tsuha, W., "Enhanced Method of Reduction of Dynamical Models," *NASA Tech Brief*, Vol. 16, No. 7, Item #68, July 1992.
81. Lekszycki, T., Olhoff, N., and Pedersen, J.J., "Modelling and Identification of Viscoelastic Properties of Vibrating Sandwich Beams," *Composite Structures*, Vol. 22, No. 1, 1992, pp. 15-31.
82. Lenz, K., Özbay, H., Tannenbaum, A., Janus, T., and Morton, B., "Frequency Domain Analysis and Robust Control Design for an Ideal Flexible Beam," *Automatica*, Vol. 27, No. 6, 1991, pp. 947-961.
83. Leonhard, A., "Determination of Transient Response from Frequency Response," *Frequency Response*, ed. by R. Oldenbyrger, The MacMillan Co., 1953.
84. Lin, J.G., Hegg, D.R., Lin, Y.H., and Keats, J.E., "Output Feedback Control of Large Space Structures: An Investigation of Four Design Methods," *Proceedings of 2nd Symposium on Dynamics and Control of Large Flexible Spacecraft*, Blacksburg, Virginia, 1979, pp. 1-18.
85. Lions, J.L., "Remarks on the Theory of Optimal Control of Distributed Systems," *Control Theory of Systems Governed by Partial Differential Equations*, A.K. Aziz, J.W. Wingate, and M.J. Balas, eds., Academic Press, New York, 1976, pp. 1-103.
86. Lundén, R., "Optimum Distribution of Additive Damping for Vibrating Beams," *Journal of Sound and Vibration*, Vol. 66, No. 1, 1979, pp. 25-37.
87. McLeish, T.C.B, Jordan, T., and Shaw, M.T. "Viscoelastic Response of Electrorheological Fluids. I. Frequency Dependence," *Journal of Rheology*, Vol. 35, No. 3, April 1991, pp. 427-448.

88. Maghami, P.G. and Joshi, S.M., "Sensor-Actuator Placement for Flexible Structures with Actuator Dynamics," *Journal of Guidance, Control, and Dynamics*, Vol. 16, No. 2, 1993, pp. 301-307.
89. Mead, D.J. and Markus, S., "The Forced Vibration of a Three-Layer, Damped Sandwich Beam with Arbitrary Boundary Conditions," *Journal of Sound and Vibration*, Vol. 10, No. 2, 1969, pp. 163-175.
90. Mead, D.J. and Markus, S., "Loss Factors and Resonant Frequencies of Encastré Damped Sandwich Beams," *Journal of Sound and Vibration*, Vol. 12, No. 1, 1970, pp. 99-112.
91. Meirovitch, L. and Öz, H., "Modal-Space Control of Distributed Gyroscopic Systems," *Journal of Guidance and Control*, Vol. 3, No. 2, 1980, pp. 140-150.
92. Meirovitch, L. and Baruh, H., "Effect of Damping on Observation Spillover Instability," *Journal of Optimization Theory and Applications*, Vol. 35, No. 1, 1981, pp. 31-44.
93. Meirovitch, L. and Baruh, H., "Control of Self-Adjoint Distributed-Parameter Systems," *Journal of Guidance and Control*, Vol. 5, No. 1, 1982, pp. 60-66.
94. Meirovitch, L. and Norris, M.A., "Vibration Control," *Proceedings of Inter-Noise*, 1984, pp. 477-482.
95. Meirovitch, L., *Dynamics and Control of Structures*, John Wiley & Sons, New York, 1990.
96. Middleton, R.H., "Trade-offs in Linear Control Design," *Automatica*, Vol. 27, No. 2, 1991, pp. 281-292.
97. Milanese, M. and Vicino, A., "Optimal Estimation Theory for Dynamic Systems with Set Membership Uncertainty: An Overview," *Automatica*, Vol. 27, No. 6, 1991, pp. 997-1009.
98. Mills, R., Beckert, B., Kempfer, L., and Chakma, J., "Technology for World-Class Engineering," *Machine Design*, Vol. 64, No. 14, July 23, 1992, pp. CC1-CC10.
99. Milman, M., Salama, M., Scheid, R., Bruno, R., and Gibson, J.S., "Continuation Methods in Multiobjective Optimization for Combined Structure Control Design," *NASA Tech Brief*, Vol. 16, No. 7, #64, July 1992.

100. Moore, A.D., ed., *Electrostatics and its Applications*, John Wiley & Sons, New York, 1973.
101. Morari, M. and Zafiriou, E., *Robust Process Control*, Prentice-Hall, Englewood Cliffs, New Jersey, 1989.
102. Nashif, A.D., Jones, D.I.G., and Henderson, J.P., *Vibration Damping*, J. Wiley & Sons, New York, 1985.
103. Nokes, D.S. and Nelson, F.C., "Constrained Layer Damping with Partial Coverage," *Shock and Vibration Bulletin*, No. 38, Part 3, Nov. 1968, pp. 5-12.
104. Olson, H.F., "Electronic Control of Noise, Vibration, and Reverberation," *The Journal of the Acoustical Society of America*, Vol. 28, No. 5, 1956, pp. 966-972.
105. Onoda, J. and Haftka, R.T., "An Approach to Structural/Control Simultaneous Optimization for Large Flexible Spacecraft," *AIAA Journal*, Vol. 25, No. 8, 1987, pp. 1133-1138.
106. Ortega, R., "Adaptive Control of Discrete-Time Systems: A Performance-Oriented Approach," *Control and Dynamic Systems*, Vol. 55, Part 1 of 2, 1993, pp. 471-516.
107. O'Young, S.O., and Francis, B.A., "Optimal Performance and Robust Stabilization," *Automatica*, Vol. 22, No. 1, 1986, pp. 171-183.
108. Pagano, N.J., "Exact Solutions for Rectangular Bidirectional Composites and Sandwich Plates," *Journal of Composite Materials*, Vol. 4, 1970, pp. 20-35.
109. Pahl, G. and Beitz, W., *Engineering Design*, ed. by K. Wallace, Springer-Verlag, The Design Council, London, 1988.
110. Pierson, B.L., "An Optimal Control Approach to the Design of Vibrating Elastic-Viscoelastic Sandwich Beams," *Computer Methods in Applied Mechanics*, Vol. 57, No. 1, 1986, pp. 37-49.
111. Reddy, A.S.S.R., "A Method for Frequency Domain Simplification of Transfer Functions," *International Journal of Control*, Vol. 23, No. 3, 1976, pp. 403-408.

112. Reddy, J.N., "A Simple Higher-Order Theory for Laminated Composite Plates," *Journal of Applied Mechanics*, Vol. 51, No. 3, 1984, pp. 745-752.
113. Reiner, E.S. and Radke, C.J., "Electrostatic Interactions in Colloidal Suspensions: Tests of Pairwise Additivity," *AIChE Journal*, Vol. 37, No. 6, June 1991, pp. 805-824.
114. Rogers, C.A., "Intelligent Material Systems- The Dawn of a New Materials Age," *Journal of Intelligent Material Systems and Structures*, Vol. 4, No. 1, 1993, pp. 4-12.
115. Sakawa, Y. and Luo, Z., "Modeling and Control of Coupled Bending and Torsional Vibrations of Flexible Beams," *IEEE Transactions on Automatic Control*, Vol. 34, No. 9, Sept 1989, pp. 970-977.
116. Sastry, S.S. and Isidori, A., "Adaptive Control of Linearizable Systems," *IEEE Transactions on Automatic Control*, Vol. 34, No. 11, Nov. 1989, pp. 1123-1131.
117. Sattinger, S.S., "Direct Method for Measuring the Dynamic Shear Properties of Damping Polymers," Chapter 5 of *Sound and Vibration Damping with Polymers*, R.D. Corsaro and L.H. Sperling, eds., American Chemical Society Symposium Series, 1991, No. 424, pp. 79-91.
118. Schweppe, F.C., *Uncertain Dynamic Systems*, Prentice-Hall, Englewood Cliffs, New Jersey, 1973.
119. Shames, I.H. and Dym, C.L., *Energy and Finite Element Methods in Structural Mechanics*, Hemisphere Publishing Corp., New York, 1985.
120. Shulman, Z.P., Khusid, B.M., Korobko, E.V., and Khizhinsky, E.P., "Damping of Mechanical-Systems Oscillations by a Non-Newtonian Fluid with Electric-Field Dependent Parameters," *Journal of Non-Newtonian Fluid Mechanics*, Vol. 25, No. 2, 1987, pp. 329-346.
121. Sianak, A-H., Firoozian, R., Peel, D.J., Bollough, W.A., "Comparative Methods for the Derivation of In-Flow Electrical Characteristics of Electro-Rheological Fluids," *Journal of Intelligent Material Systems and Structures*, Vol. 3, No. 1, 1992, pp. 96-114.

- 122. Skelton, R.E. and Likins, P.W., "Orthogonal Filters for Modal Error Compensation in the Control of Nonrigid Spacecraft," *AIAA Journal of Guidance, Control, and Dynamics*, Vol. 1, 1978, pp. 41-49.
- 123. Stangroom, J.E., *Physics Technology*, Vol. 14, 1983, pp. 290-296.
- 124. Stanway, R., Sproston, J.L., and Firoozian, R., "Identification of the Damping Law of an Electro-Rheological Fluid: A Sequential Filtering Approach," *ASME Journal of Dynamic Systems, Measurement, and Control*, Vol. 111, No. 1, March 1989, pp. 91-96.
- 125. Stevens, N.G., Sproston, J.L., and Stanway, R., "Experimental Evaluation of a Simple Electroviscous Damper," *Journal of Electrostatics*, Vol. 15, 1984, pp. 275-283.
- 126. Stevens, N.G., Sproston, J.L., and Stanway, R., "The Influence of Pulse D.C. Input Signals on Electrorheological Fluids," *Journal of Electrostatics*, Vol. 17, 1985, pp. 181-191.
- 127. Stevens, N.G., Sproston, J.L., and Stanway, R., "On the Mechanical Properties of Electro-Rheological Fluids," Report, August 1986.
- 128. Takahashi, Y., Rabins, M. J., and Auslander, D. M., *Control and Dynamic Systems*, Addison-Wesley Publishing Co., 1970.
- 129. Tamura, H. and Yoshikawa, T., eds., *Large-Scale Systems Control and Decision Making*, Marcel-Dekkar, New York, 1990.
- 130. Tate, R.E., "Examination of Boundary Conditions for Sixth-Order Damped Beam Theory," *Proceedings of Damping '91*, Vol. 1, Feb 13-15, San Diego, California, 1991, pp. BBA-1-15.
- 131. Tate, R.E., "The Effect of Source Impedance on Damping Measurements Using Resonance Dwell Testing," *Proceedings of Damping '91*, Vol. 2, Feb 13-15, San Diego, California, 1991, pp. IBA-1-14.
- 132. Treasurer, U.Y., Filisko, F.E., and Radzilowski, L.H., "Polyelectrolytes as Inclusions in Electrorheologically Active Materials: Effect of Chemical Characteristics on ER Activity," *Journal of Rheology*, Vol. 35, No. 6, August 1991, pp. 1051-91.

133. Treloar, L.R.G., *The Physics of Rubber Elasticity*, 3rd ed., Oxford University Press, 1975.
134. Tzou, H.S., "Distributed Modal Identification and Vibration Control of Continua: Theory and Applications," *Journal of Dynamic Systems, Measurement, and Control*, Vol. 113, No. 3, Sept. 1991, pp. 494-499.
135. Tzou, H.S. and Tseng, C.I., "Distributed Modal Identification and Vibration Control of Continua: Piezoelectric Finite Element Formulation and Analysis," *Journal of Dynamic Systems, Measurement, and Control*, Vol. 113, No. 3, Sept. 1991, pp. 500-505.
136. Uejima, H., "Dielectric Mechanism and Rheological Properties of Electro-Fluids," *Japanese Journal of Applied Physics*, Vol. 11, No. 3, March 1972, pp. 319-326.
137. Vidyasagar, M., "Input-Output Stability of a Broad Class of Linear Time Invariant Multivariable Systems," *SIAM Journal of Control*, Vol. 13, No. 1, pp. 203-209.
138. Walker, B.M. and Rader, C.P., *Handbook of Thermoplastic Elastomers*, 2nd ed., Van Nostrand Reinhold, New York, 1988.
139. Weiss, K.D., Carlson, J.D., and Coulter, J.P., "Material Aspects of Electrorheological Systems," *Journal of Intelligent Material Systems and Structures*, Vol. 4, No. 1, 1993, pp. 13-34.
140. Whitney, J.M., *Structural Analysis of Laminated Plates*, Technomic Publishing Co., Lancaster, U.K., 1987.
141. Wie, B. and Bernstein, "A Benchmark Problem for Robust Controller Design," *Proceedings of the American Controls Conference*, San Diego, CA, May 23-25, 1990.
142. Yang, B. and Mote, C.D., "On Time Delay in Noncollocated Control of Flexible Mechanical Systems," *Journal of Dynamic Systems, Measurement, and Control*, Vol. 114, No. 3, 1992, pp. 409-413.

- 143. Yen, W.S. and Achorn, P.J., "A Study of the Dynamic Behavior of an Electrorheological Fluid," *Journal of Rheology*, Vol. 35, No. 7, October 1991, pp. 1375-84.
- 144. Zimmerman, D.C., "Structure/Control Synthesis with Nonnegligible Actuator Mass," *Journal of Aerospace Engineering*, Vol. 6, No. 1, 1993, pp.76-89.

MICHIGAN STATE UNIV. LIBRARIES



31293008929667